THE ROLE OF CHD7 IN THE TRANSCRIPTIONAL CONTROL OF HEART DEVELOPMENT

Sophie Payne

University College London

Thesis submitted for the award of

Doctor of Philosophy

Supervisors

Peter Scambler
Philip Stanier

I, Sophie Payne, confirm that the work presented in this thesis is my own. Where information has been derived from other sources, I confirm that this has been indicated in the thesis

ABSTRACT

Chromatin remodelling provides a key mechanism for the regulation of gene expression through dynamic alterations in nucleosome occupancy at promoters and enhancers. Haploinsufficiency for the ATP-dependent chromatin remodeller chromodomain-helicase-DNA-binding protein 7 (CHD7) causes human CHARGE syndrome. CHARGE is characterised by a distinct pattern of congenital anomalies, including cardiovascular malformations, and has traditionally been considered a neurocristopathy. However, a number of the congenital heart defects associated with CHARGE cannot be attributed to disruption to the neural crest alone. This thesis therefore addresses the tissue-specific requirements and roles for CHD7 during cardiogenesis.

CHD7 protein is shown to be present throughout the developing heart until E13.5. Conditional ablation of *Chd7* in the early cardiogenic mesoderm results in embryonic lethality due to severe cardiovascular defects. These include haemorrhaging and oedema, major venous and arterial pole malformations, and disruption to cardiac innervation and vascularisation. To further dissect tissue-specific requirements for CHD7, cardiomyocyte-, second heart field- and endothelial-specific knockdowns were also performed. Each cross results in a milder subset of the cardiac defects observed after mesodermal ablation, indicating that CHD7 is required in multiple lineages within the cardiogenic mesoderm.

Microarray analysis and validation by *in situ* hybridisation were used to identify genes dysregulated in the heart following mesodermal *Chd7* ablation. These included components of the Semaphorin and Slit-Robo signalling pathways, which have known roles in heart development. Furthermore, aberrant expression of genes involved in calcium handling within cardiomyocytes is seen. Excitation-contraction coupling is disrupted in mutant embryonic cardiomyocytes, demonstrating relevance of the gene expression changes at the cellular level.

This work reveals a requirement for CHD7 in mesodermal cardiac progenitors for both inflow and outflow tract development. Novel pathways are identified downstream of CHD7 activity in the developing heart, including the extracellular Semaphorin and Slit-Robo pathways, as well as components of the excitation-contraction coupling machinery.

ACKNOWLEDGEMENTS

I would firstly like to say a huge thank you to my supervisor, Pete, both for giving me the opportunity to undertake my PhD as part of the BHF programme, and for ongoing support throughout the thesis project. Your scientific input and guidance has been invaluable. I have also greatly appreciated the encouragement from my secondary supervisor, Phil, who has supported me along the way and shown such interest in the project.

I have been incredibly lucky to work with a fantastic group of people in "Team CHD7" - thank you all so much!! Karen, for taking such good care of me in my first year and teaching me so much in that time, both your kindness and your baking skills are still much missed in the lab. Nelo, you have been a complete star throughout my whole time here, I'm honestly not sure I could have done it without your friendship and support, and of course your beautiful renditions of the 'going home' song! Matt, thank you for reading through oh-so-many drafts of both the paper and thesis (I like to think that deep-down you secretly enjoyed it!), and of course for the many, many cups of tea. Fancy a brew?! And Joel, you were so much fun to work with, thank you for all the random conversations over genotyping and kebabs, for introducing me to Walter White, and for breaking THAT chair.

There are many more members of Pete's lab and MMU/DBBD, past and present, who have supported me along the way and made it so enjoyable, so thank you to everyone over the past 4 years. In particular - Irinna, thank you for all your help when I first joined the lab and your continued friendship, I cannot think of anyone better to have taught me the dreaded in situ protocol! Dan, your enthusiasm is infectious and you have made me laugh so many times, it has been fantastic to have you as my fellow PhD student. Amelie, Ari, Cath and Sarah, you have all been an amazing source of knowledge on many occasions, as well as being so supportive, I will miss working with you all. Jen, your diligence and willingness to help anyone meant you came to my rescue on many occasions, thank you! You are still very much missed in lab 209. Bekky, it was so great to work with you, and I'm very happy you came back to London for your PhD so we can keep catching up! And lastly, Rowan and Rasha, you have been such lovely office companions over the last year, thank you for all the chats, encouragement, and the free food!

I also owe a huge acknowledgement to Bob Anderson, for all your help with heart anatomy and introducing me to the vestibular spine, and to Sean Davidson, for invaluable help with the calcium imaging. Also to Bertrand Vernay, for amazing microscopy and imaging support;

Angela D'Esposito, for help with the OPT; Albert Basson and his lab, for the many CHD7 collaboration meetings; and to the UCL Genomics Service for performing the microarrays.

Finally, I want to thank my family for their love and support – especially my parents, who have always encouraged me in my studies and without whom I would not have made it this far. This thesis is for you – enjoy! Thank you also to Kate, my best friend for over 20 years now, whose support has even extended to providing me with a home for the last few years. Thank you to you and Ellen for putting up with (and occasionally feeding!) a stressed final-year student in your lovely flat, I will miss you terribly when I move out. And last, but by no means least, thank you to Gary, for your unwavering love, encouragement, kindness, and knowing exactly what to say to cheer me up when experiments didn't work or papers got rejected. You mean the world to me, and I can't wait to actually live in the same country as you – what a novelty!

TABLE OF CONTENTS

LIST OF FIGURES

LIST OF TABLES

NOMENCLATURE

AA	Aortic arch
Ao	Aorta
AP	Aorto-pulmonary (septum)
AV	Atrioventricular
AVSD	Atrioventricular septal defect
BSA	Bovine serum albumen
CAT	Common arterial trunk
CHH	Congenital hypogonadotropic hypogonadism
ChIP	Chromatin immunoprecipitation
CICR	Calcium-induced calcium release
CRU	Calcium release unit
DEPC	Diethyl pyrocarbonate
DGS	DiGeorge syndrome
DILV	Double inlet left ventricle
DORV	Double outlet right ventricle
DSG	Disuccinimidyl glutarate
E	Embryonic day
ESC	Embryonic stem cell
EtOH	Ethanol
FACS	Fluorescence activated cell sorting
FBS	Fetal bovine serum
FHF	First heart field
HAT	Histone acetyl transferase
HDAC	Histone deacetylase
IAA-B	Interrupted aortic arch type B
IHC	Immunohistochemistry

ISH	*In situ* hybridisation
KS	Kallmann syndrome
LA	Left atrium
LCC	Left common carotid artery
LSC	Left subclavian artery
LTCC	L-type calcium channel
LV	Left ventricle
MeOH	Methanol
NCC	Neural crest cell
NMD	Nonsense-mediated degradation
NSC	Neural stem cell
OFT	Outflow tract
P	Postnatal day
PAA	Pharyngeal arch artery
PBS	Phosphate buffered saline
PBT	PBS/0.1% Tween-20
PDA	Patent ductus arteriosus
PE	Proepicardium
PFA	Paraformaldehyde
PSE	Pharyngeal surface ectoderm
RA	Right atrium
RCC	Right common carotid artery
RSC	Right subclavian artery
RyR	Ryanodine receptor
RV	Right ventricle
SHF	Second heart field
SR	Sarcoplasmic reticulum
VSD	Ventricular septal defect

CHAPTER ONE

INTRODUCTION

1.1 Heart and great vessel development

The heart is the first functional organ to form in the embryo, and is essential for embryonic survival. The development of the heart involves a series of tightly-regulated morphological changes, from establishment of a linear myocardial-endocardial tube to looping, chamber formation and septation. Cells from a range of developmental origins contribute to its formation. This section will provide an overview of these complex morphological events in the mouse embryo and the cellular contributions to the developing cardiac structures.

1.1.1 The cardiogenic mesoderm and formation of the linear heart tube

Mesodermal myocardial progenitor cells emerge from the primitive streak at around embryonic day (E)6.5 and migrate in an anterior-lateral direction (Garcia-Martinez and Schoenwolf, 1993) (Figure 1-1, A). As these cells then extend across the midline they form the characteristic 'cardiac crescent' by around E7.5, which sits just under the head fold and comprises differentiated myocardial cells (Figure 1-1, B). These cells then fuse at the midline at E8.0 to form the early heart tube, which from a frontal view resembles an inverted Y (Figure 1-1, C). Already this early structure consists of an interior layer of endocardial cells and an exterior layer of myocardial cells, separated by extracellular matrix, known as cardiac jelly, that is important for signalling between the two layers (Srivastava, 2006). Marking studies using iron oxide have shown that the 'arms' of the Y, which are continuous with the developing venous tributaries of the embryo, are fated to become the atrial chambers, whilst the 'stem' will become the left ventricle (Maria V. de la Cruz, 1991).

The pool of cardiogenic mesodermal cells that forms this primary heart tube is known as the first heart field (FHF) (Buckingham et al., 2005). There is also a more recently-discovered second source of myocardial cells, termed the second heart field (SHF), that lies medially to the FHF and extends into the mesodermal layer of the pharyngeal arches (Kelly et al., 2001; Mjaatvedt et al., 2001; Waldo et al., 2001) (Figure 1-1, B). It is proposed the FHF-myocardial cells provide a scaffold onto which the SHF cells migrate to both poles of the heart in order to extend the heart tube (Kodo and Yamagishi, 2011), where they then contribute to the right ventricle, both atria and the outflow tract (OFT, Figure 1-1, B-E, and Figure 1-5, A).

Concomitant with the extension of the heart tube by SHF cells, the heart tube begins to loop in a rightward direction, from about E8.5 (Figure 1-1, D-E). This looping is initiated by the detachment of the developing left ventricle from the mediastinum, so once liberated the heart tube is able to bend (Moorman et al., 2003). The heart loops in a rightward direction, which is usually considered the first visible sign of asymmetry in the early embryo, although the establishment of the left-right axis occurs much earlier during the gastrulation stage of the embryo (Shiratori and Hamada, 2006).

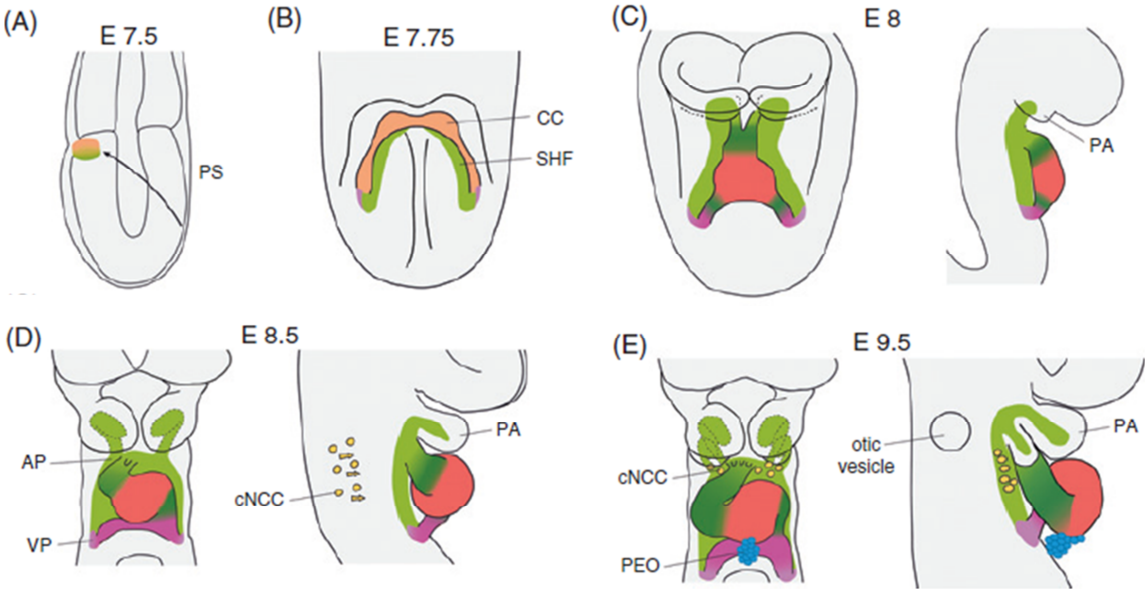

Figure 1-1: Formation and looping of the early heart tube

(A) Migration of mesodermal cardiogenic cells from the primitive streak (PS) at E7.5.

(B) The cardiac crescent (CC, orange) of FHF progenitors is located below the head folds at E7.75, with the SHF (pale green) seen medially.

(C) The primary heart tube of FHF myocardial cells is seen at E8.0, with extension at both poles of myocardium derived from the SHF (dark green). The frontal view (left) shows clearly the inverted Y shape, whilst the lateral view (right) highlights the linear tube. $Tbx18^{+}$ cells that form the sinus venosus are shown in purple.

(D) At E8.5 the heart starts to loop in a rightward direction, and cardiac neural crest cells (cNCC, yellow) start to migrate from the dorsal neural tube towards the heart.

(E) By E9.5 further looping and ballooning of chambers has occurred, and further extension of the heart tube from the SHF. The proepicardial organ (PEO, blue) has also attached to the myocardium and the cardiac NCCs are migrating through the pharyngeal arches towards the arterial pole.

Taken from Vincent (2010). PS indicates primitive streak; CC, cardiac crescent; PA, pharyngeal arch; AP, arterial pole; VP, venous pole; cNCC, cardiac neural crest cells; PEO, proepicardial organ.

1.1.2 Chamber formation and septation

As the linear heart tube undergoes looping, it is segmented into atrial, ventricular and OFT components, with a distinct atrioventricular canal (AVC) separating the atria and ventricles (Figure 1-2, A and B). The apical parts of both right and left regions of the emerging ventricular loop balloon from the outer heart curvature and become trabeculated, which gives each ventricle its characteristic morphology (Moorman and Christoffels, 2003). Similarly, the supero-lateral walls of the atrial component of the primary heart tube also balloon out to both sides of the OFT to give the atrial appendages. By around E10.5-E11.5, once looping is complete, the recognisable chamber components are assembled (Figure 1-2, C). However, the AVC opens to the developing left ventricle, whilst the OFT is supported above the developing right ventricle, so further rearrangement and separation of the right and left sides of the heart is required in a process known as septation.

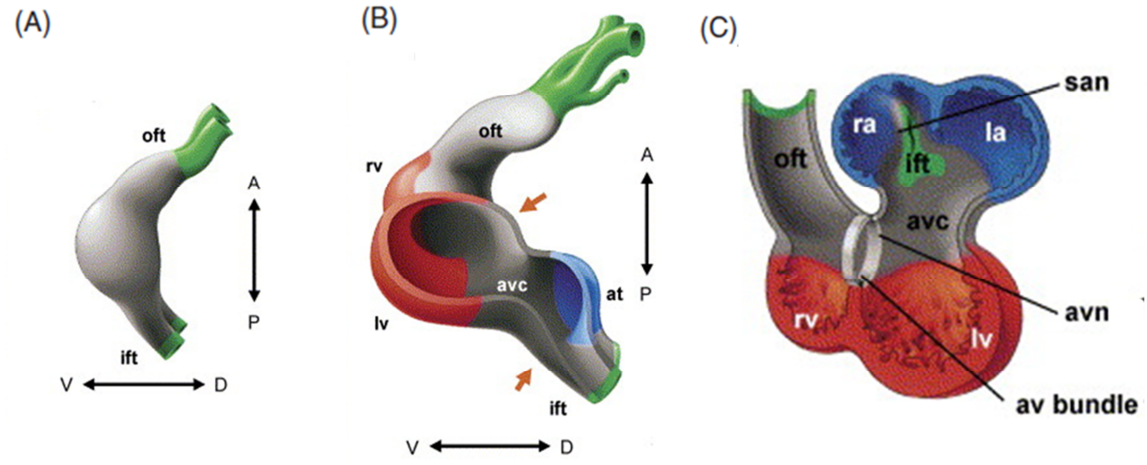

Figure 1-2: Localised chamber formation in the early heart tube

(A) Left view of a model linear heart tube at E8.0. Primary myocardium is shown in gray, the aortic sac with arterial branches is in green at the arterial (oft) pole and the systemic venous tributaries are marked in green at the inflow tract (ift). Anteroposterior (A-P) and dorsoventral (V-D) axes are shown.

(B) A model of the chamber-forming heart at ~E9.5 (also left view). Ventricular (red) and atrial (blue) myocardial appendages have been added to the ventricular loop and primary atrium, and the ventricular and atrial components are seprated by the atrioventricular canal (avc). The orange arrows indicate the ventricular and atrial inner curvatures.

(C) Frontal view of model of chamber-forming heart at ~E10.5, with same colour scheme as (A) and (B), highlights the ballooning atrial and ventricular appendages.

Taken from Christoffels et al. (2004). oft indicates outflow tract; ift, inflow tract; rv, right ventricle; lv, left ventricle; avc, atrioventricular canal; at, atrium; san, sinoatrial node; avn, atrioventricular node.

Local tissue swellings known as endocardial cushions are formed from the cardiac jelly in the lumen of the AVC, in between the endocardium and the myocardium, and are populated by mesenchymal cells of endocardial origin (Lin et al., 2012). These cushions play a key role in the septation of the atria, the AVC and the ventricles. Prior to septation of the atria, the systemic venous tributaries are re-orientated to the right side of the common atrial chamber, whilst a newly-formed pulmonary vein gains entrance to the left side (Webb et al., 2001). The primary atrial septum then forms as a muscular shelf descending from the roof of the atrial chamber into the atrial cavity, in between the systemic and pulmonary veins. A mesenchymal cap is present on the leading edge of this developing septum (Anderson et al., 2002). At the same time, another mass of mesenchyme enters the heart from the posterior mediastinum, which is referred to as the vestibular spine (also described in the literature as the dorsal mesenchymal protrusion) (Webb et al., 1998). It is the fusion of these mesenchymal primordia that both separates the right and left atria and divides the common AVC into its right and left components: the mesenchymal cap of the primary atrial septum first fuses with the vestibular spine, followed by fusion with the superior and inferior endocardial cushions, which themselves have also grown towards each other and fused (Anderson et al., 2003a).

The muscular inter-ventricular septum forms concomitantly with the ballooning of the apical components of the ventricles from the primary heart tube. As it grows into the apical cavity of the ventricles, it separates entirely the inlet component of the right ventricle from the left ventricle, as the right ventricle instead now has direct continuity from the developing right atrium. The crest of the inter-ventricular septum finally fuses with the proximal OFT cushions (see next section) by around E14.5, to ensure the aorta arises exclusively from the left ventricle and the pulmonary trunk from the right ventricle.

1.1.3 Septation of the outflow tract

The common OFT arising from the right ventricle after heart looping (Figure 1-2, C) also needs to be separated into the aorta and pulmonary trunk, which constitutes the arterial pole of the mature heart. The OFT can be arbitrarily divided into distal and proximal portions, which are separated by a characteristic ‘dog-leg bend’ (Figure 1-3, A). At this stage, the walls of the OFT have an exclusively myocardial phenotype, whilst the lumen is lined with cardiac jelly, which concentrates into two pairs of endocardial cushions that spiral around each other along the full length of the OFT (Figure 1-3, B). These cushions are populated by both mesenchymal cardiac neural crest cells (NCCs), which have delaminated from the dorsal neural tube and migrate through the pharyngeal arches to enter the distal and then proximal endocardial cushions

(Jiang et al., 2000; Kirby et al., 1983), and cells of endocardial origin that transform into mesenchyme to contribute to the more proximal cushions (Lincoln et al., 2004).

Septation of the OFT appears to be initiated by the major rearrangements in the pharyngeal region that occurs as the great vessel configuration is established (see Section 1.1.4). Although the precise mechanism underlying septation remains controversial, a septal structure known as the aorto-pulmonary (AP) septum seems to play a key role (Webb et al., 2003). The AP septum is a wedge of tissue in the dorsal wall of the aortic sac that separates the origins of the 4^{th} and 6^{th} pharyngeal arch arteries (PAAs, see Figure 1-4). It is proposed that the remodelling of the PAAs initiates fusion of the AP septum with the most distal end of the OFT endocardial cushions. Septation then proceeds in a 'zipper-like' fashion in a distal-to-proximal direction, through fusion of the endocardial cushions as they approach each other across the OFT lumen (Hutson and Kirby, 2007). The aortic blood becomes directed through the left 4^{th} PAA, which becomes part of the aortic arch, whilst the pulmonary blood exits through the left 6^{th} PAA. Finally, the proximal OFT cushions fuse with the AVC cushions where they span the ventricular septum, closing the inter-ventricular foramen and completing both septation of the OFT and the ventricles (Anderson et al., 2003b).

As septation occurs, the distal OFT region (now the intrapericardial components of the aorta and pulmonary trunk) rapidly becomes arterialised. The most proximal region instead is 'myocardialised' through invasion of the cushions by cardiac myocytes from the parietal walls of the OFT, so that as fusion with the ventricular septum is completed the aorta is completely walled into the left ventricle (van den Hoff et al., 1999). Septation of the cardiac chambers and OFT to form the well-characterised four-chambered heart ensures separation of the right and left sides of the mature heart (see Figure 1-5, B). The pulmonary trunk arises exclusively from the right ventricle to carry blood to the lungs, from which oxygenated blood can return through the left atrium and then ventricle, where it is pumped to the systemic circulatory system through the aorta. Correct septation is therefore essential for keeping the pulmonary and systemic systems separated. The development of the atrioventricular (mitral and tricuspid) valves and the semilunar (aortic and pulmonic) valves, also from the AVC and OFT endocardial cushions respectively (de Lange et al., 2004), plays a further important role in ensuring blood flows in a single direction from the atria to the ventricles and then to the arteries.

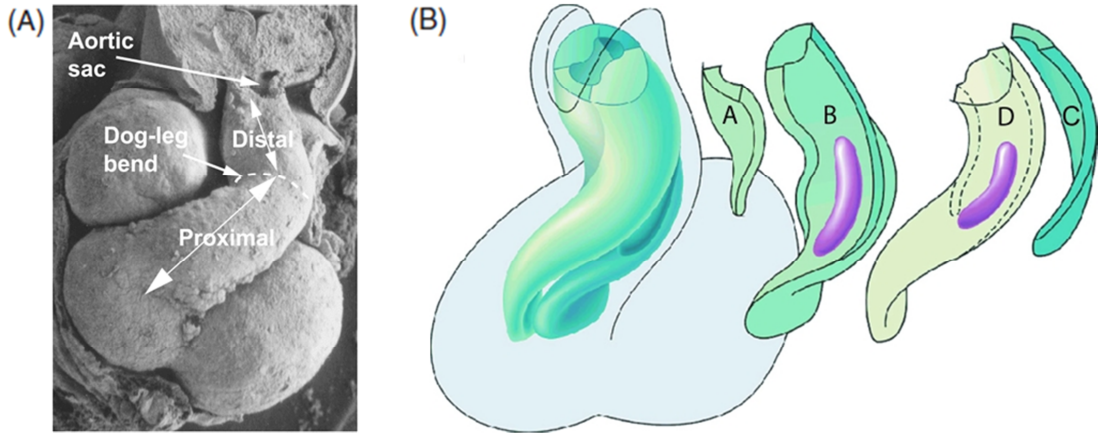

Figure 1-3: Septation of the outflow tract

(A) Scanning electron micrograph of a ventral view of a human embryonic heart at Carnegie stage 15 (approximately E11.5 in the mouse), shows a ventral view of the heart. A characteristic 'dog-leg bend' separates the distal and proximal segments of the unseptated OFT.

(B) Reconstruction of the heart to show the spiralling endocardial cushions extending along the full length of the distal and proximal OFT. A represents the aortic intercalated cushion, B the septal cushion, C the pulmonary intercalated cushion and D the parietal cushion. The mesenchymal contribution from the cardiac neural crest is indicated in purple.

Images taken from Webb et al. (2003).

1.1.4 Great vessel development

Another key process in the development of the cardiovascular system is the remodelling of the PAAs to form the mature aortic arch with right and left common carotid and subclavian arteries. Primitive pharyngeal vessels form as a result of local differentiation of mesodermal cells to endothelial cells (Graham, 2003), to which NCCs migrate and differentiate to form a layer of vascular smooth muscle cells surrounding the vessel endothelium (Jiang et al., 2000) (Figure 1-4, A). By E10.5 the 3rd, 4th and 6th PAAs have formed and connect the aortic sac to the left and right dorsal aortas in a symmetric arrangement (Figure 1-4, B). These PAAs then undergo a complete remodelling process involving programmed asymmetrical expansion, regression and spatial rearrangements of the vessels, so that by E14.5 the final aortic arch structure, derived from the aortic sac, PAAs and the left dorsal aorta, is completed (Hiruma et al., 2002) (Figure 1-4, C-E). During this process, the pharyngeal surface ectoderm plays a key role in signalling to the neural crest for aortic arch patterning (Basch and Bronner-Fraser, 2006; Kameda, 2009). After birth, the ductus arteriosus, which during development links the right ventricle to the aortic arch as part of the fetal circulation, regresses so the pulmonary and systemic circulatory systems are completely separated.

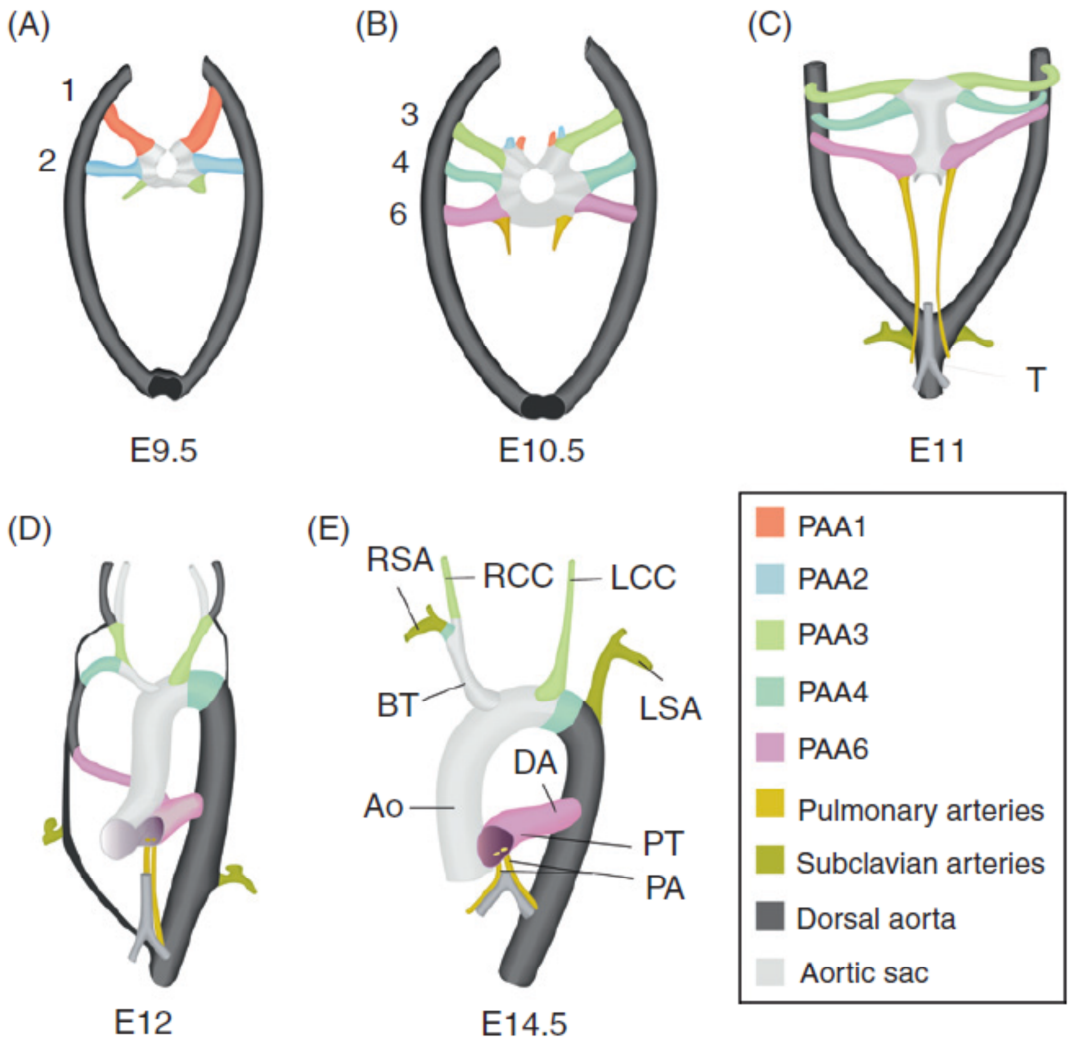

Figure 1-4: Remodelling of the Pharyngeal Arch Arteries to form the Great Vessels

(A) Ventral view shows at E9.5, only the 1st and 2nd PAAs have formed, which connect the aortic sac (light grey) at the arterial pole of the heart to the paired dorsal aortas (dark grey).

(B) By E10.5, the 1st and 2nd PAAs have formed the capillary beds of their pharyngeal arches. The aortic sac is now connected to the dorsal aortas via the 3rd, 4th and 6th PAAs, which have formed symmetrically in a rostro-caudal direction.

(C) At E11.0 the pulmonary arteries (yellow) can be clearly seen. The overall arrangement is still symmetrical at this time point.

(D) From E11.5 increased blood flow through the left 6th PAA drives asymmetrical remodelling, stabilising the aortic arch on the left and leading to its loss on the right. Segments of the dorsal aortas between the 3rd and 4th PAAs on both sides degenerate to allow individualisation of the common carotid arteries that are formed from the left and right 3rd PAAs. The right dorsal aorta is also degenerating below the regressing right 6th PAA.

(E) By E14.5 the mature configuration of the great vessels is seen. The right 6th PAA is lost completely, along with most of the right dorsal aorta. The aortic arch derived from the aortic sac and the left 4th PAA is connected solely to the (left) dorsal aorta, whilst the right 4t PAA connects the brachycephalic trunk to the right subclavian artery. The left 6th PAA has formed the ductus arteriosus, which connects the (left) dorsal aorta to the pulmonary trunk in the embryo, but will regress at birth to separate the systemic and pulmonary circulations.

Taken from Vincent (2010). PAA indicates pharyngeal arch artery; RSA, right subclavian artery; RCC, right common carotid; LSC, left subclavian artery; LCC, left common carotid; BT, brachycephalic trunk; Ao, aorta; DA, ductus arteriosus; PT, pulmonary trunk; PA, pulmonary arteries; T, trachea.

1.1.5 Contribution of different lineages to the developing heart

As mentioned in Section 1.1.1, within the cardiogenic mesoderm there are two fields of progenitor cells with myocardial potential: the FHF that forms the primary cardiac tube, and the SHF (also referred to as the anterior heart field) that contains cells recruited to both poles of the tube. This distinct second source of myocardial progenitors was first visualised in the mouse embryo using a *lacZ* transgene under the control of an *Fgf10* gene regulatory element. Cells with *lacZ* expression were seen in the pharyngeal mesoderm anteriorly and dorsally to the cardiac tube, which then contributed to the myocardium at the anterior pole of the heart (Kelly et al., 2001). This was confirmed by DI-I labelling, which also demonstrated this SHF population contributes to the right ventricle (Zaffran et al., 2004), whilst lineage tracing of *Islet1*-expressing cells showed the SHF extends further posteriorly to contribute to the venous pole as well (Cai et al., 2003).

Retrospective clonal analysis has confirmed that the FHF and SHF contain distinct myocardial lineages (Meilhac et al., 2004). This experiment was based on random labelling of precursor cells, whereby a *lacZ* reporter carrying a non-functional duplication (*laacZ*) is randomly rendered functional again by very rare spontaneous intragenic recombination events that remove the duplication, allowing clonal analysis by β-galactosidase staining. Evaluation of β-galactosidase positive cells at E8.5 identified two distinct lineages, one that contributed to both ventricles, the AVC and both atria, whilst the other contributed to the right ventricle, AVC, atria and the OFT (summarised in Figure 1-5, A). Therefore, the distinct first and second clonal lineages correspond directly with the cells from the FHF and SHF. Furthermore, this retrospective clonal analysis indicated that the first and second lineages segregate from a common mesodermal precursor before the cardiac crescent stage (Buckingham et al., 2005; Meilhac et al., 2004).

In addition to the cardiogenic mesoderm, there are two further developmental origins for cells that make up the heart: cardiac neural crest cells (NCCs) and the proepicardium (PE). The contributions of each cell type is summarised in Figure 1-5. Cardiac NCCs originate from the dorsal neural tube, between the mid-otic placode and the caudal boundary of the 3rd somite, where they undergo an epithelial-to-mesenchymal transition (EMT) to then migrate along the pharyngeal arches (Hutson and Kirby, 2007). Some cardiac NCCs contribute to the OFT, where they play a critical role in formation of the endocardial cushions for septation (as discussed in Section 1.1.3). Others are targeted to the 3rd, 4th and 6th pharyngeal arch arteries (PAAs) where they are important for the development of the aortic arch and great vessels (Waldo et al., 2005).

The importance of the cardiac NCCs is reflected in the OFT and great vessel defects that arise when the neural crest is ablated, which include common arterial trunk (CAT, also referred to as persistent truncus arteriosus) and interrupted aortic arch (Kirby and Waldo, 1990). Mapping of NCCs in the *Splotch^{2H}* (*Sp^{2H}*) NCC-deficiency mouse model, in relation to the OFT defects observed, provided valuable insights into the etiology of these defects (Bradshaw et al., 2009). Absence of NCCs in the pharyngeal region resulted in failure of the posterior PAAs to stabilise, leading to their early loss. There was also a notable reduction in the AP septum formation in the aortic sac, which is derived from NCC mesenchyme, preventing initiation of OFT septation. This resulted in CAT in 75% of *Sp^{2H}/Sp^{2H}* embryos. Furthermore, double outlet right ventricle (DORV) developed in those embryos in which the OFT was septated, which was attributed to an additional role for the NCCs in influencing the distribution of SHF cells in the pharyngeal and OFT regions (Bradshaw et al., 2009).

The PE is a transitory structure that develops near the venous pole of the heart tube, which in the chick appears to occur in response to liver-bud-derived signals to the coelomic mesothelium to drive PE-specific expression patterns including *Wt1, Tbx18 and Tcf21* (Ishii et al., 2007; Manner et al., 2001). However, this inductive relationship with the liver is not conserved in zebrafish, as PE development is not affected in *Hnf1ba^{hi2169}* mutant embryos that lack a liver (Liu and Stainier, 2010), and it remains to be seen whether this applies to the mouse embryo.

The PE extends towards the heart, attaches and spreads across the entire myocardial surface to form the epicardium (Dettman et al., 1998). Cells derived from the epicardium undergo EMT to then migrate into the myocardium to give rise to both fibroblasts and smooth muscle cells for the coronary vasculature system (Merki et al., 2005). Coronary vascular defects occur when the epicardium is disrupted: for example, in *Wt1* mutant mice epicardial cells cannot undergo EMT due to the activation of the *Snail* gene by Wt1, leading to loss of the coronary arteries, pericardial haemorrhage and embryonic lethality (Martinez-Estrada et al., 2010). It was thought that the endothelial cells of the coronary vasculature also had an epicardial origin, although this is now contested as genetic tracing indicates that they are derived from the venous plexus at the sinus venosus (Red-Horse et al., 2010). The epicardium also provides factors that promote development and expansion of the myocardium, with disruption to this signalling leading to a thin myocardium (Chen et al., 2002; Lavine et al., 2005).

Overall, it is clear that the development of the heart is an extremely complex process, with perturbation of any of the cells that contribute to it resulting in congenital cardiac malformations.

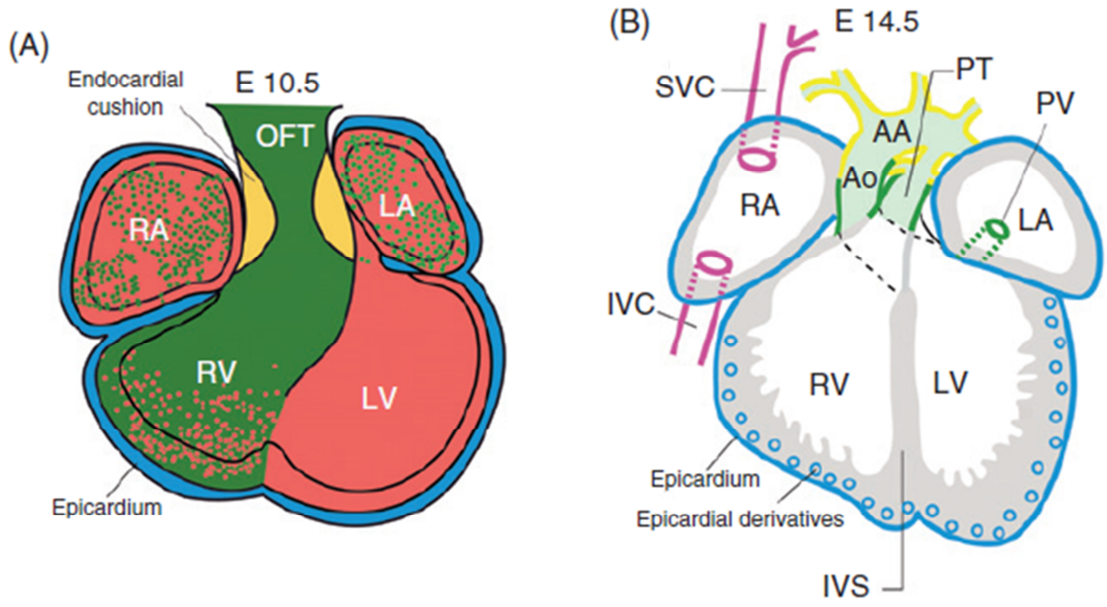

Figure 1-5: The heart before and after septation, showing the multiple cellular origins of the cardiac components

(A) Myocardium derived from the FHF (red) exclusively makes up the left ventricle, whilst cells from the SHF (green) exclusively form the myocardium of the outflow tract. Cells from both the FHF and SHF contribute to the right ventricle and both atria. The epicardium (blue) envelopes the heart, whilst the endocardial cushions (yellow) are forming in the outflow tract, with contribution from the cardiac NCCs.

(B) The heart is fully septated and the great vessels are in their mature configuration by E14.5. Epicardium and epicardial derivatives are shown in blue, the contribution of the cardiac neural crest in yellow, SHF derivatives in green, and the most posterior $Tbx18^{+}$ SHF derivatives in purple.

Taken from Vincent (2010). OFT indicates outflow tract; RA, right atrium; LA, left atrium; RV, right ventricle; LV, left ventricle; SVC, superior caval vein; IVC, inferior caval vein; AA, aortic arch; Ao, aorta.

1.2 Chromatin structure and the regulation of transcription

This thesis addresses the role of a chromatin remodelling protein, CHD7, during heart development. Cardiovascular development requires the dynamic regulation of gene expression programmes in the correct cell lineage, at the correct time and in the correct order. Alterations to chromatin structure, through both nucleosome sliding and post-translational modifications, provide key mechanisms through which such coordinated wholesale gene change can be achieved. The next two sections will therefore introduce these concepts in more detail, and give an overview of what is already known about the transcriptional regulation of heart development.

1.2.1 Chromatin structure

Genomic DNA is organised with specific proteins into chromatin: a dense, highly organised tertiary structure that allows compaction of the vast lengths of DNA in the nucleus. The basic structural and functional repeating unit of chromatin is the nucleosome (Kornberg, 1974), a length of 145-147bp of DNA wrapped twice around a histone protein octamer core comprised of two H2A-H2B dimers and a H3-H4 tetramer (Figure 1-6, A). Nucleosomes are held together largely by electrostatic interactions between the positively-charged histone proteins and the negative charges on the deoxyribose-phosphate DNA backbone (Luger et al., 1997; Van Holde et al., 1974). A number of histone variants have been identified, which can undergo different post-translational modifications to affect the local chromatin structure (reviewed in (Luger et al., 2012)).

Nucleosomes are joined by an average of 20bp of DNA 'linker' sequence, and their positioning can be highly dynamic: multiple enzymes can modify and alter nucleosome positioning and chromatin structure, which can occur either on a global scale or at individual genes in response to developmental cues or environmental changes (Smith and Peterson, 2005). The N-terminal 'tails' of the histones extend from the nucleosome to form contacts not only with DNA and other histones, but also other non-histone proteins through epigenetic post-translational modifications to specific residues on these tails. These interactions can contribute to the folding of the lengths of nucleosomal structures into complex, highly-compacted tertiary structures (Figure 1-6, B and C), or to the unwinding of these dense structures to allow access for DNA-binding enzymes (Becker and Horz, 2002). Higher-order chromatin structures are stabilised by architectural proteins such as linker histone H1, heterochromatin protein 1 (HP1), high mobility group (HMG) proteins, Polycomb group proteins and many more (Luger et al., 2012).

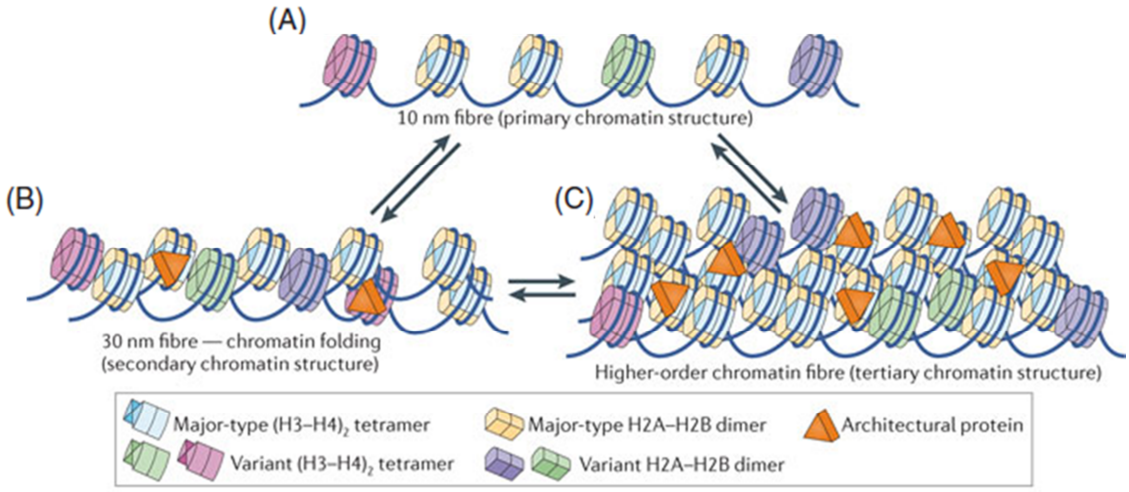

Figure 1-6: Primary, secondary and tertiary chromatin structure

(A) The primary "beads on a string" chromatin structure consists of individual nucleosomes made up with either canonical histones (indicated in light blue and yellow) or combinations of different histone variants (green, purple and pink), which are joined by a length of 'linker' DNA.

(B) Short-range nucleosome–nucleosome interactions result in folded chromatin, forming the secondary "30nm fibre" chromatin structure.

(C) Further fibre–fibre interactions, which are defined by long-range interactions between individual nucleosomes, form tertiary higher-order chromatin fibres. The primary structure, including histone variants, nucleosome spacing and post-translational histone modifications, affects both secondary and tertiary chromatin structure.

The double arrows indicate transitions between the different structural chromatin states. These can be regulated through a number of mechanisms, including changes in histone modification patterns, binding or displacement of architectural proteins (indicated by orange triangles), chromatin remodelling and exchange of histone variants.

Figure from Luger et al. (2012).

1.2.2 Epigenetic mechanisms for the regulation of transcription

In addition to its 'packaging role', highly dynamic chemical and structural alterations to chromatin enable a layer of tissue-specific regulation of transcription, replication and repair. Three main processes have been described that influence chromatin structure: DNA methylation at CpG dinucleotides, histone modification and ATP-dependent chromatin remodelling (Figure 1-7). All are dynamic and intrinsically reversible, and a complex inter-play is thought to exist between them to direct tissue-specific gene expression.

The methylation status of CpG dinucleotides are mostly stably propagated during mitosis, except during primordial germ cell specification and post-fertilisation in the early embryo, when global methylation levels are reset (Smith and Meissner, 2013). Methylation of DNA cytosines was traditionally seen as a marker of irreversible repression of gene expression.

However, technological improvements that have allowed large-scale mapping of DNA methylation have revealed that in fact during development promoter methylation can be highly dynamic in some contexts, and in many organisms DNA methylation can be found in the bodies of active genes (Suzuki and Bird, 2008). The DNA methyltransferase enzymes DNMT1, DNMT3A and DNMT3B are highly conserved, and their roles in the formation and maintenance of methylation states are essential for normal development (Li et al., 1992; Okano et al., 1999).

A wide range of post-translational modifications to histone tails have been reported, including methylation, acetylation, phosphorylation, ubiquitination and sumoylation. The properties of these chemical groups, added or removed by histone-modifying enzymes, affect the charges on the histone tails, which can lead to electrostatic repulsion between neighbouring nucleosomes, as well as affecting the affinity of the histones to the negatively-charged DNA. Thus, histone modifications alter the accessibility to DNA for transcription factors and co-regulatory proteins (Atkinson and Armstrong, 2008). Histone modifications also have a role in the recruitment of regulatory factors, through their recognition of specific combinations of post-translational modifications. Together, this results in a so-called 'histone code' for the regulation of chromatin structure and accessibility for DNA-processing enzymes (Wang et al., 2004a). For example, the addition of trimethyl (me3) groups to lysine (K) residues in the histone tails, such as H3K4me3 and H3K27me3, has been linked with the maintenance of a pluripotent state in embryonic stem cells and regulation of developmental genes. The presence of both of these chemical markers within the same region of chromatin is associated with a 'poised' transcriptional state (Bernstein et al., 2006; Mikkelsen et al., 2007), in which genes can be rapidly activated or repressed, whilst acetylation of histone residues is generally associated with active genes (Marmorstein and Roth, 2001). Therefore, the dynamics of histone modifiers, particularly those with opposing functions such as acetyltransferases and deacetylases, is very important during development and in disease states.

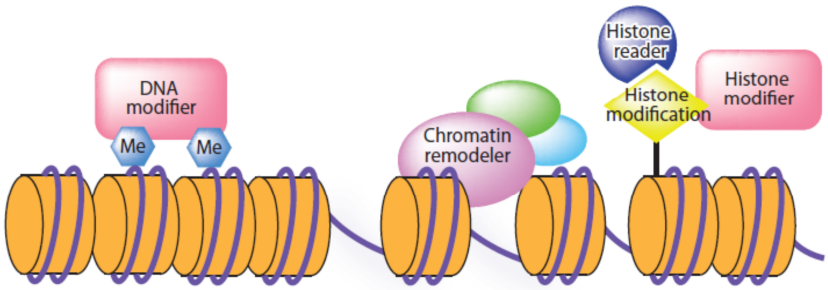

Figure 1-7: Epigenetic mechanisms for regulation of gene expression

Chromatin-level gene regulation can be achieved through methylation of the DNA strand, nucleosome rearrangements by chromatin remodellers and post-translational histone modifications. These processes require a number of different factors that influence the chromatin structure.

Image from Chang and Bruneau (2012).

1.2.3 Chromatin remodelling and nucleosome sliding

Chromatin structure can also be altered by enzymes that utilise energy from ATP-hydrolysis to disengage DNA-histone contacts for nucleosome sliding, displacement, or histone exchange (Becker, 2002; Becker and Horz, 2002). About 30 mammalian genes are known that encode the ATPase subunits found in chromatin remodelling protein complexes (Ho and Crabtree, 2010), and the activity of these enzymes can alter the chromatin structure to modulate DNA accessibility. Chromatin remodelling complexes alter nucleosome positioning and histone-DNA contacts, so in combination with other processes such as DNA methylation, chromatin in a non-permissive heterochromatic state can be changed to a permissive open euchromatic state, preparing specific genomic loci for replication, repair, recombination, or transcription (Hargreaves and Crabtree, 2011; Persson and Ekwall, 2010).

There are four main protein families of these ATP-dependent chromatin-remodelling complexes: SWI/SNF (switching defective/sucrose non-fermenting), ISWI (imitation switch), CHD (chromodomain, helicase, DNA binding) and INO80 (inositol requiring 80) complexes (Ho and Crabtree, 2010). All share an evolutionarily-conserved ATPase enzymatic domain, with additional functional domains that alter their activity and specificity. Chromatin-remodellers not only direct local changes to nucleosome positioning or composition in conjunction with co-activators or co-repressors of gene transcription, but may also regulate long-range inter- and intra-chromosomal interactions and organise the tertiary architecture of chromatin consistent with specific gene programmes (Morrison and Shen, 2009).

1.3 Transcriptional and epigenetic regulation of heart development

1.3.1 Transcription factors and congenital heart disease

Many inherited forms of congenital heart disease have been shown to be the result of mutations in cardiovascular transcription factors (Table 1-1). Heart development relies on a complex network of these evolutionarily-conserved transcription factors and molecular pathways, which are inter-linked, mutually reinforcing and often re-utilised at different stages of heart development (see Figure 1-8). A group of "core cardiac transcription factors" have been described that are critical for heart development (McCulley and Black, 2012), some examples of which will be discussed in more detail here. Key cardiac transcription factors include Nkx2-5, MEF2 factors, the zinc finger proteins GATA4, GATA5 and GATA6, the T-box factors Tbx1, Tbx2, Tbx3, Tbx5, Tbx18 and Tbx20, the Lim-homeodomain protein Islet1, and the basic helix-loop-helix proteins Hand1 and Hand2. The earliest identified molecular marker for cardiac progenitors, however, is the transiently-expressed MESP1 transcription factor.

MESP1 is expressed as the mesoderm emerges from the primitive streak, and is required for the anterior migration of these mesodermal progenitors (Saga et al., 1999). All myocardial cells are thought to descend from early *Mesp1*-expressing cells (Bondue and Blanpain, 2010), although large regions of other mesoderm-derived structures, such as the components of the skull vault and its connective tissues, also descend from *Mesp1* lineages. (Yoshida et al., 2008). A recent clonal analysis study by Lescroart and colleagues found that there are two temporally distinct pools of *Mesp1* cardiovascular progenitors: the earlier pool is restricted to the FHF and the later pool is restricted to the SHF. The FHF progenitors were shown to be unipotent, with all *Mesp1*-derived clones in the left ventricle and atria differentiated into either cardiomyocytes or endothelial cells. Interestingly, by contrast the SHF progenitors could be either unipotent or bipotent. SHF clones either differentiated into cardiomyocytes or endothelial cells, or differentiated into both cardiomyocytes and endothelial cells, or cardiomyocytes and smooth muscle cells. Molecular analysis also confirmed that these distinct lineages, whilst sharing some key cardiogenic MESP1 targets such as *Gata4* and *Gata6*, were molecularly heterogeneous (Lescroart et al., 2014).

The GATA family of zinc finger transcription factors have important roles in the differentiation, proliferation and survival of a number of cell types, including cardiomyocytes. *GATA-4*, *GATA-5* and *GATA-6* are expressed in the developing heart in partially-overlapping patterns

(Molkentin, 2000; Nemer and Nemer, 2003; Patient and McGhee, 2002), and mutations in *GATA-4* and *GATA-6* are associated with septal and OFT defects in humans (see Table 1-1).

Complete knockdown of *Gata4* and *Gata6* in murine models leads to loss of cardiac differentiation and acardia (Zhao et al., 2008), whilst compound heterozygous *Gata4*$^{+/-}$*/Gata6*$^{+/-}$ mice die around E13.5 due to vascular defects, common arterial trunk (CAT), and myocardial thinning (Xin et al., 2006). These results suggest functional interactions between GATA4 and GATA6. Loss of these genes individually also results in cardiovascular defects: haploinsufficiency of *Gata4* leads to common AV canal, DORV and hypoplastic ventricular myocardium (Pu et al., 2004), whilst *Gata6* ablation specifically in NCCs causes CAT through its role in the regulation of Semaphorin 3C (Lepore et al., 2006). Interactions between GATA5 and both GATA4 and GATA6 also appears to be important during formation of the OFT: compound heterozygous *Gata5*$^{+/-}$*/Gata4*$^{+/-}$ and *Gata5*$^{+/-}$*/Gata4*$^{+/-}$ mouse mutants die embryonically or perinatally of severe OFT defects, including double outlet right ventricle (DORV), ventricular septal defects (VSDs) and hypertrophied mitral and tricuspid valves (Laforest and Nemer, 2011). The expression of genes for key cardiac transcription was disrupted, including *Tbx20*, *Mef2c*, *Hey1* and *Hand2*.

GATA factors also act combinatorially with a number of other key transcription factors during cardiogenesis. GATA4 and GATA6 interact synergistically with MEF2C for the activation of a number of cardiac genes, including *Nppa* and *α-MHC* (Morin et al., 2000), whilst a direct interaction between GATA4 and Tbx5 activates expression of *Cx30.2*, which encodes an AV node gap junction protein required for AV delay (Munshi et al., 2009). GATA4 and Islet1 also act together at an enhancer region of *Mef2c* to drive its expression in the second heart field (Dodou et al., 2004).

Table 1-1: Genes encoding transcription factors with mutations in human patients with congenital heart defects

Gene:	Congenital Heart Defects:	References:
CITED2	VSD, ASD	(Sperling et al., 2005)
FOXH1	TGA, TOF	(Roessler et al., 2008)
GATA4	ASD, AVSD, VSD, TOF, HRHS	(Garg et al., 2003), (Okubo et al., 2004), (Sarkozy et al., 2005), (Garg et al., 2003), (Nemer et al., 2006), (Tomita-Mitchell et al., 2007), (Rajagopal et al., 2007), (Schluterman et al., 2007), (Kodo et al., 2012)
GATA6	CAT, PS, AVSD	(Kodo et al., 2009), (Lin et al., 2010), (Maitra et al., 2010), (Kodo et al., 2012)
HAND1	TOF, AI	(Hatemi et al., 2011), (Wang et al., 2011)
HAND2	TOF	(Shen et al., 2010)
HOXA1	DORV, TOF, VSD, IAA, PDA	(Bosley et al., 2008)
MEF2C	PAVSD	(Kodo et al., 2012)
NKX2.5	TOF, ASD, DORV, VSD, HLHS, CoA, IAA, TGA	(Schott et al., 1998), (Hosoda et al., 1999), (Goldmuntz et al., 2001), (Ikeda et al., 2002), (Watanabe et al., 2002), (Elliott et al., 2003), (Hirayama-Yamada et al., 2005), (Akcaboy et al., 2008), (Pabst et al., 2008), (Gioli-Pereira et al., 2010), (Kodo et al., 2012)
NKX2.6	CAT	(Heathcote et al., 2005)
PITX2	AF	(Franco et al., 2011; Gudbjartsson et al., 2007)
*TBX1**	VSD, IAA, PAVSD	(Yagi et al., 2003), (Momma, 2010), (Rauch et al., 2004), (Gong et al., 2001)
*TBX5***	ASD, VSD, AVSD	(Basson et al., 1997), (Reamon-Buettner and Borlak, 2004), (Liu et al., 2009)
TBX20	ASD, CoA, VSD, PDA, MS, HLHS	(Liu et al., 2008), (Kirk et al., 2007), (Posch et al., 2010)
ZIC3	TGA, ASD, PS	(Chhin et al., 2007), (Megarbane et al., 2000), (Ware et al., 2004)

AF indicates atrial fibrillation; AI, atrial isomerism; ASD, atrial septal defect; AVSD, atrioventricular septal defect; CAT, common arterial trunk; CoA, coarctation of aorta; DORV, double outlet right ventricle; HLHS, hypoplastic left heart syndrome; HRHS, hypoplastic right heart syndrome; IAA, interrupted aortic arch; MS, mitral valve stenosis; PAVSD, pulmonary atresia with ventricular septal defect; PDA, persistent ductus arteriosus; PS, pulmonary valve stenosis; TGA, transposition of the great arteries; TOF, tetralogy of Fallot; VSD, ventricular septal defect.

** TBX1 is associated with DiGeorge syndrome, **TBX5 is associated with Holt Oram syndrome*

Table adapted from Kodo and Yamagishi (2011) and McCulley and Black (2012).

The NK homeobox gene *Nkx2.5* is a predicted homologue of the *Drosophila* master cardiac regulator gene *tinman* (Azpiazu and Frasch, 1993; Bodmer, 1993). Nkx2-5 is also a key transcription factor for the regulation of cardiogenesis, with roles in cardiomyocyte differentiation, chamber identity and OFT formation (Harvey et al., 2002). *Nkx2.5* is expressed under the regulation of GATA factors, SMAD proteins in response to BMP signalling, and by Nkx2-5 in an auto-regulatory loop (Liberatore et al., 2002; Lien et al., 1999; Searcy et al., 1998). In the anterior SHF it is also under the regulation of Islet1 (Takeuchi et al., 2005). Nkx2-5 regulates a number of other key cardiac genes, including *Mef2c*, *Hand1* and *Jarid2* (Barth et al., 2010; Tanaka et al., 1999), with mouse knockdown models showing early embryonic lethality due to lack of cardiac looping and poor blood vessel development (Lyons et al., 1995; Tanaka et al., 1999). Mutations of *NKX2.5* are also associated with a range of congenital heart defects in humans (Table 1-1). Similarly to the GATA proteins, Nkx2-5 cooperates with a number of other core cardiac transcription factors in its multiple roles during cardiogenesis: interactions between Nkx2-5 and both Hand2 and MEF2C are required for determining ventricular identity (Vincentz et al., 2008; Yamagishi et al., 2001); Nkx2-5 and GATA4 interact to drive expression of cardiac sarcomeric protein expression (Sepulveda et al., 2002); and it regulates the expression of the transcriptional repressor *Jarid2* during OFT development (Barth et al., 2010).

Members of the T-box family of transcription factors also have critical and widely-varied roles in heart development, including cardiac fate and differentiation (Plageman and Yutzey, 2005). Overlapping expression of 7 *Tbx* genes in the FHF and SHF have been reported in amniotes (Kodo and Yamagishi, 2011), with mutant models providing further evidence of non-redundant roles: for example, defects in the posterior region of the heart tube, which develops into the atria, are reported in *Tbx5*-null mice, whilst the mouse model of DiGeorge syndrome that is haploinsufficient for *Tbx1* displays aortic arch defects. *Tbx2* and *Tbx3* meanwhile have roles in repression of chamber myocardium and in the development of the conduction system (Moorman and Christoffels, 2003), and *Tbx18* is required for venous pole development, in a population of cells at the posterior region of the SHF that are $Tbx18^{+}$ and $Nkx2\text{-}5^{-}$ (Christoffels et al., 2006). Mutations to a number of *TBX* genes are associated with a range of congenital heart defects in humans, reflecting these diverse roles (Table 1-1).

Clearly there are many more transcription factors involved in heart development, as well as many signalling pathways that provide key spatial and temporal information, including BMP, Wnt and FGF pathways. Figure 1-8 shows a gene regulatory network of both transcription factors and some key signalling pathways, which gives a good summary of the complexity of the process. With so many inter-connected components, it is evident why the system is so sensitive to disruption of any of the genes involved.

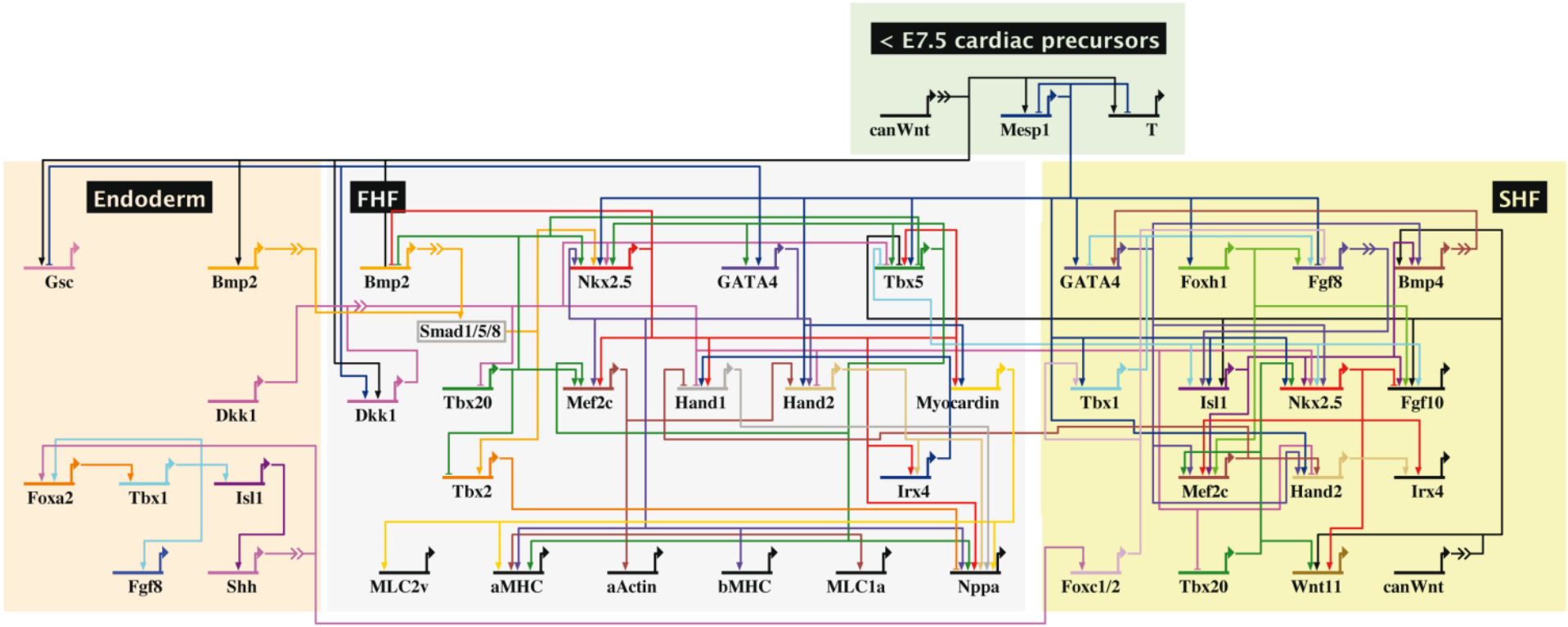

Figure 1-8: Gene regulatory network during early murine cardiac development

Published temporal and spatial expression data of cardiac genes and interactions information was combined by Herrmann and colleagues to generate a gene regulatory network, which was validated by running simulations in a Boolian computational model (Herrmann et al., 2012). Genetic interaction in the FHF and SHF are shown, as well as incorporating the influence of signals from the early mesoderm and endoderm. Genes are represented by their regulatory region and their transcriptional start site. Arrow heads indicate activation and bar heads inhibition of gene transcription. Broken lines represent intercellular signalling with an integrated signal transduction cascade.

Figure taken from Herrmann et al. (2012).

1.3.2 Histone modifying genes

It has more recently become apparent that the epigenetic landscape also plays a key role in the transcriptional regulation of heart development. Increasing numbers of interactions between chromatin modifiers or remodellers and key cardiac transcription factors are being reported, whilst human mutations or mutant mouse models also show a range of cardiovascular defects as a result of loss of epigenetic modifiers. For example, a recent study used exome sequencing of parent-offspring trios to compare 362 severe congenital heart defect patients with unaffected parents and 264 control cases, identifying an excess of *de novo* mutations in genes involved in the production, removal or reading of H3K4 methylation (Zaidi et al., 2013). Furthermore, mutations were also found in genes associated with ubiquitination of H2BK120, which is required for H3K4 methylation, as well as two different *de novo* mutations in SMAD2, which regulates H3K27 methylation (see Figure 1-9).

The human disease Wolf-Hirschhorn syndrome, which includes heart defects, is associated with a deletion mutation of a critical region of chromosome 4q16.3 (Bergemann et al., 2005). The deleted region includes the candidate gene encoding WHSC1, which contains SET domains highly homologous to the yeast H3K36 methyltransferase Set2. WHSC1 has been shown to modulate mono-, di- and tri-methylation of H3K36 on nucleosomes in HeLa cells (Sun et al., 2005), whilst mice with homozygous knockout of *Whsc1* die within 10 days of birth due to atrial and ventricular septal defects. This was attributed to functional overlap between WHSC1 and a number of key developmental transcription factors, including Nkx2-5 (Nimura et al., 2009).

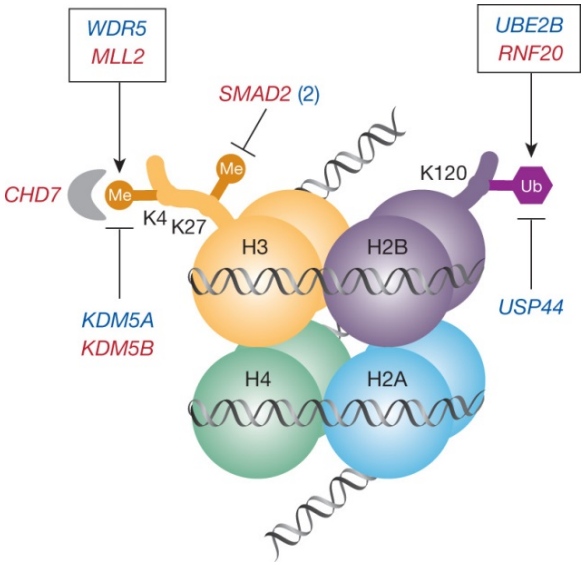

Figure 1-9: *de novo* mutations in the H3K4 and H3K27 methylation pathways identified in patients with congenital heart defects

An over-representation of genes that affect the production, removal or reading of H3K4 methylation, H3K27 methylation and H2BK120 ubiquitination was found in a study of *de novo* mutations in patients with sporadic congenital heart defects. A nucleosome is shown with DNA wrapped around a histone octamer, with mutated genes shown. Genes with nonsense, frameshift or splice site mutations are shown in red, and those with missense mutations are in blue, with those known to interact together in the same complex enclosed in boxes.

Taken from Zaidi et al. (2013)

Expression of the key cardiac transcription factor Nkx2-5 is mediated by the Polycomb group protein Rae28 (Shirai et al., 2002), which catalyses mono-ubiquitinylation of histone H2A and regulates gene silencing. Homozygous ablation of Rae28 results in defects similar to those seen in *Nkx2.5* knockout mice. Another histone modifier Jumonji (also known as Jarid2), is involved in development of the OFT, under the transcriptional regulation of Nkx2-5 (Barth et al., 2010). Jumonji is a component of a protein complex with histone demethylase and methyltransferase activities, which regulates cardiomyocyte proliferation through the repression of CyclinD1 expression (Toyoda et al., 2003). Germline deletion of *Jumonji* results in VSD, DORV and myocardial non-compaction (Lee et al., 2000).

Histone deacetylases (HDACs), which are usually associated with repression of gene expression, also have multiple, often overlapping roles during heart development. For example, HDAC1 and HDAC2 function redundantly, with deletion of both *Hdac1* and *Hdac2* in the myocardium resulting in neonatal death within 2 weeks due to arrhythmias and dilated cardiomyopathy (Montgomery et al., 2007). HDAC5 and HDAC9 also function redundantly in the repression of Mef2, SRF factors and myocardin, with double mutants showing VSDs, thin myocardium and embryonic lethality from E15.5, (Chang et al., 2004). Histone acetyltransferases (HATs) such as p300 are also important: germline deletion of p300 is embryonic lethal at E9.5-11.5, with thin myocardium and reduced trabeculation observed (Yao et al., 1998), whilst a point mutation that inactivates its acetyltransferase activity results in ASD, VSD, reduced coronary vessels and lethality at E12.5-15.5 (Shikama et al., 2003).

1.3.3 Chromatin remodelling during heart development

ATP-dependent chromatin remodelling complexes also have multiple critical roles during heart development. The chromatin remodeller CHD7 is haploinsufficient in the human disorder CHARGE syndrome, which is associated with a range of heart defects (see Sections 1.4, 1.5 and 1.6). This thesis aims to investigate further the tissue-specific role(s) of CHD7 during cardiovascular development, as this is not yet well understood.

Mutations to a number of components of the BAF complex, a major SWI/SNF ATP-dependent chromatin remodelling complex, also produce a range of congenital heart defects. The ATPase subunit of this complex is encoded by either *Brg1* or *Brm*, and whilst *Brm*-null mice seem to develop normally, *Brg1* is required in multiple tissues during heart morphogenesis (Griffin et al., 2008; Reyes et al., 1998). Briefly, in the myocardium *Brg1* promotes proliferation, so conditional ablation driven by *Sm22α-Cre* leads results in thin myocardium and absence of the inter-ventricular septum (Hang et al., 2010), whilst endocardial ablation driven by *Tie2-Cre*

result in hypotrabeculation of the myocardium and absence of the cardiac jelly (Stankunas et al., 2008). It also has roles in OFT and great vessel development, with persistent ductus arteriousus (PDA) resulting from *Brg1* deletion in smooth muscle cells driven by *smMHC-Cre* (Zhang et al., 2011). Furthermore, it has a critical role in the maintenance of a multipotent NCC reservoir, so ablation of *Brg1* in NCCs driven by *Wnt1-Cre* leads to shortened OFTs and disruption to PAA development (Li et al., 2013). These tissue-specific roles are discussed in more detail in Section 4.5.1. Allelic balance between *Brg1* and the transcription factor genes *Tbx5*, *Tbx20* and *Nkx2.5* is also crucial for heart development, with cardiac malformations seen when these sensitive interdependent relationships are disrupted in compound heterozygous mutant embryos (Takeuchi et al., 2011).

Many other BAF complex subunits also have distinct roles during cardiogenesis, including Baf60c, Baf180 and Baf45c. Baf60c is required for heart morphogenesis and the differentiation of cardiomyocytes, with the ectopic expression of *Baf60c*, *Tbx5* and *Gata4* in non-cardiogenic mesodermal cells sufficient to induce differentiation into contracting cardiomyocytes (Lickert et al., 2004; Takeuchi and Bruneau, 2009). The early embryonic lethality resulting from small interfering RNA knockdown of Baf60c in mice is accompanied by hypoplastic ventricles with reduced trabeculation and shortened OFT, with downregulation of a number of cardiac genes, including *Hand2*, *Bmp10* and *Irx3* (Lickert et al., 2004). Baf180 is required for the regulation of a subset of retinoic acid pathway genes, such as RARβ2 and CRABPII, during cardiac chamber formation, as well as the expression of angiogenic, vasculogenic and EMT genes in the epicardium for coronary vessel development (Huang et al., 2008; Wang et al., 2004b). Studies in zebrafish show that morpholino knockdown of *Baf45c* leads to abnormal heart looping and reduced contractility, although no significant developmental defects are seen in *Baf45c*-null mice, so there may be redundancy in higher vertebrates (Lange et al., 2008; Mertsalov et al., 2008).

The INO80 chromatin remodelling complexes contain the DNA helicase subunits Pontin and Reptin, whose activity is essential for the chromatin remodelling function of the INO80 complexes (Gallant, 2007). Whilst these subunits have not been studied in mice, work in zebrafish has indicated they have an antagonistic role in the regulation of myocardial growth, through their opposing effects on β-catenin signalling: morpholino knockdown of *pontin* causes cardiac hyperplasia, whilst over-activation of Reptin ATPase activity through an insertional mutation also stimulates cardiomyocyte proliferation (Rottbauer et al., 2002). These roles of Pontin and Reptin in the regulation of cardiac muscle growth strongly suggest that INO80 complexes are also involved in cardiovascular development.

Histone modifiers and chromatin remodellers often interact with regulatory enhancer sequences at their target genes. Whilst a large number of cardiac transcriptional enhancer sequences have been identified, these sequences appear to be weakly conserved between vertebrates. A ChIP-seq study on E11.5 heart tissue using the enhancer-associated protein p300 identified over 3000 candidate heart enhancers with good functional reproducibility, although compared to other tissues studied at the same time point these sequences were less deeply conserved between vertebrates (Blow et al., 2010). A further 1375 heart-specific enhancers were predicted through genome-wide binding of multiple cardiac transcription factors, including GATA4, Nkx2-5, Tbx5, SRF and Mef2A (He et al., 2011), whilst over 6200 candidate enhancer sequences were identified from fetal and adult human heart tissue (May et al., 2012). Recently, distinct chromatin signatures of histone modifications have also been identified through studying either human or mouse embryonic stem cells (ESCs) at distinct stages during differentiation into cardiomyocytes, which can be correlated with cardiac-specific gene expression (Paige et al., 2012; Wamstad et al., 2012). These findings again highlight the importance of transitions in chromatin state during heart development, so improving our understanding of it can provide further insights into cardiovascular development and disease.

1.4 CHD7 biological function

1.4.1 The CHD protein family

There are nine known mammalian chromodomain-helicase-DNA-binding (CHD) proteins, which utilise ATP hydrolysis to alter the structure of nucleosomes, thereby regulating the accessibility of DNA sequences (Becker and Horz, 2002; Lusser and Kadonaga, 2003; Woodage et al., 1997). A conserved feature of the CHD proteins is the presence of a centrally-located helicase region, which contains an SNF2 and DNA helicase domain (Figure 1-10). In addition, all CHD proteins contain two adjacent chromodomains, which cooperate to interact with one methylated histone tail (Flanagan et al., 2005). CHD7, as a member of the class III sub-family of CHD proteins, also contains a SANT domain, believed to be involved in binding histone tails (Boyer et al., 2004); two BRK domains, the function of which appears to be restricted to higher eukaryotes and may be involved in the reorganisation of chromatin structure (Daubresse et al., 1999; Doerks et al., 2002); and several nuclear localisation sequences.

Whilst sequence homology with other CHD proteins predicted CHD7 to have chromatin remodelling activity, it has only recently been confirmed by biochemical studies, as functional analysis is made difficult by its large size (336kDa). However, Bouazoune and Kingston recently utilised a dual-tag system to purify recombinant histidine- and FLAG-tagged CHD7 protein, which they used to demonstrate, through a restriction enzyme accessibility assay, that CHD7 has ATP-dependent nucleosome remodelling activity. Furthermore, through testing remodelling of nucleosome constructs with varying lengths of DNA overhang, CHD7 activity was found to be distinct to SWI/SNF-type remodellers. Instead, the remodelling reaction was more similar to that seen for ISWI enzymes and yeast Chd1, which require longer extra-nucleosomal DNA for nucleosome sliding activity (Bouazoune and Kingston, 2012; Gangaraju and Bartholomew, 2007; McKnight et al., 2011).

Chd7 is ubiquitously expressed in early development, with expression patterns later becoming more restricted to CHARGE-related tissues such as the developing ear, eye, and olfactory system (Bosman et al., 2005; Hurd et al., 2007; Sanlaville et al., 2006). Its widespread expression during development, combined with the range of congenital symptoms seen in CHARGE, implies that CHD7 has multiple important tissue-specific roles during development.

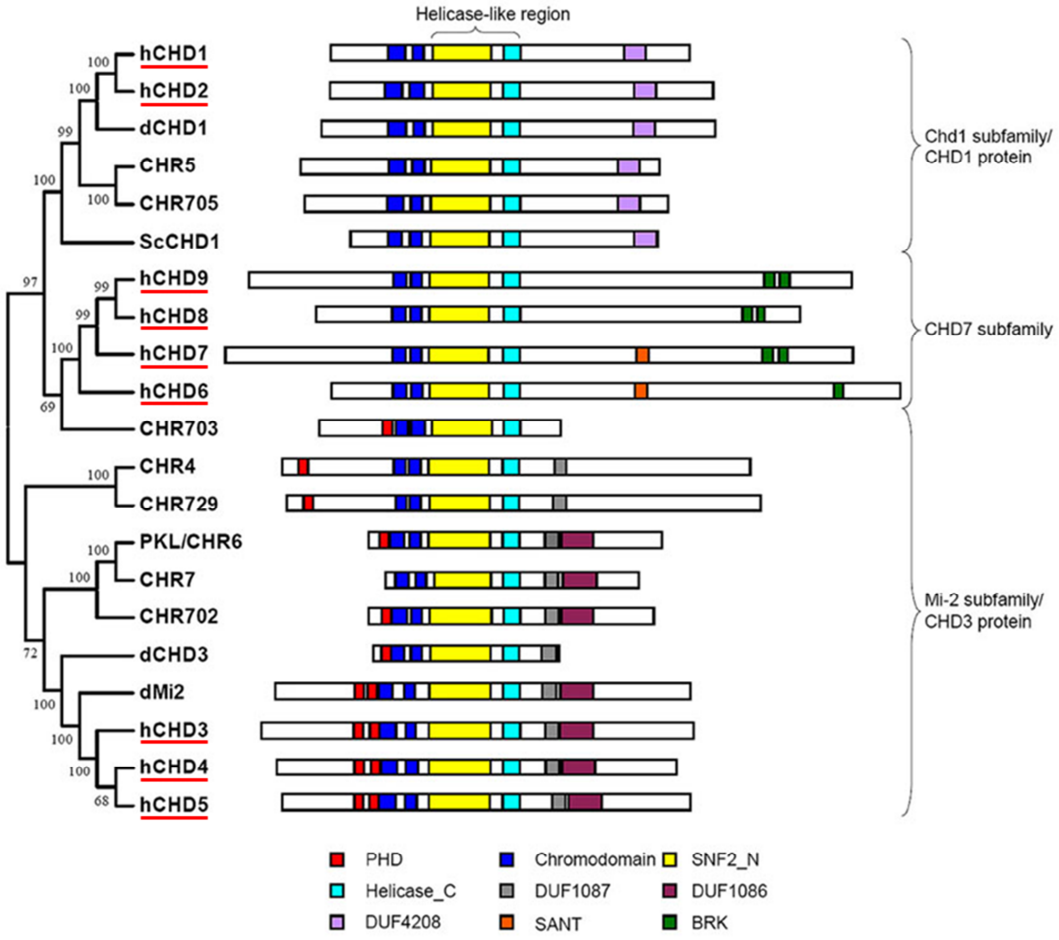

Figure 1-10: Conserved structural domains of the CHD protein family

The central helicase-like region, containing SNF2_N and Helicase_C domains, and two chromodomains are conserved in all CHD proteins from yeast to humans. Distinct additional domains are used to divide the CHD proteins into three subfamilies: the Chd1 subfamily (Class I in mammals), the Mi-2 subfamily (Class II), and the Chd7 subfamily (Class III). CHD proteins are clustered based on structure and functional conservation, with proteins from *Saccharomyces cerevisiae* (Sc), *Drosophila* (d), humans (h), *Arabidopsis* (CHR4, CHR5, CHR6 and CHR7) and rice (CHR702, CHR703, CHR705 and CHR729). Human CHD1-CHD9 are underlined in red.

Figure adapted from Hu et al. (2014).

1.4.2 CHD7 isoforms

Three splice isoforms have been reported for mammalian CHD7: full-length $CHD7_L$, $CHD7_S$ and CRA_E (Colin et al., 2010; Kita et al., 2012). CRA_E is formed by joining exons 3 and 36 of the human *Chd7* gene, and lacks most of the functional domains of the canonical $CHD7_L$ transcript. $CHD7_S$ is generated by alternative splicing of exon 6 and lacks the DNA-binding domain, the helicase/ATPase domain, the BRK domains and one of the two chromodomains that make up the full-length $CHD7_L$ protein. The CHD_L and $CHD7_S$ isoforms are predicted to function differently: $CHD7_S$ localises specifically to the nucleolus whereas CHD_L localises to both the

nucleus and the nucleolus, and depletion of both $CHD7_L$ and $CHD7_S$ inhibits cell proliferation and production of 45S precursor ribosomal RNA to a greater extent than depletion of $CHD7_L$ alone. Furthermore, whilst both isoforms interact with Sox2, overexpression of $CHD7_L$ increases Sox2-mediated transcription whereas overexpression of $CHD7_S$ represses it (Kita et al., 2012). $CHD7_S$ therefore appears to have both antagonistic and agonistic roles in relation with full-length CHD7 protein function.

1.4.3 The Drosophila Chd7 orthologue Kismet

CHD7 activity has been studied in numerous model organisms. The *Drosophila* gene *Kismet* (*kis*) is the closest homologue to the mammalian *Chd7* (Srinivasan et al., 2008), and KIS-L - one of two major protein isoforms encoded by *kis* - contains a BRK domain, an ATPase domain and two chromodomains (Srinivasan et al., 2005). KIS-L is a member of the trithorax group of proteins. During *Drosophila* development, spatial information within the embryo initially establishes expression patterns of the key Hox transcription factors, and these patterns are then maintained by the ubiquitously-expressed trithorax group of activators and the Polycomb group of repressors (Ringrose and Paro, 2004; Schuettengruber et al., 2007; Schwartz and Pirrotta, 2007). These proteins therefore play a vital role in the regulation of cellular pluripotency and differentiation. KIS-L appears to facilitate an early step in transcriptional elongation by RNA Polymerase II (Srinivasan et al., 2005), acting downstream of P-TEFb recruitment, and co-localising with the histone methyltransferases ASH1 and TRX on polytene chromosomes in larvae (Srinivasan et al., 2008). Loss of *kis* activity results in an increase in histone 3 lysine 27 (H3K27) methylation, a key marker for repression of Polycomb activity, and a reduction in the recruitment of ASH1 and TRX to chromatin (Srinivasan et al., 2008).

Due to its key role in cell fate determination, null mutations of *kis* are embryonic lethal (Daubresse et al., 1999), but studies utilising the GAL4/UAS system have further helped to establish *Drosophila* as a model organism in which to study CHARGE. It has been shown that adult flies with knockdown of *kis* show defects in motor coordination, learning and memory, similar to symptoms observed in some CHARGE patients, which may be linked to its developmental role in axonal pruning, guidance and extension (Melicharek et al., 2010). However, to date a role for *kis* in cardiac development in *Drosophila* has not been reported.

1.4.4 CHD7 co-localises with enhancer and promoter sites

Genome-wide studies of CHD7 distribution on chromatin were first carried out on human colorectal carcinoma cells, human neuroblastoma cells and mouse ESCs cells before and after differentiation into neural precursors (Schnetz et al., 2009). This work, using chromatin immunoprecipitation followed by genomic tiling microarray hybridisation (ChIP-chip), indicated that the binding pattern of CHD7 is cell-type specific, although in each cell type it correlated with H3K4 methylation. These binding sites were most often contained within DNase hypersensitive sites, at highly conserved sites distal to transcriptional start sites, and often near genes expressed at relatively high levels, indicating it acts in enhancer-mediated transcription (Schnetz et al., 2009).

ChIP followed by massively parallel DNA sequencing (ChIP-seq) identified over 10,000 discrete CHD7-binding chromatin sites in mouse ESCs, many of which are predicted enhancer sequences and, less frequently, promoter sequences (Schnetz et al., 2010). CHD7 co-localises at many sites with potentially unique combinations of DNA-binding proteins, including the known enhancer-binding protein p300 and the ESC 'master regulators' OCT4, SOX2 and NANOG. The transcription factors SMAD1 and STAT3 were also found to co-localise with CHD7 at multiple sites, as well as the chromatin remodelling protein BRG1, although the overlap in binding with BRG1 was not as extensive (Schnetz et al., 2010).

CHD7 binding sites were mostly located distal to transcriptional start sites, and comparison of global gene expression profiles of ES cells with different doses of *Chd7* indicated that CHD7 can modulate gene expression in either a positive or negative direction, although there was some bias towards the repression of gene expression (Schnetz et al., 2010). It has therefore been proposed that CHD7 plays a role in enhancer-mediated regulation of gene expression, although it is not clear whether this is through mediation of long-range communication between enhancers and promoters via chromosome looping, or whether CHD7 acts locally to open up the DNA structure for access by transcriptional activators. CHD7 has also been proposed to function as a positive regulator of ribosomal RNA biogenesis in the nucleolus, with ChIP assays on human DLD1 cells and mouse ESCs showing a physical association between CHD7 and hypomethylated, active ribosomal DNA (Zentner et al., 2010a). Consistent with this observation, knockdown or over-expression of CHD7 resulted in decreased or increased 45S pre-rRNA levels, respectively, and altered the methylation state of the rRNA promoter. Therefore, CHD7 appears to function both in the nucleoplasm and nucleolus for the regulation of mRNA and rRNA expression.

1.4.5 CHD7-protein interactions

Chromatin remodelling enzymes are often found in large, multi-protein complexes (Vignali et al., 2000), the components of which are likely to be tissue- and/or temporally-specific and play a role in the regulation of binding to specific DNA loci. A number of cofactor interactions have been reported for CHD7: during osteoblast formation CHD7 forms a complex with SETDB1, NLK and PPAR-γ as part of the non-canonical Wnt pathway (Takada et al., 2007), whilst *in vitro* studies show CHD7 interacts with CHD8 both directly and indirectly through FAM124B, suggesting a putative CHD7-CHD8 complex (Batsukh et al., 2010; Batsukh et al., 2012).

In neural stem cells (NSCs) CHD7 has been shown to physically interact with Sox2 and to have overlapping binding sites: 43% of genes misregulated in NSCs with knockdown of *Sox2* were also misregulated in *Chd7*-knockdown cells, often in the same direction (Engelen et al., 2011). Loss-of-function mutations in *SOX2* in humans results in a characteristic developmental disorder known as SOX2 Anophthalmia, or Anophthalmia-Esophageal-Genital (AEG), syndrome (Ragge et al., 2005; Williamson et al., 2006a), and as previously mentioned there is considerable overlap in the symptoms of AEG and CHARGE syndromes. Furthermore, Sox2 and CHD7 have been shown to regulate a common set of target genes, including the *Jag1*, *Gli3* and *Mycn* genes that are associated with the human disorders Alagille, Pallister-Hall and Feingold syndromes respectively (Kang et al., 1997; Okuno et al., 1990; van Bokhoven et al., 2005). It is unsurprising therefore that these syndromes also show overlapping malformations with AEG and CHARGE syndromes.

CHD7 has been shown by co-immunoprecipitation in human neural crest-like cells (NCLCs) to also interact with a number of components of the SWI/SNF chromatin remodelling complexes BAF and PBAF, including BRG1, BAF170, BAF155, BAF57, PB1, ARID2, and BRD7 (Bajpai et al., 2010). Interaction between BRG1 and CHD7 was also seen in murine cardiac neural crest tissue, where they co-occupy the PlexinA2 promoter region to activate its expression (Li et al., 2013).

These interaction studies add to the information gained from ChIP-based studies that have identified DNA-binding sites for CHD7 at enhancers, and proteins with overlapping DNA-binding profiles. However, the complexes that CHD7 is found in at different binding sites, in different tissue-types and in different stages in development may vary a great deal in order to regulate its activity, so it is a challenge both to identify further interacting proteins and to elucidate the contexts in which they may be found in complexes together.

1.4.6 CHD7 and cardiovascular development

Whilst there is clearly an association between *CHD7* mutations and congenital cardiovascular defects (as described in Section 1.4), our understanding of the functional role of CHD7 during heart development remains fairly limited. Currently, just one study has been published investigating the role of CHD7 during early cardiogenesis (Liu et al., 2014). Hearts were examined in *Chd7*-null mice at E9.5 and E10.5, which displayed hypocellular myocardial walls and AV cushions, with embryonic lethality occuring soon after E10.5. Consistent with this phenotype, increased cell death and reduced cell proliferation was seen at E10.0 in the myocardium, alongside impaired BMP-dependent formation of the cushion mesenchyme. Expression of a subset of BMP-dependent cardiogenic genes, including *Nkx2.5*, *Gata4* and *Tbx20*, was reduced in *Chd7*-null sections through the heart, whilst the presence of active chromatin marks H3K4me2 and H3K4me3 at *Nkx2.5* enhancers and its transcription start site was significantly reduced. Furthermore, *in vitro* studies showed CHD7 is an interaction partner of the BMP-activated SMAD1 transcription factor, and it binds *Nkx2.5* enhancer regions in a BMP-dependent manner. Overall, this work indicates that CHD7 interacts with BMP-activated SMAD1/5/8 to regulate the chromatin landscape and thus expression of BMP cardiogenic target genes such as *Nkx2.5* during early cardiogenesis and chamber formation (Liu et al., 2014).

Given the high incidence of interrupted aortic arch defects in CHARGE patients, great vessel development has also been studied in heterozygous gene-trapped *Chd7*$^{xk/+}$ embryos, which showed a high penetrance of 4th PAA defects at E10.5 leading to great vessel malformations at E14.5 (Randall et al., 2009). Interestingly, restoration of *Chd7* expression specifically in the pharyngeal surface ectoderm (PSE) rescued the PAA malformations, indicating a crucial role for CHD7 in regulating the signalling from the PSE to migratory NCCs during PAA formation. Furthermore, compound heterozygous mutation of *Chd7* and *Tbx1* increased the PAA phenotype, indicating a dosage sensitive relationship between CHD7 and Tbx1 is important for great vessel development. Therefore, whilst some insights have been gained into the role of *Chd7* in cardiovascular development, it is likely that further roles for such an important chromatin remodelling protein remain to be discovered.

1.4.7 CHD7 activity in the neural crest

Several studies have addressed the role of CHD7 in NCCs, which have shown it is required for both activation of the NCC transcriptional programme and for regulating NCC guidance signals. This role is consistent with many of the congenital anomalies seen in CHARGE patients, which

are associated with malformation of tissues derived from the neural crest (Siebert et al., 1985). Having shown the interaction of CHD7 with multiple BAF and PBAF components, Bajpai and colleagues demonstrated in *Xenopus* embryos an essential role of CHD7, in cooperation with PBAF, for activation of the NCC transcriptional programme. Target genes included *Sox9*, *Twist* and *Slug*, which are crucial for the epithelial-mesenchymal transition to migratory NCCs (Bajpai et al., 2010). CHD7 has also been shown to bind directly at the *PlexinA2* promoter in NCCs in mouse embryos, which encodes a key cell surface receptor expressed in migratory NCCs and is required for guidance of the cardiac NCCs during OFT development (Brown et al., 2001; Li et al., 2013). CHD7 binds as part of a complex that also contains BRG1, with *PlexinA2* promoter activity activated in a dose-dependent manner by both CHD7 and BRG1 (Li et al., 2013).

Another study using whole-genome microarray analysis to compare the expression profiles of E9.5 wild-type, *Chd7*$^{Whi/+}$ and *Chd7*$^{Whi/Whi}$ female mouse embryos also identified disruption in the expression of multiple genes involved in NCC migration and guidance (Schulz et al., 2014b). Whilst this did not give any tissue-specific information on where these genes are being altered by the loss of CHD7 activity, the misregulation of genes such as *Sema3A*, *Sema3C* and *Sema3D* (encoding Semaphorin signalling molecules), and *Epha3*, *Epha5* and *Epha7* (encoding Ephrin receptors) do support a role for CHD7 in the regulation of NCC migration.

Conditional deletion of *Chd7* driven by *Wnt1-Cre* or *Foxg1-Cre* revealed CHD7 is important for craniofacial and tracheal development (Sperry et al., 2014). NCC- specific deletion using *Wnt1-Cre* produced hypoplastic maxillary shelves and mandible, abnormal frontal occipital bone formation and cleft palate. The ectodermal and endodermal marker *Foxg1-Cre* ablated CHD7 activity in the developing eye, ear, nose, pharyngeal pouch, forebrain, and gut, which also resulted in hypoplasia of the maxillary shelves and nasal epithelia, alongside abnormal development of the eyes, concha and frontal bone, and reduced tracheal rings. Both conditional lines resulted in postnatal respiratory distress and death. Whilst the molecular basis for these defects caused by loss of CHD7 activity in the endoderm, ectoderm or NCCs is not yet determined, comparison with the skeletal development of heterozygous Chd7$^{Gt/+}$ mice revealed the role of *Chd7* in craniofacial development is dosage-dependent (Sperry et al., 2014).

An interesting link between CHD7 activity and p53 activation in NCCs has recently been reported: loss of *Chd7* in mouse NCCs or CHARGE syndrome patient samples resulted in increased p53 activity (Van Nostrand et al., 2014). CHD7 was shown to bind at the p53 promoter site in NCCs, indicating it directly represses transcription of p53 to promote cell survival. Strikingly, heterozygosity for p53 partially rescued the developmental delay seen in

Chd7-null embryos, whilst a mouse model with hyper-activated p53 phenocopied many CHARGE features, together indicating that inappropriate p53 activation in CHARGE patients contributes to the disease phenotypes (Van Nostrand et al., 2014).

1.4.8 Other tissue-specific developmental roles of Chd7

Many studies have shown CHD7 functions in neural stem cell (NSC) populations and is important for neurogenesis during different developmental processes, which again are consistent with the range of symptoms seen in CHARGE patients. During inner ear morphogenesis, CHD7 is required for the proliferation of inner ear neuroblasts, with targeted *Chd7* deletion in the otocyst driven by *Foxg1-Cre* leading to cochlear hypoplasia and absence of the semicircular canals and cristae (Hurd et al., 2010). CHD7 also functions cooperatively with retinoic acid signalling in the stem cell niche of the subventricular zone (SVZ) and inner ear, which are important for olfactory bulb formation, hearing and balance (Micucci et al., 2014). This role in the SVZ is maintained into adulthood, when the SVZ and subgranular zone (SGZ) contain pools of multipotent NSCs for active neurogenesis (Gage, 2000). CHD7 expression is specifically enriched in active NSCs in the SVZ and SGZ, with deletion of *Chd7* induced in adult mice resulting in a dramatic decrease in neurogenesis due to loss of *Sox4* and *Sox11* expression ((Feng et al., 2013)). Interestingly, this phenotype could be rescued by physical exercise, indicating that exercise-induced neurogenesis is independent of CHD7 activity.

Layman and colleagues also highlighted the importance of CHD7 for development of olfactory tissue. High *Chd7* expression was shown in basal olfactory epithelial NSCs, and *Chd7* heterozygotes displayed smaller olfactory bulbs, reduced olfactory sensory neurons and disorganisation of the epithelial structure due to loss of NSC proliferation. Consistent with these observations, *Chd7* deficient mice showed signs of loss of olfaction (Layman et al., 2009). Furthermore, CHD7 has a critical role in the development and maintenance of gonadotropin-releasing hormone (GnRH) neurons in the hypothalamus and embryonic nasal region, which are important for reproduction (Layman et al., 2011).

The development of several brain structures are also found to be disrupted in *Chd7* mutant mice. For example, *Chd7* haploinsufficiency results in a small cerebellar vermis, due to reduced *Fgf8* expression in the isthmus organiser (Yu et al., 2013). This cerebellar hypoplasia phenotype was identified in 35% of a cohort of CHD7 mutation-positive CHARGE patients. Furthermore, a synergistic relationship between *Chd7* and *Fgf8* loss-of-function alleles was shown, demonstrating the importance of this genetic interaction (Yu et al., 2013). Development of the

forebrain also relies on CHD7 activity: *Chd7* heterozygotes show defects in the telencephalic midline, including reduced cerebral cortex and dilated third and lateral ventricles (Jiang et al., 2012). Apoptosis of cells in the telencephalic midline zone was impaired, along with disruption to expression of *Bmp4*, a key factor in regulation of midline cell fate.

Finally, studies in zebrafish have identified CHD7 as the first chromatin remodeller to have a role in somitogenesis (Jacobs-McDaniels and Albertson, 2011). *Chd7* morpholino-knockdown showed CHD7 functions in directing the bilaterally-symmetric expression of somitogenesis genes in the pre-somitic mesoderm, including *cdx1a*, *dlc*, *her7*, *mespa* and ripply1, leading to left-right asymmetry defects in zebrafish *chd7*-morphants. Overall, these studies clearly show CHD7 has multiple crucial roles during development, regulating many key transcriptional programmes in a tissue-specific manner.

1.5 CHARGE syndrome

The human disorder CHARGE syndrome provides a key example of the severe congenital anomalies that can arise when chromatin remodelling is disrupted during development, including a range of cardiovascular malformations, which will be discussed in this section.

1.5.1 Clinical presentation

CHARGE syndrome (OMIM# 214800) is a developmental disorder with an estimated prevalence of 1 in 15,000 to 1 in 17,000 live births (Janssen et al., 2012). It is characterised by a specific pattern of anomalies, first described in 1979 (Hall, 1979). The acronym 'CHARGE' was introduced two years later to summarise the major clinical features: ocular coloboma, heart malformations, atresia of the choanae, retardation of growth or development, genital hypoplasia and ear anomalies (Pagon et al., 1981). It was originally proposed that a clinical diagnosis of CHARGE required 4/7 of these signs to be present (Oley et al., 1988), one of which must be either choanal atresia or a coloboma (Pagon et al., 1981). Many other clinical findings have since been frequently reported in CHARGE patients, including anomalies of the cranial and CNS midline, brainstem dysfunctions, dysmorphic features, and hypoplasia of the semicircular canals. Updates to the clinical criteria include these additional signs (Blake et al., 1998; Verloes, 2005), with the most recent criteria summarised in Tables 1-2 and 1-3.

Table 1-2: Updated clinical criteria for CHARGE syndrome (Verloes, 2005)

Major Criteria	Minor Criteria
1. Ocular coloboma 2. Choanal atresia 3. Hypoplastic semicircular canals	1. Rhombocephalic dysfunction (brainstem and cranial nerve III to XII anomalies, including sensorineural deafness) 2. Hypothalamo-hypophyseal dysfunction 3. Abnormal middle or external ear 4. Malformation of heart or oesophagus 5. Mental retardation

Table 1-3: Definition of Typical, Atypical, and Partial CHARGE syndrome (Verloes, 2005)

Typical	Atypical	Partial/Incomplete
3 major signs 2/3 major + 2/5 minor signs	2/3 major + 0/5 minor signs 1/3 major + 2/5 minor signs	2/3 major + 1/5 minor signs

1.5.2 Genetic basis

CHARGE is an autosomal dominant disorder that usually occurs sporadically, although rarely it has been transmitted from a mildly affected parent. It is caused by heterozygosity for loss-of-function mutations of *CHD7*, the gene encoding the ATP-dependent chromatin remodelling protein CHD7 (Vissers et al., 2004). *CHD7* is located at chromosome 8q12 and consists of 38 exons. Estimates for the *CHD7* mutation frequency in CHARGE patients vary depending on the selection criteria, with recent studies giving a range of 58-71% of cases (Aramaki et al., 2006; Lalani et al., 2006; Zentner et al., 2010b). This figure rises to over 90% if only patients meeting the clinical diagnostic criteria of Blake and/or Verloes are included (Jongmans et al., 2006).

Mutations are found along the entire coding region and splice sites of the *CHD7* gene (Figure 1-11) (Bartels et al., 2010; Lalani et al., 2006). Most reported mutations are unique for a patient or family, although recurrent *de novo* mutations do occur rarely. The two most frequently reported *CHD7* mutations are the nonsense mutations C1480T and C7879T, which both result in the introduction of a stop codon in the place of an arginine codon (Janssen et al., 2012). Interestingly, a significant number of mutations reported in CHARGE patients involve the substitution of the arginine CGA codon, which occurs 27 times in *CHD7*, for a TGA stop codon (Bartels et al., 2010; Janssen et al., 2012). This is consistent with a previous report that CG to TG mutations are highly frequent in the human genome (Antonarakis et al., 2000).

Nearly 80% of *CHD7* mutations reported in CHARGE patients are predicted to be nonsense or frameshift (Janssen et al., 2012). These mutations would likely result in nonsense-mediated mRNA degradation (NMD), or else production of a truncated CHD7 protein. Investigation of CHD7 protein deletion mutants *in vitro* indicates that the ATPase and nucleosome remodelling activities of CHD7 are severely impaired or ablated following various truncations of the protein, including truncation of the C-terminal domain or the chromodomains (Bouazoune and Kingston, 2012). Therefore, the combination of degradation of mutant mRNA through the NMD pathway and the loss of CHD7 activity caused by protein truncation indicates that the pathogenic mechanism underlying the majority of CHARGE syndrome cases is haploinsufficiency for CHD7.

Splice site (11%) and missense *CHD7* mutations (8%) are found less commonly in CHARGE patients (Janssen et al., 2012), and are thought to have variable effects on CHD7 remodelling activity. Site-directed mutagenesis has been used to engineer *in vitro* a number of point mutations reported in CHARGE patients at highly conserved residues in the *CHD7* locus. K907T

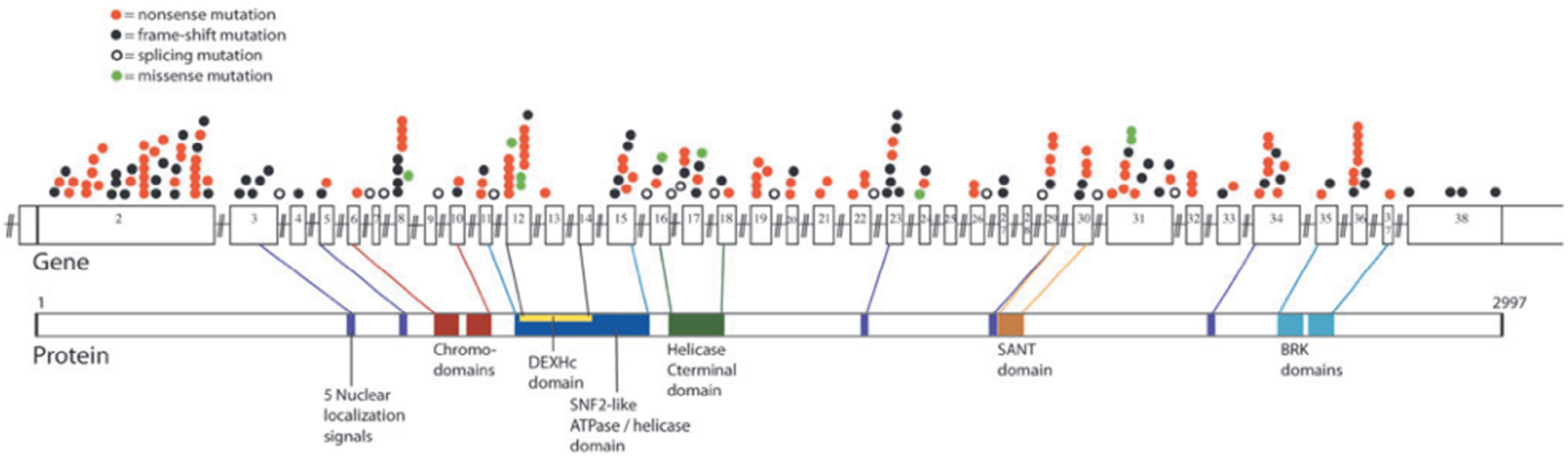

Figure 1-11: Distribution of mutations along the *CHD7* locus and corresponding CHD7 protein domains

Coloured circles depict the loci of 200 CHARGE-causing mutations, as defined by the introduction of stop codons or frameshifts, or mutations of the canonical splice donor–acceptor pair (GT-AG). Missense changes or other putative splice site changes were only considered disease-causing if the change was a *de novo* mutation not found in either parent, or if it was reported in the literature as a *de novo* mutation. Overlapping circles indicate identical mutations. Protein domains are labeled and lines indicate where each protein domain is encoded on the gene.

Diagram taken from Bartels et al. (2010).

and T917M mutations, which affect the second chromodomain of CHD7, show a 3.5-fold and 1.5-fold reduction in ATPase activity respectively, whilst the S834F missense mutation found in the first chromodomain completely abolishes both ATPase and nucleosome remodelling activity (Bouazoune and Kingston, 2012). Again, these mutations appear to result in a non-functional CHD7 protein, supporting the hypothesis that CHD7 haploinsufficiency causes CHARGE syndrome.

The genetic basis of CHARGE remains unclear in approximately 10% of patients that fulfil the clinical criteria for typical CHARGE, and many more patients with either the atypical or partial CHARGE phenotype. The only other gene that has been implicated in CHARGE syndrome is *SEMA3E*, which was mutated in one *CHD7*-negative CHARGE patient and disrupted in another patient with a *de novo* chromosomal translocation between chromosomes 2 and 7 (Lalani et al., 2004). Other candidate genes have been tested in CHARGE patients, including *PITX2*, *PAX2* and *CHD8*, but none of these studies identified any pathogenic mutations (Batsukh et al., 2010; Martin et al., 2002; Tellier et al., 2000). Undetectable disruption to the *CHD7* locus, such as intra-genic rearrangements, intronic mutations affecting unknown splice sites, or mutations in regulatory regions could explain the presence of CHARGE in patients for which a pathogenic mutation has not been identified.

1.5.3 Heart defects associated with CHD7 mutations

Whilst cardiac malformations are not considered a major criterion for the diagnosis of CHARGE (see Table 1-2), there is a high incidence of congenital heart defects in CHARGE syndrome. A review of 379 clinical cases of CHARGE found 77% of *CHD7* mutation-positive patients had cardiovascular defects (Zentner et al., 2010b), whilst a more recent study of 299 patients with a pathogenic *CHD7* mutation reported that 74% of the cohort had a congenital heart defect (Corsten-Janssen et al., 2013a). A wide range of heart malformations are reported, including Tetralogy of Fallot (characterised by ventricular septal defects, pulmonary stenosis, right ventricular hypertrophy, and an overriding aorta), patent ductus arteriosus (PDA), septal defects, aortic valve stenosis, and interrupted aortic arch (IAA) (Aramaki et al., 2006; Lalani et al., 2006; Lin et al., 1987; Tellier et al., 1998; Wyse et al., 1993).

The most detailed study of the congenital heart defects found in patients with a pathogenic *CHD7* mutation was carried out by Corsten-Janssen and colleagues. They classified the heart defects of 220 CHARGE patients and compared them to a cohort of 1,007 non-syndromic heart defects. High variability in the types of congenital heart defects was observed, with conotruncal defects, septal defects and atrioventricular septal defects (AVSDs) most commonly

seen, either in isolation or in combination with other defects. Comparing the distribution of cardiac defects between the CHARGE patients cohort and the non-syndromic cohort identified an over-representation of AVSDs and conotruncal defects in patients with a *CHD7* mutation (Figure 1-12) (Corsten-Janssen et al., 2013a). However, the same group also reported that *CHD7* mutations are not present in a group of patients with these heart defects plus one other feature of CHARGE (Corsten-Janssen et al., 2014). This indicates that *CHD7* mutations are associated with heart defects predominantly in the context of CHARGE syndrome, so analysis of the *CHD7* gene is not recommended in patients presenting with an AVSD or conotruncal defects, even when an additional feature of CHARGE is present.

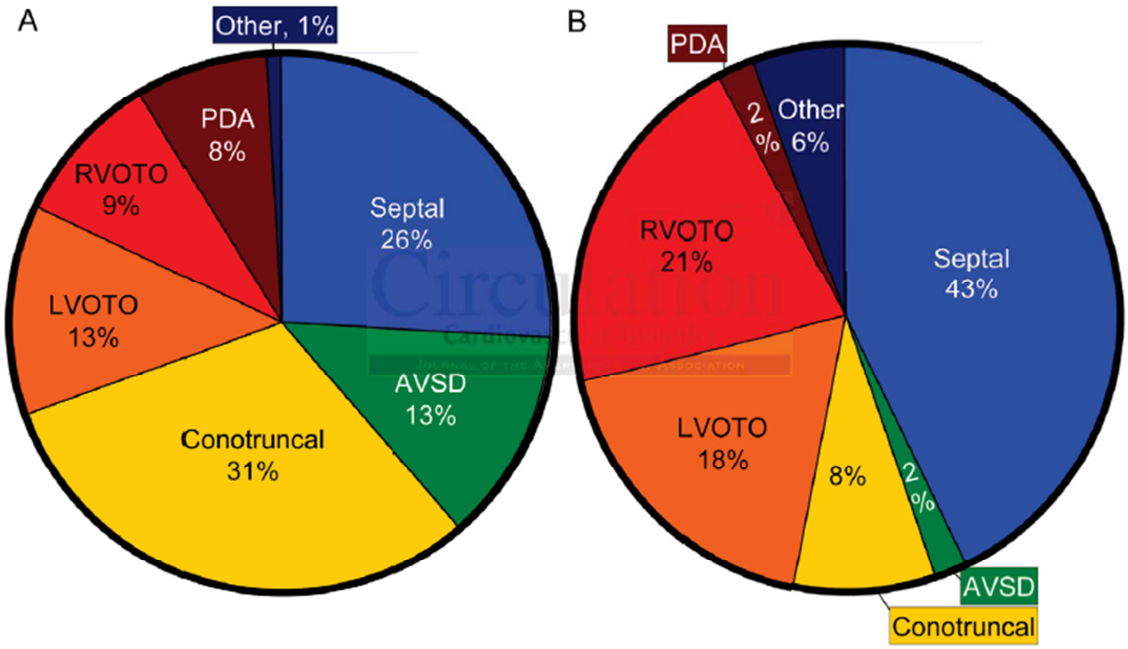

Figure 1-12: Comparison of heart malformations associated with *CHD7* mutations (A) and non-syndromic heart defects (B)

Classification of 239 congenital hearts defects in a cohort of 202 patients with *CHD7* mutations (A) is compared to 1,007 patients with non-syndromic heart defects (B), showing over-representation of AVSDs and conotruncal defects in *CHD7*-mutation patients.

Figure taken from Corsten-Janssen et al (2013a). AVSD is atrioventricular defects; LVOTO, left ventricular outflow tract obstruction; RVOTO, right ventricular outflow tract obstruction; PDA, patent ductus arteriosus.

The incidence of heart defects is significantly higher in CHARGE patients with truncating nonsense or frameshift deletions (80%) compared to those with missense or splice site mutations (58%) (Corsten-Janssen et al., 2013a). This is consistent with biochemical studies that found variable effects of missense mutations on the biological function of CHD7 (Bouazoune and Kingston, 2012). Of 139 patients for which information about cardiac surgery was available, 12 patients died before surgery could be performed, whilst 88 patients had undergone surgery and a further 3 were predicted to need surgery in the future (Corsten-Janssen et al., 2013a). Therefore, nearly 75% of CHARGE patients required cardiac surgery, showing that congenital heart malformations have a significant impact on the morbidity and mortality associated with CHARGE syndrome. *CHD7* has also been detected in a large-scale study of *de novo* mutations in human sporadic congenital heart defects (Zaidi et al., 2013), again indicating an important role for *CHD7* in the development of the heart.

1.5.4 Overlap with other developmental disorders

Phenotypic overlap has been noted between CHARGE syndrome and a number of other developmental disorders, such as DiGeorge syndrome, Anophthalmia-Esophageal-Genital syndrome, Kabuki syndrome and Kallman syndrome. Understanding of the molecular and genetic basis for these disorders can lead to the identification of overlapping tissue requirements and roles for the genes involved, as well as being informative for the clinical diagnosis and genetic counselling of patients.

DiGeorge syndrome (DGS, OMIM# 188400) - also known as 22q11.2 Deletion syndrome – is a genetic disorder caused by a 1.5- to 3.0-Mb hemizygous interstitial deletion of chromosome 22q11.2. The anomalies are largely attributed to the loss of the *TBX1* gene in this region, leading to haploinsufficiency for the transcription factor TBX1 (Paylor et al., 2006; Yagi et al., 2003). DGS commonly features heart defects, most often affecting the outflow tract and aortic arch (Momma, 2010). Furthermore, craniofacial dysmorphia, cleft palate, aplasia/hypoplasia of the thymus gland, and ear defects are all characteristics associated with both CHARGE and DGS. During development, the tissues affected by these overlapping anomalies are all associated with the pharyngeal apparatus, indicating overlapping roles for *Chd7* and *Tbx1* in this region. Hypo/aplasia of the fourth pharyngeal arch artery (PAA) at E10.5 is seen in both *Tbx1* and *Chd7* heterozygous mice (Randall et al., 2009). Furthermore, *Tbx1* and *Chd7* have been shown to be in epistasis, with biallelic expression of both genes required in the pharyngeal surface ectoderm for normal PAA morphogenesis (Randall et al., 2009). It is therefore unsurprising that patients clinically diagnosed as having CHARGE syndrome have

been found to have 22q11.2 deletions, whilst patients with the DGS phenotype have been identified with truncating CHD7 mutations (Corsten-Janssen et al., 2013b).

Anophthalmia-Esophageal-Genital (AEG) syndrome (OMIM# 206900) is caused by heterozygous mutations in *SOX2*, which encodes a SOX family transcription factor (Fantes et al., 2003; Kelberman et al., 2006; Williamson et al., 2006b). Again, a number of the congenital anomalies seen in AEG patients overlap with CHARGE patients, including atresia of the oesophagus, pituitary and genital abnormalities, and neurocognitive delays. Engelen and colleagues have identified a molecular basis for the phenotypic overlap resulting from mutations of *SOX2* and *CHD7*, showing that CHD7 and SOX2 proteins physically interact and have overlapping genome-wide binding sites in neural stem cells. They act synergistically to regulate a common set of target genes, of which *MYCN*, *GLI3* and *JAG1* are also associated with human syndromes that overlap with AEG and CHARGE (Engelen et al., 2011).

Kabuki syndrome (OMIM# 147920) shares a number of features with CHARGE syndrome, including cleft palate, congenital heart, ear and eye defects, genital hypoplasia and retardation of growth and development (Schulz et al., 2014a). The major cause of Kabuki syndrome is mutations in the *KMT2D* gene, which encodes a SET1 histone H3 lysine 4 (H3K4) methyltransferase also known as MLL2 (Li et al., 2011; Ng et al., 2010). It is only functional as a methyltransferase when in a multi-subunit complex, including a core complex comprised of WDR5, ASH2L and RbBP5 (Ernst and Vakoc, 2012; Zhang et al., 2012). CHD7 has also been shown to interact with these three proteins, suggesting a possible mechanistic link between CHD7 and KMT2D during chromatin modification, which would explain the phenotypic overlap between CHARGE and Kabuki syndrome (Schulz et al., 2014a).

The disorder Kallman syndrome (KS, OMIM# 308700) combines congenital hypogonadotropic hypogonadism (CHH) and anosmia (Kallmann FJ, 1944), which are features also frequently seen in CHARGE patients (Pinto et al., 2005). Mutations in a number of genes have been implicated in KS, including *KAL1*, *FGFR1*, *PROK2, PROKR2,* and *SEMA3A* (Dode et al., 2003; Dode et al., 2006; Hanchate et al., 2012; Legouis et al., 1991). CHH in KS is caused by incomplete embryonic migration of gonadotropin-releasing hormone (GnRH) cells along the olfactory nerve fibers from the olfactory epithelium to the forebrain, so it is proposed that the protein products of the genes associated with KS are involved in this process (Kim et al., 2008b; Oliveira et al., 2001). Mutations in *CHD7* have also recently been reported in 5.4-8.3% of KS patients (Bergman et al., 2012; Jongmans et al., 2009; Kim et al., 2008a). It is therefore possible that CHD7 has a role in the regulation, through chromatin remodelling, of *KAL1*, *FGFR1*, *PROK2*, *PROKR2* and/or *SEMA3A* during GnRH cell migration. Interestingly, the

prevalence of *CHD7* missense versus truncating mutations is higher in KS patients compared to typical CHARGE patients, indicating that the clinical spectrum associated with *CHD7* mutations may at least partly be explained by genotype/phenotype correlations (Marcos et al., 2014).

1.6 Mouse models to investigate *Chd7* activity

Both human and mouse *CHD7*/*Chd7* genes comprise 38 exons with similar intron-exon structures, which produce proteins with 94.7% sequence identity (Layman et al., 2010). Mouse models have therefore been widely used to study the function of CHD7 and the etiology of CHARGE syndrome. A large number of mutant *Chd7* alleles have now been reported, which have been generated through various methods, including ethylnitrosurea (ENU) mutagenesis, gene trapping and gene targeting (see Table 1-4). This final section will give an overview of these mutant lines.

Table 1-4: Published *Chd7* mutant alleles

Allele:	Derivation:	Mutation:	Effect:	Reference:
Coa1	ENU	c.2155A>T	p.K719X	(Jiang et al., 2012)
Cycn	ENU	c.4286T>A	p.L1429X	(Bosman et al., 2005)
Dz	ENU	c.5536G>T	p.E1846X	(Bosman et al., 2005)
Edy	ENU	c.3070C>T	p.Q103X	(Bosman et al., 2005)
Flo	ENU	IVS27+2T>C	p.S1864X	(Bosman et al., 2005)
Gt(RRR136)Byg	Gene trap	Insertion in intron 4	Reporter fusion	(Randall et al., 2009)
Gt(S20-7E1)Sor	Gene trap	Insertion in exon 1	Reporter fusion	(Hurd et al., 2007)
Gt(XK403)Byg	Gene trap	Insertion in intron 36	Reporter fusion	(Randall et al., 2009)
Lda	ENU	c.3195T>A	p.Y1066X	(Bosman et al., 2005)
Looper	ENU	c.5690C>A	p.S1897X	(Ogier et al., 2014)
Mt	ENU	IVS22-2A>G	p.V1688X	(Bosman et al., 2005)
Obt	ENU	c.3945T>A	p.Y1315X	(Bosman et al., 2005)
Ome	Spontaneous	Del. exons 2 & 3	No protein	(Tian et al., 2012)
tm1.1Dmm	Gene targeting	Floxed exon 2	No effect	(Hurd et al., 2010)
tm1.2Dmm	Gene targeting	Del. exon 2	No protein	(Hurd et al., 2010)
tm2a-(EUCOMM)Wtsi	Gene targeting	Floxed exon 2	No protein	(Feng et al., 2013)
Todo	ENU	IVS3+2T>C	p.H539X	(Bosman et al., 2005)
Vik	ENU	c.4377T>A	p.Y1459X	(Lenz, 2010)
Whi	ENU	c.2918G>A	p.W973X	(Bosman et al., 2005)

1.6.1 Chd7 ENU mutants

The first reported heterozygous *Chd7* mutant mice were generated through ENU mutagenesis screens that selected for mice displaying hyperactivity, circling and headshaking phenotypes in heterozygotes, which is characteristic of inner ear defects (Bosman et al., 2005). ENU mutagenesis involves the injection of the alkylating agent N-Ethyl-N-nitrosourea into adult males to induce single nucleotide substitutions into mouse spermatogonia DNA at a frequency of approximately one new mutation per gene in 700 first-generation progeny (Hitotsumachi et al., 1985). Progeny with the desired/interesting phenotypes can then be selected, and linkage analysis using microsatellite markers to identify the chromosomal location of the mutation, to enable a non-biased approach to identifying important developmental genes based on their mutant phenotype (Liu and Eggenschwiler, 2014). 12 lines were identified with the inner ear defect and a mutation mapping to the proximal region of chromosome 4, and exon re-sequencing identified a single nonsense or splice-site mutation in the *Chd7* locus in nine of these lines, which were spread throughout the gene (Table 1-4) (Bosman et al., 2005). A range of defects were seen that are reminiscent of the human CHARGE symptoms, including cleft palate, choanal atresia, septal defects of the heart, vulva and clitoral defects.

The *Whi* line, which carries a nonsense mutation in exon 11, which is predicted to produce a truncated protein missing most of the SNF2 helicase domain and all other more C-terminal domains, was characterised further. *Whi*/+ embryos were examined during development at E15.5, when 45% had either mild or severe oedema, 10% had haemorrhage and 3 out of 5 showed VSDs. Post-natally, approximately 50% of *Whi*/+ mice died before weaning, and in those that survived to adulthood, all showed the inner ear defect behaviour (Bosman et al., 2005).

Three further ENU-generated lines with mutations in *Chd7* have been reported, all with similar phenotypes. Both the *Volchok* (*Vlk*) and *Coa1* lines were also originally selected based on their circling and head bobbing behaviour. Similar structural inner ear defects were described in *Vlk/+* mice to those seen by Bosman and colleagues, which was accompanied by mild hearing loss (Lenz, 2010). Developmental defects in the telencephalic midline were characterised in the *Coa1* line, identifying a role for CHD7 in the regulation of *Bmp4* expression during development of the forebrain (Jiang et al., 2012). The most recently-reported *Chd7* ENU line, Looper, was identified in a screen using acoustic startle response testing, so again have hearing impairments as well as a range of CHARGE-associated phenotypes (Ogier et al., 2014).

1.6.2 Chd7 gene-trap mice

Gene-trapping enables the generation of a well characterised insertional mutation into a random intronic or coding region of genomic DNA, which is introduced by electroporation or retroviral infection of a vector into ESCs (Figure 1-13) (Stanford et al., 2001). The trapped locus is identified using primer sequences from the ends of the vector to sequence mRNA surrounding the vector cassette, and the mutant ESCs can be injected into blastocysts to generate chimeric mice, from which germline transmissions of the gene-trapped allele can be obtained. Hurd and colleagues characterised a loss of function *Chd7* mouse line (*Chd7*$^{Gt(S20\text{-}7E1)Sor}$, or *Chd7*^{Gt}) generated from *Chd7*-deficient gene-trapped *lacZ* reporter ESCs, which were produced by retroviral infection of the ROSAFARY viral vector (Chen et al., 2004). The vector cassette was inserted between exons 1 and 2 at the *Chd7* locus (Hurd et al., 2007). Heterozygous *Chd7*$^{Gt/+}$ mice had phenotypes very similar to those seen in the ENU-mutated mice, whilst complete knock-out in *Chd7*$^{Gt/Gt}$ mice was embryonic lethal by E10.5 (Hurd et al., 2007). *Chd7*$^{Gt/GT}$ embryos exhibited delayed turning, and sectioning at E10.5 revealed hypoplasia of a number of structures, including the neuroepithelium, optic eminence and hindlimbs. The otocyst, which develops into the inner ear, was also thickened and reduced in size in *Chd7*$^{Gt/Gt}$ embryos (Hurd et al., 2007). Two further gene-trapped reporter lines have also been generated, which showed similar embryonic lethality in homozygotes and great vessel defects in heterozygotes (Randall et al., 2009).

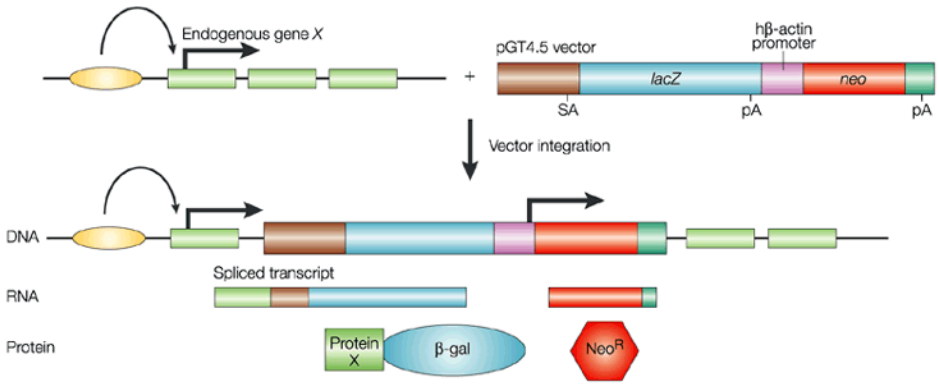

Figure 1-13: Conventional gene-trap mutagenesis in ESCs

The pGT4.5 vector, containing a *lacZ* reporter gene and a neomycin resistance gene (*neo*) that is driven by an autonomous hβ-actin promoter, is shown 'trapping' an endogenous gene 'X' by insertion in an intron. The presence of the splice acceptor site (SA) immediately upstream of the *lacZ* gene interrupts normal splicing of the gene, leading to transcription of the vector cassette sequence downstream of the gene X exon when gene X expression is activated. The polyadenylation site (pA) at the end of the lacZ gene signals a stop in translation. This therefore results in a fusion protein of the truncated protein X with C-terminal β-galactosidase (β-gal), which can be used as a reporter to show successful integration of the vector into an expressed gene. If it is inserted close enough to the 5' end of the gene this should lead to a null allele. Integration into the genome will also lead to neomycin resistance, which allows selection of ESCs with inserted mutations.

Adapted from Stanford et al. (2001).

1.6.3 *Conditional Chd7^{fl} allele*

Due to the embryonic lethality of ubiquitous homozygous *Chd7* mutation, conditional floxed *Chd7* alleles (*Chd7^{fl}*) have also been generated, to study further the tissue-specific roles of *Chd7* (Feng et al., 2013; Hurd et al., 2010). Briefly, a neomycin/kanamycin (N/k) cassette was introduced between exons 2 and 3 of the *Chd7* gene using recombineering techniques, with LoxP sites positioned upstream of exon 2 and downstream of the N/k cassette ('Floxed allele', Figure 1-14). Breeding with FLPeR mice (MGI; Gt(ROSA)26Sor$^{tm1(FLP1)Dym}$, (Farley et al., 2000)) results in recombination at the frt sites to excise the N/k cassette, leaving a conditional *Chd7^{fl}* allele with LoxP sites surrounding exon 2 ('Flp-recombined allele). When this Flp-recombined allele is crossed with a tissue-specific Cre recombinase mouse, the *Chd7* exon 2 is excised due to recombination at the LoxP sites, which is predicted to lead to nonsense-mediated decay of *Chd7* mRNA. This allows conditional ablation of *Chd7* in specific tissues relevant for different organs or systems, such as cardiovascular development.

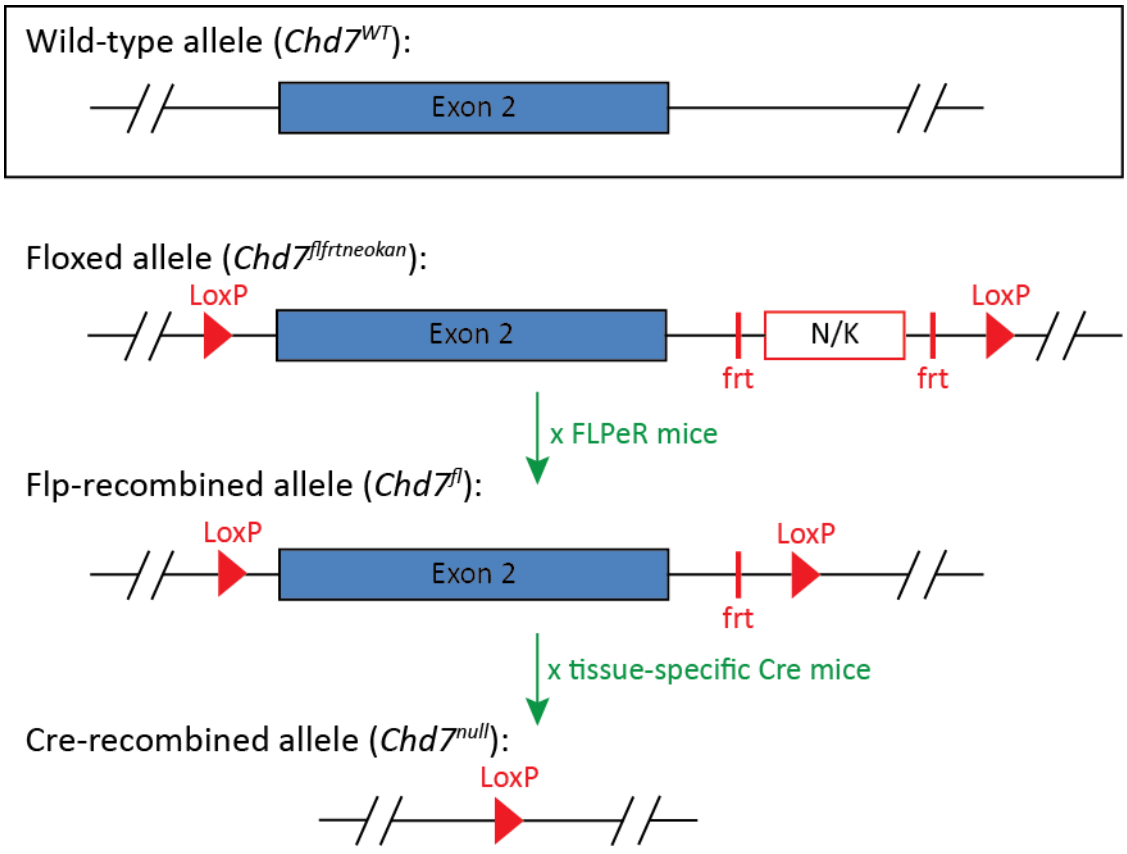

Figure 1-14: Schematic showing the generation of the conditional *Chd7* construct

Adapted from Hurd et al. (2010)

1.7 Scope of the thesis

It is clear from the literature that chromatin remodelling by CHD7 is extremely important during development in a range of different tissues. Whilst congenital heart defects are commonly seen in CHARGE patients, the specific role of CHD7 during cardiogenesis is still poorly understood. This is partly due to the early embryonic lethality of constitutive *Chd7*$^{-/-}$ embryos. The overall aim of this thesis was to investigate the role of *Chd7* during heart development, using a conditional floxed *Chd7* allele to allow examination of hearts at later stages in development. Specifically, three key questions will be addressed:

- When and where is CHD7 protein present in the developing heart?
- What is the cardiovascular phenotype when *Chd7* is ablated in the cardiogenic mesoderm, and subsets of this lineage?
- What are the downstream transcriptional effects of loss of CHD7 activity in the heart?

Immunohistochemistry and western blot analysis data will be presented, along with detailed morphological analysis of conditional *Chd7* mutant embryos, to determine the tissue-specific requirements for *Chd7* in the developing heart. Microarray experiments will also be presented, which were used to identify genome-wide transcriptional changes underlying the cardiac defects caused by *Chd7* ablation, with selected genes validated further by *in situ* hybridisation and by functional calcium imaging assays.

CHAPTER TWO

EXPERIMENTAL PROCEDURES

2.1 Mouse lines and genotyping

2.1.1 Mouse lines

Animal maintenance, husbandry and procedures were carried out in accordance with British Home Office regulations. All genetically-modified lines were maintained on a C57Bl/6J background. The mouse lines used were:

Whirligig - MGI: 3588650, Chd7^{Whi,} (Bosman et al., 2005)

Conditional *Chd7^{fl}* – MGI: 4433295, Chd7$^{tm2a(EUCOMM)Wtsi}$ (Feng et al., 2013)

Conditional *Brg1^{fl}* - MGI: 3605892, Smarca4^{tm1Pcn} (Indra et al., 2005)

Conditional *Sema3C^{fl}* - MGI: 5428549, Sema3c$^{tm1a(KOMP)Wtsi}$, Wellcome Trust Sanger Institute

Mesp1-Cre - MGI: 2176467, Mesp1$^{tm2(cre)Ysa,}$ (Saga et al., 1999)

Nkx2.5-Cre - (MGI:2654594, Nkx2-5$^{tm1(cre)Rjs,}$ (Moses et al., 2001)

Mef2c-Cre - (MGI: 3639735, Tg(Mef2c-cre)2Blk, (Verzi et al., 2005)

Tie2-Cre - (MGI: 2450311, Tg(Tek-cre)1Ywa, (Kisanuki et al., 2001)

R26RYFP - (MGI: 2449038, Gt(ROSA)26Sor$^{tm1(EYFP)Cos,}$ (Srinivas et al., 2001).

CD1 mice were also used, for anti-CHD7 immunohistochemistry on cryosections.

2.1.2 Mouse breeding

Mice were determined to have reached sexual maturity at 6 weeks of age for females and 8 weeks for males. Breeding pairs were set up once mice were sexually mature, and resulting pups were ear-clipped at ~10 days of age for genotyping and identification. Offspring were weaned at 21 days of age.

2.1.3 Embryo collection

Timed-matings were set up overnight and female mice checked for vaginal plugs the following morning. The date of observation of a vaginal plug was considered embryonic day E0.5. Pregnant females were culled by cervical dislocation followed by decapitation, and embryos harvested into phosphate buffered saline (PBS) on ice. For embryos at E10.5, E11.5, E12.5, E13.5, E15.5 or E18.5, collection was mid-late afternoon, and for E15.0 embryos collection was

early in the morning. Embryos were dissected from the uterus and yolk sacs and/or tail tips collected for genotyping.

2.1.4 Genomic DNA extraction

Genomic DNA was extracted from yolk sacs, tail tips or ear clips by incubation in Tail Lysis buffer (10mM Tris-HCl pH8.0, 100mM NaCl, 10mM EDTA pH 8.0, 10mM EDTA pH 8.0, 0.5% SDS, 400µg ml^{-1} Proteinase K (Sigma)) overnight at 56°C, followed by enzyme heat inactivation for 5 minutes at 95-100°C. DNA was precipitated by addition of an equal volume of isopropanol, separated by centrifugation, and the pellet washed in ice-cold 70% ethanol (EtOH) before air drying and resuspension in 100-150µl distilled H_2O.

2.1.5 Polymerase chain reaction

Illustra PuReTaq Ready-To-Go PCR Beads (GE Healthcare) were used for genotyping the conditional *Chd7*^{fl}, *Brg1*^{fl} and *Sema3C*^{fl} alleles, the *Chd7*^{Whi} allele and the *R26RYFP* allele. Beads were dissolved in reaction mixes to contain a final concentration of 0.8µM of each required primer (Table 2-1) and 20-50ng genomic DNA in a total volume of 25µl. PCR reactions were carried out in a Thermal Cycler PCR machine (PTC-225, MJ Research) and PCR products run on a 2% or 3% agarose gel.

The *Chd7*^{Whi} genotyping required an additional MfeI digestion step after the PCR reaction, as the wild-type *Chd7* sequence contains an MfeI recognition site in exon 11 that is lost in the ENU-generated *Chd7*^{Whi} mutant allele. Digestion of PCR products for 2-3 hours at 37°C with MfeI (New England Biolabs) produced a band of 204bp for the wild-type allele and 233bp for the mutant *Chd7*^{Whi} allele, which could be resolved on a 3% agarose gel.

BIOTAQ^{TM} DNA polymerase kits (Bioline) were used for genotyping the *Cre* alleles. Reaction mixtures were prepared containing 1x NH_4 Reaction Buffer (Bioline), 1.5mM $MgCl_2$, 0.8mM dNTP mix (Bioline), 0.4mM Cre primers, 0.04u $µl^{-1}$ Taq DNA Polymerase and 20-50ng genomic DNA in a total volume of 25µl. PCR reactions were again carried out in the Thermo Cycler PCR machine and the products run on a 2% agarose gel.

Table 2-1: Genotyping primer sequences, annealing temperatures and PCR product sizes

Allele:	Primer sequences (5'-3'):	Annealing temp (°C):	Size of PCR products (bp):
Chd7^{fl}	F: TGCAGATGGGACGTTTTCAG WT-R: CTGCAAGAACACAGGGCAAG Mut-R: TCGTGGTATCGTTATGCGCC	58°C	*Chd7^{WT}*: 610 *Chd7^{fl}*: 411
Brg1^{fl}	F: GCCTTGTCTCAAACTGATAAG R: GTCATACTTATGTCATAGCC	60°C	*Brg1^{WT}*: 268 *Brg1^{fl}*: 387
Sema3C^{fl}	F: GAATCTGGCAAAGGACGATG R: GACCACTGGGCTTGAGAGAG	60°C	*Sema3C^{WT}*: ~400 *Sema3C^{fl}*: ~350
Chd7^{Whi}	F: ACTCAGGGAATACCAATTGGAG R: CAAAGAAAAGTTCCCAGCAAAC	58°C	*Chd7^{WT}*: 204 *Chd7^{Whi}*: 233
Cre	F: TGGAAAATGCTTCTGTCCGTTTGC R: AACGAACCTGGTCGAAATCAGTG	60°C	WT: No product Cre: 300
R26RYFP	F: AAGTCGCTCTGAGTTGTTAT WT-R: 3: GGAGCGGGAGAAATGGATATG Mut-R: GCGAAGAGTTTGTCCTCAACC	55°C	WT: 500 R26RYFP: 250

2.2 Phenotyping of morphological defects

2.2.1 Haemotoxylin and Eosin staining

Dissected embryos were fixed overnight in 4% paraformaldehyde (PFA) in PBS and then dehydrated through an EtOH series to 100% EtOH, cleared by washing in histoclear (National Diagnostics), and embedded in paraffin after overnight washes at 60°C. A microtome was used to section embryos to 12-15µm thickness and sections were transferred onto 3-triethoxysilylpropylamine (TESPA)-coated SuperFrost® microscope slides (VWR) for overnight drying. E10.5-E115 embryos were sectioned in a coronal plane, and E13.5-E18.5 embryos in a transverse plane.

For morphological examination, sections were warmed to 60°C and rinsed in histoclear to de-wax, then rehydrated through an EtOH series to H_2O. Slides were stained using freshly-filtered Mayer's Hemotoxylin solution (Sigma-Aldrich) followed by aqueous Eosin solution (Sigma-Aldrich) and rinsed further in H_2O. Slides were mounted with glass coverslips using DPX solution (Merck).

2.2.2 Intracardiac Ink Injection

Following overnight fixation of E10.5 embryos in 4% PFA/PBS at 4°C, outflow tracts were injected with India ink (Pélican) using a pulled glass capillary to fill the 3rd, 4th and 6th pharyngeal arch arteries (PAAs, as previously described (Lindsay et al., 1999)). Aplasia of the 4th PAA was only recorded for embryos in which the 6th PAA was present.

Fixed E15.5 embryos were opened to view the chest cavity and India ink injected into the cardiac ventricles by the same method when insufficient blood remained in the great vessels to view their structure.

2.2.3 Optical Projection Tomography

Embryos were fixed overnight in 4% PFA/PBS, rinsed in PBS then mounted in 1% low-melting agarose (Life Technologies). Samples were then trimmed and washed in 100% methanol (MeOH) followed by the organic clearing agent BABB (2 parts benzyl alcohol to 1 part benzyl benzoate), with several changes of each wash. Optical projection tomography was run on a Bioptonics OPT Scanner 3001M (MRC Technology, Edinburgh, UK), with NRecon software (Skyscan NV) used for image reconstruction from projections using a back-projection algorithm. Images were analysed and digitally re-sectioned using ImageJ.

2.3 Immunostaining

2.3.1 Cryosection preparation

Following dissection, E10.5-13.5 CD1 embryos were fixed in 4% PFA/PBS at 4°C for 30-60 minutes, washed in PBS and then incubated overnight in 30% sucrose/PBS at 4°C. This was followed by incubation in a 50/50 mixture of 30% sucrose/OCT embedding matrix (Fisher) until the embryos sank, and then incubation in 100% OCT. Samples were mounted into moulds on dry ice and stored at -80°C before crysectioning at 10µM thickness onto SuperFrost® Plus glass slides (VWR). Sections were either used immediately for immunohistochemistry (IHC) or stored at -80°C then brought to room temperature on the day of staining.

2.3.2 Immunohistochemistry on cryosections

Sections were rinsed twice in PBS and permeabilised with 0.5% Triton X-100 (Sigma-Aldrich)/PBS for 10 minutes before further rinses in PBS. Sections were incubated in blocking solution (1% bovine serum albumin (BSA, Sigma-Aldrich), 10% goat serum (Sigma-Aldrich), 0.1% Triton X-100, PBS) for 1 hour in a humidified chamber, then incubated overnight at 4°C in anti-CHD7 antibody (NBP1-77393, Novus Biologicals) diluted 1:200 in the blocking solution. Following washes in 0.1% Triton X-100/PBS and then PBS, slides were incubated in AlexaFluor® 594 goat anti-rabbit-IgG (Invitrogen) diluted 1:1000 in blocking solution, before finally washing again and counter-staining with DAPI. Slides were mounted with glass coverslips using VECTASHIELD® mounting medium

2.3.3 Immunostaining on paraffin sections

Tissue sections were prepared in the same way as for Haemotoxylin and Eosin staining (section 2.2.1). Slides were de-waxed by pre-warming at 60°C followed by two 10 minute washes in histoclear, and rehydrated by 5 minute washes through an EtOH series down to 30% EtOH. Antigen retrieval was then carried out by incubation in pre-warmed Target Retrieval Solution (Dako) for 30 minutes at 94-96°C, 20 minutes at room temperature, and then 5 minutes under running water.

For immunofluorescence staining for *RosaYFP* lineage tracing, sections were incubated for 1 hour at room temperature in blocking solution (1% BSA, 2% fetal bovine serum (FBS, Life Technologies), PBS) followed by incubation overnight at 4°C in anti-GFP antibody (ab13970, Abcam) diluted 1:500 in the blocking solution. Slides were then rinsed in PBS and incubated in

AlexaFluor® 488 goat anti-chicken IgG (Invitrogen) diluted 1:500 in blocking solution for 1 hour at room temperature. Finally, slides were rinsed further in PBS, stained with DAPI and then mounted with glass coverslips using VECTASHIELD® mounting medium.

For immunohistochemical staining for Notch1, antigen retrieval was followed by quenching of endogenous peroxidase activity by incubation for 30 minutes in 0.3% H_2O_2. Slides were then washed in PBS for 5 minutes and incubated at room temperature for 30 minutes in the Blocking Serum included in the VECTASTAIN® ABC Kit (Vector Laboratories). Slides were then incubated for 30 minutes in anti-Notch1 rabbit monoclonal antibody (#3608, Cell Signaling Technology) diluted 1:100 in the Blocking Serum. Following a further PBS wash, slides were incubated in VECTASTAIN® biotinylated secondary anti-rabbit IgG antibody solution, followed by incubation with VECTASTAIN® ABC reagent solution, which contains both Avidin DH and biotinylated peroxidase H. Slides were then stained using the *NovaRED*™ Substrate Kit for Peroxidase (Vector Laboratories), rinsed in H_2O and again mounted using VECTASHIELD® mounting medium.

2.3.4 Immunocytochemistry

Cultured embryonic cardiomyocytes grown on laminin-coated coverslips (see section 2.6.1) were gently rinsed in PBS and fixed in 4% PFA/PBS for 10 minutes, followed by further PBS washes. Cells were permeabilised in 0.1% Triton-X100/PBS for 5 minutes, rinsed in PBS and then incubated for 1 hour in primary antibodies diluted in 10% goat serum/PBS (1:50 anti-Nkx2-5 rabbit polyclonal antibody, ab35842 Abcam, and 1:100 anti-cardiac heavy chain Myosin mouse monoclonal antibody, ab15 Abcam). After further PBS washes, cells were incubated for 30 minutes in 10% goat serum/PBS containing 1:1000 AlexaFluor® 594 goat anti-rabbit-IgG and 1:1000 AlexaFluor® 488 goat anti-mouse-IgG (Invitrogen). Cells were finally rinsed again in PBS, stained with DAPI and mounted on SuperFrost® microscope slides using ProLong® Gold antifade reagent (Life Technologies). All incubations were carried out in a humidified chamber at room temperature.

2.3.5 Visualising Parasympathetic Innervation on Wholemount Hearts

E14.5-E15.0 hearts were dissected into PBS before fixation for 20-30 minutes in 4% PFA/PBS at room temperature. Hearts were then permeabilised by incubation in 0.5% Triton-X/PBS for 5 minutes, washed in PBS and stored overnight at 4°C in blocking solution (1% BSA, 10% sheep serum, 0.1% Triton-X, PBS). Hearts of the required genotype were incubated overnight at 4°C with rotation in anti-Neurofilament-66 antibody (04-1032, Millipore) diluted 1:50 in blocking

solution, washed in PBS at room temperature, incubated overnight at 4°C in AlexaFluor® 594 goat anti-rabbit-IgG (Invitrogen) diluted 1:1000 in blocking solution, and finally washed again in PBS.

2.3.6 Visualising Coronary Veins on Wholemount Hearts

E15.5 hearts were dissected into PBS, fixed in 4% PFA/PBS for 40 minutes at room temperature, washed in PBS and then dehydrated through a methanol (MeOH) series and stored at -20°C in 100% MeOH until genotyped. After rehydration to PBS, hearts were permeabilised by washing twice in 0.1% Tween-20/PBS (PBT) before blocking for 2 hours at room temperature in 10% goat serum/PBT and then overnight incubation in anti-Endomucin antibody (sc-65495, Santa Cruz) diluted 1:50 in the blocking solution. Samples were washed in PBT at room temperature and then incubated overnight at 4°C in secondary Alexafluor-594-conjugated anti-rat-IgG antibody (Invitrogen) diluted 1:1000 in blocking solution, before final PBT washes.

2.3.7 Fluorescence microscopy

Immunofluorescently-stained cardiomyocytes or tissue sections were imaged using a Zeiss AxioImager Z1 upright microscope equipped with an AxioCam MRm camera and UV lamp, using either the Ec-Plan-Neofluar 5x/0.16, Achro-Plan 10x/0.25 or Ec-Plan-Neofluar 20x/0.5 objectives as needed. Wholemount hearts stained with anti-Neurofilament-66 or anti-Endomucin antibodies were photographed using a Zeiss SteREO Lumar.V12 microscope with attached AxioCam HRc camera and UV lamp.

All images were processed using ImageJ.

2.4 Measurement of gene expression changes

2.4.1 RNA extraction

For qRT-PCR analysis of *Chd7* expression, total RNA was isolated from E11.5 hearts using the TRIzol reagent (Invitrogen). Briefly, hearts were dissected in RNase-free PBS, 350µl TRIzol reagent was added per dissected heart and samples stored at -80°C. Samples of the required genotypes were thawed and homogenised using a 25G 0.5x25mm needle and syringe before 5 minutes incubation at room temperature. 60µl chloroform was then added and tubes shaken vigorously, followed by a further 5 minutes incubation and centrifugation for 15 minutes. The upper aqueous layer was transferred to a fresh tube, 150µl isopropanol added and samples left for 10 minutes before further centrifugation for 10 minutes. RNA pellets were washed in 70% EtOH, air dried and resuspended in 30µl RNase-free H_2O. All incubations were at room temperature and centrifugations were 10,00rpm at 4°C.

For microarray or TaqMan® Array Micro Fluidic Card experiments, E11.5 or E13.5 hearts were dissected into RNase-free PBS and stored in 300µl Buffer RLT (Qiagen) containing 10µl ml^{-1} β-mercaptoethanol (Sigma-Aldrich) at -80°C until genotyped. Total RNA was isolated using RNeasy Mini kits (Qiagen) according to manufacturer's instructions, including the optional on-column DNase digestion step, and eluted into 30µl RNase-free H_2O.

2.4.2 Reverse transcription

For *Chd7* qRT-PCRs, cDNA was generated from total RNA extracts using Superscript® II Reverse Transcriptase kits from Invitrogen. Immediately before reverse-transcription, samples were DNase-treated utilising the RQ1 RNase-Free DNase kit (Promega). Digestion reactions were set up comprising 1µg RNA, 1µl 10x reaction buffer, 1 unit RQ1 RNase-Free DNase, and ddH_2O to a total volume of 10µl, and incubated at 37°C for 30 minutes. 1µl RQ1 DNase Stop Solution was added to terminate the reaction, and samples incubated at 65°C for 10 minutes to deactivate the DNase enzyme.

DNase-treated RNA was incubated with 300ng Oligo(dT) Random Primer mix (Invitrogen) and ddH_2O to a total volume of 37µl for 5 minutes at 65°C and then 10 minutes at room temperature. 10µl 5x Superscript® buffer, 2µl 10mM dNTPs and 1µl Superscript® II Reverse Transcriptase was then added to each sample, pipetted up and down to gently mix and incubated for 1 hour at 37°C. The enzyme was then deactivated for 5 minutes at 95°C, and samples cooled on ice before storage at -20°C.

The High-Capacity Reverse Transcription Kit with RNase Inhibitor (Applied Biosystems) was used to make cDNA for loading on TaqMan® Array Micro Fluidic Cards, according to manufacturer's instructions.

2.4.3 Real-time PCR for Chd7 expression

TaqMan® gene expression assay probes Mm01219527_m1 and Mm99999915_g1 were used for quantitative real-time-PCR (qRT-PCR) analysis of mouse *Chd7* and *Gapdh* expression levels, respectively. Reactions were carried out in 96-well plates, with each well containing 1µl cDNA, 12.5µl Taqman® Universal PCR Master Mix (Life Technologies), 1µl TaqMan® assay, and 10.5µl ddH_2O. Plates were set up with 3 replicates of each sample, and 2 samples per genotype tested. qRT–PCR analysis was performed on a CFX96 Touch™ Real-Time PCR Detection System (Bio-Rad). Data were normalised to *Gapdh* expression and fold-changes in gene expression determined by the $2^{-\Delta\Delta CT}$ method (Livak and Schmittgen, 2001).

2.4.4 Real-time PCR using TaqMan® Array Micro Fluidic Cards

600ng cDNA per lane was loaded on custom-designed TaqMan® Array Micro Fluidic Cards, according to manufacturer's instructions. Cards were run on an Applied Biosystems 7900HT Fast Real-Time PCR System using a TaqMan® Array Micro Fluidic Card Thermal Cycling Block with SDS Software v2.1. The comparative $2^{-\Delta\Delta CT}$ method was again used for determination of gene expression changes, normalised to *Gapdh* expression, and p-values calculated using two-tailed Student's t-Test.

2.4.5 Affymetrix mouse gene microarrays

For each time point, cDNA from four individual *Chd7$^{fl/fl}$;Mesp1-Cre* hearts was compared to cDNA from four *Chd7$^{+/+}$;Mesp1-Cre* hearts. Sense-strand cDNA was generated from total RNA using the Ambion® WT Expression Kit (Affymetrix), which was then processed for hybridisation onto the Affymetrix Mouse Gene 1.0 ST Array according to manufacturer's protocols. Scanning was performed on an Affymetrix GeneChip Scanner. The array QC was performed using Expression Console first and then Bioconductor. This work was performed by the UCL Genomics facility. The data was normalised with the RMA normalisation algorithm using the Affy R package (Gautier et al., 2004) provided as part of the Bioconductor libraries (Gentleman et al., 2004) and analysed for differential expression using LIMMA (Smyth, 2004). Clustering was performed using the Heatmap.2 package, with gene ontology (GO) annotation on

representative clusters computed using DAVID (Huang da et al., 2009). Data has been submitted to the Gene Accession Omnibus (accession number GSE59963).

2.5 RNA *in situ* hybridisation

2.5.1 RNA plasmid sources

Plasmids for synthesizing antisense RNA probes were kindly donated from the following sources: *Sox10*, *Sema3A* and *Sema3C* from Christiana Ruhrberg; *Robo1* and *Robo2* from Gail Martin; *Slit2* from Bill Andrews (original clone from David Ornitz's lab); *PlexinA2* from Addgene (plasmid 16423), deposited by Jonathan A. Raper ((Brown et al., 2001)); *Wnt2* from Kathleen M. Stewart; and *Tgfbr2* from Elazar Zelzer. The *Chd7* probe was generated using TOPO® TA Cloning® Kits (Life Technologies) with previously reported primers (F: 5'-CTATGCACCCTTCACAGCCTCAGGG-3'; R: 5'-GGGACACATCCAGTGAGTTCCTGCG-3') (Bosman et al., 2005).

Table 2-2: Restriction enzyme and RNA Polymerase combinations used for generation of anti-sense and sense RNA probes

Probe:	Anti-sense RNA probe:	Sense RNA probe:	Length:
Chd7	SpeI, T7	NotI, T3	764bp
PlexinA2	BamHI, T3	XhoI, T7	2200bp
Robo1	EcoRI, T7	XhoI, T3	1000bp
Robo2	NotI, T7	XhoI, T3	1700bp
Slit2	NcoI, SP6	SpeI, T7	1300bp
Sema3A	BamHI, T7	EcoRI, T3	1200bp
Sema3C	NotI, T3	XhoI, T7	2500bp
Sox10	NcoI, T7	Unknown	Unknown
Tgfbr2	BamHI, T7	SmaI, SP6	350bp
Wnt2	BamHI, T7	NotI, M13	500bp

2.5.2 RNA Probe Preparation

Plasmids were linearised overnight using the appropriate restriction enzymes for generating antisense probes (see Table 2-2), and extracted from a 1% agarose gel using the QIAquick Gel Extraction Kit (Qiagen). *In vitro* transcription of probes was carried out by incubating 1µg of linearised plasmid for 2 hours with 1x DIG RNA Labelling Mix (Roche), 1x Transcription Optimised Buffer (Promega), 24u RNasin® Plus RNase Inhibitor(Promega), 10mM DTT (Promega) and 20-40u RNA polymerase (T3, T7 or SP6). Incubations were at 37°C for T3 or T7 RNA Polymerases and 40°C for SP6 RNA Polymerase. Probes were precipitated by addition of 2µl 0.5M EDTA (pH 8), 5µl 4M LiCl and 150µl EtOH to the reaction, incubation on ice for 1 hour, and extraction by centrifugation. Probes were resuspended in diethyl pyrocarbonate (DEPC)-treated water.

2.5.3 In Situ Hybridisation on Paraffin Sections

Paraffin sections were prepared as previously described (section 2.2.1). Slides were rehydrated then incubated in 20µg ml^{-1} Proteinase K (Sigma-Aldrich) for 8 min, washed in 2mg ml^{-1} glycine then PBS, and fixed in 4% PFA/PBS for 20 minutes. Following further PBS washes they were incubated for 1 hour at 70°C in a humidified chamber in hybridisation buffer (50% formamide (Promega), 5xSSC pH 4.5, 50µg ml^{-1} yeast RNA (Sigma-Aldrich), 50µg ml^{-1} heparin (Sigma-Aldrich), 1% SDS) followed by overnight incubation in hybridisation buffer containing 1µg ml^{-1} antisense RNA probe. Slides were then rinsed twice in 2x SSC buffer pH4.5, followed by three washes in Solution I (50% formamide, 5x SSC pH4.5, 1% SDS) at 65°C, two washes in Solution II (50% formamide, 2x SSC pH4.5) and finally two washes at room temperature in MABT (0.1M maleic acid, 0.15M NaCl, 0.01% Tween-20, 2mM Levamisole hydrochloride (Sigma-Aldrich), pH7.5).

Slides were then incubated in blocking buffer (2% Boehringer Blocking Reagent (Roche), 10% sheep serum, MABT) for 1 hour followed by overnight incubation at 4°C with an alkaline-phosphatase (AP) conjugated anti-DIG antibody (Roche) diluted 1:2000 in blocking buffer. Following further washes in MABT and then AP buffer (100mM Tris, pH 9.5, 50mM $MgCl_2$, 100mM NaCl, 0.1% Tween-20, 2mM Levamisol in DEPC-treated water), AP activity was detected using BM Purple (Roche). Once stain had developed sufficiently, slides were rinsed in PBST and H_2O, dried and mounted using DPX solution. Sections were pictured using an Axiophoto2 microscope.

2.5.4 Wholemount in situ hybridisation

Embryos were dissected in PBS and fixed overnight in 4% PFA/PBS, before dehydration through a MeOH series to 100% MeOH and storage at -20°C until ready to use. For mutant vs control wholemount *in situ* hybridisation, embryos were processed in the same well, with removal of tails used for identification, and all washes/incubations were carried out with rotation.

Embryos were rehydrated through a successive series of MeOH/PBT solutions and then bleached for 1 hour in 6% H_2O_2 solution (Sigma-Aldrich) at room temperature. After several PBT washes, E9.5 embryos were incubated for 7 minutes and E10.5 embryos for 9 minutes in 10mg ml^{-1} Proteinase K, followed by further PBT washes and then fixation for 20 minutes in fixing solution (4% PFA, 0.2% glutaraldehyde (Sigma-Aldrich), PBS). Pre-hybridisation was carried out at 70°C in pre-warmed hybridisation solution (50% formamide, 5xSSC pH 4.5, 50µg ml^{-1} yeast RNA, 50µg ml^{-1} heparin, 0.1% SDS) followed by overnight hybridisation at 70°C with 100ng ml^{-1} anti-sense RNA probe.

Following a 5-minute rinse in the hybridisation buffer, embryos were washed three times at 70°C in Solution I (50% formamide, 5x SSC pH4.5, 1% SDS) and then three times at 65°C in Solution II (50% formamide, 2x SSC pH4.5, 0.2% SDS, 0.1% Tween-20). Embryos were cooled, washed three times in MABT and incubated for 2-3 hours in blocking buffer (2% Boehringer Blocking Reagent, 10% sheep serum, MABT). During this time, the anti-DIG antibody (Roche) was pre-absorbed with embryo powder (see next section) in antibody solution (2% BBR, 1% sheep serum, MABT) at 4°C with rotation for 1.5 hours, before centrifugation to remove the embryo powder. Embryos were incubated in the antibody solution containing 1:2000 pre-absorbed anti-DIG antibody overnight at 4°C, 6-8 MABT washes throughout the following 24 hours, and then three 10-minute washes in AP buffer (100mM Tris, pH 9.5, 50mM $MgCl_2$, 100mM NaCl, 0.1% Tween-20, 2mM Levamisol in DEPC-treated water). AP activity was again detected using BM Purple, and the staining reaction stopped by incubation in 2mM EDTA/PBT, followed by final PBT washes.

2.5.5 Preparation of embryo powder

E13.5 embryos were dissected in ice-cold PBS and the heads discarded. They were homogenised thoroughly with 3ml PBS in a glass homogeniser. 12ml ice cold acetone was then added and mixed in well, followed by incubation on ice for 30 minutes, with frequent mixing. The mixture was then centrifuged at 10,000rpm at 4°C for 10 minutes and the supernatant

discarded. The pellet was resuspended in ice-cold acetone, mixed and incubated on ice for 10 minutes, followed by another 10-minute centrifugation. The pellet was then transferred to clean filter paper (Whatman), spread thinly and air-dried overnight in a fume hood. Once dried, the pellet was spread and dispersed with a spatula multiple times to form a fine powder, which was stored at 4°C until needed.

2.6 Investigating calcium handling function

2.6.1 Culture of Embryonic Cardiomyocytes

Individual E13.5 embryonic hearts were dissected in PBS on ice, then incubated at 37°C for 45 minutes in 200µl 0.05% Trypsin-EDTA (Life Technologies) containing 10µg ml^{-1} DNase I (Sigma), with pipetting every 5-10 minutes. 500µl DMEM (Life Technologies) containing 10% FBS was then added to block the Trypsin activity, and samples fed through a 23G needle three times to further aid dissociation. Cells were spun at 1500 rpm for 5 minutes and resuspended in 1ml culture medium (10% FCS, 1x PenStrep, 1x Non-essential amino acids (Gibco) in DMEM) before plating in a 24-well dish for 1.5 hours to allow adherence of fibroblasts. The supernatant enriched for cardiomyocytes was then plated onto laminin-coated (Sigma) coverslip dishes (PAA200350X), and cells cultured at 37°C, 5% CO_2 for 36 hours, with culture medium replaced when needed.

2.6.2 Measurement of Ca^{2+} Transients

Cells were first washed in imaging buffer (156mM NaCl, 3mM KCl, 2mM $MgSO_4.7H_20$, 1.25mM K_2HPO_4, 2mM $CaCl_2$, 10mM HEPES, 10mM D-Glucose, pH7.4). They were then incubated at 37°C for 10 minutes in 500µl of imaging buffer / Opti-MEM® (50/50, Life Technologies) containing 5µM Cal-520™ (Stratech). Rapid line scan analysis (400Hz) of Ca^{2+} transients in individual cells was carried out on a Leica SP5 confocal inverted microscope using the 488nm line of an argon laser set at 0.1% power, and by collecting emitted light between 500-600nm.

Cells producing Ca^{2+} transients were chosen randomly and were electrically paced by field stimulation at 1Hz using platinum electrodes. Data was collected and analysed by averaging values across the line, over time, using Leica LAS AF software. “Paced” cells were classified as those in which Ca^{2+} transients were observed every 1Hz over a 40 s interval, whereas in “non-paced”, Ca^{2+} transients were absent or unsynchronised. P-values were calculated using the two-tailed Fisher’s exact test.

CHAPTER THREE

CHD7 IS EXPRESSED IN THE DEVELOPING HEART AND IS REQUIRED IN THE CARDIAC MESODERM

To begin to address the role of CHD7 during cardiovascular development, it was important to establish its spatial and temporal expression patterns. *CHD7/Chd7* is ubiquitously expressed early in development in both humans and mice, with expression later becoming restricted to CHARGE-related tissues such as the ear, eye, and olfactory system (Randall et al., 2009; Sanlaville et al., 2006). However, its expression specifically in the heart during development has not been fully characterised. Immunohistochemistry (IHC) and western blotting on wild-type CD1 hearts are presented here, which determine for the first time the developmental window in which CHD7 protein is present in cardiac tissues.

The importance of CHD7 activity in neural crest cell (NCC) development has previously been emphasised, such that CHARGE syndrome is often classified as a disease arising from maldevelopment of the neural crest, known as a neurocristopathy (Etchevers et al., 2006). CHARGE patients, however, present with a wide range of congenital heart defects, with an overrepresentation of atrioventricular septal defects (AVSDs) and OFT defects (Corsten-Janssen et al., 2013a). We therefore postulated that CHD7 function is required in the cardiogenic mesoderm and its derivatives for the regulation of transcriptional programmes during heart development. To investigate this, tissue-specific ablation of *Chd7* was performed, driven by a *Mesp1-Cre* allele, and the resulting cardiac defects are presented in this chapter.

3.1 CHD7 expression in the developing heart until E13.5

3.1.1 Immunohistochemical detection of CHD7 protein expression in the heart

Randall and colleagues reported ubiquitous *Chd7* expression in the embryonic region at E7.5 using LacZ reporter staining, and continued widespread expression throughout the embryo at E8.5 and E9.5, although with weaker expression seen in the early heart tube. At E10.5 expression was seen in the OFT and presumptive ventricles of the heart, as well as the pharyngeal arches, otic vesicle and developing forelimbs (Randall et al., 2009). To investigate further the developmental window in which CHD7 protein is present in the heart, IHC using an antibody raised against CHD7 was carried out on cryosections through the hearts of wild-type CD1 embryos at E10.5, E11.5 and E13.5.

At E10.5 nuclear CHD7 protein was detected throughout the pharyngeal region, with high magnification imaging showing it is present in the outer ectodermal, inner endodermal and mesodermal tissue layers in each of the 3rd, 4th and 6th pharyngeal arches (Figure 3-1, panel A). It was also seen throughout the heart, with higher magnification confirming it is present in both endocardial and myocardial cells (Figure 3-1, panel B). Similar nuclear expression was seen at E11.5, with CHD7 present throughout the endocardial cushions and walls of the OFT and again in the endocardium and myocardium (Figure 3-1, panels C and D). However, at E13.5 no CHD7 protein was detectable in the aorta, pulmonary trunk, atria or ventricles (Figure 3-1, panels E and F).

3.1.2 Western blot analysis of CHD7 protein in the developing heart

To confirm the timing of CHD7 expression seen by IHC, western blot analysis was carried out on total protein extracts from dissected CD1 hearts between stages E10.5 and E15.5 (Figure 3-2). CHD7 is reported as having a molecular weight of 336kDa. A clear band on the blots above 300kDa in size can be seen, with little additional background staining and no equivalent band in the HEK293T cell line negative control sample, so we can be confident this is CHD7 protein. Consistent with the IHC data, a steady decrease in the amount of CHD7 protein can be seen as development progresses, with a band barely detectable by E13.5 and E15.5. Together, these experiments indicate that CHD7 protein is present in the developing heart until E13.5.

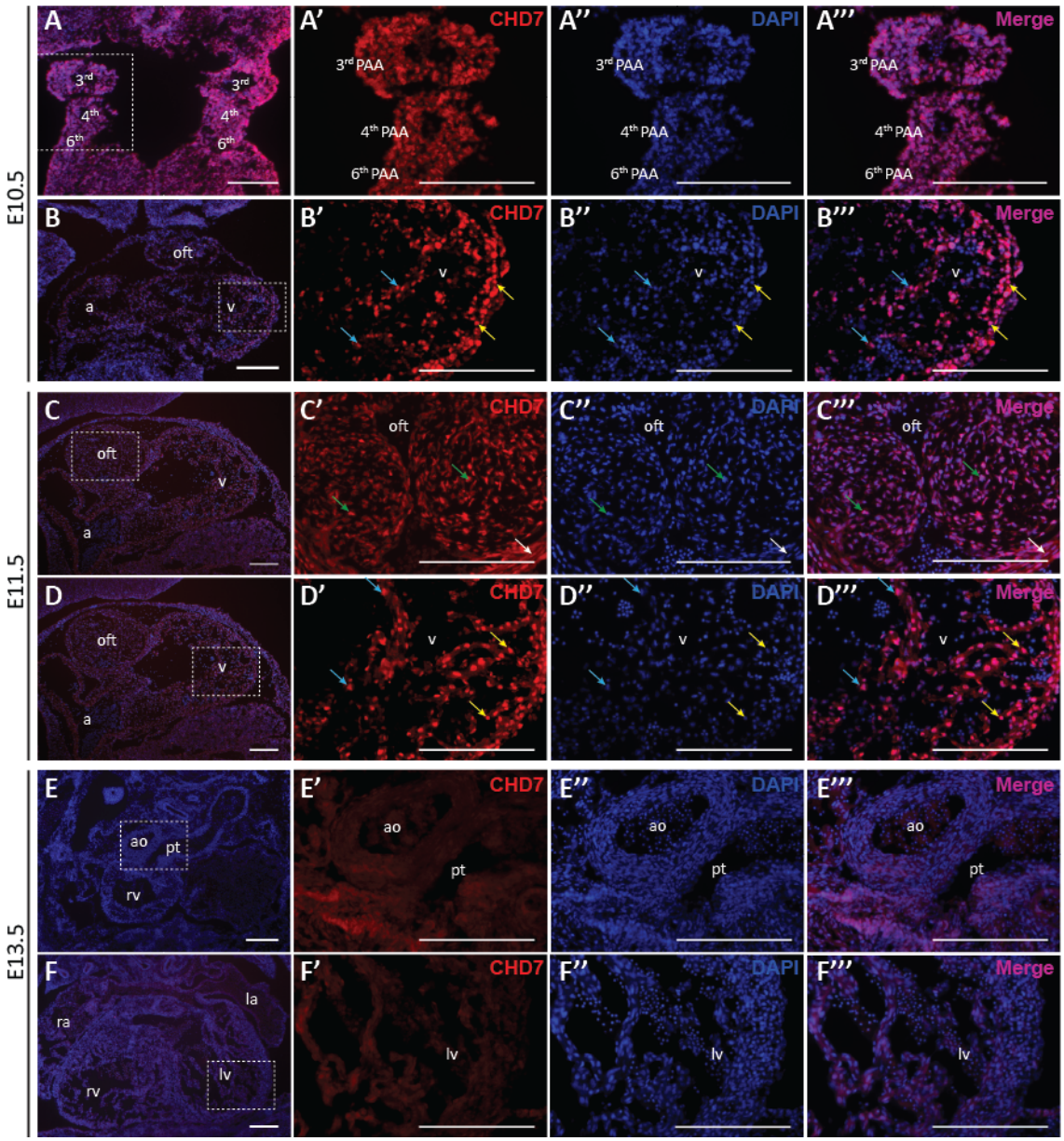

Figure 3-1: CHD7 protein levels during heart development

Immunohistochemistry on cryosections through wild-type CD1 hearts between developmental stages E10.5 to E13.3.

(A, B) Ubiquitous CHD7 expression was seen at E10.5 in the pharyngeal region (A) and throughout the heart (B), including the endocardial (blue arrows) and myocardial layers (yellow arrows). Higher magnification imaging showed overlap with DAPI staining, confirming its nuclear localisation.

(C, D) Similar widespread CHD7 expression was seen in the endocardial cushions (green arrows) and endothelial lining (white arrows) of the proximal outflow tract (C) and again in the myocardium and endocardium of the ventricles (D).

(E, F) At E13.5 CHD7 protein could no longer be detected anywhere in the heart.

All scale bars represent 0.2mm. PAA indicates pharyngeal arch arteries; oft, outflow tract; a, atrium; rv, right ventricle; lv, left ventricle; ao, aorta; pt, pulmonary trunk.

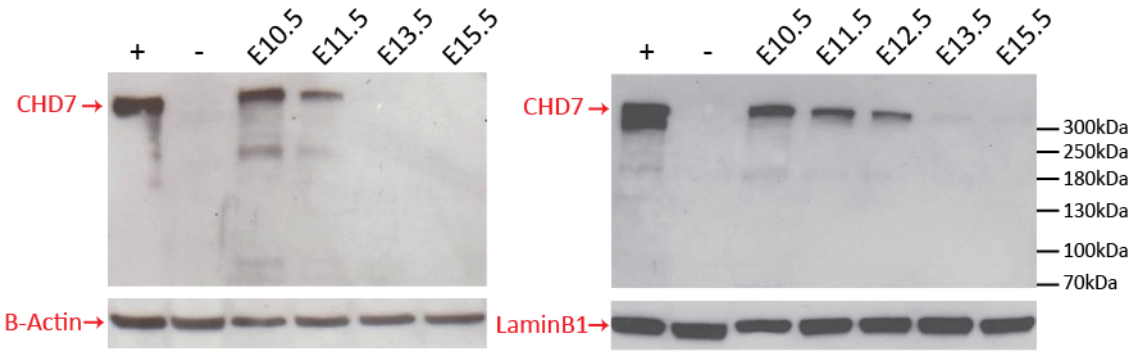

Figure 3-2: Western blot analysis of whole heart protein extracts

Two replicates of western blots on heart total protein extracts are shown, analysing CHD7 protein levels between E10.5 to E15.5. CHD7 protein levels are undetectable by E13.5. Positive controls (+) were protein extracts from mouse embryonic stem cells, and negative controls (-) were from the human embryonic kidney 293T (HEK293T) cell line. B-Actin or nuclear LaminB1 were used as protein loading controls.

These blots were produced by Nelo Popal, and included with her permission.

3.2 Tissue-specific ablation of *Chd7* in the cardiogenic mesoderm

3.2.1 Specificity of the Mesp1-Cre allele

Mesp1 is expressed transiently from E6.5, at the onset of gastrulation, in a heterogeneous population of cells that ingress into and exit the primitive streak. These *Mesp1*-expressing cells give rise to the cranial and cardiac mesoderm, including both the FHF and SHF of cardiac progenitors (Saga et al., 1996). Genetic lineage tracing has been carried out using a knock-in allele with Cre recombinase under the control of *Mesp1* regulatory sequences (*Mesp1-Cre*) crossed with a *LacZ* reporter, so that all *Mesp1*-expressing cells and their progeny can be identified by β-galactosidase staining. These studies have shown β-galactosidase positive cells in all cardiac lineages, including the myocardium, endothelium, endocardium, epicardium and conduction cells (Saga et al., 1999). *Mesp1*-derived cells also contribute to muscles and bones of the face, the embryonic liver and to some fetal haematopoietic stem cells (Asahina et al., 2009; McBratney-Owen et al., 2008; Yoshida et al., 2008).

The expression of *Mesp1* in the earliest cardiac progenitors made *Mesp1-Cre* an ideal *Cre* allele for studying the tissue-specific role of *Chd7* in the developing heart. Previous work in the lab confirmed mesodermal-specific *LacZ* expression driven by *Mesp1-Cre* at E10.5, with coronal sections clearly showing β-galactosidase staining specifically in the mesoderm of the 3rd and 4th pharyngeal arches and throughout the OFT and ventricles of the heart (Figure 3-3).

To confirm its specificity at E13.5, *Mesp1-Cre* was crossed with a *R26RYFP* reporter allele. Consistent with previous data, examination of YFP expression at E13.5 showed *Mesp1-Cre* is active throughout the heart, as well as cells in the cranial and trunk mesoderm (Figure 3-4). Immunostaining for YFP on sections through the heart at E13.5 showed the endothelial lining of the aortic arch, aorta and pulmonary trunk, and most endocardial and myocardial cells were YFP-positive (Figure 3-4, panels A-D). Some cells are seen around the OFT and top of the interventricular septum that do not express YFP, which are most likely cells derived from the neural crest. Furthermore, YFP expression driven by *Mesp1-Cre* was also examined on a conditional floxed *Chd7* background (*Chd7*$^{fl/fl}$), to ensure the conditional allele did not interfere in any way with the *Cre* expression. Comparing *Chd7*$^{+/+}$*;R26RYFP;Mesp1-Cre* and *Chd7*$^{fl/fl}$*;R26RYFP;Mesp1-Cre* embryos at E10.5 and E13.5 showed no difference in YFP expression (Figure 3-4, panels E-H).

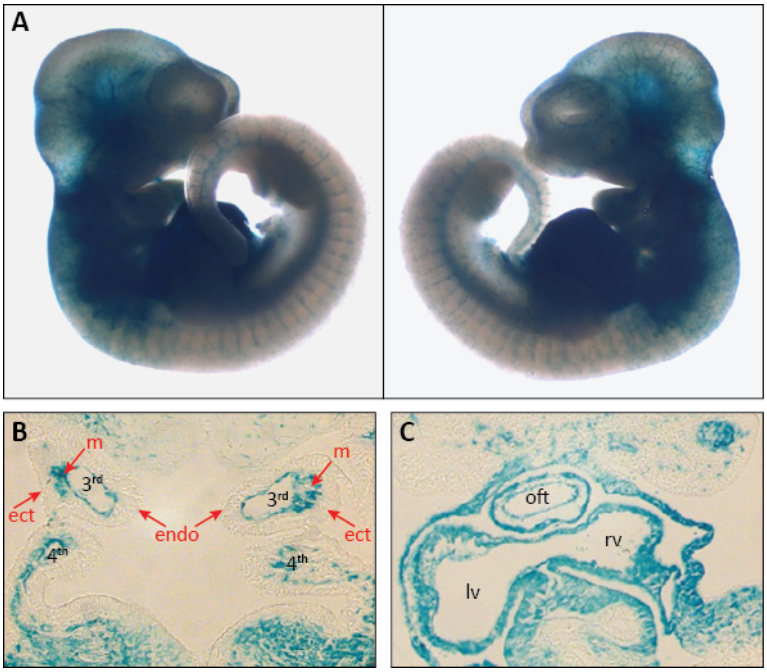

Figure 3-3: LacZ lineage trace of Mesp1-Cre activity at E10.5

(A) Wholemount images of an E10.5 *R26RLacZ;Mesp1-Cre* embryo after β-galactosidase staining, showing Cre activity in the cardiac, trunk and cranial mesoderm.

(B) Coronal sections through the 3rd and 4th pharyngeal arches showed β-galactosidase staining specifically in the mesoderm of the arches.

(C) Section through the heart confirmed Mesp1-Cre activity throughout the left and right ventricles and the outflow tract.

m indicates mesoderm; ect, ectoderm; endo, endoderm; oft, outflow tract; lv, left ventricle; rv, right ventricle. Printed with permission of Karen McCue.

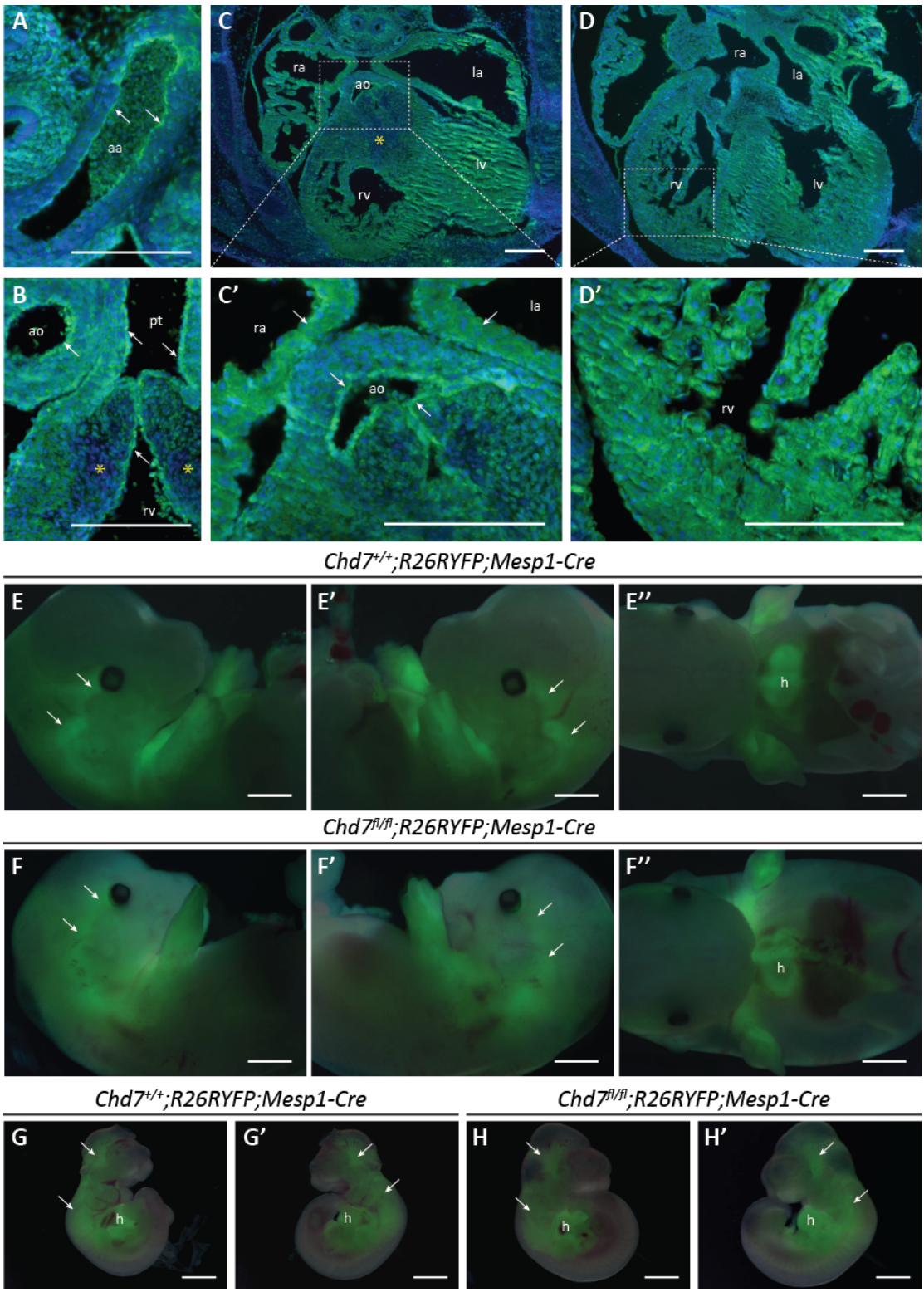

Figure 3-4: YFP lineage trace of *Mesp1-Cre* activity

(A-D) Immunohistochemistry for YFP on transverse paraffin sections through the heart of an E13.5 *Chd7$^{fl/fl}$;R26RYFP;Mesp1-Cre* embryo marked Cre activity (white arrows) in endothelial cells of the aortic arch (A), aorta and pulmonary trunk (B, C) and throughout the atria and ventricles (D). Yellow stars in B and C highlight non-YFP expressing cells, presumably of neural crest origin.

(E-H) Wholemount images showed similar YFP expression in the heart, trunk and cardiac mesoderm on a wild-type or conditional *Chd7$^{fl/fl}$* background at both E13.5 (E, F) and E10.5 (G, H).

Scale bars represent 0.2mm (A-D) or 2mm (E-H). aa indicates aortic arch; ao, aorta; pt, pulmonary trunk; ra, right atrium; la, left atrium; rv, right ventricle; lv, left ventricle; h, heart.

3.2.2 *Validation of Chd7 ablation in the heart*

The conditional floxed *Chd7*^{fl} allele described in section 1.6.3 was used in this project for tissue-specific ablation of *Chd7* expression. *Chd7*$^{fl/fl}$ mice were crossed with *Chd7*$^{fl/+}$*;Mesp1-Cre* mice in order to delete homozygously *Chd7* expression in the cardiac and anterior mesoderm. *In situ* hybridisation (ISH) confirmed loss of *Chd7* mRNA throughout the heart at E11.5 in *Chd7*$^{fl/fl}$*;Mesp1-Cre* embryos, whilst in other regions such as the neural tube the level of *Chd7* expression remained unaffected (Figure 3-5, A and B).

Quantitative real-time PCR (qRT-PCR) using TaqMan® probes was also used to examine *Chd7* mRNA levels in dissected E11.5 hearts after conditional *Chd7* ablation. This analysis showed in heterozygous *Chd7*$^{fl/+}$*;Mesp1-Cre* hearts *Chd7* expression was reduced to ~75% of wild-type levels, whilst in *Chd7*$^{fl/fl}$*;Mesp1-Cre* hearts it was reduced to ~45% (Figure 3-5, C). A number of reasons could underlie the fact that complete ablation of *Chd7* expression is not seen in *Chd7*$^{fl/fl}$*;Mesp1-Cre* hearts. In the E11.5 embryonic hearts, there are likely to be some non-*Mesp1*-derived cells, predominantly from the neural crest lineage, in which *Chd7* expression would be normal. The efficacy of recombination by the Cre-LoxP system using this combination of floxed allele and tissue-specific Cre line may also be limiting the level of *Chd7* deletion.

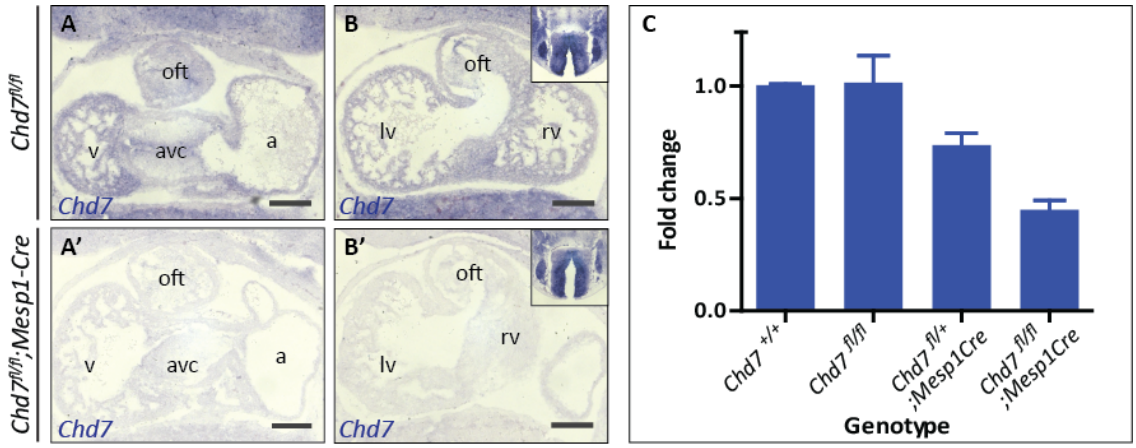

Figure 3-5: *Chd7* ablation in E11.5 *Chd7*$^{fl/fl}$*;Mesp1-Cre* embryos

(A, B) *Chd7 in situ* hybridisation on E11.5 *Chd7*$^{fl/fl}$ coronal sections showed *Chd7* expression throughout the heart, which was lost in the *Chd7*$^{fl/fl}$*;Mesp1-Cre* hearts. Inserts show sections through the neural tube, showing *Chd7* ablation was tissue-specific.

(C) Taqman RT-PCR for *Chd7* on cDNA from dissected E11.5 hearts, showing *Chd7* expression was unaffected in *Chd7*$^{fl/fl}$ hearts, but reduced after heterozygous and homozygous ablation driven by *Mesp1-Cre*.

Scale bars represent 0.2mm. oft indicates outflow tract; avc, atrioventricular canal; (l/r)v, (left/right) ventricle.

3.3 The cardiovascular phenotype of *Chd7$^{fl/fl}$;Mesp1-Cre* embryos

3.3.1 The Chd7$^{fl/fl}$;Mesp1-Cre genotype is embryonic lethal

To examine the survival of *Chd7$^{fl/fl}$;Mesp1-Cre* mice, timed matings were set up to cross *Chd7$^{fl/fl}$* with *Chd7$^{fl/+}$;Mesp1-Cre* mice. The probability of each of the four possible genotypes from this breeding pair – *Chd7$^{fl/+}$*, *Chd7$^{fl/fl}$*, *Chd7$^{fl/+}$;Mesp1-Cre* and *Chd7$^{fl/fl}$;Mesp1-Cre* - was 25%, based on Mendelian inheritance (Table 3-1).

The observed and expected numbers of each genotype were compared at different developmental stages. Table 3-2 shows that at E10.5 and E13.5, there was no significant difference between the observed and expected numbers of *Chd7$^{fl/fl}$;Mesp1-Cre* embryos, and no necrotic embryos were collected at these stages. However, at E15.5 noticeably fewer than expected *Chd7$^{fl/fl}$;Mesp1-Cre* embryos were seen, and a significant number of necrotic embryos of this genotype were also collected. By the end of gestation, at E18.5, there was a significant loss of *Chd7$^{fl/fl}$;Mesp1-Cre* embryos, with only 2 *Chd7$^{fl/fl}$;Mesp1-Cre* embryos found in a total of 41 embryos collected. Pups were ear-clipped for genotyping at postnatal day (P)10, and no *Chd7$^{fl/fl}$;Mesp1-Cre* pups survived to this stage. Therefore, homozygous ablation of *Chd7* in the cardiac mesoderm is embryonic lethal, with embryos mostly dying around E15.5, although a small number survive to the end of gestation but are not viable postnatally.

Table 3-1: Punnett Square to show the possible outcomes of the *Chd7$^{fl/fl}$* x *Chd7$^{fl/+}$;Mesp1-Cre* cross

		Chd7$^{fl/WT}$;Cre$^{+/-}$			
		Chd7^{fl};Cre^{+}	***Chd7^{fl};Cre^{-}***	***Chd7^{WT};Cre^{+}***	***Chd7^{WT};Cre^{-}***
Chd7$^{fl/fl}$	***Chd7^{fl}***	*Chd7$^{fl/fl}$;Cre^{+}*	*Chd7$^{fl/fl}$;Cre^{-}*	*Chd7$^{fl/WT}$;Cre^{+}*	*Chd7$^{fl/WT}$;Cre^{-}*
	Chd7^{fl}	*Chd7$^{fl/fl}$;Cre^{+}*	*Chd7$^{fl/fl}$;Cre^{-}*	*Chd7$^{fl/WT}$;Cre^{+}*	*Chd7$^{fl/WT}$;Cre^{-}*

Table 3-2: Embryonic lethality of the *Chd7$^{fl/fl}$;Mesp1-Cre* genotype

Developmental Stage:	Genotype:	Observed:	Expected:	Necrotic:
E10.5	*Chd7$^{fl/+}$*	22	18	0
	Chd7$^{fl/fl}$	19	18	0
	Chd7$^{fl/+}$;Mesp1-Cre	15	18	0
	Chd7$^{fl/fl}$;Mesp1-Cre	**15**	**18**	**0**
E13.5	*Chd7$^{fl/+}$*	17	14	0
	Chd7$^{fl/fl}$	18	14	0
	Chd7$^{fl/+}$;Mesp1-Cre	8	14	0
	Chd7$^{fl/fl}$;Mesp1-Cre	**13**	**14**	**0**
E15.5	*Chd7$^{fl/+}$*	36	36	0
	Chd7$^{fl/fl}$	43	36	1
	Chd7$^{fl/+}$;Mesp1-Cre	36	36	1
	Chd7$^{fl/fl}$;Mesp1-Cre	**27**	**36**	**7****
E18.5	*Chd7$^{fl/+}$*	13	10	0
	Chd7$^{fl/fl}$	13	10	0
	Chd7$^{fl/+}$;Mesp1-Cre	13	10	0
	Chd7$^{fl/fl}$;Mesp1-Cre	**2***	**10**	**1**
P10	*Chd7$^{fl/+}$*	12	9	-
	Chd7$^{fl/fl}$	8	9	-
	Chd7$^{fl/+}$;Mesp1-Cre	15	9	-
	Chd7$^{fl/fl}$;Mesp1-Cre	**0****	**9**	**-**

Expected numbers are based on Mendelian ratios, rounded to the nearest whole number.

** p <0.05, ** p<0.01, based on Chi squared analysis.*

3.3.2 Chd7$^{fl/fl}$;Mesp-1Cre embryos exhibit oedema and haemorrhaging

Chd7$^{fl/fl}$;Mesp1-Cre embryos collected at E10.5 did not show any obvious external phenotype when compared to littermates. However, at E13.5 around two-thirds of *Chd7$^{fl/fl}$;Mesp1-Cre* embryos (n=15) had oedema, which was often severe, and approximately one-third also had some signs of haemorrhaging (Figure 3-6, Table 3-3). By E15.5, oedema and/or haemorrhaging was seen in over 90% (n=22) of *Chd7$^{fl/fl}$;Mesp1-Cre* embryos, and the haemorrhaging was usually more widespread than at E13.5 (Figure 3-7, A-C). Necrotic embryos collected at this stage also showed signs of previous haemorrhaging (Figure 3-7, D). These results suggest the haemorrhagic phenotype occurs slightly later than oedema during development, and may be contributing to the embryonic lethality. Consistent with this, the two *Chd7$^{fl/fl}$;Mesp1-Cre* embryos that were collected at E18.5 did not show any evidence of oedema or haemorrhaging. However, these two embryos still exhibited severe cardiovascular defects so would have been highly unlikely to survive postnatally. The lack of developmental delay in the *Chd7$^{fl/fl}$;Mesp1-Cre* embryos indicates bypass of the p53-dependent pathway actively regulated by CHD7 during early embryogenesis (Van Nostrand et al., 2014), allowing examination of the role of *Chd7* later in cardiogenesis than can be achieved in constitutively-null embryos.

Table 3-3: External phenotypes observed at E13.5 and E15.5

Genotype:	E13.5			E15.5		
	n:	Oedema:	Haemorrhage:	n:	Oedema:	Haemorrhage:
Chd7$^{fl/+}$	19	0%	11%	23	4%	4%
Chd7$^{fl/fl}$	20	0%	10%	33	12%	6%
Chd7$^{fl/+}$;Mesp1-Cre	9	11%	0%	22	9%	0%
Chd7$^{fl/fl}$;Mesp1-Cre	**15**	**67%**	**33%**	**22**	**68%**	**64%**

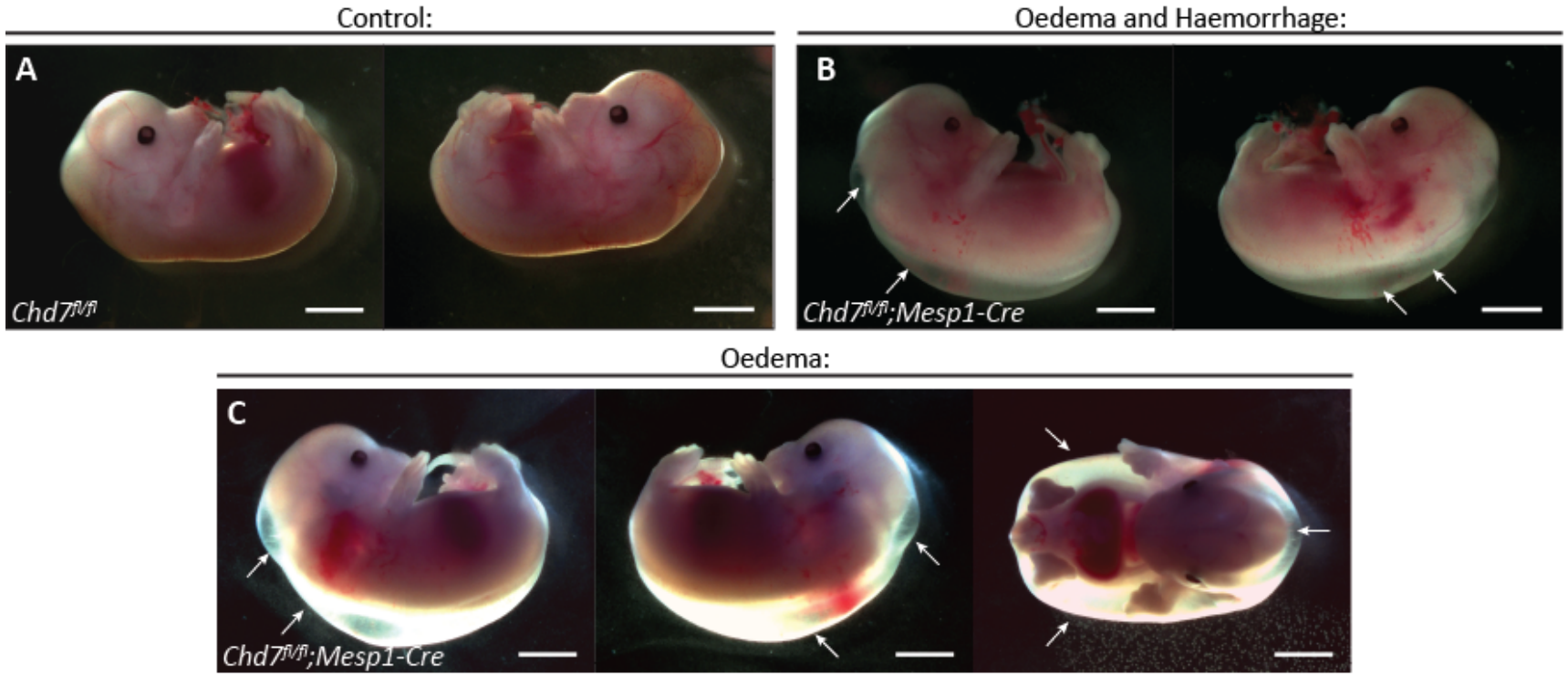

Figure 3-6: External phenotypes seen with E13.5 *Chd7$^{fl/fl}$;Mesp1-Cre* embryos

(A-C) Embryos collected at E13.5, *Chd7$^{fl/fl}$;Mesp1-Cre* embryos predominantly exhibited oedema, often severe, as can be seen in B and C (white arrows). Some haemorrhagic patches were also seen (C).

Scale bars represent 2mm.

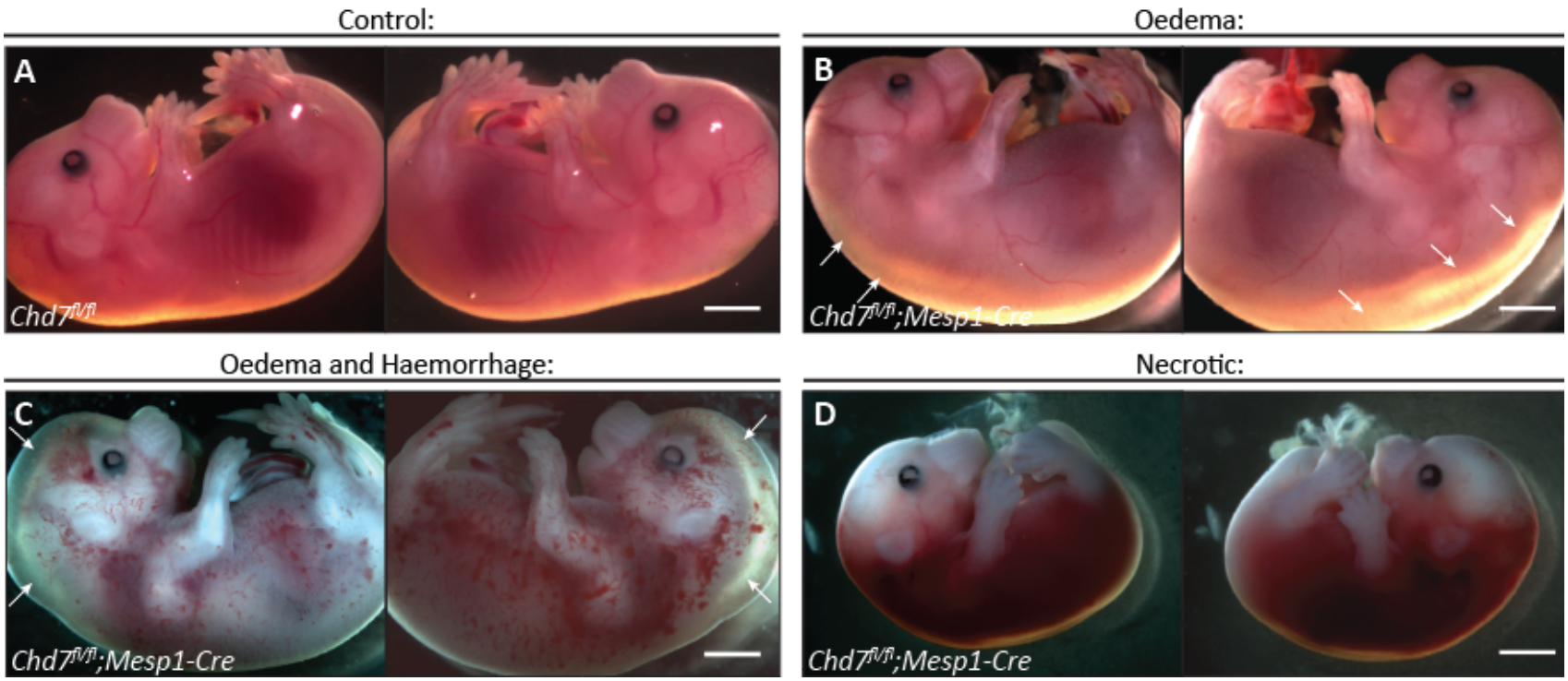

Figure 3-7: Oedema, haemorrhaging and necrotic *Chd7$^{fl/fl}$;Mesp1-Cre* embryos at E15.5

(A) At E15.5 control *Chd7$^{fl/fl}$* embryos again appeared normal, whilst *Chd7$^{fl/fl}$;Mesp1-Cre* embryos showed oedema (white arrows, B and C) and often severe haemorrhaging (C). Necrotic embryos collected at the stage also usually showed previous signs of haemorrhaging (D).

Scale bars represent 2mm.

3.3.3 Chd7$^{fl/fl}$;Mesp1-Cre embryos have great vessel remodelling defects

Great vessel defects have been reported with partial penetrance in heterozygous gene-trapped *Chd7$^{+/-}$* embryos, including interrupted aortic arch type B (IAA-B) and absence of the right subclavian artery (Randall et al., 2009). *Chd7$^{fl/fl}$;Mesp1-Cre* embryos were therefore examined at E15.5 for similar defects. This revealed that 21% (n=14) of *Chd7$^{fl/fl}$;Mesp1-Cre* embryos at E15.5 had IAA-B (Figure 3-8, A', and Table 3-4). One embryo examined had a vascular ring: this phenotype will be addressed further in Chapter 4. The great vessels of the E18.5 *Chd7$^{fl/fl}$;Mesp1-Cre* embryos were also found to have structural defects: one had a right-sided aortic arch (Figure 3-8, B'), and the other had aberrant posterior branching of the right subclavian from the right common carotid (Figure 3-8, B'').

Structural defects of the great vessels are often associated with earlier defects in the symmetrical formation of the pharyngeal arch arteries (PAAs) around E10.5, which then undergo a complex process of programmed asymmetrical expansion, regression and spatial rearrangements of the vessels to form the final aortic arch structure. Specifically, hypo/aplasia of the 4th PAA leads to defects such as IAA-B (Lindsay et al., 1999), although recovery from earlier PAA defects can occur (Lindsay and Baldini, 2001). The reported great vessel defects in Chd7$^{+/-}$ heterozygotes were attributed to PAA defects at E10.5, which predominantly affected the 4th PAA (Randall et al., 2009). However, examination of the PAAs at E10.5 in revealed no defects in *Chd7$^{fl/fl}$;Mesp1-Cre* embryos (Figure 3-8, panel C, and Table 3-4), indicating that the great vessel defects observed are likely due to a later remodelling defect.

Table 3-4: Frequency of PAA defects at E10.5 and IAA-B at E15.5

Genotype:	n:	4th PAA defects:	n:	IAA-B:
Chd7$^{fl/+}$	16	6%	11	0%
Chd7$^{fl/fl}$	18	0%	16	6%
Chd7$^{fl/+}$;Mesp1-Cre	15	7%	9	11%
Chd7$^{fl/fl}$;Mesp1-Cre	**14**	**0%**	**14**	**21%**

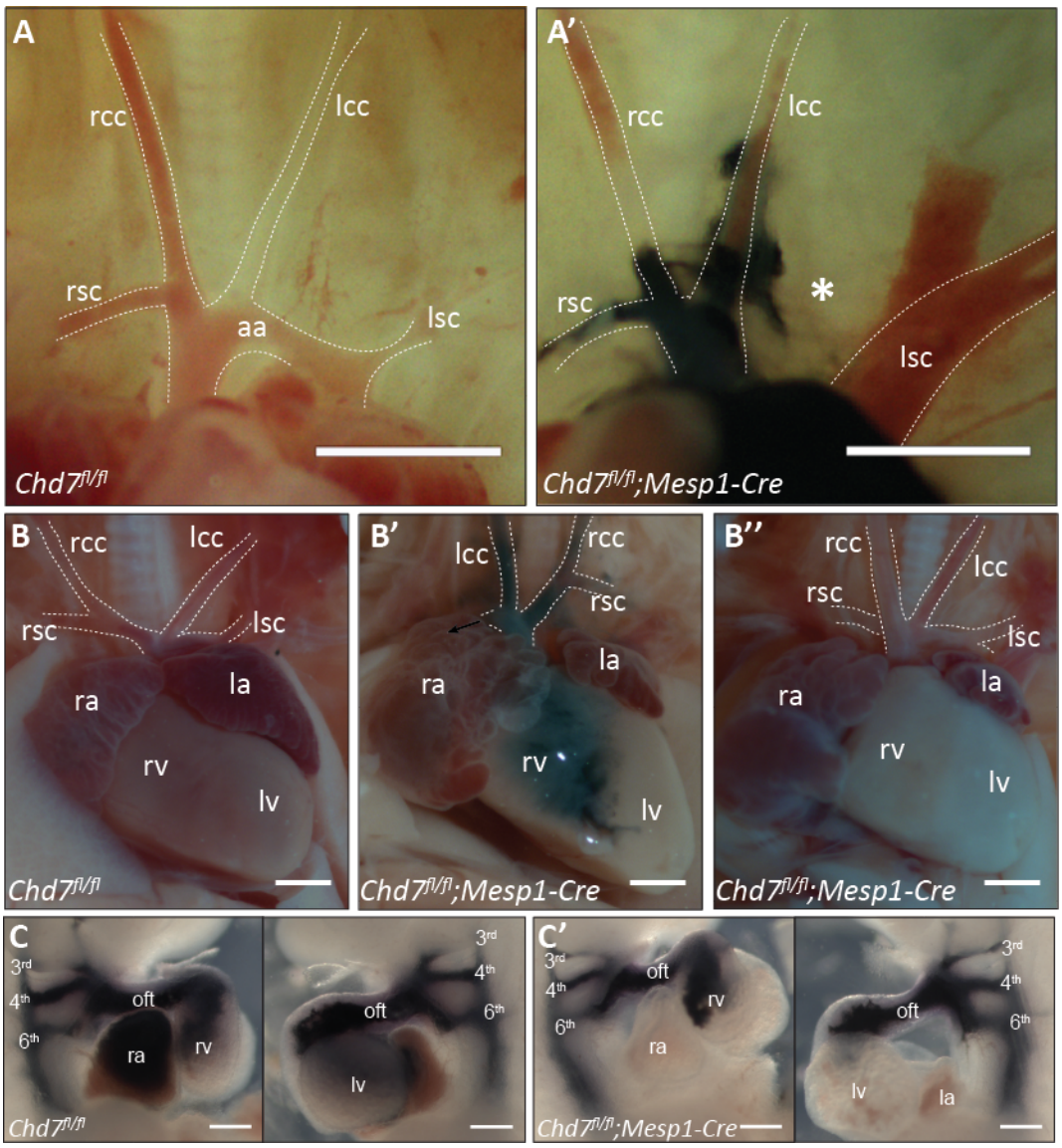

Figure 3-8: Great vessel defects in *Chd7$^{fl/fl}$;Mesp1-Cre* embryos

(A) The great vessels at E15.5. In *Chd7$^{fl/fl}$* embryos the normal arrangement was seen (A), whilst 21% of *Chd7$^{fl/fl}$;Mesp1-Cre* embryos had interrupted aortic arch type B, where the aortic arch is disrupted between the left common carotid and left subclavian arteries (star, A').

(B) The heart and great vessels at E18.5. In one *Chd7$^{fl/fl}$;Mesp1-Cre* embryo right-sided aortic arch was seen (arrow, B'), whilst in the other the branching of the right subclavian artery was dorsal to the right common carotid (B'').

(C) Ink injection of the pharyngeal arch arteries (PAAs) at E10.5 showed normal formation of the 3rd, 4th and 6th PAAs bilaterally in both *Chd7$^{fl/fl}$* (C) and *Chd7$^{fl/fl}$;Mesp1-Cre* (C') embryos.

Scale bars represent 0.5mm. aa indicates aortic arch; rsc, right subclavian artery; rcc, right common carotid artery; lcc, left common carotid artery; lsc, left subclavian artery; ra, right atrium; la, left atrium; rv, right ventricle; lv, left ventricle; oft, outflow tract.

3.3.4 Further arterial pole defects in Chd7$^{fl/fl}$;Mesp1-Cre hearts

Haematoxylin and eosin (H&E) staining of transverse sections showed major structural defects in *Chd7$^{fl/fl}$;Mesp1-Cre* hearts. 60% of hearts examined at E15.5 (n=10) had double outlet arising from the right ventricle (DORV, Figure 3-9). This occurs when the OFT is not aligned correctly, so rather than the aorta arising exclusively from the left ventricle and the pulmonary trunk arising exclusively from the right ventricle, both the aorta and pulmonary trunk arise from the right ventricle. This is a serious structural defect as it means the pulmonary and systemic circulations are not separated.

Common arterial trunk (CAT, also known as persistent truncus arteriosus) occurs when the OFT fails to septate properly, and so a connection between the aorta and pulmonary trunk remains. This was seen in an E13.5 *Chd7$^{fl/fl}$;Mesp1-Cre* embryo (Figure 3-10, A'), although not in any of the E15.5 *Chd7$^{fl/fl}$;Mesp1-Cre* hearts examined, so the penetrance is low. Therefore, to increase the efficiency of *Chd7* deletion and further impact downstream CHD7 targets, the *Chd7* ENU mutant *Whirligig* mouse (*Chd7^{Whi})* (Bosman et al., 2005) was used for mesodermal *Chd7* ablation on a constitutively heterozygous background (*Chd7$^{Whi/fl}$;Mesp1-Cre*). Optical projection tomography (OPT) imaging at E13.5 showed CAT arising from the right ventricle in 50% (n=4) of *Chd7$^{Whi/fl}$;Mesp1-Cre* embryos and DORV in the other 50%, along with IAA-B and DILV (see Figure 3-10, B' and B'', and Movies 1 and 2).

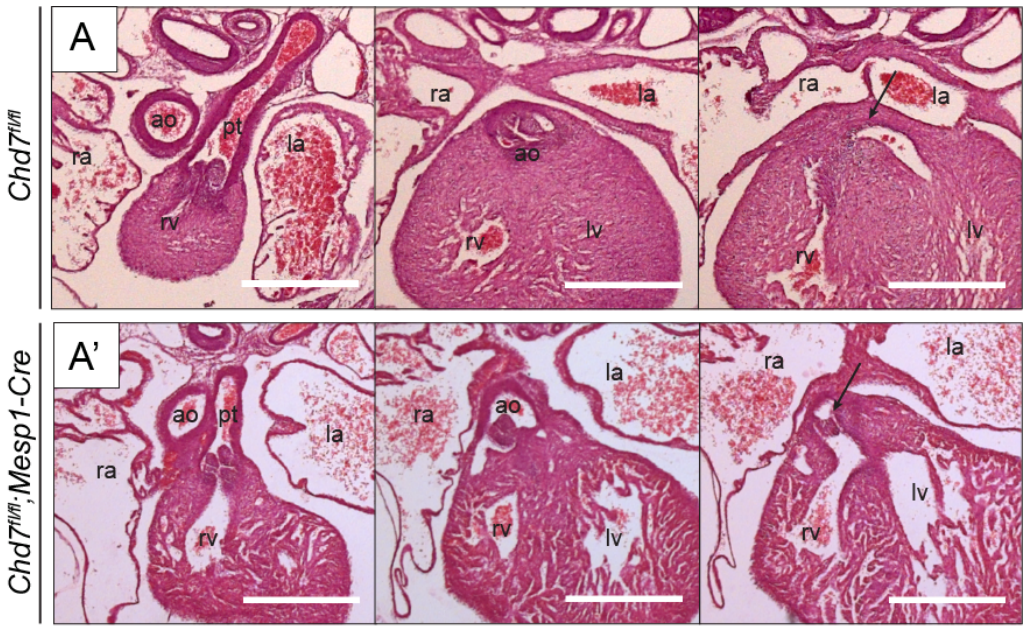

Figure 3-9: Double outlet right ventricle in *Chd7$^{fl/fl}$;Mesp1-Cre* hearts

Transverse sections at E15.5 showed DORV in 60% of *Chd7$^{fl/fl}$;Mesp1-Cre* hearts (A'), whereas in all *Chd7$^{fl/fl}$* controls the aorta arises as normal from the left ventricle (A). In the mutant sections, both the pulmonary trunk and then the base of the aorta (arrow) can be seen opening from the right ventricle.

Scale bars represent 0.5mm. rv indicates right ventricle; lv, left ventricle; ra, right atrium; la, left atrium; ao, aorta; pt, pulmonary trunk.

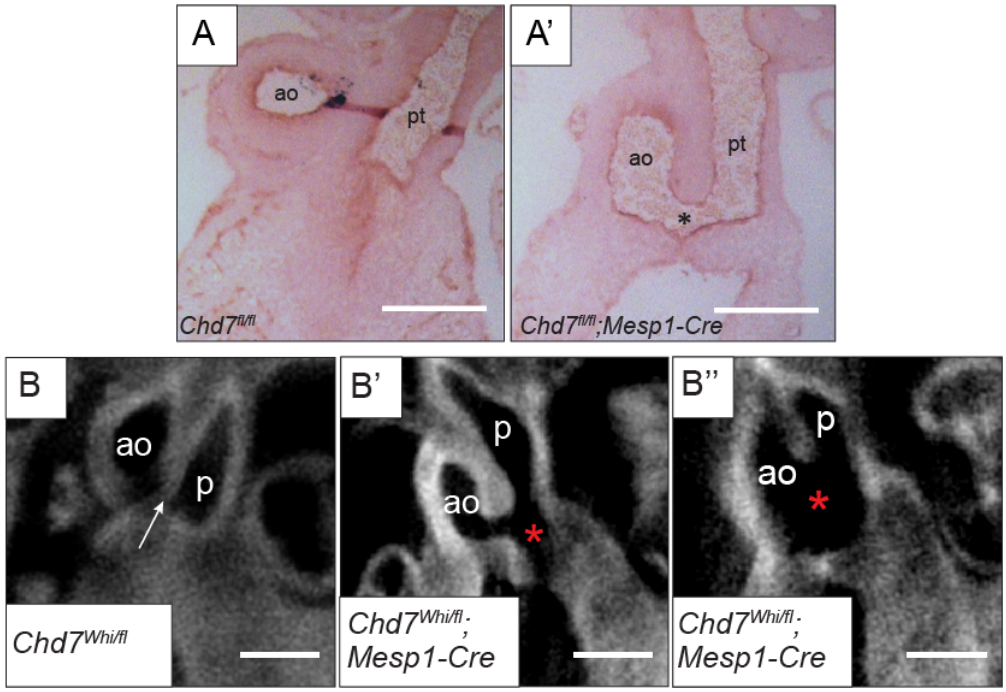

Figure 3-10: Common arterial trunk *in Chd7$^{fl/fl}$;Mesp1-Cre* and *Chd7$^{Whi/fl}$;Mesp1-Cre* hearts

(A) CAT was seen in a *Chd7$^{fl/fl}$;Mesp1-Cre* embryo at E13.5 (star, A'), compared to normal OFT septation in *Chd7$^{fl/fl}$* controls (A).

(B) OPT imaging at E13.5 also showed 50% of *Chd7$^{Whi/fl}$;Mesp1-Cre* embryos also had CAT (red stars, B' and B''), whereas the OFT was fully septated in *Chd7$^{Whi/fl}$* controls (white arrow, B).

Scale bars represent 0.2mm. ao, indicates aorta; pt/p, pulmonary trunk.

3.3.5 Mesp1-Cre driven ablation of Chd7 provides a model for the "Holmes Heart"

All hearts examined at E15.5 had double inlet left ventricle (DILV), whereby both atria were connected through a common atrioventricular (AV) valve to a dominant left ventricle, with no access from the AV junction to the incomplete right ventricle (Figure 3-11, panel A). The venous valves were absent or poorly formed and an inter-ventricular communication was observed in all hearts. Furthermore, the ventricular mural myocardium was often poorly compacted (Figure 3-11, panel B).

The rare combination of DILV with concordant ventriculo-arterial connections is known in humans as the "Holmes heart" (Dobell and Van Praagh, 1996). The arrangement seen in the *Chd7$^{fl/fl}$;Mesp1-Cre* hearts with DILV and spiralling arterial trunks is therefore analogous to the situation found in the Holmes heart.

Table 3-5 and Figure 3-12 summarise the major structural cardiovascular defects seen in the E15.5 embryos collected from the *Chd7$^{fl/fl}$* x *Chd7$^{fl/+}$;Mesp1-Cre*. Whilst severe defects were seen with high frequency in the *Chd7$^{fl/fl}$;Mesp1-Cre* embryos, malformations were not seen above background levels in the *Chd7$^{fl/fl}$;Mesp1-Cre* embryos. This lack of haploinsufficiency for *Chd7* in the mesoderm was unexpected, given the cardiac defects observed in both CHD7-haploinsufficient CHARGE patients and constitutive *Chd7$^{+/-}$* mouse models, and is discussed further in section 3.4.4.

Table 3-5: Major cardiac phenotypes observed at E15.5

Genotype:	IAA-B:	AVSD:	DILV:	DORV:	Myocardial non-compaction:	Venous valve defect:
Chd7$^{fl/+}$	0/11	0/7	0/7	0/7	0/7	0/7
Chd7$^{fl/fl}$	1/16	0/5	0/5	0/5	0/5	0/5
Chd7$^{fl/+}$;Mesp1-Cre	1/9	0/4	0/4	0/4	0/4	0/4
Chd7$^{fl/fl}$;Mesp1-Cre	**3/14**	**10/10**	**10/10**	**6/10**	**8/10**	**9/10**

IAA-B indicates interrupted aortic arch type-B; AVSD, atrioventricular septal defect; DILV, double inlet left ventricle; DORV, double outlet right ventricle.

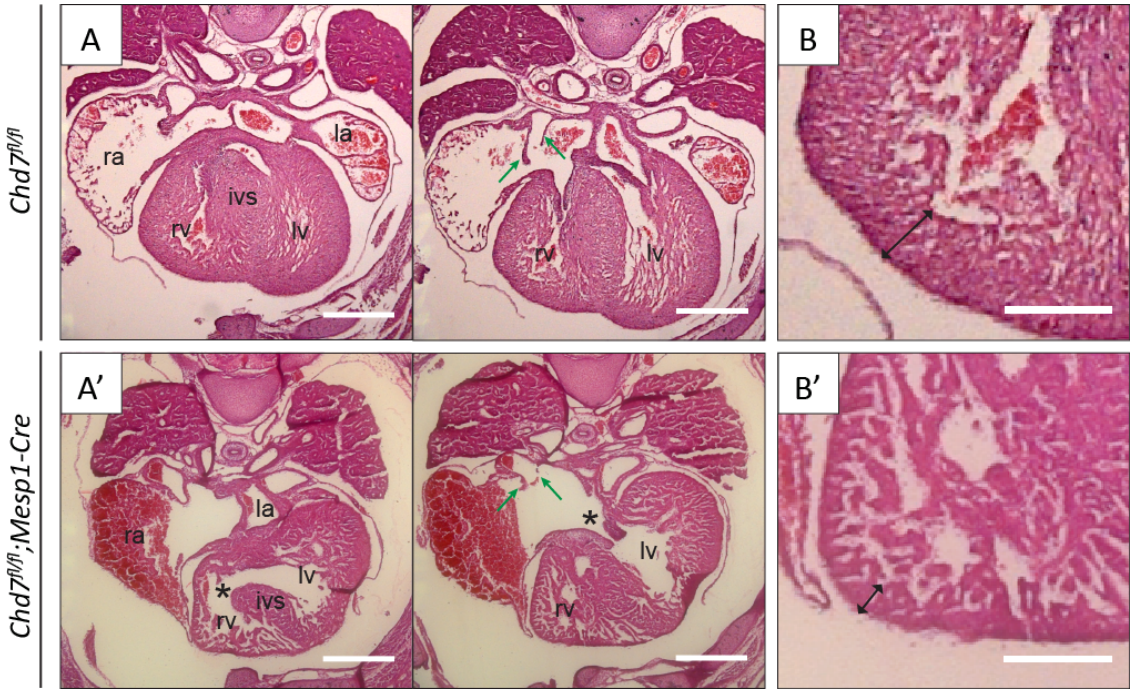

Figure 3-11: Double inlet left ventricle and thin myocardial walls in *Chd7$^{fl/fl}$;Mesp1-Cre* hearts

(A) H&E transverse heart sections at E15.5 showed normal morphology in *Chd7$^{fl/fl}$* embryos, whilst all *Chd7$^{fl/fl}$;Mesp1-Cre* hearts had DILV, including inter-ventricular communication, common AV valves (stars, A') and poor formation of the venous valves (green arrows, A').

(B) The compact layer of the ventricular myocardial wall should be well formed by E15.5, but was also thin in 80% of *Chd7$^{fl/fl}$;Mesp1-Cre* hearts (B').

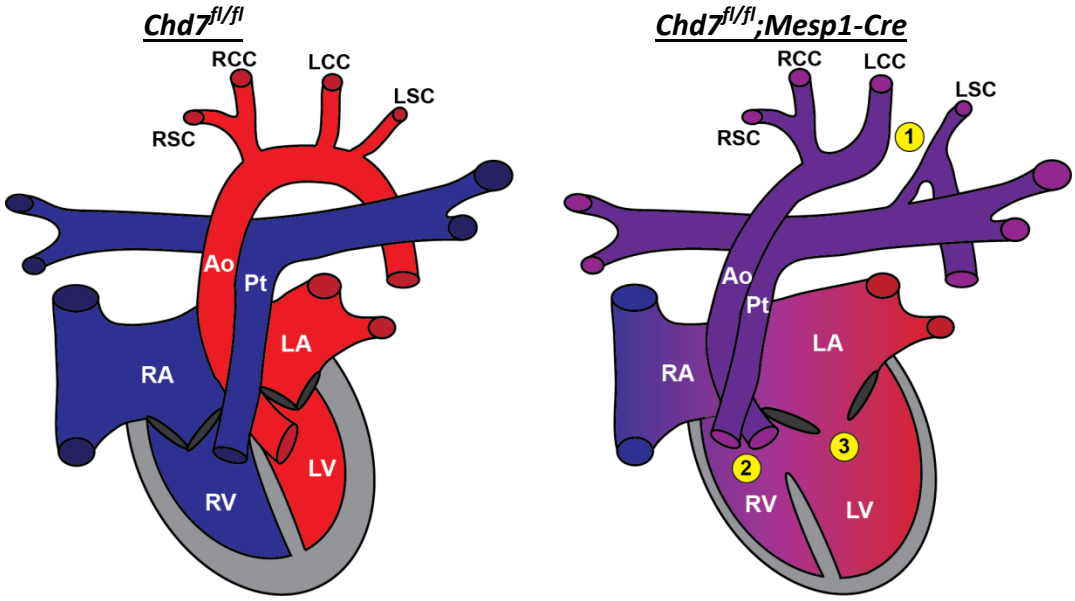

Figure 3-12: Schematic to show the major structural defects seen in *Chd7$^{fl/fl}$;Mesp1-Cre* hearts

The normal configuration of the heart in *Chd7$^{fl/fl}$* controls has complete separation of the pulmonary and systemic circulatory systems, compared to major septation and alignment defects seen in *Chd7$^{fl/fl}$;Mesp1-Cre* hearts. These included interrupted aortic arch type B (1), double outlet right ventricle (DORV - 2) and double inlet left ventricle (DILV - 3).

3.3.6 Cardiac neural crest cell migration is abrogated in Chd7$^{fl/fl}$;Mesp1-Cre embryos

Although the expression of *Chd7* in NCCs would not be cell-autonomously affected in conditional *Chd7$^{fl/fl}$;Mesp1-Cre* embryos, NCC migration was investigated as aberrant NCC behaviour could be contributing to the OFT defects observed. The cardiac neural crest plays a crucial role in septation and alignment of the outflow tract and aortic arch artery development, with classic studies in chick embryos demonstrating interrupted aortic arch, common arterial trunk and DORV after disruption to neural crest migration (Kirby et al., 1983). Wholemount ISH analysis of *Sox10* expression, which marks migrating NCCs (Kuhlbrodt et al., 1998), showed similar patterns of expression in *Chd7$^{fl/fl}$* and *Chd7$^{fl/fl}$;Mesp1-Cre* somite-matched embryos at E10.5 (Figure 3-13, A and B). NCCs were seen beginning to enter the 4th PAA in both genotypes, although the post-otic stream appeared to be slightly shorter in *Chd7$^{fl/fl}$;Mesp1-Cre* embryos.

PlexinA2 is expressed by NCCs that surround the aortic arches and migrate into the OFT in a distal to proximal direction (Brown et al., 2001). Sequential coronal sections through the OFT of *Chd7$^{fl/fl}$* and *Chd7$^{fl/fl}$;Mesp1-Cre* embryos were therefore also analysed at E11.5 for *PlexinA2* expression (Figure 3-13, C-J). At the distal end of the OFT, similar *PlexinA2* expression can be seen in both genotypes, showing migratory NCCs are present. However, towards the proximal end of the OFT the two characteristic clusters of NCCs in the endocardial cushions are not seen in *Chd7$^{fl/fl}$;Mesp1-Cre* embryos (Figure 3-13, H'-J'). Together, these results indicate that NCCs migrate normally through the pharyngeal region at E10.5, but as they are populating the OFT at E11.5 their migration is abrogated following mesodermal ablation of *Chd7*.

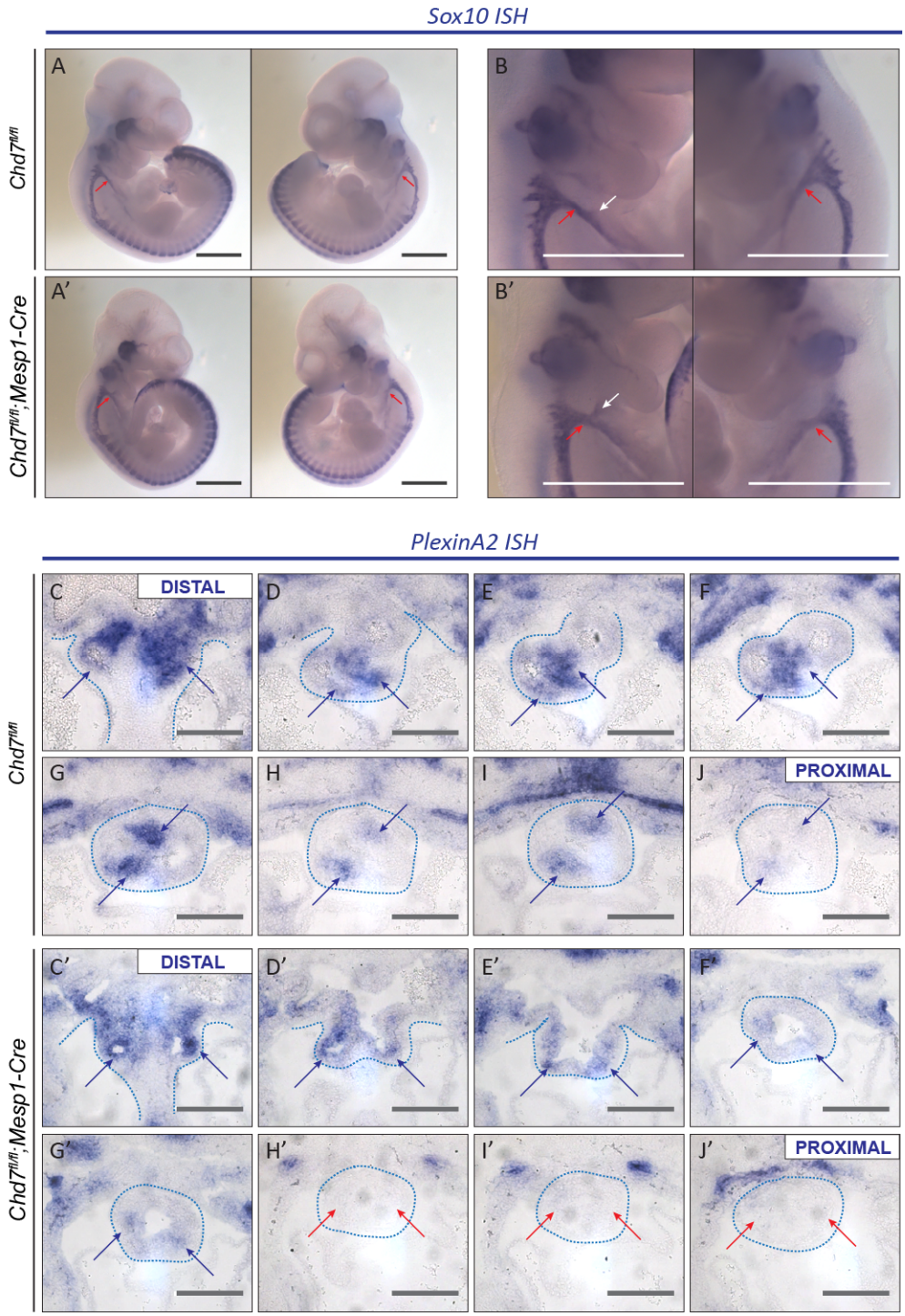

Figure 3-13: Neural crest cell migration in *Chd7$^{fl/fl}$;Mesp1-Cre* embryos

(A, B) *Sox10* ISH on E10.5 *Chd7$^{fl/fl}$* and *Chd7$^{fl/fl}$;Mesp1-Cre* embryos (both 27 somites) showed post-otic streams of neural crest cells migrating through the pharyngeal arches (red arrows, A and A'). Higher magnification images showed neural crest cells beginning to branch off to the 4th PAA in both genotypes (white arrows, B and B').

(C-J) Comparison of *PlexinA2* ISH on coronal E11.5 sections through the outflow tract in a *Chd7$^{fl/fl}$* (C-J) and *Chd7$^{fl/fl}$;Mesp1-Cre* (C'-J') embryo. Sections were arranged sequentially in a distal to proximal direction through the outflow tract, with equivalent sections (C and C', D and D' etc.) matched as closely as possible. *PlexinA2*-expressing cardiac neural crest cells were seen migrating through to the most proximal section in the *Chd7$^{fl/fl}$* control (blue arrows, J), whilst neural crest cell migration was abrogated in the *Chd7$^{fl/fl}$;Mesp1-Cre* (red arrows, H'-J').

Scale bars represent 2mm (A-B) or 0.2mm (C-J).

3.3.7 *Malformation of the vestibular spine and AV cushions at E11.5*

The presence of a common AV valve and lack of venous valves is indicative of a failure of the vestibular spine (also referred to as the dorsal mesenchymal protrusion) to form at the venous pole. The vestibular spine is a mesenchymal structure, derived from the dorsal mesocardium, that drives the separation of the AV canal into its left and right components and carries forward the inferior ends of the venous valves (Anderson et al., 2003a). To investigate its formation in *Chd7$^{fl/fl}$;Mesp1-Cre* embryos, OPT was used to image hearts at E11.5. The vestibular spine was found to be absent or reduced in size in *Chd7$^{fl/fl}$;Mesp1-Cre* hearts (Figure 3-14, Movies 3 and 4).

The OPT imaging also showed grossly abnormal positioning of the AV endocardial cushions, which were markedly rotated within the AV canal compared to the control heart (Figure 3-14, C). As these endocardial cushions are also crucial for AV canal septation, their misalignment could therefore also be contributing to the AVSDs observed at later stages.

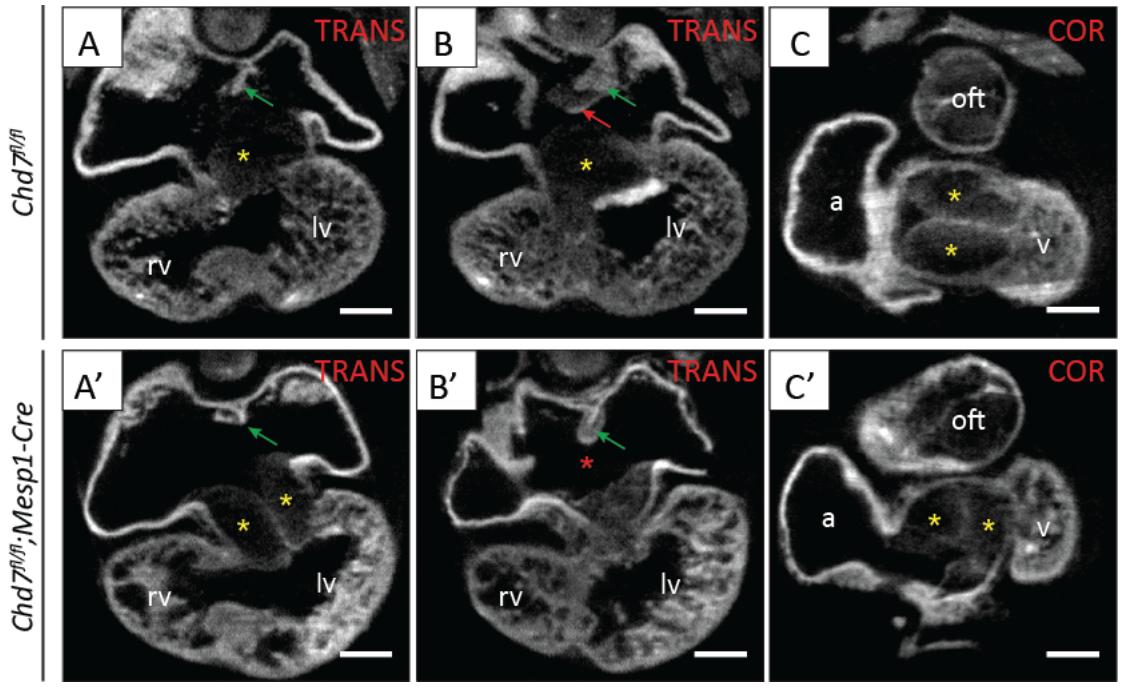

Figure 3-14: OPT imaging of hearts at E11.5

(A, B) Transverse images through a *Chd7$^{fl/fl}$* heart showed formation of the primary atrial septum (green arrow, A), and the vestibular spine (red arrow, B). The endocardial superior and inferior AV cushions were seen sequentially in A and B (yellow stars). In the *Chd7$^{fl/fl}$;Mesp1-Cre* heart the atrial septum formed as expected (green arrow, A'), but the vestibular spine was completely absent (red star, B'). The arrangement of the cushions was also grossly abnormal, with both seen adjacently in the same plane (yellow stars, A').

(C, C') Digital re-slicing was used to produce coronal sections of the same hearts, which highlighted the abnormal positioning of the endocardial cushions (yellow stars).

Scale bars represent 0.2mm. oft indicates outflow tract; rv, right ventricle; lv, left ventricle; a, atrium; v, ventricle.

3.3.8 Disruption to Cardiac Innervation and Coronary Vein Development

To characterise further the cardiac phenotype following mesodermal *Chd7* ablation, the innervation and vascularisation of *Chd7$^{fl/fl}$;Mesp1-Cre* hearts was also investigated. Immunostaining using an antibody against Neurofilament-66 at E15.0 showed major disruption to the innervation of *Chd7$^{fl/fl}$;Mesp1-Cre* hearts (Figure 3-15, panel A). The neuronal axons extending down from the cardiac plexus to the ventricles were extremely truncated in all the *Chd7$^{fl/fl}$;Mesp1-Cre* hearts examined (n=4), and did not branch out through the ventricles at all. Furthermore, anti-Endomucin immunostaining revealed severe disruption to the coronary veins on the surface of the heart at E15.5 in *Chd7$^{fl/fl}$;Mesp1-Cre* hearts, with either truncation of vessels or ectopic formation of multiple under-developed veins (Figure 3-15, panel B). However, coronary plexus formation looked relatively normal at E13.5, as determined by expression of the arterial marker Notch1 (Figure 3-15, panel D).

Interestingly, the coronary veins developed normally following endothelial-specific *Chd7* ablation using *Tie2-Cre* (Figure 3-15, C). CHD7 activity within the myocardium therefore appears to have a non-cell-autonomous effect on the migratory endothelial cells required for the development of the coronary veins.

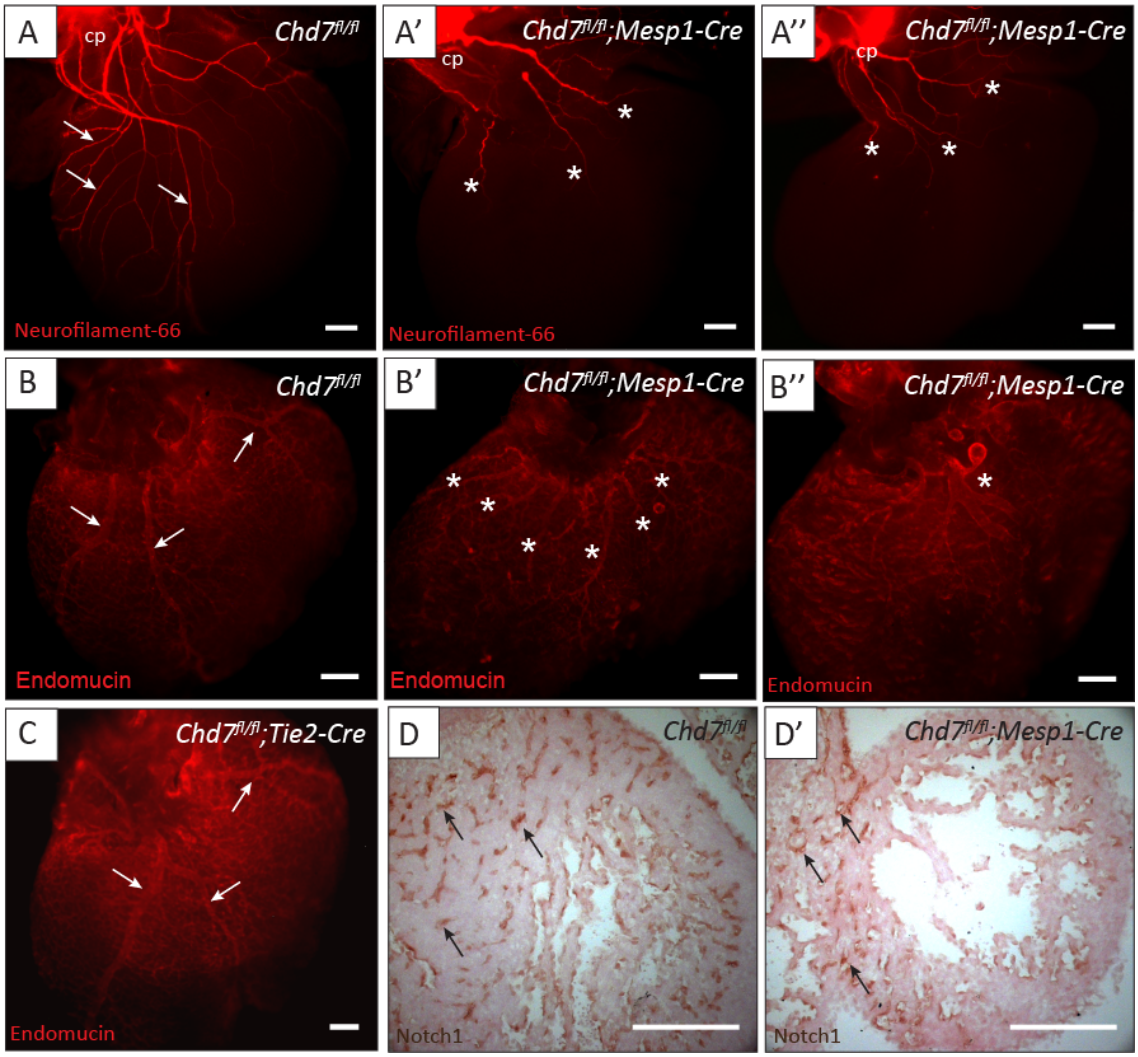

Figure 3-15: Innervation and vascularisation of *Chd7$^{fl/fl}$;Mesp1-Cre* hearts

(A) Wholemount immunostaining at E15.0 for Neurofilament-66 allowed visualisation of the parasympathetic and sympathetic axons descending from the cardiac plexus and branching into the ventricles (white arrows, A). Severe truncation of axons was seen in *Chd7$^{fl/fl}$;Mesp1-Cre* hearts (stars, A' and A'').

(B) Dorsal view of E15.5 hearts immunostained with anti-Endomucin antibody showed formation of three main coronary veins (white arrows, B). In *Chd7$^{fl/fl}$;Mesp1-Cre* hearts patterning of the veins was disrupted, with either extra, smaller vessels (stars, B') or truncated vessels (star, B'').

(C) Coronary vein development was normal in *Chd7$^{fl/fl}$;Tie2-Cre* hearts (arrows, C).

(D) Despite morphological differences, Notch1 staining on E13.5 transverse sections showed similar establishment of the vascular plexus (arrows) in both *Chd7$^{fl/fl}$* (D) and *Chd7$^{fl/fl}$;Mesp1-Cre* (D') hearts.

Scale bars represent 0.2mm. cp indicates cardiac plexus.

3.4 Discussion

This chapter has demonstrated a novel role for *Chd7* in mesodermal cardiac progenitors. CHD7 protein was shown to be present in the developing heart until E13.5, including within the walls and cushions of the OFT, and in the endocardial and myocardial layers of the atria and ventricles. To investigate the role of *Chd7* specifically in the mesoderm, a conditional floxed *Chd7* allele was crossed with the *Mesp1-Cre* allele, and analysis of *Chd7* mRNA levels in the heart confirmed that *Chd7* expression was reduced. Homozygous ablation of *Chd7* in the mesoderm was embryonic lethal, with embryos showing severe oedema and haemorrhaging, and major structural cardiovascular defects. Double inlet left ventricle (DILV) with concordant ventriculo-arterial connections was fully penetrant, making this an excellent model for the rare human condition known as the "Holmes heart" (Dobell and Van Praagh, 1996). Furthermore, many *Chd7*$^{fl/fl}$*;Mesp1-Cre* hearts also had double outlet from the right ventricle (DORV), poor compaction of the myocardium, and great vessel defects. Disruption of NCC migration towards the proximal end of the OFT, failure of formation of the vestibular spine, and misalignment of the atrioventricular (AV) endocardial cushions all likely underlie the defects observed by E15.5. This requirement for *Chd7* in mesodermal cardiac progenitors suggests the current hypothesis that CHARGE syndrome is a neurocristopathy may be an over-simplification, at least regarding the cardiac malformations associated with this syndrome.

3.4.1 CHD7 expression

Following early ubiquitous expression of *Chd7*, from around E10.5 its expression pattern becomes more restricted and tissue-specific (Bosman et al., 2005; Randall et al., 2009). CHD7 protein was present throughout the heart until E13.5. This temporal cardiac expression pattern of CHD7 is reminiscent of BRG1, the ATPase subunit of the SWI/SNF chromatin remodelling complex BRG1/BRM-associated factor (BAF) (Wang et al., 1996). BRG1 is similarly highly expressed during development (Stankunas et al., 2008) but repressed in the adult heart (Hang et al., 2010). *Brg1* is reactivated by cardiac stresses, inducing a pathological shift from the adult myosin heavy chain isotope *α-MHC* to the fetal *β-MHC*. Preventing *Brg1* re-expression reduces cardiac hypertrophy, thereby identifying it as a therapeutic target (Hang et al., 2010). Given their similarities in expression and chromatin remodelling activity, it would be interesting to see if a similar pathological reactivation of *Chd7* occurs in the context of cardiac failure.

Whilst this work provides new insights into the timing of CHD7 protein expression in the developing heart, the mechanisms involved in the regulation of its expression remain unknown. The loss of CHD7 protein by E13.5 could be resulting from downregulation or inhibition of transcription factors and other regulatory proteins that are required at the *Chd7* locus. Transcriptional repression could also be initiated at the epigenetic level through post-translational modifications to the histone tails, chromatin remodelling to a heterochromatic state, or DNA methylation. However, no studies have been carried out into the mechanism(s) of regulation of *Chd7* expression during development, to the author's knowledge. Given the variation in *Chd7* expression in different tissue types and organs during development, it would be useful to understand more about its cell-specific regulation. Functional splice variants of CHD7 have also been reported (Aramaki et al., 2006; Colin et al., 2010), but again there is no information on the mechanisms that may be regulating the splicing of the different CHD7 isoforms.

3.4.2 Structural cardiovascular defects in Chd7$^{fl/fl}$;Mesp1-Cre embryos

C*hd7*$^{-/-}$ mouse mutants are embryonic lethal at E10.5 due to growth failure (Alavizadeh et al., 2001), making it difficult to study the role of *Chd7* in the heart beyond this stage. Although it has recently been shown that heterozygosity for p53 can partially rescue the *Chd7*$^{-/-}$ phenotype (Van Nostrand et al., 2014), at least in terms of embryonic growth, conditional mutagenesis is required to bypass the early lethality and allow a proper assessment of heart development. *Chd7*$^{fl/fl}$*;Mesp1-Cre* embryos survived until E15.5, when the heart is fully septated and the vessels are in their proper configuration. At this stage, *Chd7*$^{fl/fl}$*;Mesp1-Cre* embryos exhibited severe oedema and haemorrhaging along with major structural cardiovascular defects.

Oedema is the accumulation of fluid within body tissues, and is a classic sign of poor cardiac function resulting from underlying cardiovascular defects (Conway et al., 2003). It can also be caused by defective development of the lymphatic vasculature, for example when *Prox1* is knocked out during development (Wigle and Oliver, 1999). The lymphatic system was examined in two *Chd7*$^{fl/fl}$*;Mesp1-Cre* embryos and loss of expression of lymphatic markers was seen in one embryo, but this was not confirmed in the other mutant. The first embryo was determined to be likely dead *in utero* or compromised in some way, which would explain the aberrant gene expression, but these investigations were not taken any further (personal communication, Elizabeth Illingworth). Given the severe cardiovascular malformations found in the *Chd7*$^{fl/fl}$*;Mesp1-Cre* embryos, poor cardiac function is the most likely underlying cause of the oedema. The haemorrhagic phenotype indicates poor vessel integrity in these embryos, although this was not investigated further. Mild or more severe haemorrhaging was also seen

in heterozygous ENU mutant *Whirligig* embryos (*Chd7*$^{Whi/+}$), supporting a role for *Chd7* in blood vessel development.

Great vessel defects were found with partial penetrance in *Chd7*$^{fl/fl}$*;Mesp1-Cre* embryos. At E15.5, interrupted aortic arch type-B (IAA-B) was seen in 21% of these embryos, compared to just 4% of heterozygous gene-trapped *Chd7*$^{xk/+}$ embryos (Randall et al., 2009). Interestingly, in the *Chd7*$^{xk/+}$ embryos the great vessel defects were attributed to a high penetrance of pharyngeal arch artery (PAA) malformations at E10.5, particularly affecting the 4th PAA, but no PAA defects were observed in E10.5 *Chd7*$^{fl/fl}$*;Mesp1-Cre* embryos. Randall and colleagues showed that in their haploinsufficient model, restoration of *Chd7* expression in the pharyngeal surface ectoderm (PSE) rescued the PAA malformations, indicating a vital role for *Chd7* in the regulation of signalling from the ectoderm to the mesenchymal NCCs populating the PAAs. However, restoration of *Chd7* driven by *Mesp1-Cre* did not rescue the early phenotype. Together, these findings suggest that biallelic expression of *Chd7* in the PSE, but not in mesodermal cardiac progenitors, is required for PAA morphogenesis (Randall et al., 2009).

The lack of PAA defects in *Chd7*$^{fl/fl}$*;Mesp1-Cre* embryos indicates that even with further levels of *Chd7* ablation in the cardiac mesoderm the PAAs form normally, confirming CHD7 activity in these cells is not required for early PAA development. Instead, it seems to be required later in mesodermal derivatives, most likely the SHF, for remodelling of the OFT and PAAs to form the mature configuration of the aortic arch and great vessels. It is relatively unusual to find great vessel defects without earlier underlying disruption to the PAAs, but examples have been reported following targeted mutagenesis of *Sema3C* (Feiner et al., 2001), endothelial-specific conditional double-knockout of α5 and αv integrins (van der Flier et al., 2010) and neural crest-specific ablation of *Alk5* (Wang et al., 2006).

Mesodermal *Mesp1-Cre*-driven ablation of *Chd7* produced serious structural defects affecting both the inflow and outflow tracts. Correct alignment and septation of the developing cardiac components ensures the complete separation of the pulmonary and systemic circulations, which is vital for effective cardiovascular function. An overrepresentation of conotruncal defects and common arterial trunk (CAT, also known as persistent truncus arteriosus) was seen in a cohort of patients with CHD7 mutations compared to a control group of non-syndromic heart defects (Corsten-Janssen et al., 2013a). Consistent with this, CAT was present in one *Chd7*$^{fl/fl}$*;Mesp1-Cre* embryo as well as in *Chd7*$^{Whi/fl}$*;Mesp1-Cre* embryos, and conotruncal defects such as DORV and great vessel defects were frequently seen.

Defects affecting the arterial pole of the heart are often attributed to disruption to the migration or differentiation of the cardiac NCCs. This transient cell population migrates from the neural tube through the pharyngeal arches towards the proximal OFT, contributing in complex tissue interactions that are vital for formation and remodelling of the PAAs and for septation of the OFT (Hutson and Kirby, 2007). The abrogation of the cardiac neural crest in the OFT seen in E11.5 *Chd7$^{fl/fl}$;Mesp1-Cre* embryos could therefore be contributing to the DORV and IAA-B defects that develop subsequently. This indicates that *Chd7* expression in the *Mesp1*-derived tissue in the walls of the OFT has a cell non-autonomous effect on the cardiac neural crest, presumably through extracellular guidance signalling. This would support the hypothesis that the neural crest is involved in the pathogenesis of the heart defects associated with CHARGE syndrome (Siebert et al., 1985), but loss of *Chd7* expression in the OFT myocardium and endocardium is sufficient to disrupt cardiac neural crest migration and lead to the OFT defects described.

The presence of DILV with spiralling arterial trunks in all *Chd7$^{fl/fl}$;Mesp-1Cre* hearts was analogous to the "Holmes heart" seen in humans. The original formalin-fixed specimen described by Holmes in 1823, which is still on display at McGill University, had absence of the inflow tract of the right ventricle and thus a single morphologically left ventricle with DILV, and normally-related great arteries (Dobell and Van Praagh, 1996). DILV is predicted to make up 1% of congenital heart malformations (Franklin et al., 1991). In a study of 60 cases of human single-ventricle hearts, 15% were found to have this "Holmes heart" configuration with normally related arteries (also known as type I), 42% had the aorta positioned anterior and rightward (type II), and 43% had an anterior and leftward-transposed aorta (type III) (Vanpraagh et al., 1964).

Although DILV is not reported in CHARGE patients, atrioventricular septal defects (AVSDs) were also significantly overrepresented in patients with CHD7 mutations (Corsten-Janssen et al., 2013a). DILV represents one of the two extreme ends of the spectrum of ventricular imbalance that can be seen with AVSDs (see Figure 3-16). This increase in severity of the alignment and septation defects affecting the AV canal in the *Chd7$^{fl/fl}$;Mesp1-Cre* embryos compared to the human CHARGE phenotype reflects the importance of *Chd7* dosage: CHARGE patients are haploinsufficient for *CHD7,* whilst in this mouse model the cells in the cardiogenic mesoderm undergo homozygous ablation of *Chd7* driven by *Mesp1-Cre,* thereby producing a more severe defect.

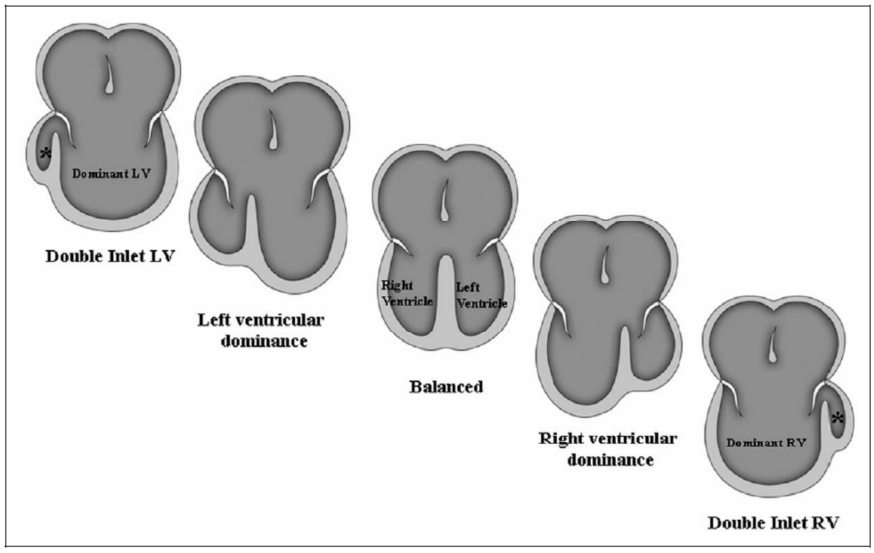

Figure 3-16: Spectrum of ventricular balance in atrioventricular septal defects

Abnormal hearts with a common AV junction can range in the severity of the structural misalignment from the most extreme double inlet left ventricle through a common AV valve with an incomplete right ventricle (asterisk, upper left panel) through to double inlet right ventricle with an incomplete left ventricle (asterisk, lower right panel).

The common AV junction and AV valves in the *Chd7$^{fl/fl}$;Mesp1-Cre* embryos was likely caused by failure of the formation of the vestibular spine and disorganisation of the AV endocardial cushions, as seen at E11.5. Septation of the AV canal involves multiple developmental structures (Figure 3-17). The muscular primary atrial septum descends from the roof of the primary atrial component of the heart tube, extending into the atrial cavity between the openings of the pulmonary and systemic veins, and carrying a prominent mesenchymal cap on the extending edge. Concurrently, a further mass of mesenchyme known as the vestibular spine extends inferiorly into the heart from the mediastinum (Webb et al., 1998). The mesenchymal masses capping the primary atrial septum and the vestibular spine first merge and fuse, followed by fusion with the inferior endocardial cushion in the AV canal, which subsequently fuses with the superior endocardial cushion. The fusion of these primordial mesenchymal structures therefore closes the gap below the primary atrial septum (the primary atrial foramen) and divides the common AV junction into its right and left components (Anderson et al., 2003a). Given the crucial roles of both the vestibular spine and the endocardical cushion in the septation and alignment of the AV canal, it is clear how their absence or abnormal positioning can result in the lack of fusion of the central mesenchymal mass, and thus in AVSDs and DILVs (Figure 3-17). The venous valve defects recorded in almost all *Chd7$^{fl/fl}$;Mesp1-Cre* are also characteristic of malformation of the vestibular spine, as it should normally drive forward the inferior ends of the venous valves as it extends into the heart (Anderson et al., 2003a).

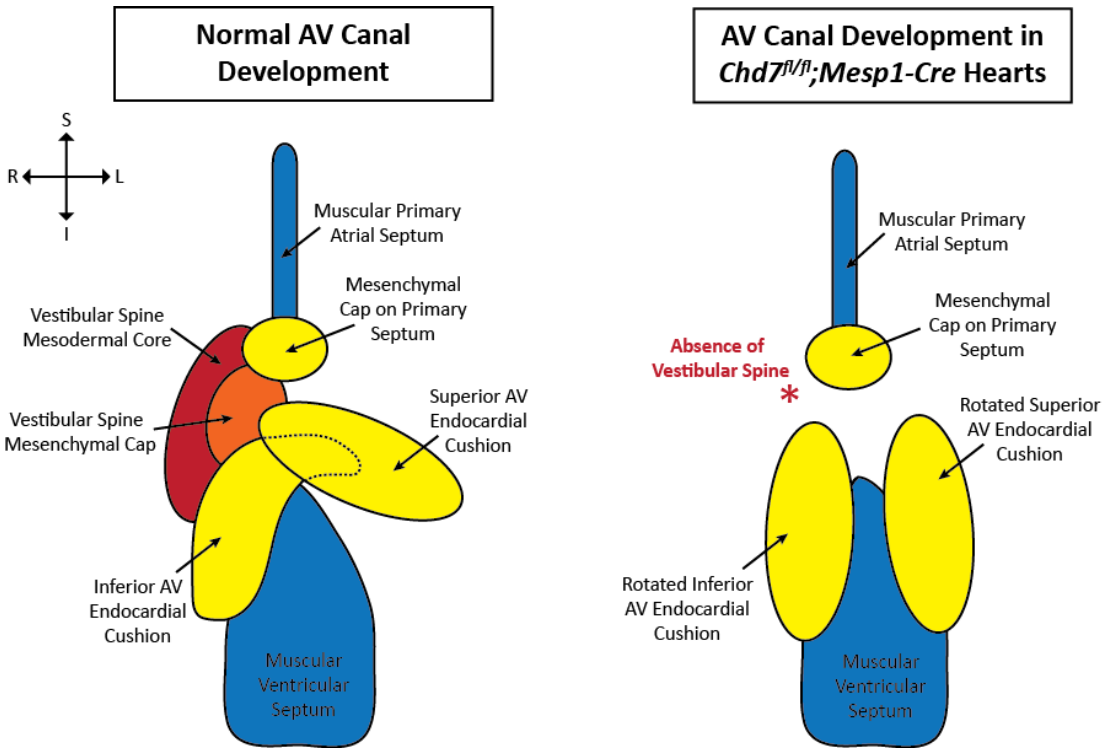

Figure 3-17: Schematic diagram showing the developmental primordia that form the central mesenchymal mass

Normal fusion occurs between the mesenchymal caps of the vestibular spine and primary atrial septum, followed by fusion with the endocardial cushions. In the *Chd7*$^{fl/fl}$*;Mesp1-Cre* hearts, the vestibular spine is absent or reduced in size and the endocardial cushions are abnormally arranged in the AV canal, resulting in loss of fusion of the mesenchymal structures and subsequent AVSD and DILV.

Adapted from Webb et al. (1998). On the directional arrows, S indicates superior; I, inferior; R, right; and L left.

It is interesting to note that the combination of DILV and DORV in *Chd7*$^{fl/fl}$*;Mesp1-Cre* hearts is reminiscent of the earliest formation of the heart tube following looping and chamber myocardial ballooning, prior to growth of the primary atrial septum. At this stage, around E10.5, the AV canal opens to the developing left ventricle, whilst the OFT is supported above the developing right ventricle (Anderson et al., 2003a), i.e. DILV and DORV (see Figure 1-2, C). This can be considered the "default option" of the heart. During normal development this arrangement is soon remodelled as the right ventricle expands, with concomitant remodelling of the inner heart curvature, to allow formation of the right AV orifice, and the AV canal is septated through fusion of the mesenchymal components described above. However, in the *Chd7*$^{fl/fl}$*;Mesp1-Cre* embryos this default configuration still persists at E15.5, leading to cardiac failure and embryonic lethality.

3.4.3 Disruption to cardiac innervation and vascularisation

In *Chd7*$^{fl/fl}$*;Mesp1-Cre* embryos, loss of *Chd7* expression in the ventricular myocardium also appeared to have a non-cell autonomous effect on the development of the coronary veins and the innervation of the heart, as shown by wholemount immunostaining. Strikingly, the coronary veins formed normally when *Chd7* was ablated specifically in endothelial cells using *Tie2-Cre*. This indicates that it is extracellular guidance signalling from the myocardium to the venous endothelial cells that is disrupted in *Chd7*$^{fl/fl}$*;Mesp1-Cre* hearts, leading to aberrant coronary vein formation. Large diameter coronary veins develop in the subepicardium from an existing primary capillary plexus through angiogenesis, a remodelling process in which endothelial cells re-organise into a network of branching vessels (Lavine and Ornitz, 2009). Key developmental signalling pathways, such as FGF and Hedgehog signalling, operate between the myocardium, endocardium and developing vasculature to control pro-angiogenic factor expression and coronary vessel development. Disruption to this signalling in the myocardium in *Chd7*$^{fl/fl}$*;Mesp1-Cre* hearts could therefore be disrupting the reorganisation of endothelial cells into the coronary veins. Unfortunately the embryos did not survive long enough through gestation to also examine the formation of the coronary arteries by staining for smooth muscle markers.

Severe truncation of the neuronal axons and branching into the ventricles was also seen on *Chd7*$^{fl/fl}$*;Mesp1-Cre* hearts. Both sympathetic and parasympathetic neuronal axons can be seen on the dorsal surface of the heart at E15.0, although they are predominantly sympathetic (Nam et al., 2013). They are derived from NCCs, which migrate to the dorsal aorta, differentiate into neurons and extend axonal projections into the cardiac tissue (Hasan, 2013). As *Chd7* expression would not have been be ablated in NCCs in *Chd7*$^{fl/fl}$*;Mesp1-Cre* embryos, this may again be indicative of a non-cell autonomous effect of mesodermal *Chd7* knockdown on the NCCs or neurons that contribute to cardiac innervation. Alternatively, this innervation defect may be secondary to the disruption to the coronary veins: sympathetic axons have been demonstrated to extend along the developing large coronary veins in the dorsal subepicardium of the ventricles, with mutant analysis indicating that this association is important for proper cardiac innervation, but not for coronary vascular patterning (Nam et al., 2013). This close link between nerve and blood vessel patterning is well established throughout the developing embryo (Carmeliet and Tessier-Lavigne, 2005).

3.4.4 The conditional *Chd7*^{fl} allele is slightly hypomorphic

A small proportion of *Chd7*$^{fl/+}$ and *Chd7*$^{fl/fl}$ embryos presented with a phenotype, despite the absence of a Cre allele, as seen in Tables 3-3, 3-4 and 3-5. This ranged from mild defects such as slight oedema or developmental delay, to occasionally more severe problems including haemorrhage or great vessel malformations. This indicates that the floxed *Chd7*^{fl} allele is slightly hypomorphic, possibly resulting in a reduction in *Chd7* expression levels compared to a wild-type allele, even without Cre-driven recombination. This may be due to the remaining frt site or the loxP sites present either side of exon 2 in the Flp-recombined *Chd7*^{fl} allele after Flipase-recombination for removal of the N/k cassette (see 'Flp-recombined *Chd7*^{fl} *allele'*, Figure 1-14). These sites should not affect *Chd7* expression, but may be increasing the probability for spontaneous recombination events to occur at the *Chd7* locus, or it is possible that they are disrupting a transcriptional regulatory element or an intronic splice acceptor or repressor. In a small proportion of embryos this disruption to the *Chd7* locus has resulted in a sufficient reduction in CHD7 levels for an observable phenotype.

The *Chd7* expression levels in wild-type and *Chd7*$^{fl/fl}$ E11.5 embryos did not appear to be different in the qRT-PCR data shown in Figure 3-5. However, to further investigate this hypomorphic behaviour, further expression analysis was carried out on total RNA from E10.5 embryos, comparing *Chd7*$^{+/+}$, *Chd7*$^{fl/+}$ and *Chd7*$^{fl/fl}$ embryos. It was apparent from this data that some embryos carrying the *Chd7*^{fl} allele had some reduction in *Chd7* mRNA. This reduction was generally greater in *Chd7*$^{fl/fl}$ embryos compared to *Chd7*$^{fl/+}$, although there was also a noticeable level of biological variation seen between all embryos, even those with the same genotype and collected from the same litter (Karen McCue and Nelo Popal, personal communication). Whilst this hypomorphic behaviour must be kept in consideration, the affect is still relatively mild and infrequent, and the severe cardiac structural defects seen in *Chd7*$^{fl/fl}$*;Mesp1-Cre* embryos remain very distinctive for this genotype.

3.4.5 Relevance to CHARGE syndrome

In contrast with human CHARGE and constitutive heterozygous *Chd7*$^{+/-}$ mouse models, cardiac defects were not observed in *Chd7*$^{fl/+}$*;Mesp1-Cre* embryos above background levels. Haploinsufficiency in non-mesodermal tissues is known to contribute to the syndromic phenotype, for example, biallelic expression of *Chd7* in the PSE is required for great vessel development. Therefore, hemizygosity for CHD7 protein in multiple tissue types may be required for the disease phenotype to become manifest. This is consistent with the drastically

increased frequency of CAT in *Chd7*$^{Whi/fl}$*;Mesp1-Cre* hearts compared with *Chd7*$^{fl/fl}$*;Mesp1-Cre* hearts. Furthermore, *Chd7*$^{Whi/fl}$*;Mesp1-Cre* hearts were embryonic lethal approximately 2 days earlier than *Chd7*$^{fl/fl}$*;Mesp1-Cre* embryos, with none surviving to E15.5 (data not shown). The background of constitutive *Chd7* heterozygous mutation in non-mesodermal tissue is likely to be contributing to the more severe OFT defects and earlier cardiac failure.

The efficacy of Cre-driven recombination at the LoxP sites in the *Chd7*^{fl} allele is also an important consideration, as less than 100% recombination efficiency and selection for dizygous cells could result in a lack of haploinsufficiency in the mesodermal conditional mutants. A recent study has shown non-parallel recombination of different Cre reporter alleles in otherwise genetically identical cell types, with high variation in recombination efficacy (Liu et al., 2013). Differences can be attributed to the chromosomal location of LoxP sites (Vooijs et al., 2001) and to the distances between the LoxP sites (Collins et al., 2000; Koike et al., 2002), with sensitivity to recombination inversely correlated with this distance (Liu et al., 2013). The sequences around the LoxP sites can also affect Cre efficacy, as epigenetic mechanisms such as methylation of the promoter sequence may induce a heterochromatic state and therefore inhibit the Cre enzyme activity (Long and Rossi, 2009). Therefore, although *Chd7* mRNA levels were reduced in *Chd7*$^{fl/+}$*;Mesp1-Cre* and *Chd7*$^{fl/fl}$*;Mesp1-Cre* embryos, as shown by RT-PCR and ISH, this was not sufficient to produce the characteristic heart malformations seen with CHD7 haploinsufficiency in other mouse models. *Chd7* expression is also not ablated until the Cre recombinase is expressed, at around E6.5 (Saga et al., 1999), unlike in CHARGE patients or gene-trap and ENU-generated mouse models. This delay in *Chd7* ablation could allow very early CHD7 activity to reduce the severity of phenotype seen in heterozygous *Chd7*$^{fl/+}$*;Mesp1-Cre* embryos.

Despite the requirement for homozygous ablation of *Chd7* in the cardiogenic mesoderm, this conditional deletion does provide a useful model for studying the role of *Chd7* during cardiovascular development. The defects produced are similar to those seen in CHARGE patients, and importantly, the early lethality seen in homozygous *Chd7*$^{-/-}$ mutants is bypassed, allowing for detailed phenotyping of the cardiac defects.

Overall, this chapter has shown that CHD7 is present throughout the developing heart until E13.5, and has demonstrated a crucial role for this protein in the anterior mesoderm for cardiogenesis. Conditional ablation of *Chd7* expression in the early cardiogenic mesoderm resulted in major structural cardiac defects affecting both the venous and arterial poles of the heart, as well as disruption to cardiac innervation and vascularisation, leading to embryonic lethality. This requirement for *Chd7* in the cardiogenic mesoderm alters our perspective on the hypothesis that the cardiac malformations seen in CHARGE arise due to it being a neurocristopathy.

CHAPTER FOUR

CARDIOVASCULAR DEFECTS FOLLOWING CARDIOMYOCYTE-, SECOND HEART FIELD- AND ENDOTHELIAL-SPECIFIC ABLATION OF *CHD7*

The results in Chapter Three indicate that *Chd7* plays a vital role in the cardiogenic mesoderm. To delineate further the tissue-specific requirements of *Chd7* within this cell population, the *Chd7*^{fl} allele was also crossed with *Nkx2.5-Cre*, *Mef2c-Cre* and *Tie2-Cre* mice. These *Cre* lines are all expressed in distinct subsets of cells derived from *Mesp1*-expressing progenitors, and the resulting range of cardiovascular defects are presented.

This chapter also includes the results of an investigation into possible epistatic interactions between *Chd7* and *Brg1* during heart development. An essential allelic balance between *Brg1* and the haploinsufficiency genes *Tbx5* and *Nkx2.5* has previously been demonstrated (Takeuchi et al., 2011). *Brg1* has a similar temporal expression pattern to *Chd7* in the heart, and has well-established roles in a number of processes during heart development (Chang and Bruneau, 2012). Furthermore, CHD7 and Brg1 proteins have also been shown to interact in murine neural crest cells *in vivo* (Li et al., 2013) and in human neural crest-like cells *in vitro* (Bajpai et al., 2010). We therefore hypothesised that interaction between these proteins may also be important for heart development, so compound conditional heterozygotes for *Chd7* and *Brg1* driven by *Mesp1-Cre* were generated.

4.1 *Nkx2.5-Cre* driven ablation of *Chd7* expression

4.1.1 Nkx2.5-Cre expression in cardiomyocytes

The transcription factor Nkx2-5 is one of the earliest markers of cardiac-specific fate in vertebrates (Lints et al., 1993; Moses et al., 2001). *Nkx2.5* is a predicted homologue of the *Drosophila* gene *tinman*, which is required for specification of the heart and visceral muscles (Azpiazu and Frasch, 1993; Bodmer, 1993). Murine *Nkx2.5* is expressed from E7.5, when it is seen in the early cardiac crescent, and its expression continues throughout the myocardium of the heart tube as it undergoes looping (Moses et al., 2001). At E11.5, it is seen throughout the myocardium, but not in the endocardial cushions. It is also expressed in the pharyngeal ectoderm and endoderm (Lints et al., 1993; Moses et al., 2001). More recently, the endothelium of the pharyngeal arch arteries (PAAs) has also been shown to be derived from *Nkx2.5*$^{+}$ progenitors within the lateral plate mesoderm, which were previously thought to contribute solely to the heart (Paffett-Lugassy et al., 2013).

This section addresses the cardiac phenotype resulting from conditional *Chd7* ablation driven by a knock-in *Nkx2.5-Cre* allele, which has the Cre recombinase gene introduced into exon 2 of the *Nkx2.5* locus (Moses et al., 2001). This allowed for investigation into the role of *Chd7* specifically in the myocardium, without affecting expression in the endocardial cushions. It would also indicate whether disruption to CHD7 activity in the endothelium of the PAAs is contributing to the great vessel defects observed in *Chd7*$^{fl/fl}$*;Mesp*- embryos.

4.1.2 The Chd7$^{fl/fl}$*;Nkx2.5-Cre genotype is embryonic lethal*

Chd7$^{fl/fl}$ mice were mated with *Chd7*$^{fl/+}$*;Nkx2.5-Cre* mice in order to generate *Chd7*$^{fl/fl}$*;Nkx2.5-Cre* offspring. Embryos were collected at E15.5, or pups genotyped at postnatal day (P)10, in order to examine whether the *Chd7*$^{fl/fl}$*;Nkx2.5-Cre* genotype was observed in the expected Mendelian ratios. Table 4-1 shows that the expected number of *Chd7*$^{fl/fl}$*;Nkx2.5-Cre* embryos was seen at E15.5, and no necrotic embryos were recorded at this stage for any genotype. However, no *Chd7*$^{fl/fl}$*;Nkx2.5-Cre* pups survived to P10, indicating that this genotype is not viable. Unfortunately none of the litters were seen straight after birth, but it is likely the *Chd7*$^{fl/fl}$*;Nkx2.5-Cre* pups died neonatally and were cannibalised, as no trace of them was found.

Table 4-1: Survival of embryos from the *Chd7$^{fl/fl}$* x *Chd7$^{fl/+}$;Nkx2.5-Cre* cross

Developmental Stage:	Genotype:	Observed:	Expected:
E15.5	*Chd7$^{fl/+}$*	17	17
	Chd7$^{fl/fl}$	16	17
	Chd7$^{fl/+}$;Nkx2.5-Cre	19	17
	Chd7$^{fl/fl}$;Nkx2.5-Cre	**16**	**17**
P10	*Chd7$^{fl/+}$*	8	8
	Chd7$^{fl/fl}$	8	8
	Chd7$^{fl/+}$;Nkx2.5-Cre	18	8
	Chd7$^{fl/fl}$;Nkx2.5-Cre	**0****	**8**

*** p<0.01, based on Chi squared analysis*

4.1.3 *E15.5 Chd7$^{fl/fl}$;Nkx2.5-Cre embryos show no external phenotype or great vessel defects*

All of the embryos collected at E15.5 were examined upon dissection for external phenotypes such as oedema or haemorrhaging, which were seen with high frequency in the *Chd7$^{fl/fl}$;Mesp1-Cre* embryos. However, none of the *Chd7$^{fl/fl}$;Nkx2.5-Cre* embryos (n=16) exhibited any abnormal phenotype, and could not be distinguished from their littermates (Figure 4-1, A and B) . Similarly, the great vessels were formed normally in all these embryos, with no examples of interrupted aortic arch or right-sided arch (Figure 4-1, C and D), indicating that *Chd7* ablation in the *Nkx2.5*-expressing myocardial lineage is not sufficient to reproduce the great vessel defects seen in *Chd7$^{fl/fl}$;Mesp1-Cre* embryos. Given the normal configuration of the vessels at E15.5, the PAAs were not examined at E10.5 for this cross.

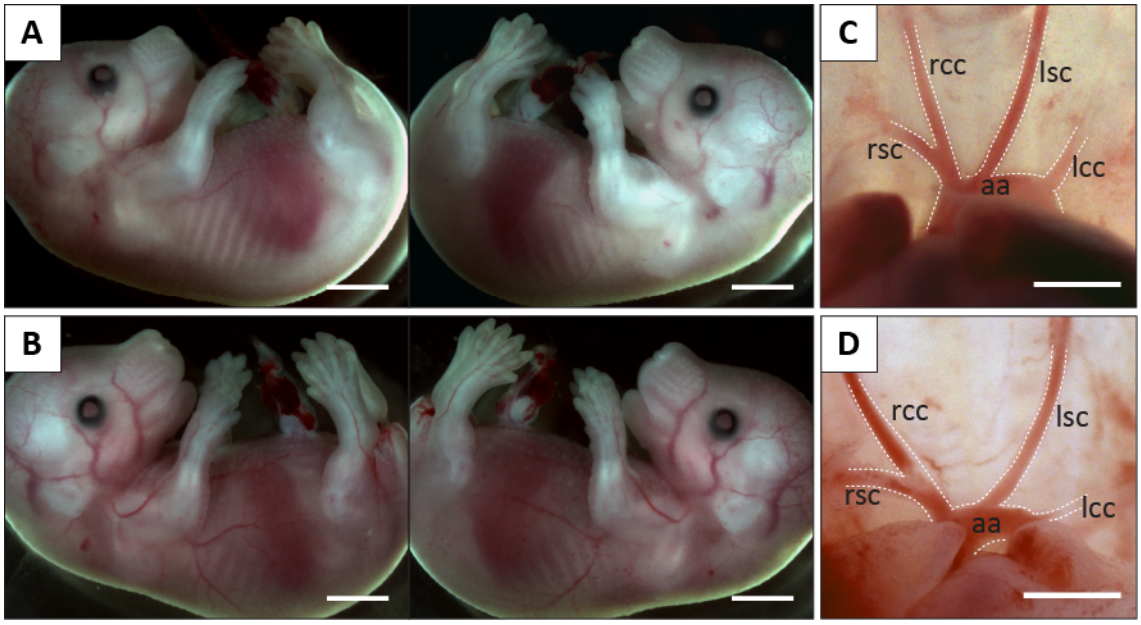

Figure 4-1: Normal external appearance and great vessel development in E15.5 *Chd7$^{fl/fl}$;Nkx2.5-Cre* embryos

(A, B) Two examples of embryos at E15.5 are shown, with no evidence of the external phenotypes of haemorrhaging or oedema seen in *Chd7$^{fl/fl}$;Mesp1-Cre* embryos.

(C, D) Great vessel development was also normal in all *Chd7$^{fl/fl}$;Nkx2.5-Cre* embryos examined (n=16).

Scale bars represent 2mm (A, B) or 0.5mm (C, D). rsc indicates right subclavian artery; rcc, right common carotid; lsc, left subclavian; lcc, left common carotid; aa, aortic arch.

4.1.4 Chd7$^{fl/fl}$;Nkx2.5-Cre hearts have atrioventricular septal defects

Whilst no external or great vessel defects were seen in the *Chd7$^{fl/fl}$;Nkx2.5-Cre* embryos, 90% of hearts examined (n=10) had either a VSD or an AVSD (see Table 4-5). Two examples of these are shown in Figure 4-2. The first heart had an AVSD with common atrioventricular (AV) valve and left ventricular dominance (Figure 4-2, A''). The right component of the common valve opened into a sequestrated inlet component of the right ventricle, with myocardium supporting the bridging part of the superior leaflet, and blood was able to enter the right ventricle beneath the superior bridging leaflets via the common AV junction. Minimal formation of the venous valves was also seen. Together, these defects indicate a failure of the vestibular spine to form, as seen in *Chd7$^{fl/fl}$;Mesp1-Cre* hearts. There was also poor compaction of the myocardium, which was seen in 60% of *Chd7$^{fl/fl}$;Nkx2.5-Cre* hearts.

The second example of an *Chd7$^{fl/fl}$;Nkx2.5-Cre* heart had separate AV junctions, but the tricuspid valve that connects the right atrium and ventricle was grossly hypoplastic and dysplastic (Figure 4-2, B''). The apical component of the right ventricle was fed through a VSD, which opened beneath the aortic root (Figure 4-2, B'). Fusion of the atrial septum to separate the AV junctions was seen, but there was minimal formation of the vestibular spine-derived buttress that supports the septum, and poorly-formed venous valves. Therefore, the septation defects seen in *Chd7$^{fl/fl}$;Nkx2.5-Cre* hearts appear to be caused by disruption to the vestibular spine. The most severe examples that showed common AV valves and left ventricular dominance were again analogous to the Holmes heart. Unlike the *Chd7$^{fl/fl}$;Mesp1-Cre* hearts, however, the arterial pole of all the *Chd7$^{fl/fl}$;Nkx2.5-Cre* hearts was formed normally, with no alignment or septation defects (Figure 4-2, A and B).

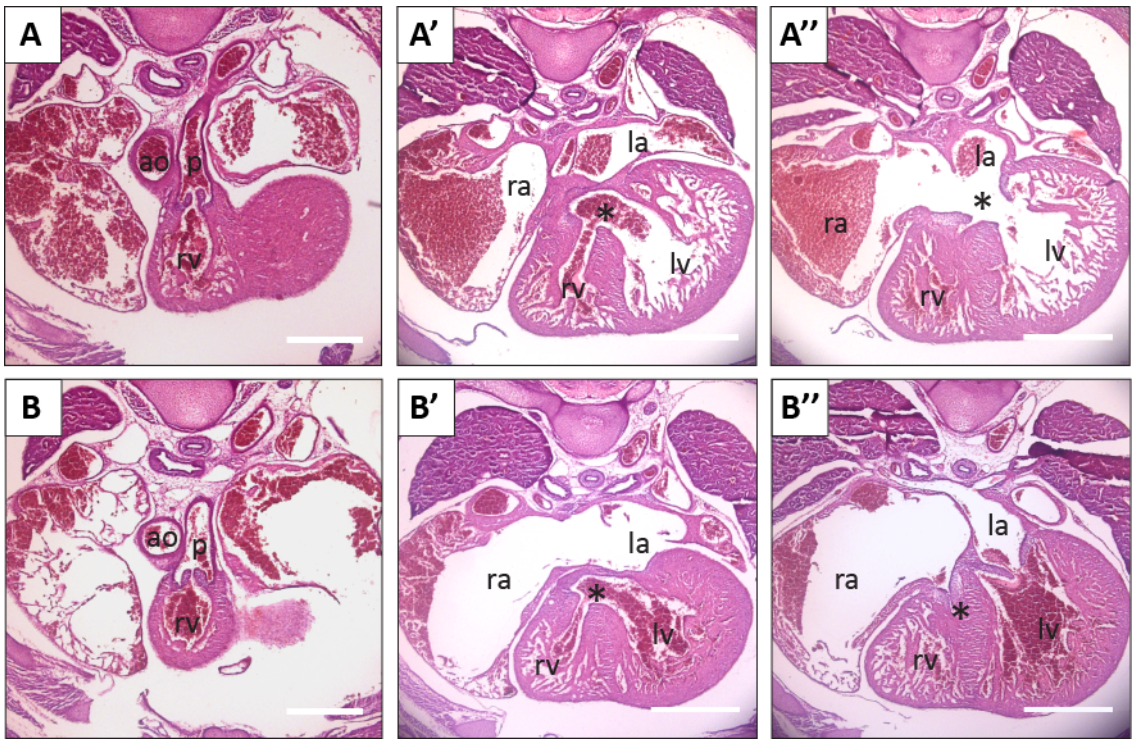

Figure 4-2: Atrioventricular septal defects in *Chd7$^{fl/fl}$;Nkx2.5-Cre* hearts

Transverse H&E sections through two examples of *Chd7$^{fl/fl}$;Nkx2.5-Cre* hearts. The OFT region of all *Chd7$^{fl/fl}$;Nkx2.5-Cre* hearts were normally septated and aligned (A and B), whilst inter-ventricular communication was highly penetrant (stars, A' and B'). Further towards the apex of the heart, example A shows an AVSD with common AV valves and dominant left ventricle, as seen in 30% of *Chd7$^{fl/fl}$;Nkx2.5-Cre* hearts (star, A''). Example B shows a grossly hypoplastic and dysplastic tricuspid valve opening into a sequestrated inlet component of the right ventricle (star, B'').

Scale bars represent 0.5mm. ao indicates aorta; p, pulmonary trunk; ra, right atrium; la, left atrium; rv, right ventricle; lv, left ventricle.

Heterozygous *Chd7$^{fl/+}$;Nkx2.5-Cre* embryos did not show any similar septation defects (n=3, data not shown). Similar to the *Chd7$^{fl/+}$;Mesp1-Cre* embryos, this indicates that either the Cre-driven ablation was not efficient enough to reduce *Chd7* levels sufficiently in the cardiomyocytes, or that heterozygosity in multiple tissue types is required for the CHD7 haploinsufficient cardiac phenotype. The lack of cardiac phenotype in these hearts also provided a control for possible effects of the *Nkx2.5-Cre* allele, as this is a knock-in construct so could be affecting the levels of *Nkx2.5* expression. Haploinsufficiency for *Nkx2.5* causes disruption to cardiovascular development (Jay et al., 2004; Jay et al., 2005), whilst complex dosage interactions between *Nkx2.5* and the chromatin remodeller *Brg1* also affect cardiogenesis (Takeuchi et al., 2011). Therefore, it was important to confirm that the phenotype seen in *Chd7$^{fl/fl}$;Nkx2.5-Cre* hearts is due to the specific ablation of *Chd7* in cardiomyocytes, rather than the *Nkx2.5-Cre* allele itself.

4.2 *Mef2c-Cre* driven ablation of *Chd7*

4.2.1 Mef2c-Cre expression in the second heart field

Mef2c is expressed around E7.5, shortly after *Nkx2.5* expression, in a subset of cardiac progenitors known as the anterior or second heart field (SHF) (Dodou et al., 2004; Edmondson et al., 1994). The SHF cells reside in the splanchic and pharyngeal mesoderm, lying medially to the cardiac crescent of the FHF. They are seen to be progressively added to the arterial and venous poles of the heart around the time of cardiac looping (Kelly et al., 2001; Mjaatvedt et al., 2001; Waldo et al., 2001). The primary heart tube of FHF-myocardial cells provides a scaffold onto which the SHF cells can migrate in order to extend the heart tube (Kodo and Yamagishi, 2011), where they contribute to the right ventricle, OFT and atrial myocardium (Buckingham et al., 2005; Meilhac et al., 2004).

Figure 4-3 highlights the heterogeneity of cells within the SHF, which is now considered to have a number of subdomains distinguished by their gene expression patterns and contribution to the different parts of the heart. *Mef2c* is expressed in the anterior region of the SHF. Two linked enhancer elements have been identified that drive *Mef2c* expression in the SHF, one of which is activated by Gata4 and Isl1 (Dodou et al., 2004), and the other by Fox1h and Nkx2-5 (von Both et al., 2004). *Mef2c* expression in the SHF has been traced using both transgenic mice expressing lacZ under control of a *Mef2c* transcriptional enhancer, and by a *Mef2c-Cre* allele crossed to Cre-dependent lacZ reporter mice. The first study confirmed the *Mef2c* enhancer begins to function at E7.5 in the pre-cardiac SHF mesoderm, and traces its derivatives to the OFT and right ventricle (Dodou et al., 2004). Further detailed study using the *Mef2c-Cre* allele traced both endothelial and myocardial components of the OFT, right ventricle and ventricular septum as derivatives of *Mef2c*-expressing cells, whilst excluding the atria, epicardium, coronary vessels and the majority of OFT smooth muscle (Verzi et al., 2005).

The *Mef2c-Cre* construct generated by Verzi and colleagues is used in this section to drive conditional *Chd7* ablation in the anterior SHF. This again should provide valuable information on how much of the *Chd7*$^{fl/fl}$*;Mesp1-Cre* phenotype can be attributed to *Chd7* activity in this smaller population of cardiac progenitors.

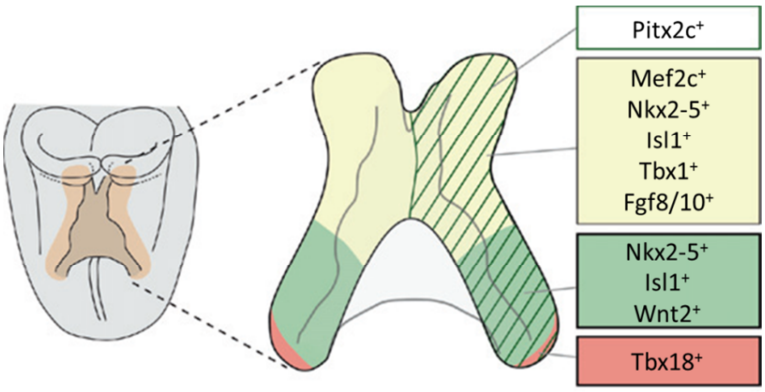

Figure 4-3: Subdomains within the second heart field

Schematic of the SHF in an E8.0 embryo. The SHF is characterised by expression of Nkx2-5 and Islet1. The anterior region (yellow) also expresses Mef2c, along with Tbx1, Fgf8 and Fgf10, whilst in the posterior region (green) Wnt2 is additionally expressed. The most posterior region is distinguished by expression of Tbx18 (red), which contains the progenitors for the sinus horn. Pitx2c is expressed throughout the left side of the SHF only (striped).

Adapted from Vincent (2010).

4.2.2 Chd7$^{fl/fl}$;Mef2c-Cre mice are viable

Chd7$^{fl/+}$;Mef2c-Cre mice were crossed to mice homozygous for the conditional *Chd7^{fl}* allele. As can be seen in Table 4-2, at E15.5 *Chd7$^{fl/fl}$;Mef2c-Cre* embryos were collected in their expected Mendelian ratios. A number of *Chd7$^{fl/fl}$;Mef2c-Cre* mice were also seen at P10, unlike the *Chd7$^{fl/fl}$;Mesp1-Cre* or *Chd7$^{fl/fl}$;Nkx2.5-Cre* genotypes. These mice were able to survive to adulthood and could be used for breeding. There were fewer than expected *Chd7$^{fl/fl}$;Mef2c-Cre* pups compared to the other genotypes in the litter, but Chi squared analysis did not indicate this was a significant reduction in numbers.

Table 4-2: Survival of embryos from the *Chd7$^{fl/fl}$* x *Chd7$^{fl/+}$;Mef2c-Cre* cross

Developmental Stage:	Genotype:	Observed:	Expected:
E15.5	*Chd7$^{fl/+}$*	12	20
	Chd7$^{fl/fl}$	19	20
	Chd7$^{fl/+}$;Mef2c-Cre	29	20
	Chd7$^{fl/fl}$;Mef2c-Cre	**20**	**20**
P10	*Chd7$^{fl/+}$*	13	9
	Chd7$^{fl/fl}$	8	9
	Chd7$^{fl/+}$;Mef2c-Cre	9	9
	Chd7$^{fl/fl}$;Mef2c-Cre	**5**	**9**

4.2.3 Great vessel defects are present after ablation of Chd7 in the second heart field

At E15.5, just one of the *Chd7$^{fl/fl}$;Mef2c-Cre* embryos collected (n=20) exhibited some external oedema (Figure 4-4, A), whilst the remainder showed no external difference to control littermates (Figure 4-4, B). Examination of the great arteries, however, showed that 25% of *Chd7$^{fl/fl}$;Mef2c-Cre* embryos had IAA-B – that is, disruption of the aortic arch between the left common carotid and left subclavian arteries (Figure 4-4, C and D). This was very similar to the penetrance of the same defect in *Chd7$^{fl/fl}$;Mesp1-Cre* embryos.

When the pharyngeal arch arteries (PAAs) were examined in E10.5 *Chd7$^{fl/fl}$;Mef2c-Cre* embryos, the left 4th PAA was absent in 20% of embryos (Figure 4-4, E and F). This was unexpected, as early PAA defects were not seen in *Chd7$^{fl/fl}$;Mesp1-Cre* embryos. It indicates that the IAA-B seen following second heart field-specific ablation of *Chd7* is due to early disruption to the formation of the PAAs, unlike in the *Chd7$^{fl/fl}$;Mesp1-Cre* embryos, which appeared to be caused by later remodelling defects.

Table 4-3: Frequency of PAA defects at E10.5 and IAA-B at E15.5 in embryos from the *Chd7$^{fl/fl}$* x *Chd7$^{fl/+}$;Mef2c-Cre* cross

Genotype:	n:	4th PAA defects:	n:	IAA-B:
Chd7$^{fl/+}$	5	0%	12	0%
Chd7$^{fl/fl}$	14	0%	19	0%
Chd7$^{fl/+}$;Mef2c-Cre	4	0%	29	0%
Chd7$^{fl/fl}$;Mef2c-Cre	**10**	**20%**	**20**	**25%**

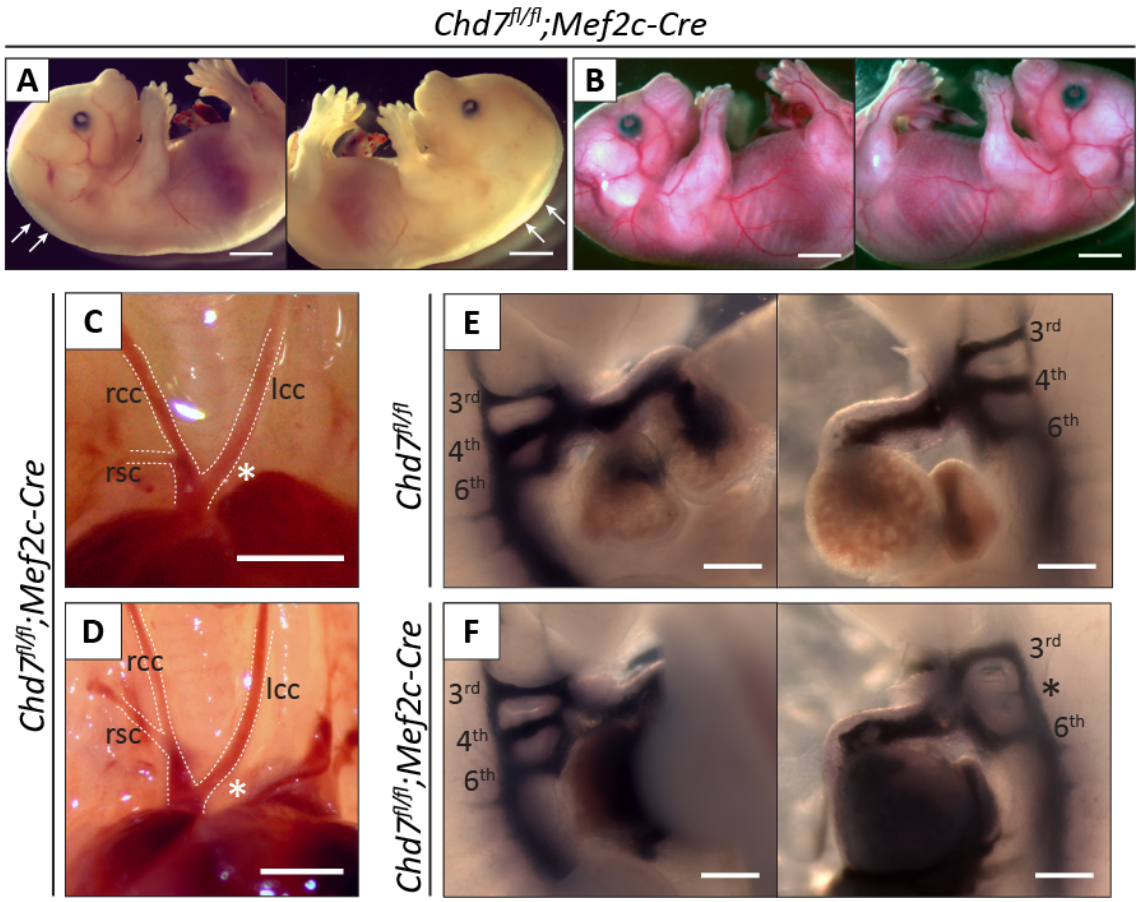

Figure 4-4: External appearance and great vessel development in *Chd7$^{fl/fl}$;Mef2c-Cre* embryos

(A and B) External examination of *Chd7$^{fl/fl}$;Mef2c-Cre* embryos at E15.5 found only one embryo with mild oedema (arrows, A), whilst most *Chd7$^{fl/fl}$;Mef2c-Cre* embryos were indistinguishable from their control littermates (B).

(C and D) Two examples of interrupted aortic arch type B (IAA-B) in *Chd7$^{fl/fl}$;Mef2c-Cre* embryos. The white stars highlight the interruption between the left common carotid and left subclavian arteries.

(E and F) Ink injection of the pharyngeal arch arteries (PAAs) at E10.5 shows normal bilateral formation of the 3rd, 4th and 6th PAAs in a control *Chd7$^{fl/fl}$* embryo (E), whilst in the *Chd7$^{fl/fl}$;Mef2c-Cre* embryo the left 4th PAA is absent (star, F).

Scale bars represent 2mm (A and B), 0.5mm (C and D) or 0.2mm (E and F). rsc indicates right subclavian; rcc, right common carotid; lcc, left common carotid.

4.2.4 Low frequency of cardiovascular septation defects in Chd7$^{fl/fl}$;Mef2c-Cre hearts

The most notable defects seen on H&E sections through *Chd7$^{fl/fl}$;Mef2c-Cre* hearts were vascular rings, which were present in 3 out of 8 hearts examined. This was a higher frequency than was noted in *Chd7$^{fl/fl}$;Mesp1-Cre* hearts, in which just 10% of hearts exhibited this defect (Table 4-5). Vascular rings can be formed by a number of different abnormal combinations of derivatives of the aortic arch system, which encircle the trachea and oesophagus (Hernanz-Schulman, 2005). Two examples of these are shown in Figure 4-5. The first had a vascular ring produced by a right aortic arch and a ductal arch, with the dorsal part of the left 4th PAA running retro-oesophageally to supply the left subclavian and common carotid arteries (Figure 4-5, A). The second example shows another variant of vascular ring more commonly seen in humans, where again the aorta was right-sided, but in this case gave rise to the left common carotid artery as its first branch. It then continued as a right aortic arch, giving rise to the right common carotid and subclavian arteries, before running retro-oesophageally to give rise to the left subclavian artery (Figure 4-5, B). The ring was completed by the left-sided arterial duct, which was widely patent. These slightly differing configurations were distinguished by studying serial sections through the great vessels (full series not shown). Reconstructions of the vascular rings are shown in Figure 4-10, and the developmental processes underlying these structural defects are addressed in the discussion section of this chapter.

Despite the occurrence of great artery defects, the proximal OFT region of all the *Chd7$^{fl/fl}$;Mef2c-Cre* hearts examined were normally septated and aligned. Fewer AV septation defects were also observed following SHF-specific *Chd7* ablation. Only one heart (12.5%) had an AVSD, which still showed separate left and right AV orifices within the common AV junction (Figure 4-5, A''). Therefore, the left ventricular dominance observed in *Chd7$^{fl/fl}$;Mesp1-Cre* and some *Chd7$^{fl/fl}$;Nkx2.5-Cre* hearts was not recapitulated. Furthermore, just one heart had a VSD, meaning that the majority of *Chd7$^{fl/fl}$;Mef2c-Cre* hearts were normally septated.

Non-compaction of the myocardium of the right ventricle could be seen in 37.5% of *Chd7$^{fl/fl}$;Mef2c-Cre* hearts. This is consistent with the specificity of the Cre line, as the left ventricular walls - which are not derived from *Mef2c*-expressing cells - formed normally (Figure 4-5, B' and B''). Overall, SHF-driven ablation of *Chd7* predominantly resulted in great vessel defects, along with some septation and myocardial compaction defects, which are consistent with the known contribution of this cell population to the developing heart. However, the cardiovascular defects were not severe enough to induce embryonic or post-natal lethality.

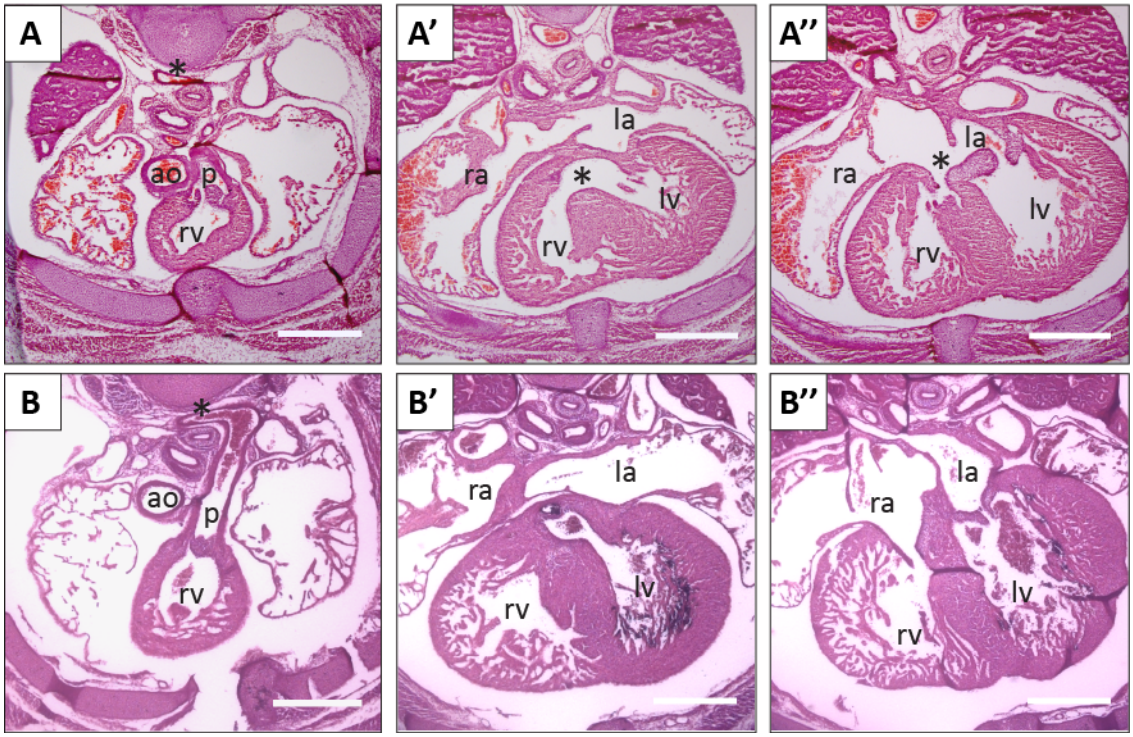

Figure 4-5: Vascular rings and septation defects in *Chd7$^{fl/fl}$;Mef2c-Cre* hearts

Transverse H&E sections through two examples of E15.5 *Chd7$^{fl/fl}$;Mef2c-Cre* hearts. The proximal OFT region was normal in all *Chd7$^{fl/fl}$;Mef2c-Cre* hearts, although vascular rings were observed in 30% of hearts (the retro-oesophageal components of the vascular rings are starred in A and B). Example A has inter-ventricular communication (star, A') and AVSD (star, A''), although there are separate right and left AV orifices. Other than the vascular ring, heart B was anatomically normal, although non-compaction of the right ventricle can be seen in B''.

Scale bars represent 0.5mm. ao indicates aorta; p, pulmonary trunk; ra, right atrium; la, left atrium; rv, right ventricle; lv, left ventricle.

4.3 Tie2-Cre driven deletion of *Chd7*

4.3.1 Tie2-Cre expression in endothelial cells

Tie2 promoter and enhancer regions drive expression in a pan-endothelial-specific manner in both embryonic and adult mice (Schlaeger et al., 1997). *Tie2* expression is seen in the embryo from E8.0 as the first endothelial cells arise, as well as in a subset of extraembryonic mesodermal cells from E7.5 (Kisanuki et al., 2001; Sato et al., 1993). *Tie2-lacZ* transgenic mice were first generated using the promoter and an enhancer region located in the first intron of the *Tie2* gene, that could drive universal endothelial-specific lacZ staining (Schlaeger et al., 1997), and the same promoter/enhancer region was then used to generate a transgenic *Tie2-Cre* line (Kisanuki et al., 2001).

Lineage tracing of *Tie2*-expressing cells and their derivatives using this *Tie2-Cre* allele showed that at E8.5 only a subset of the endocardium and endothelial cells in the aorta expressed *lacZ*. It was only from E9.5 that *lacZ* expression was seen in the majority of endocardial and endothelial cells, as well as in the first mesenchymal cells that appear in the cushions of the AV canal and proximal OFT (but not the distal OFT). This is consistent with cells in the cushions being derived from *Tie2*-expressing endocardial cells that have undergone endocardial-mesenchymal transitions to form the endocardial cushions (Kisanuki et al., 2001).

This *Tie2-Cre* allele was used to drive *Chd7* ablation, firstly to examine whether the oedema and haemorrhaging seen in $Chd7^{fl/fl}$*;Mesp1-Cre* embryos could be attributed to a cell autonomous role for CHD7 activity in vessel development and integrity. It would also elucidate whether loss of *Chd7* expression specifically in the endocardium and endocardial cushions would be sufficient to recapitulate the alignment and septation defects seen in $Chd7^{fl/fl}$*;Mesp1-Cre* embryos*,* as the endocardial cushions were malformed in these hearts.

4.3.2 Chd7$^{fl/fl}$;Tie2-Cre mice are viable

Endothelial-specific ablation of *Chd7* was not embryonic lethal, with the expected numbers of *Chd7$^{fl/fl}$;Tie2-Cre* embryos collected at E15.5 (Table 4-4). Similar to the SHF-specific ablation, these offspring were also viable, with pups genotyped at P10 and surviving to adulthood, although *Chd7$^{fl/fl}$;Tie2-Cre* mice were seen at slightly lower numbers than their expected Mendelian ratios. Again, Chi squared analysis indicated this was not a significant loss of the *Chd7$^{fl/fl}$;Tie2-Cre* genotype, so this may be a result of normal biological variability.

Table 4-4: Viability of offspring from the *Chd7$^{fl/fl}$* x *Chd7$^{fl/+}$;Tie2-Cre* cross

Developmental Stage:	Genotype:	Observed:	Expected:
E15.5	*Chd7$^{fl/+}$*	9	11.5
	Chd7$^{fl/fl}$	9	11.5
	Chd7$^{fl/+}$;Tie2-Cre	16	11.5
	Chd7$^{fl/fl}$;Tie2-Cre	**12**	**11.5**
P10	*Chd7$^{fl/+}$*	9	8
	Chd7$^{fl/fl}$	6	8
	Chd7$^{fl/+}$;Tie2-Cre	13	8
	Chd7$^{fl/fl}$;Tie2-Cre	**5**	**8**

4.3.3 *Chd7$^{fl/fl}$;Tie2-Cre embryos exhibit some cardiovascular septation defects*

Mild oedema was only seen in two *Chd7$^{fl/fl}$;Tie2-Cre* embryos (n=11), and no embryos exhibited signs of haemorrhaging (Figure 4-6, A and B). This indicates the main underlying cause of these phenotypes in *Chd7$^{fl/fl}$;Mesp1-Cre* embryos was poor cardiac function, rather than a requirement for CHD7 activity in endothelial cells during vessel formation. Furthermore, coronary vein formation was normal in *Chd7$^{fl/fl}$;Tie2-Cre* hearts, as previously discussed (see Figure 3-15), again indicating that vascular defects were not due to a cell autonomous effect of *Chd7* ablation in the endothelial lineage.

Whilst *Tie2-Cre* is expressed in the endothelial lining of the aorta and PAAs, IAA-B was observed in just one *Chd7$^{fl/fl}$;Tie2-Cre* embryo at E15.5 (n=8, Figure 4-6, C). 87.5% of the embryos had a normal configuration of the great vessels, suggesting that CHD7 activity in the *Tie2*-expressing lineage is not playing a significant role in great vessel formation (Figure 4-6, D).

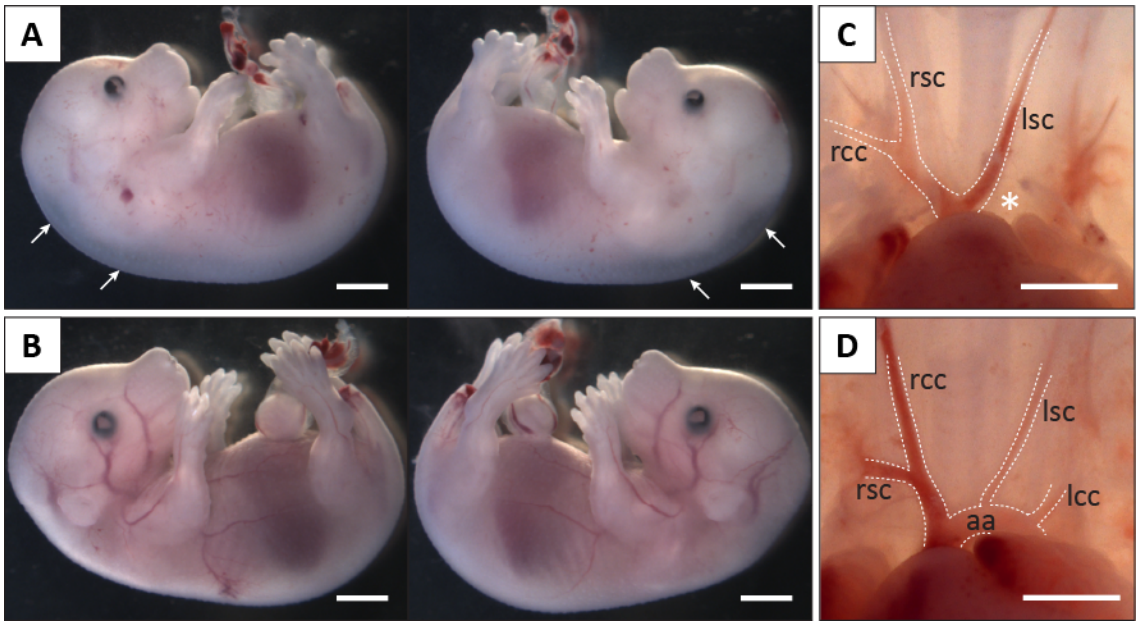

Figure 4-6: *Chd7$^{fl/fl}$;Tie2-Cre* embryos show a low penetrance of oedema and IAA-B

(A and B) A small number of *Chd7$^{fl/fl}$;Tie2-Cre* embryos showed some oedema (arrows, A), but none as severe as the *Chd7$^{fl/fl}$;Mesp1-Cre* phenotype. Most *Chd7$^{fl/fl}$;Tie2-Cre* embryos looked normal at E15.5 (B).

(C and D) The great vessels were examined at E15.5. Just one embryo (n=8) had an interrupted aortic arch type B (star, C), but again the majority had normally-developed great vessels (D).

Scale bars represent 2mm (A and B) or 0.5mm (C and D). rsc indicates right subclavian artery; rcc, right common carotid; lcc, left common carotid; lsc, left subclavian; aa, aortic arch.

Similar frequencies of septation defects were seen in *Chd7$^{fl/fl}$;Tie2-Cre* hearts compared to *Chd7$^{fl/fl}$;Mef2c-Cre* embryos (see Table 4-5). Again, the OFT tracts in all *Chd7$^{fl/fl}$;Tie2-Cre* hearts were normally aligned and septated (Figure 4-7, A and B), and the overall ventricular balance was normal. The first example of a *Chd7$^{fl/fl}$;Tie2-Cre* heart in Figure 4-7 shows the only AVSD seen for this cross, which had a ventricular connection seen below the aortic opening (A') and separate right and left AV junctions, although the mitral and tricuspid AV valves were slightly dysplastic (A''). Interestingly, the venous valves do not appear as under-developed as in previous AVSDs, possibly indicating that the primary cause of this malformation is disruption to the endocardial cushion formation rather than the vestibular spine. The second example shows one of two VSDs seen in *Chd7$^{fl/fl}$;Tie2-Cre* hearts, with the rest of the heart looking anatomically normal. Unlike *Chd7$^{fl/fl}$;Mef2c-Cre* embryos, no vascular rings were observed on the H&E sections through *Chd7$^{fl/fl}$;Tie2-Cre* hearts, again suggesting CHD7 activity in vessel endothelium is not crucial for great vessel formation.

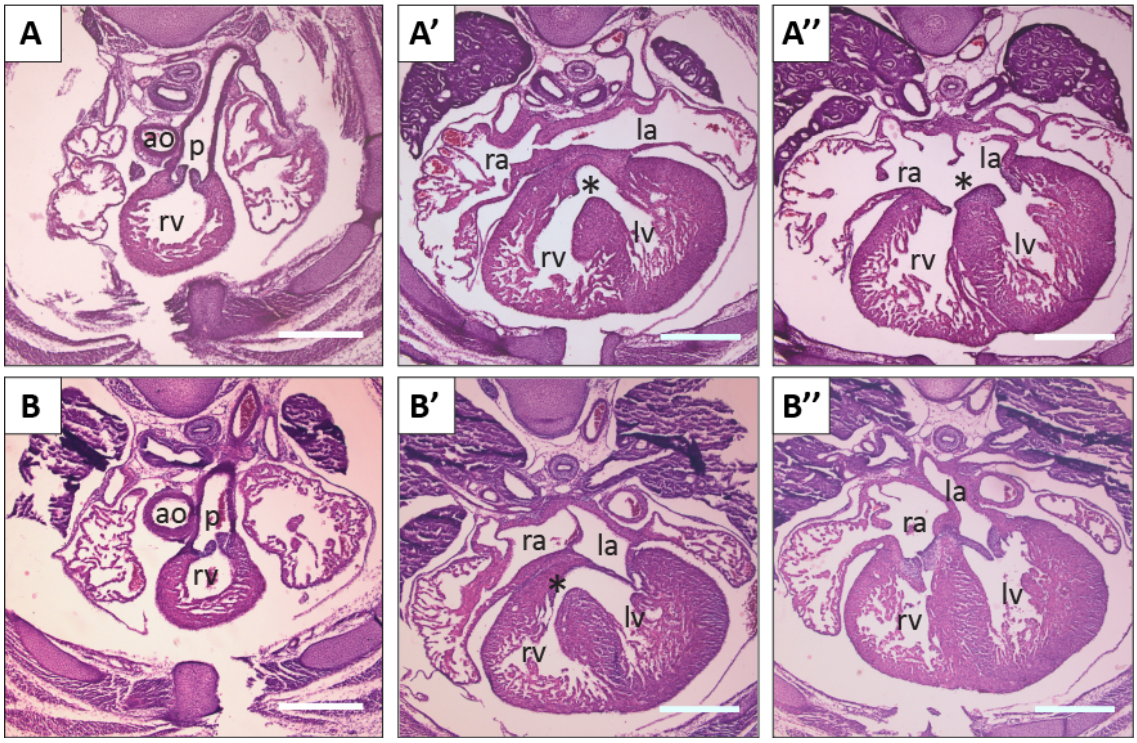

Figure 4-7: Septation defects in *Chd7$^{fl/fl}$;Tie2-Cre* embryos

Transverse H&E sections through two examples of E15.5 *Chd7$^{fl/fl}$;Tie2-Cre* hearts. Endothelial-ablation of *Chd7* also did not produce any OFT defects (A and B), although some septation defects were again present. One AVSD with separate right and left AV valves was observed (stars, A' and A''), whilst 25% of *Chd7$^{fl/fl}$;Tie2-Cre* hearts had a VSD (star in B') but the AV junction was normally septated (B'').

Scale bars represent 0.5mm. ao indicates aorta; p, pulmonary trunk; ra, right atrium; la, left atrium; rv, right ventricle; lv, left ventricle.

4.4 Overview of lineage-specific *Chd7* ablation

Table 4-5 summarises the major cardiovascular phenotypes seen in all of the conditional *Chd7* mutants described so far. External signs of oedema or haemorrhaging at E15.5 were highly penetrant in *Chd7$^{fl/fl}$;Mesp1-Cre* embryos, but absent or much lower penetrance and severity in *Chd7$^{fl/fl}$;Nkx2.5-Cre*, *Chd7$^{fl/fl}$;Mef2c-Cre* and *Chd7$^{fl/fl}$;Tie2-Cre* embryos. IAA-B was found in comparable proportions of *Chd7$^{fl/fl}$;Mesp1-Cre* and *Chd7$^{fl/fl}$;Mef2c-Cre* embryos, and in one *Chd7$^{fl/fl}$;Tie2-Cre* embryo. However, no great vessel defects were identified in *Chd7$^{fl/fl}$;Nkx2.5-Cre* embryos, which was surprising given its overlapping expression with *Mef2c*.

The most severe structural cardiac defects were seen in *Chd7$^{fl/fl}$;Mesp1-Cre* hearts: CAT, DORV and DILV were only seen with this genotype. A high penetrance of septation defects was also seen in *Chd7$^{fl/fl}$;Nkx2.5-Cre* embryos, along with myocardial non-compaction and venous valve defects. Some septation defects were also present in *Chd7$^{fl/fl}$;Mef2c-Cre* and *Chd7$^{fl/fl}$;Tie2-Cre* hearts. The lower penetrance and less severe cardiac phenotype of these two genotypes is reflected in the fact that only these mice were viable.

Table 4-5: Comparison of cardiovascular defects seen at E15.5 and viability following homozygous *Chd7* ablation using different *Cre* lines

	Mesp1-Cre:	***Nkx2.5-Cre:***	***Mef2c-Cre:***	***Tie2-Cre:***
Oedema	68%	0%	5%	18%
Haemorrhage	64%	0%	0%	0%
IAA-B	21%	0%	25%	12.5%
Vascular ring	10%	0%	37.5%	0%
AVSD	100%	30%	12.5%	12.5%
VSD only	N/A	60%	12.5%	25%
ASD only	N/A	0%	0%	12.5%
DILV	100%	0%	0%	0%
DORV	60%	0%	0%	0%
Myocardial non-compaction	80%	60%	37.5%	37.5%
Venous valve defects	90%	50%	0%	0%
Viable?	No - 0/9	No - 0/8	Yes - 5/9	Yes - 5/8

Genotypes were recorded as viable if live pups were found at P10, the numbers indicate the number of observed pups compared to the expected number based on Mendelian ratios.

IAA-B indicates interrupted aortic arch type-B; AVSD, atrioventricular septal defect; VSD, ventricular septal defect; ASD, atrial septal defect; DILV, double inlet left ventricle; DORV, double outlet right ventricle.

4.5 Investigating a possible epistatic interaction between *Chd7* and *Brg1* during heart development

4.5.1 The role of Brg1 in heart development

The SWI/SNF chromatin remodelling complex BRG1/BRM-associated factor (BAF) is composed of at least 11 subunits, with the incorporation of different subunit isoforms allowing it to perform distinct functions during development (Bruneau, 2010). The ATPase subunit of the complex is encoded by one of two homologous genes, *Brm* or *Brg1* (Chiba et al., 1994). Whilst *Brm* is dispensable during mammalian development, *Brg1*-null mutant embryos die in the peri-implantation stage before E6.5 (Bultman et al., 2000). Heterozygous *Brg1* mice show 50% lethality before 3 weeks of age, with congenital heart defects such as dilated hearts, muscular VSDs and patent foramen ovale, suggesting haploinsufficiency of Brg1 during heart development (Takeuchi et al., 2011). Tissue-specific ablation of *Brg1* expression in different lineages has identified multiple roles during heart development.

Brg1 is required in the endocardium for the dynamic regulation of the expression of the secreted matrix metalloproteinase *Adamts1* (Stankunas et al., 2008). *Brg1* represses *Adamts1* expression between E9.5 to E11.5, in order to allow establishment of the cardiac jelly and promote myocardial trabeculation, before de-repression between E12.5 to E14.5 for degradation of the cardiac jelly and termination of trabeculation. Endocardial ablation of *Brg1* driven by *Tie2-Cre* resulted in hypotrabeculation of the myocardium and absence of the cardiac jelly, leading to embryonic lethality around E10.5-E11.5 (Stankunas et al., 2008).

In the myocardium *Brg1* also plays an important role in the transcriptional regulation of cardiac growth and differentiation (Hang et al., 2010; Takeuchi et al., 2011). Myocardial ablation of *Brg1* results in embryonic lethality at E11.5, with thin myocardium and absence of the interventricular septum. *Brg1* promotes cardiomyocyte proliferation through maintenance of Bmp10 expression and suppression of the cyclin-dependent kinase inhibitor $p57_{kip2}$, which prevents cell cycle progression (Hang et al., 2010). Furthermore, *Brg1* ablation in the SHF using *Mef2c-Cre* resulted in a hypoplastic OFT and right ventricle, phenocopying the *Bmp10* downregulation, ectopic $p57_{kip2}$ expression and reduced proliferation, whilst the $Brg1^{+/+}$ left ventricle developed normally (Hang et al., 2010).

Additional roles for *Brg1* have been identified for development of the OFT and great vessels. Loss of *Brg1* expression in smooth muscle cells results in patent ductus arteriosus (PDA) in approximately one-third of mice, leading to cyanosis and dilated cardiac chambers by P3

(Zhang et al., 2011). Closure of the ductus arteriosus is mediated by contraction of smooth muscle cells during the neonatal period, in order to switch from fetal to adult circulation, and in cultured cells *Brg1* promotes expression of smooth muscle contractile genes. Furthermore, embryos lacking *Brg1* in NCCs have aberrant PAA development and shortened OFTs, and embryonic lethality occurs between E11.5-E12.5 (Li et al., 2013). This was attributed to a role for *Brg1* in maintaining a multipotent NCC reservoir through repressing the apoptotic factor *Ask1* and the cell cycle inhibitor $p21_{cip1}$. It is also located at the *PlexinA2* promoter in NCCs to directly promote the expression of this semaphorin receptor (Li et al., 2013), which has a role in guidance of cardiac NCCs within the OFT (Brown et al., 2001). Overall, it is clear *Brg1* is required in multiple lineages for a diverse range of processes during heart development.

4.5.2 Interaction between Brg1 and Chd7

CHD7 and the polybromo- and BRG1-associated factor (PBAF) complex have been reported to interact in human neural crest-like cells (hNCLCs), with multiple components of PBAF identified by mass spectrometry analysis of CHD7-associated proteins and confirmed by reciprocal co-immunoprecipitations (Bajpai et al., 2010). Similar phenotypes were seen following *Chd7* or *Brg1* morpholino (MO) injection into eight-cell-stage *Xenopus* embryos, including eye coloboma and craniofacial malformations. Downregulation of the NCC-specific transcription factors *Twist* and *Slug* genes was also seen following both MO knockdowns, with a dosage-dependent synergistic effect observed following co-injection of *Chd7* and *Brg1* MOs. Furthermore, comparison of genome-wide CHD7 and Brg1 occupancy datasets showed 81% of Brg1 regions were bound by CHD7, whilst 34% of CHD7 sites were co-occupied by Brg1. Chromatin immunoprecipitation (ChIP) analyses from hNCLCs showed both chromatin remodellers occupy a NCC-specific distal *SOX9* enhancer and a conserved upstream region of TWIST1, indicating that CHD7 and BRG1 together directly regulate expression of the critical NCC transcriptional circuitry (Bajpai et al., 2010).

Li and colleagues also demonstrated an interaction between *Brg1* and Chd7 whilst studying the role of *Brg1* in NCCs. ChIP analysis on dissected neural crest tissues from the rhombomere 6-8 region using an anti-CHD7 antibody showed enrichment for CHD7 within 9 conserved regions of the *PlexinA2* promoter, which was also enriched for Brg1 in a similar ChIP-qPCR experiment. This indicated Brg1 and CHD7 were in close proximity, and a physical interaction between them was confirmed by co-immunoprecipitation, again on dissected neural crest tissue. Furthermore, reporter assays on the *PlexinA2* promoter showed an approximately two-fold synergistic effect of co-expression of *Brg1* and *Chd7* on promoter activation (Li et al., 2013).

4.5.3 Lack of epistasis following Chd7 and Brg1 ablation in the cardiac mesoderm

Given the roles for *Brg1* in many cardiogenic lineages during development, including the *Mesp1*-derived myocardium and endocardium, and the formation of functional complexes containing both CHD7 and Brg1 at genomic regulatory elements, we postulated that similar interactions may be important in the cardiogenic mesoderm and its derivatives. *Chd7$^{fl/fl}$* mice were therefore crossed with *Brg1$^{fl/+}$;Mesp1-Cre* mice, in order to generate mesodermal conditional compound heterozygous *Chd7$^{fl/+}$;Brg1$^{fl/+}$;Mesp1-Cre* offspring. Table 4-6 shows the *Chd7$^{fl/+}$;Brg1$^{fl/+}$;Mesp1-Cre* genotype was seen in Mendelian ratios at E15.5 and P10, indicating it does not cause embryonic or postnatal lethality.

Table 4-6: Offspring generated from the *Chd7$^{fl/fl}$* x *Brg1$^{fl/+}$;Mesp1-Cre* cross

Developmental Stage:	Genotype:	Observed:	Expected:
E15.5	*Chd7$^{fl/+}$*	6	7
	Chd7$^{fl/+}$;Brg1$^{fl/+}$	8	7
	Chd7$^{fl/+}$;Mesp1-Cre	8	7
	Chd7$^{fl/+}$;Brg1$^{fl/+}$;Mesp1-Cre	**7**	**7**
P10	*Chd7$^{fl/+}$*	6	5
	Chd7$^{fl/+}$;Brg1$^{fl/+}$	7	5
	Chd7$^{fl/+}$;Mesp1-Cre	2	5
	Chd7$^{fl/+}$;Brg1$^{fl/+}$;Mesp1-Cre	**4**	**5**

Chd7$^{fl/+}$;Brg1$^{fl/+}$;Mesp1-Cre embryos (n=7) were examined at E15.5 for cardiovascular defects. None of the embryos showed any abnormal external phenotypes (data not shown), and the great vessels all formed the correct mature configuration (Figure 4-8, A-C). Furthermore, H&E sectioning to investigate the cardiac morphology of these embryos did not reveal any obvious structural defects: the hearts were all fully septated and the alignment appeared normal (Figure 4-8, D-G). Consistent with this lack of embryonic cardiovascular phenotype, the four *Chd7$^{fl/+}$;Brg1$^{fl/+}$;Mesp1-Cre* pups that were seen at P10 survived to adulthood and had no obvious defects. Together, this data suggests that a synergistic relationship does not occur between *Brg1* and *Chd7* in the cardiogenic mesoderm, and so this hypothesis was not pursued any further.

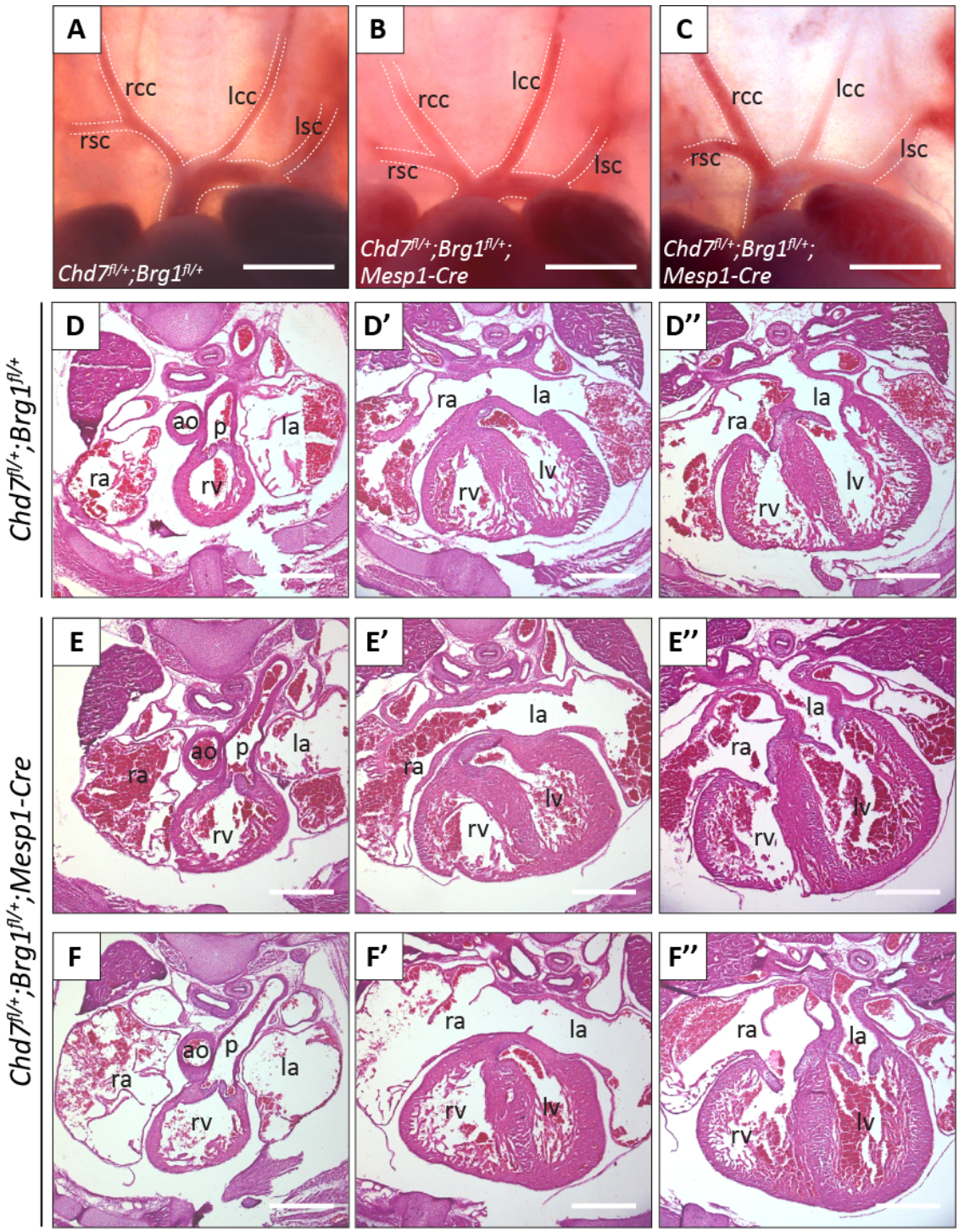

Figure 4-8: No cardiovascular phenotype in *Chd7$^{fl/+}$;Brg1$^{fl/+}$;Mesp1-Cre* embryos

(A-C) dissection of E15.5 control *Chd7$^{fl/+}$;Brg1$^{fl/+}$* embryos (A) and *Chd7$^{fl/+}$;Brg1$^{fl/+}$;Mesp1-Cre* embryos (B and C) revealed there were no great vessel defects in the compound heterozygotes.

(D-F) Transverse H&E sections also revealed no apparent cardiac defects in any *Chd7$^{fl/+}$;Brg1$^{fl/+}$* (D) or *Chd7$^{fl/+}$;Brg1$^{fl/+}$;Mesp1-Cre* hearts (E and F)

Scale bars represent 0.5mm. rsc indicates right subclavian; rcc, right common carotid; lcc, left common carotid; lsc, left subclavian; aa, aortic arch; ao, aorta; p, pulmonary trunk; ra, right atrium; la, left atrium; rv, right ventricle; lv, left ventricle.

4.6 Discussion

This chapter has presented cardiovascular phenotypes resulting from *Chd7* ablation driven by *Nkx2.5-Cre*, *Mef2c-Cre* and *Tie2-Cre*. These lineages are all derived from *Mesp1*-expressing progenitors, but none of the crosses completely reproduced the *Chd7$^{fl/fl}$;Mesp1-Cre* phenotype. Instead, each cross resulted in a milder subset of the cardiac defects observed after mesodermal ablation, indicating a continued requirement for *Chd7* in multiple lineages within the cardiogenic mesoderm. This spectrum of defects will be discussed further, to attempt to attribute different aspects of the *Chd7$^{fl/fl}$;Mesp1-Cre* phenotype to CHD7 activity in different cardiogenic lineages.

Compound conditional heterozygotes for *Chd7* and *Brg1* were also generated to investigate whether these genes interact epistatically in the cardiogenic mesoderm. However, no cardiac phenotype was identified, suggesting independent roles for these genes in the development of cardiac structures derived from the mesoderm.

4.6.1 Perinatal lethality and external phenotypes

Chd7 ablation driven by *Nkx2.5-Cre* was the only cross that was not viable, other than *Mesp1-Cre,* although at E15.5 *Chd7$^{fl/fl}$;Nkx2.5-Cre* embryos were collected in Mendelian ratios and no necrotic embryos were observed. It is therefore likely these pups were dying in the perinatal period. Given the high penetrance of cardiac septation defects seen in the *Chd7$^{fl/fl}$;Nkx2.5-Cre* embryos at E15.5, but otherwise morphologically normal appearance, cardiac failure is the most likely cause. The initiation of breathing at birth is associated with significant changes in the circulatory system, as it switches from fetal to respiratory circulation (Turgeon and Meloche, 2009). Correct septation is required to keep the oxygenated and deoxygenated blood of the systemic and pulmonary systems separated, and the heart must also be strong enough to produce increased blood flow to the lungs. Cardiac abnormalities such as VSDs and AVSDs, which alone may not be sufficient to cause embryonic lethality, are therefore associated with neonatal death through poor blood oxygenation, congenital cyanosis and respiratory distress (Turgeon and Meloche, 2009).

It is likely that some of the more severely affected *Chd7$^{fl/fl}$;Mef2c-Cre* and *Chd7$^{fl/fl}$;Tie2-Cre* pups also died perinatally and were cannibalised, as the numbers of each of these genotypes seen at P10 were slightly lower than their expected Mendelian numbers. However, the penetrance of the septation defects seen in these genotypes was much lower than for *Chd7$^{fl/fl}$;Nkx2.5-Cre*, which is reflected in a number of them surviving to full maturity.

Whilst severe oedema and haemorrhaging was seen in E15.5 *Chd7*$^{fl/fl}$*;Mesp1-Cre* embryos, only a small proportion of *Chd7*$^{fl/fl}$*;Mef2c-Cre* and *Chd7*$^{fl/fl}$*;Tie2-Cre* embryos exhibited much milder oedema. This indicates that the structural heart defects found in *Chd7*$^{fl/fl}$*;Nkx2.5-Cre, Chd7*$^{fl/fl}$*;Mef2c-Cre* and *Chd7*$^{fl/fl}$*;Tie2-Cre* embryos did not cause major loss of fetal cardiac function, and were not severe enough to recapitulate the major external phenotype of the *Chd7*$^{fl/fl}$*;Mesp1-Cre* embryos. Furthermore, the lack of external phenotype in *Chd7*$^{fl/fl}$*;Tie2-Cre* embryos indicates that loss of CHD7 activity in the endothelial cells of blood vessels is not sufficient to produce severe oedema or haemorrhaging. Instead, given the most severe structural heart malformations were seen in *Chd7*$^{fl/fl}$*;Mesp1-Cre* embryos (Table 4-5), it seems likely their external phenotypes were primarily due to cardiac failure rather than primary disruption to vessel integrity.

4.6.2 Great vessel defects following second heart field-specific ablation

The presence of great vessel defects predominantly in *Chd7*$^{fl/fl}$*;Mef2c-Cre* embryos indicates that the IAA-B and other aortic arch defects observed in *Chd7*$^{fl/fl}$*;Mesp1-Cre* embryos were predominantly due to a requirement for CHD7 activity in the anterior SHF. This was unsurprising given the well-established importance of signalling between the migratory cardiac neural crest and SHF derivatives during great vessel development (Dyer and Kirby, 2009). Consistent with this, a number of other transcriptional regulators expressed in the SHF, such as Tbx1 and Pitx2c, have roles in the development of the PAAs and great vessels (Liu et al., 2002; Vitelli et al., 2002). It is unclear why atresia of the 4th PAA was only seen in E10.5 *Chd7*$^{fl/fl}$*;Mef2c-Cre* embryos, but not in *Chd7*$^{fl/fl}$*;Mesp1-Cre* embryos. This observation suggests that different mechanisms underlie the IAA-B observed in both genotypes: in *Chd7*$^{fl/fl}$*;Mef2c-Cre* embryos early PAA formation appears to be disrupted, whilst in *Chd7*$^{fl/fl}$*;Mesp1-Cre* embryos later remodelling defects appear to be the more likely mechanism. It is possible, however, that examination of a greater number of E10.5 *Chd7*$^{fl/fl}$*;Mesp1-Cre* embryos might reveal that 4th PAA aplasia is found in *Chd7*$^{fl/fl}$*;Mesp1-Cre* embryos, but due to biological variability the sample size of 14 embryos was not high enough to detect this phenotype.

The much lower frequency of IAA-B in *Chd7*$^{fl/fl}$*;Tie2-Cre* embryos indicates that it is predominantly the SHF-derived myocardium at the arterial pole in which CHD7 is important, rather than in the endothelial lining of the vessels. It was, however, surprising not to see any great vessel defects in *Chd7*$^{fl/fl}$*;Nxk2.5-Cre* embryos, given that *Mef2c-Cre* should be expressed in a subset of *Nkx2.5*-expressing cells in the anterior SHF. The most likely explanation is that there was a difference in the levels of Cre-driven *Chd7* ablation in the SHF in *Chd7*$^{fl/fl}$*;Mef2c-Cre* and *Chd7*$^{fl/fl}$*;Nxk2.5-Cre* embryos, with a greater impact on CHD7 activity in *Chd7*$^{fl/fl}$*;Mef2c-Cre*

embryos. Consistent with this hypothesis, the levels of NKX2-5 protein have been shown to be five-fold lower in the anterior SHF than in the myocardium of the primary heart tube at E9.0 (Prall et al., 2007). Unlike *Nkx2.5*, *Mef2c* is also expressed in arch mesoderm, which is contiguous with the anterior SHF, which could have both autonomous and non-cell autonomous effects on great vessel development in *Chd7$^{fl/fl}$;Mef2c-Cre e*mbryos.

Investigating the relative levels of *Chd7* mRNA in the SHF in *Chd7$^{fl/fl}$;Mef2c-Cre* and *Chd7$^{fl/fl}$;Nxk2.5-Cre* embryos would have been beneficial to this study, although this presented a number of technical difficulties. ISH could have been used to compare *Chd7* mRNA expression in the two genotypes, as was done on *Chd7$^{fl/fl}$;Mesp1-Cre* hearts in chapter 3, as this would allow examination specifically of SHF-derived structures. However, this technique is qualitative, so a large difference in *Chd7* ablation in the SHF would be required to convincingly show a difference in the Cre-driven recombination levels. qRT-PCR would be much more sensitive for quantitatively identifying subtle changes in *Chd7* dosage, but it would be difficult to specifically isolate SHF-derived cells to carry out such analysis. Manual dissection of predominantly SHF-derived structures would be difficult and likely to contain additional cell types that would increase background in the analysis. Alternatively, the introduction of reporter lines that could be used for FACS of SHF cells would require complex breeding programmes and large numbers of litters in order to generate sufficient samples of the required genotype.

The higher frequency of vascular rings seen in *Chd7$^{fl/fl}$;Mef2c-Cre* embryos compared to *Chd7$^{fl/fl}$;Mesp1-Cre* embryos was also surprising, although again relatively low sample numbers and biological variability could explain this apparent inconsistency. Vascular rings make up less than 1% of cardiovascular congenital abnormalities in humans, and involve the encirclement of the trachea and oesophagus by an abnormal combination of derivatives of the PAA system (Park, 2008). They can be comprised of purely vascular components, or contain ligamentous components to complete the ring, and either way result in obstruction to the trachea and oesophagus with varying degrees of severity (Hernanz-Schulman, 2005). The best way to understand the development of vascular rings is to use the hypothetical model of a double aortic arch, introduced by Jesse E. Edwards to explain both normal and abnormal aortic arch artery remodelling (Edwards, 1948). This hypothetical model represents a relatively late stage of great vessel development, with the OFT fully septated and the descending aorta centrally positioned (Figure 4-9 and Figure 4-10). Symmetrical aortic arches are seen either side of the trachea and oesophagus to connect the ascending and descending aorta bilaterally, with a common carotid and subclavian artery arising from each arch. Right-sided and left-sided arterial ducts also connect the pulmonary arteries to the distal ends of each aortic arch, so in

total the model contains two vascular rings around the trachea and oesophagus, formed of the bilateral aortic arches and bilateral arterial ducts.

Figure 4-9 shows the normal development of the great vessels, in which the right-sided arterial duct and the right aortic arch (distal to the right subclavian artery) regress, whilst the left aortic arch and left-sided duct persist, to form the recognisable left aortic arch configuration. The remaining proximal region of the right aortic arch persists as the brachiocephalic artery, which connects the right subclavian and right common carotid arteries to the aortic arch (Figure 4-9, middle panel). Further regression of the left arterial duct postnatally separates the systemic and pulmonary circulations (Figure 4-9, right panel).

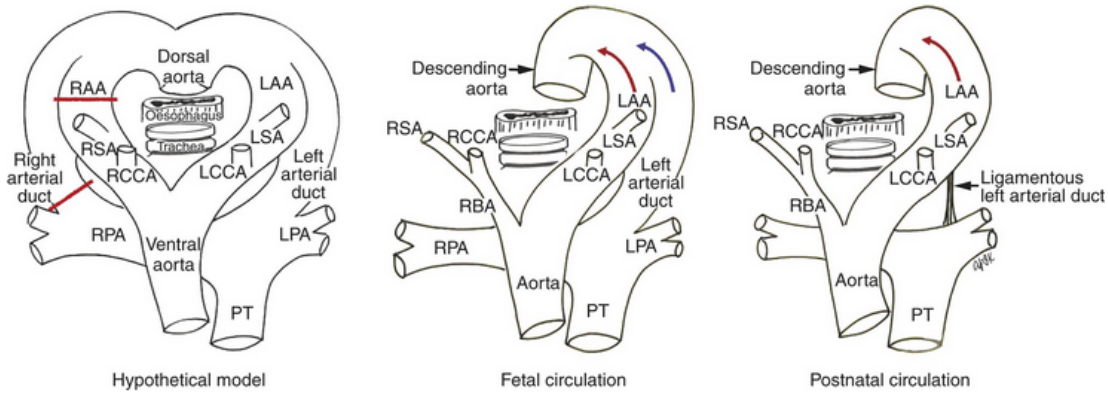

Figure 4-9: The Edwards Hypothetical Model of a Double Aortic Arch

The left panel shows the hypothetical double aortic arch formation proposed by Edwards in 1948, which was used to predict vascular rings that were only later reported. The red lines highlight the normal breakage points in the right aortic arch and right arterial duct, which lead to the normal left-sided aortic arch seen in fetal circulation (middle panel). Oxygenated (red arrow) and deoxygenated (blue arrow) blood, from the aorta and pulmonary trunk respectively, continue to mix in the descending aorta. Soon after birth, the left arterial duct (also known as ductus arteriosus) regresses, so the pulmonary trunk no longer connects to the dorsal aorta and the systemic and pulmonary circulations are separated (right panel).

RAA indicates right aortic arch; LAA, left aortic arch; RSA, right subclavian artey; RCCA, right common carotid artery; LSA, left subclavian artery; LCCA, left common carotid artery; RPA, right pulmonary artery; LPA, left pulmonary artery; PT, pulmonary trunk; RBA, right brachiocephalic artery.

Figure from Shi-Joon Yoo (2009)

In most cases, structural anomalies such as vascular rings can be explained by incorrect persistence or regression of one or more components of this hypothetical double arch. These alterations correspond to different 'breakage points' on the hypothetical arch (Figure 4-10, left panel). Two subtly different vascular rings were seen in *Chd7$^{fl/fl}$;Mef2c-Cre* hearts, both of which included a right-sided arch. The first (example A in Figure 4-5) is a variant rarely seen in humans, involving abnormal regression of the left aortic arch proximal to the origin of the left common carotid artery (i.e. breakage point 5, middle panel on Figure 4-10). The persisting arterial duct was left-sided, as is most commonly seen, completing the vascular ring.

The second variant, seen in two *Chd7$^{fl/fl}$;Mef2c-Cre* hearts (including example B in Figure 4-5), also had a right-sided arch, but with an aberrant left subclavian artery. In this case, regression of the left aortic arch occurs in between the origins of the left common carotid and left subclavian arteries (breakage point 3, right panel on Figure 4-10), so the distal remnant of the left aortic arch and aberrant left subclavian artery form the retro-oesophageal component of the ring. As with the first variant, the ring was again completed by persistence of the left arterial duct, connecting the left aortic arch remnant and left pulmonary artery. The vascular ring recorded in one *Chd7$^{fl/fl}$;Mesp1-Cre* embryo also had this configuration, consistent with its higher incidence in humans.

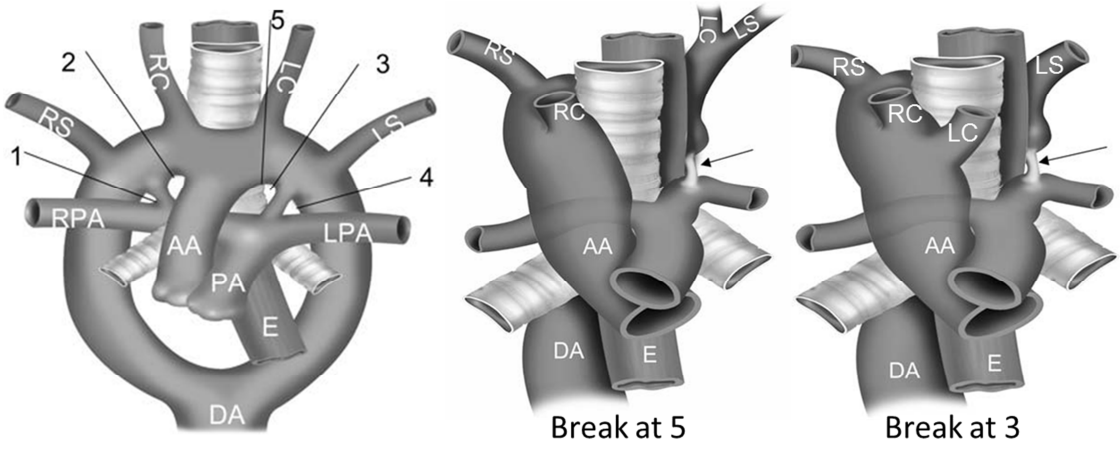

Figure 4-10: Vascular rings seen in *Chd7$^{fl/fl}$;Mef2c*-Cre embryos

The Edwards hypothetical arch is shown again to indicate the possible regression, or breakage, points around the double arch, labelled 1 to 5 (left panel). Breaks at 1 or 2 would lead to a left-sided arch, whilst breaks at 3, 4 or 5 would lead to a right-sided arch.

The middle panel corresponds to the vascular ring seen in Figure 4-5 (A), due to breakage of the double arch at position 5, and the right panel corresponds to the ring seen in Figure 4-5, (B) due to a breakage at position 3. Both rings are completed by a left ductal ligament (arrows).

AA indicates ascending aorta; DA, descending aorta; PA, pulmonary artery; RPA, right pulmonary artery; LPA, left pulmonary artery; RS, right subclavian; RC, right common carotid; LS, left subclavian; LC, left common carotid; E, oesophagus.

Adapted from Hernanz-Schulman (2005).

The Edwards Hypothetical Double Aortic Arch model therefore provides an excellent basis for understanding the mechanisms underlying the formation of vascular rings, including those seen in *Chd7$^{fl/fl}$;Mef2c-Cre* and *Chd7$^{fl/fl}$;Mesp1-Cre* embryos. Vascular rings have been reported in CHARGE syndrome patients (Blake and Prasad, 2006; Turkoz et al., 2012), so these tissue-specific *Chd7* mutant models indicate that loss of CHD7 activity in the anterior SHF makes an important contribution to the great vessel defects seen in CHARGE patients.

4.6.3 Spectrum of septation defects in Chd7$^{fl/fl}$;Nkx2.5-Cre, Chd7$^{fl/fl}$;Mef2c-Cre and Chd7$^{fl/fl}$;Tie2-Cre embryos

The *Chd7$^{fl/fl}$* allele was crossed with the *Nkx2.5-Cre*, *Mef2c-Cre* and *Tie2-Cre* lines in order to try to dissect further the tissue-specific roles of *Chd7* within the cardiogenic mesoderm. We postulated that if one of these crosses could completely recapitulate the severe cardiovascular defects seen in *Chd7$^{fl/fl}$;Mesp1-Cre* embryos, this would narrow down the requirement for *Chd7* to a smaller sub-population of cardiac progenitors. Alternatively, if different aspects of the *Chd7$^{fl/fl}$;Mesp1-Cre* phenotype were seen with each cross, this would be informative for assigning specific defects to CHD7 activity in different lineages.

As discussed in the previous section, the great vessel defects seen in *Chd7$^{fl/fl}$;Mesp1-Cre* embryos can be largely attributed to loss of CHD7 activity in the anterior, *Mef2c*-expressing SHF. The *Nkx2.5-Cre* cross, meanwhile, showed the most similar cardiac septation phenotype to the *Chd7$^{fl/fl}$;Mesp1-Cre* embryos: *Chd7$^{fl/fl}$;Nkx2.5-Cre* hearts had the highest penetrance of severe septation defects, and these defects were characteristic of malformation of the vestibular spine. This is consistent with the expression of *Nkx2.5* in the posterior region of the SHF (see Figure 4-3), which also expresses *Islet1* and *Wnt2* - but not *Mef2c* - from which the vestibular spine is derived (Vincent, 2010). Just one AVSD, with no left ventricular dominance, was seen in a *Chd7$^{fl/fl}$;Tie2-Cre* heart, indicating that loss of CHD7 activity in the vestibular spine has a greater effect on AV canal septation than loss in the endocardial cushions. However, ablation in both the vestibular spine and endocardial cushions is required to produce the most severe DILV defect seen only in *Chd7$^{fl/fl}$;Mesp1-Cre* hearts. This is consistent with the roles of both of these mesenchymal structures during development of the AV canal (see Figure 3-17), as well as the observed disruption to both vestibular spine and endocardial cushion formation in *Chd7$^{fl/fl}$;Mesp1-Cre* hearts.

The DORV phenotype seen frequently in *Chd7$^{fl/fl}$;Mesp1-Cre* hearts was also not observed following *Chd7* ablation driven by any of the Cre lines investigated in this chapter. *Nkx2.5-Cre* should be expressed in a large proportion of *Mesp1*-expressing cells throughout the FHF and

SHF, whilst *Tie2-Cre* is expressed in the endocardium that contributes to the OFT cushions. Therefore, loss of CHD7 activity in both myocardial and endocardial cells at the arterial pole contribute to the OFT defects seen in *Chd7$^{fl/fl}$;Mesp1-Cre* hearts. The earlier expression of *Mesp1-Cre* compared to *Nkx2.5-Cre*, *Mef2c-Cre* and *Tie2-Cre*, could also be contributing to the increased severity of the cardiovascular phenotype seen in *Chd7$^{fl/fl}$;Mesp1-Cre* embryos. *Mesp1-Cre* is activated at approximately E6.5, whereas the other Cre lines are activated from E7.5, so this longer exposure to Cre expression would be expected to increase the efficiency of recombination.

Overall, it appears that the activity of CHD7 within multiple lineages in the cardiogenic mesoderm is required for cardiovascular development, and the most severe combination of cardiovascular phenotypes is only seen when *Chd7* is ablated in all of these lineages.

4.6.4 Independent roles for Chd7 and Brg1 during heart development

A number of previous reports suggested that Brg1 could be a candidate interaction partner of CHD7 in the cardiogenic mesoderm. As discussed in sections 4.5.1 and 4.5.2, *Brg1* plays multiple roles in the transcriptional control of heart development in endocardial, myocardial, smooth muscle and neural crest cells (Hang et al., 2010; Li et al., 2013; Stankunas et al., 2008; Zhang et al., 2011). In particular, the thin ventricular walls seen following myocardial *Brg1* ablation are reminiscent of the thin walls and poor compaction observed in some of the conditional *Chd7* mutants described here. CHD7 and Brg1 are also known to synergistically interact in NCCs, where they have common binding sites and regulatory activity (Bajpai et al., 2010; Li et al., 2013). Furthermore, Brg1 has been shown to interact with two other chromatin-modifying enzymes, histone deacetylases (HDACs) and poly(ADP-ribose) polymerase (PARP), to activate the embryonic *β-MHC* whilst repressing the adult *α-MHC* within cardiomyocytes. Together, these three factors cooperate to regulate gene expression to maintain cardiomyocytes in an embryonic state during cardiac growth, differentiation, and pathologically during cardiac hypertrophy (Hang et al., 2010).

Synergistic interactions between *Brg1* and other cardiac-related genes have also previously been reported: disruption to the allelic balance between *Brg1* and the crucial cardiac transcription factors *Tbx5*, *Tbx20* and *Nkx2.5* has been shown to lead to severe cardiovascular malformations (Takeuchi et al., 2011). Generation of compound heterozygous mice for *Brg1* and each transcription factor resulted in significant increases in phenotype severity compared with heterozygosity for each gene alone. For example, loss of endocardial cushion formation was seen in *Brg1$^{+/-}$;Tbx5$^{+/-}$* and *Brg1$^{+/-}$;Nkx2.5$^{+/-}$* hearts, whilst thinned ventricular walls were

seen in *Brg1*$^{+/-}$*;Nkx2.5*$^{+/-}$ and *Brg1*$^{+/-}$*;Tbx20*$^{+/-}$ hearts. None of the compound heterozygous mice survived past E14.5, indicating complex dosage-sensitive interdependent relationships exist between transcription factors and BAF complexes during heart development (Takeuchi et al., 2011). *Chd7* also shows dosage dependence with the transcription factor *Tbx1* in the pharyngeal surface ectoderm during great vessel development.

Despite the combination of coincidental evidence indicating that synergistic interplay between *Chd7* and *Brg1* could be functioning in the cardiogenic mesoderm, the data collected here using compound conditional *Chd7* and *Brg1* heterozygotes suggests that this is not the case. Whilst it is possible that the recombination of the conditional floxed *Brg1* allele, driven by *Mesp1-Cre*, was insufficient to produce an epistatic effect with *Chd7,* this floxed allele has been reported in a number of published articles with deletion driven by other Cre lines, so this seems unlikely (Glaros et al., 2008; Griffin et al., 2008; Indra et al., 2005). Instead, it would appear these chromatin remodellers have independent roles in mesodermal derivatives, indicating that association between CHD7 and Brg1 is cell-type specific during development. It is well established that the subunit composition of the BAF and PBAF complexes, in which Brg1 is found, varies between different cell types and contexts. These variations influence the function of the complexes, presumably through interaction with different partner proteins (Ho et al., 2009; Lessard et al., 2007; Lickert et al., 2004; Wu et al., 2007). It is therefore likely that the composition of BAF and PBAF complexes in the cardiogenic mesoderm does not promote interaction with CHD7.

In summary, this chapter has demonstrated a requirement for *Chd7* activity in multiple lineages within the cardiogenic mesoderm, consistent with the widespread expression of *Chd7* throughout the developing heart until E13.5. *Chd7* ablation in the posterior *Mef2c-Cre*-expressing SHF was sufficient to reproduce the great vessel defects observed in *Chd7*$^{fl/fl}$*;Mesp1-Cre* embryos, indicating a crucial role for *Chd7* in this subpopulation during aortic arch development. CHD7 activity is also very important in the vestibular spine for septation of the AV canal, although it appears ablation in both endocardial and myocardial precursors is required to produce the characteristic combination of DORV and DILV seen in *Chd7*$^{fl/fl}$*;Mesp1-Cre* embryos. Consequently, external phenotypes and embryonic lethality associated with cardiac failure were most severe in *Chd7*$^{fl/fl}$*;Mesp1-Cre* embryos. The hypothesis that CHD7 and BRG1 act synergistically in the cardiogenic mesoderm has also been tested, although the data presented indicates that this is not an important interaction during cardiovascular development.

CHAPTER FIVE

ANALYSIS OF DOWNSTREAM TRANSCRIPTIONAL CHANGES FOLLOWING CHD7 ABLATION IN THE CARDIOGENIC MESODERM

Ablation of *Chd7* expression in the cardiogenic mesoderm results in severe cardiovascular malformations. To investigate the transcriptional changes underlying these defects, microarrays were performed to compare genome-wide expression in *Chd7*$^{fl/fl}$*;Mesp1-Cre* versus *Chd7*$^{+/+}$*;Mesp1-Cre* hearts. Gene expression was examined at both E11.5 and E13.5, as growth of the vestibular spine, development of the endocardial cushions, and septation occur at these stages. The resulting lists of dysregulated genes were analysed for over-represented gene ontology (GO) terms, to indicate processes or pathways that could be disrupted in *Chd7*$^{fl/fl}$*;Mesp1-Cre* hearts.

Following qRT-PCR validation of the microarray datasets, several genes of interest were further investigated, based on their known roles during heart development. *In situ* hybridisation provided spatial information on the specific regions of downregulation to components of Semaphorin and Slit-Robo signalling pathways in *Chd7*$^{fl/fl}$*;Mesp1-Cre* hearts. Functional studies were also performed on *Chd7*$^{fl/fl}$*;Mesp1-Cre* cardiomyocytes to investigate the effect of *Chd7* ablation on excitation-contraction coupling, as multiple genes associated with this process were dysregulated in the microarray datasets.

This chapter presents the results of these studies, which identify genes affected by CHD7 activity during cardiovascular development and correlate their aberrant expression to the phenotypes seen in *Chd7*$^{fl/fl}$*;Mesp1-Cre* hearts.

5.1 Microarray datasets at E11.5 and E13.5

5.1.1 RNA collection and quality control

To perform genome-wide analysis of gene expression, total RNA was extracted from dissected E11.5 and E13.5 hearts. At E11.5, the hearts have just undergone looping, the endocardial cushions are forming, the primary atrial septum and vestibular spine are developing, and robust levels of CHD7 protein are seen. By E13.5, the chambers should be well formed and septation almost complete, and whilst CHD7 levels are reduced, transcriptional changes identified at this stage should still reflect earlier activity due to the epigenetic nature of chromatin remodelling. Furthermore, at these stages there were no gross structural changes, and embryos were not yet becoming necrotic, which would confound interpretation of the microarray data. Therefore, examining transcriptional changes at these time points in *Chd7$^{fl/fl}$;Mesp1-Cre* hearts should be informative for understanding the cardiovascular defects in these hearts. Microarray analysis at two different stages would also give an indication of whether gene expression changes caused by loss of CHD7 activity are transient or maintained.

For each time point, gene expression was compared in four biological replicates of *Chd7$^{fl/fl}$;Mesp1-Cre* and *Chd7$^{+/+}$;Mesp1-Cre* hearts, bled out as much as possible following dissection, which would contain cells predominantly derived from the *Mesp1*-lineage. The quality of the RNA template for each sample was important to ensure successful hybridisation onto the microarrays, so each sample was analysed spectrophotometrically and on an Agilent 2100 Bioanalyzer. Tables 5-1 and 5-2 summarise this quality control for each of the samples.

The RNA Integrity Number (RIN) calculated by the Bioanalyzer apparatus gives an overall measure of the quality of the RNA (Schroeder et al., 2006). A value above 8 is considered suitable for microarray applications. All of the RNA samples used for the microarray experiments fulfilled this requirement, and many had a value over 9. This is reflected in the electrophoretic traces for each sample, which show distinct 18S and 28S rRNA peaks with very little background contamination (Figure 5-1).

The 260nm/280nm ratio generated by spectrophotometric analysis gives an indication of the presence of protein, phenol or other contaminants, which absorb strongly at or near 280nm. A ratio of close to 2.0 is desirable, as this indicates a high ratio of RNA (which absorbs at 260nm) compared to contaminants. The E11.5 RNA samples all had 260/280 values very close to 2.0, indicating very little contamination. The E13.5 samples were slightly more variable, but as the RIN values were very high it was decided they should still be suitable for microarray analysis.

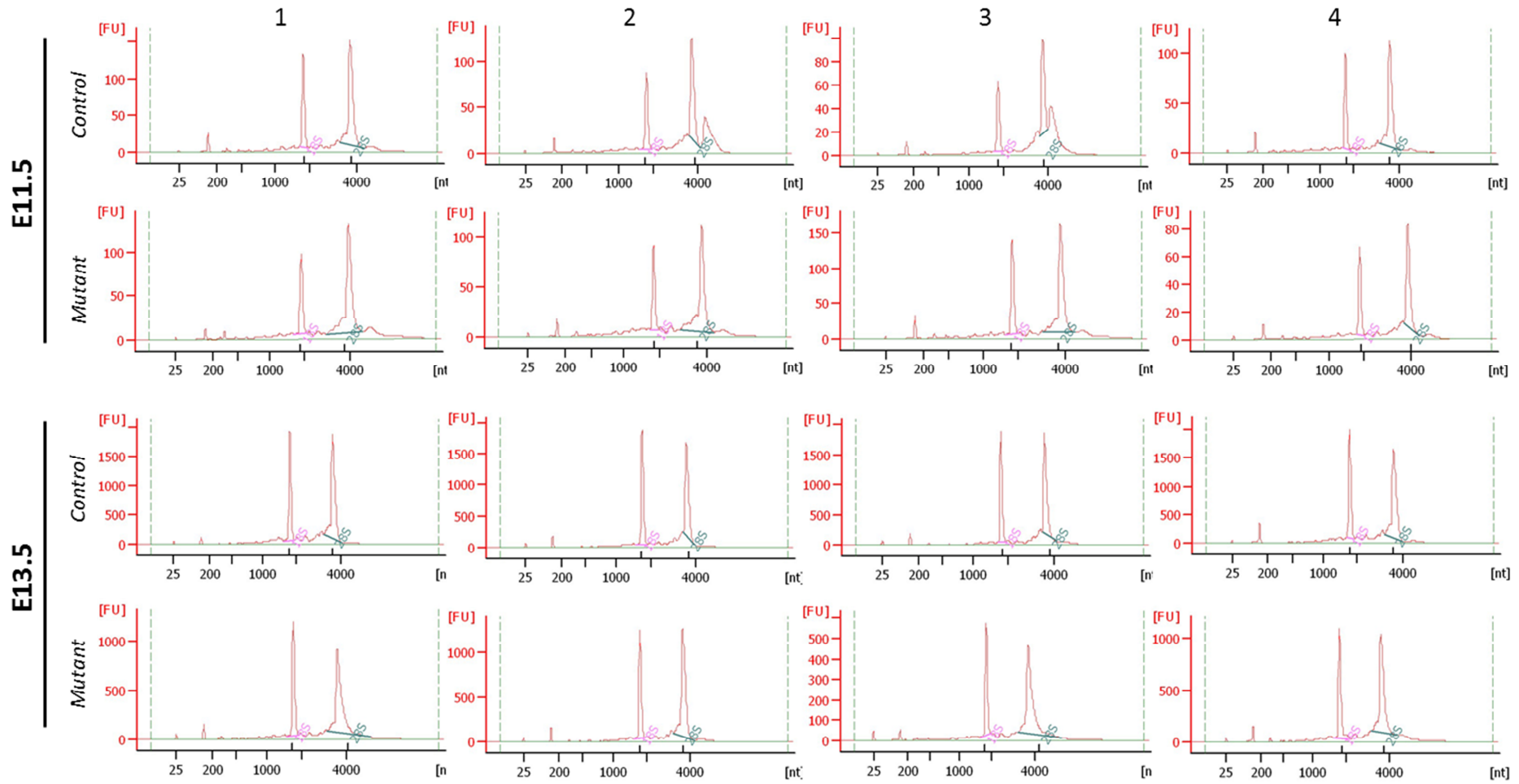

Figure 5-1: Bioanalyzer traces for *Chd7*$^{+/+}$*;Mesp1-Cre* and *Chd7*$^{fl/fl}$*;Mesp1-Cre* RNA samples collected for microarray analysis

E11.5 (top panel) and E13.5 (bottom panel) RNA samples were run on RNA 6000 Pico Chips using an Agilent 2100 Bioanalyzer, which showed two distinct peaks corresponding to 18S and 28S rRNA, with little background contamination. Control samples are *Chd7*$^{+/+}$*;Mesp1-Cre* and mutant samples are *Chd7*$^{fl/fl}$*;Mesp1-Cre.*

Table 5-1: Quality control parameters for E11.5 RNA samples

Genotype:	Sample:	RIN:	260/280:	Concentration (ng µl^{-1}):
Chd7$^{+/+}$;Mesp1-Cre	1	8.8	2.02	118.4
	2	8.5	2.06	83.2
	3	8.2	2.07	78.4
	4	8.9	1.98	83.4
Chd7$^{fl/fl}$;Mesp1-Cre	1	9.3	2.03	85.1
	2	8.4	1.93	79.5
	3	9.0	2.05	134.3
	4	8.5	1.94	48.8

RIN is the RNA Integrity Number, 260/280 indicates the A_{260}/A_{280} absorption ratio detected by spectrophotometric analysis

Table 5-2: Quality control parameters for E13.5 RNA samples

Genotype:	Sample:	RIN:	260/280:	Concentration (ng µl^{-1}):
Chd7$^{+/+}$;Mesp1-Cre	1	9.1	1.76	198.99
	2	9.4	1.84	159.94
	3	9.4	2.04	160.51
	4	9.0	2.13	210.95
Chd7$^{fl/fl}$;Mesp1-Cre	1	9.5	1.78	130.36
	2	9.5	2.06	128.55
	3	9.4	1.41	112.55
	4	9.2	1.96	137.63

RIN is the RNA Integrity Number, 260/280 indicates the A_{260}/A_{280} absorption ratio detected by spectrophotometric analysis

5.1.2 Differential gene expression in E11.5 and E13.5 hearts following mesodermal ablation of Chd7

The RNA samples collected at E11.5 and E13.5 were reverse-transcribed and processed for hybridisation onto GeneChip® Mouse Gene 1.0 ST Arrays by the UCL Genomics Service. The array data for both time points passed the quality control criteria using both Affymetrix Expression Console and Bioconductor. Data was normalised using an RMA normalisation algorithm (Gautier et al., 2004), and analysis of differential gene expression performed using the R package LIMMA (Smyth, 2004).

The fold change values for differences in gene expression between the *Chd7$^{fl/fl}$;Mesp1-Cre* and *Chd7$^{+/+}$;Mesp1-Cre* groups were calculated on a binary logarithmic scale ($\log_2$FC), and initial p-

values of significance calculated using a Bayes moderated t-test. Taking parameters of $\log_2$FC > 0.5 and $p < 0.05$, 338 genes were significantly downregulated and 281 genes upregulated at E11.5 in *Chd7$^{fl/fl}$;Mesp1-Cre* hearts compared to control *Chd7$^{+/+}$;Mesp1-Cre* hearts. Fewer genes showed altered expression at E13.5, with 142 genes downregulated and 125 genes upregulated, which likely reflects the lower levels of CHD7 protein at this later time point. Both time points showed more genes downregulated than upregulated. Of the genes with expression changes at E11.5, 15% (91 genes) were also altered at E13.5 (Figure 5-2, panel A). Lists of these up- and downregulated genes at each time point can be found in Appendix B.

Differentially-expressed genes were clustered based on their similarity of expression changes following *Chd7* ablation at both E11.5 and E13.5 (Figure 5-2, panel B). Gene ontology (GO) analysis performed on the three resultant clusters highlighted a number of processes relevant for cardiac development and the defects observed in *Chd7$^{fl/fl}$;Mesp1-Cre* embryos, including neuron projection development, regulation of neurotransmitter levels, blood vessel development, and regulation of muscle contraction (Figure 5-2, panel B). GO analysis will be discussed further in section 5.1.4.

Although a moderated t-test was used to calculate the p-values for the differences in expression for each gene, accounting to some extent for large sample sizes, with over 21,000 genes tested in the microarray there will still be a high occurrence of false positive results. This is because the p-values (i.e. the probability that any difference in expression level between the mutant and control is due to chance alone) are calculated independently for each individual gene. Therefore, whilst for an individual gene a p value of 0.05 means there is a probability of just 5% that a change from the control expression value is due to chance alone, as the sample size increases the probability of genes being called significant by random chance also increases. In order to reduce this false discovery rate, multiple testing correction was carried out to adjust the individual p-values. The Benjamini and Hochberg False Discovery Rate was used to calculate adjusted p-values, as this method provides a good balance between limiting false positive occurences whilst not being so stringent as to prevent discovery of statistically significant genes (Benjamini, 1995).

Following multiple testing correction, a list of four genes were found to be downregulated and one gene upregulated in both the E11.5 and E13.5 datasets (Table 5-3). The gene with the largest decrease in expression was *Chd7*, which validates the knockdown model. At E11.5 a further 20 genes were downregulated and 13 upregulated (Table 5-4), whilst at E13.5 one further gene was downregulated and two were upregulated (Table 5-5).

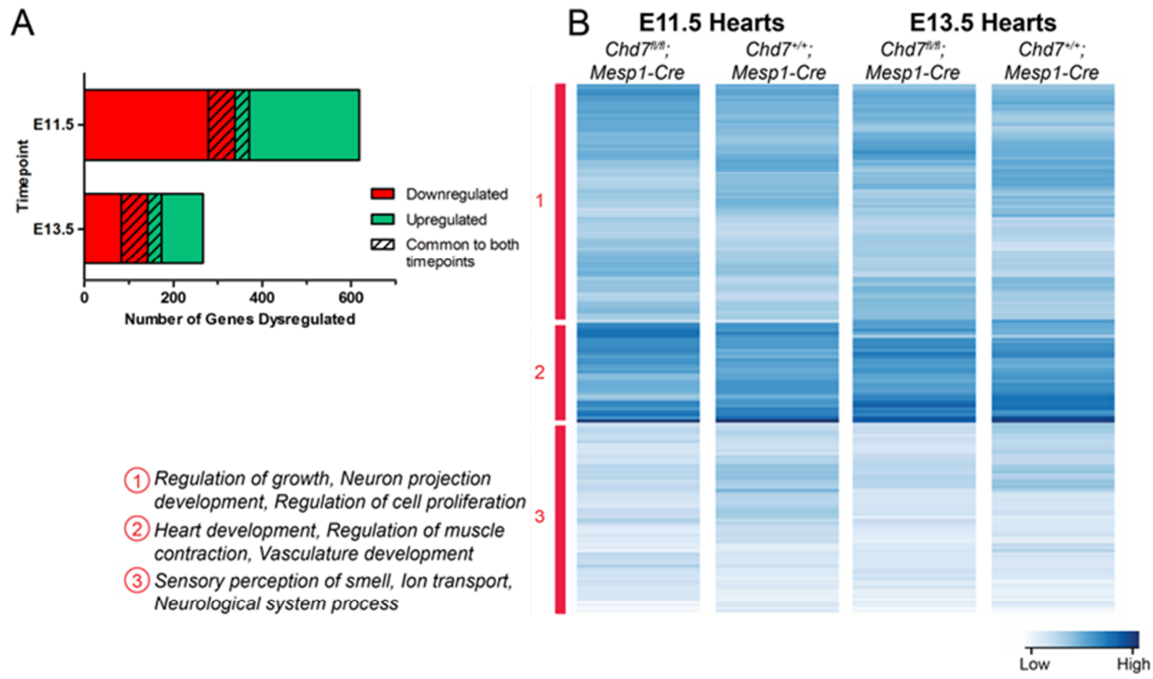

Figure 5-2: Microarray analysis of gene expression at E11.5 and E13.5

(A) Bar graph showing the number of genes up- and down-regulated at E11.5 compared to E13.5 ($p < 0.05$, $\log_2FC > 0.5$). Fewer genes showed altered expression at E13.5, with 91 genes common to both time points.

(B) Heat map to show clustering of dysregulated genes ($p < 0.05$, $\log_2FC > 0.5$) based on gene expression changes. Selected GO terms for the three main clusters are highlighted.

Table 5-3: Genes with significantly altered expression at both E11.5 and E13.5 following multiple testing correction

Ensembl ID:	Symbol:	Chrom:	Description:	E11.5 log_2FC	E11.5 adj.P.Value	E13.5 log_2FC	E13.5 adj.P.Value
ENSMUSG00000041235	Chd7	4	chromodomain helicase DNA binding protein 7	-1.6829	0.0002	-1.5832	0.0005
ENSMUSG00000069171	Nr2f1	13	nuclear receptor subfamily 2, group F, member 1	-1.2412	0.0277	-1.4321	0.0366
ENSMUSG00000023964	Calcr	6	calcitonin receptor	-1.0667	0.0548	-1.3886	0.0403
ENSMUSG00000028883	Sema3a	5	sema domain, immunoglobulin domain (Ig), short basic domain, secreted, (semaphorin) 3A	-0.8941	0.0026	-0.7043	0.0437
ENSMUSG00000025196	Cpn1	19	carboxypeptidase N, polypeptide 1	1.4687	0.0085	1.9251	0.0040

Chrom indicates the chromosome on which the gene is found, and FC indicates fold change (this also applies for Tables 5-4 and 5-5).

Table 5-4: Genes with altered expression at E11.5 following multiple testing correction

Ensembl ID:	Symbol:	Chrom:	Description:	Log_2FC:	adj.P.Val:
ENSMUSG00000026678	Rgs5	1	regulator of G-protein signaling 5	-2.0388	0.0340
ENSMUSG00000019906	Lin7a	10	lin-7 homolog A (C. elegans)	-1.5660	0.0179
ENSMUSG00000027463	Slc52a3	2	solute carrier protein family 52, member 3	-1.3710	0.0287
ENSMUSG00000035551	Igfbpl1	4	insulin-like growth factor binding protein-like 1	-1.3022	0.0009
ENSMUSG00000020061	Mybpc1	10	myosin binding protein C, slow-type	-1.2496	0.0303
ENSMUSG00000024868	Dkk1	19	dickkopf homolog 1 (Xenopus laevis)	-1.2324	0.0127
ENSMUSG00000018893	Mb	15	Myoglobin	-1.1955	0.0059
ENSMUSG00000025488	Cox8b	7	cytochrome c oxidase, subunit VIIIb	-1.1717	0.0323
ENSMUSG00000019787	Trdn	10	triadin	-1.0781	0.0024
ENSMUSG00000033737	Fndc3c1	X	fibronectin type III domain containing 3C1	-1.0672	0.0354
ENSMUSG00000059742	Kcnh7	2	potassium voltage-gated channel, subfamily H (eag-related), member 7	-0.9919	0.0354
ENSMUSG00000031558	Slit2	5	slit homolog 2 (Drosophila)	-0.9871	0.0003
ENSMUSG00000074491	Clec4g	8	C-type lectin domain family 4, member g	-0.9857	0.0203
ENSMUSG00000039579	Grin3a	4	glutamate receptor ionotropic, NMDA3A	-0.9720	0.0024
ENSMUSG00000052516	Robo2	16	roundabout homolog 2 (Drosophila)	-0.9067	0.0201
ENSMUSG00000044067	Gpr22	12	G protein-coupled receptor 22	-0.8386	0.0188
ENSMUSG00000073764	Gm12888	4	predicted gene 12888	-0.8374	0.0282
ENSMUSG00000007653	Gabrb2	11	gamma-aminobutyric acid (GABA) A receptor, subunit beta 2	-0.8214	0.0292
ENSMUSG00000023328	Ache	5	acetylcholinesterase	-0.7994	0.0497
ENSMUSG00000039057	Myo16	8	myosin XVI	-0.7174	0.0446
ENSMUSG00000029322	Plac8	5	placenta-specific 8	1.8213	0.0077
ENSMUSG00000027942	4933434E 20Rik	3	RIKEN cDNA 4933434E20 gene	1.7283	0.0396
ENSMUSG00000027861	Casq2	3	calsequestrin 2	1.6910	0.0003
ENSMUSG00000026471	Mr1	1	major histocompatibility complex, class I-related	1.2335	0.0028
ENSMUSG00000022103	Gfra2	14	glial cell line derived neurotrophic factor family receptor alpha 2	1.1899	0.0108
ENSMUSG00000058952	Cfi	3	complement component factor i	1.1009	0.0446
ENSMUSG00000053519	Kcnip1	11	Kv channel-interacting protein 1	0.9434	0.0287

ENSMUSG00000021219	Rgs6	12	regulator of G-protein signaling 6	0.8952	0.0061
ENSMUSG00000070933	Speer4d	5	spermatogenesis associated glutamate (E)-rich protein 4d	0.8779	0.0445
ENSMUSG00000070867	Trabd2b	4	predicted gene 12824	0.8600	0.0048
ENSMUSG00000020427	Igfbp3	11	insulin-like growth factor binding protein 3	0.8543	0.0453
ENSMUSG00000095241	Gm5478	15		0.7317	0.0322
ENSMUSG00000029309	Sparcl1	5	SPARC-like 1	0.7226	0.0433

Table 5-5: Genes with altered expression at E13.5 following multiple testing correction

Ensembl ID:	Symbol:	Chrom:	Description:	Log_2FC:	adj.P.Val:
ENSMUSG00000073007	Fam46d	X	family with sequence similarity 46, member D	-1.1136	0.0425
ENSMUSG00000069792	Wfdc17	11	predicted gene 11428	1.6059	0.0367
ENSMUSG00000055312	0610012H 03Rik	2	RIKEN cDNA 0610012H03 gene	0.9106	0.0273

5.1.3 qRT-PCR shows similar trends for dysregulated genes to the microarray datasets

To validate the microarray datasets, further samples of RNA were collected from dissected *Chd7$^{fl/fl}$;Mesp1-Cre* and *Chd7$^{+/+}$;Mesp1-Cre* hearts at both E11.5 and E13.5. Again, RNA from 4 hearts for each genotype at each developmental stage were compared. Following reverse transcription to cDNA, quantitative real-time PCR (qRT-PCR) analysis was performed on a panel of 39 genes that were found to be differentially regulated in the microarray datasets, using custom-designed TaqMan® Array Micro Fluidic Cards.

Figures 5-3 and 5-4 show the results of the qRT-PCR experiments alongside the log_2FC values calculated from the microarrays. Overall there was very good agreement between the trends seen in up- or downregulation of each gene: at both time points the qRT-PCR data showed the same direction of gene expression change for 33 out of the 39 genes tested. Using a null hypothesis that there is no correlation between the microarray and qRT-PCR data, Chi-squared analysis indicated that this is a highly significant level of correlation ($p < 0.0001$). At E11.5, major differences in the direction of gene change were seen for *Gabrb3*, *Myom2*, *Plxna2* and *Thbs2*, whilst smaller changes (log2FC < 0.5 in both datasets) were seen for *Hand1* and *Slit3*. At E13.5, large changes were seen with *Edn1*, *Myom2* and *Slit3*, and smaller changes with *Kitl*, *Nedd4l* and *Robo1*. However, overall the strong agreement between log_2FC values in both the microarray and qRT-PCR datasets increases our confidence in the microarray experiments.

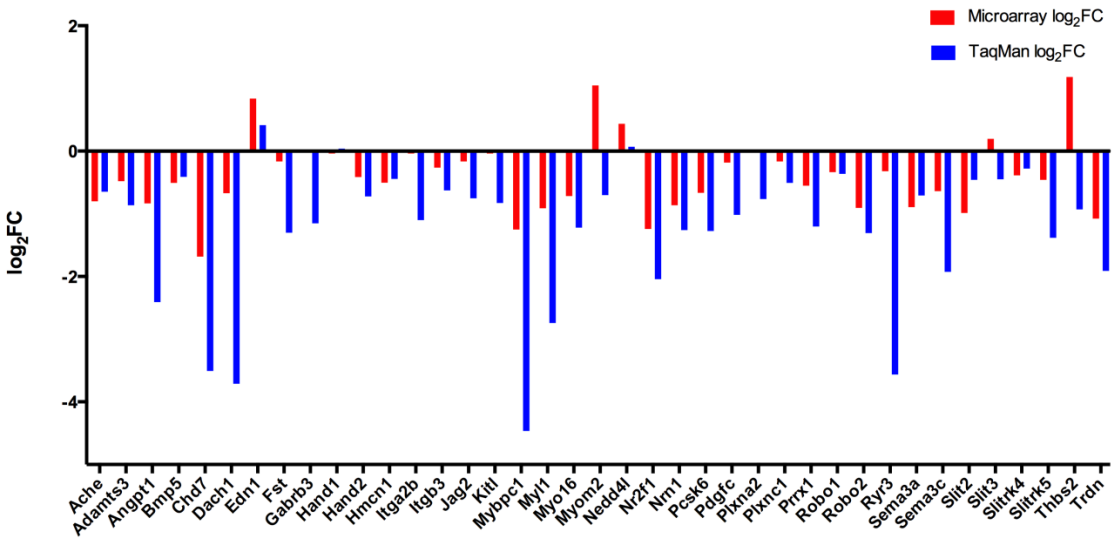

Figure 5-3: Comparison of gene expression changes identified at E11.5 through microarray and TaqMan qRT-PCR analysis

Calculated log_2FC values from the microarray (red) and qRT-PCR (blue) experiments are shown for the panel of genes tested, which are listed along the x-axis of the graph. Error bars are not included for log_2FC values, as comparison focussed on the direction of gene expression change.

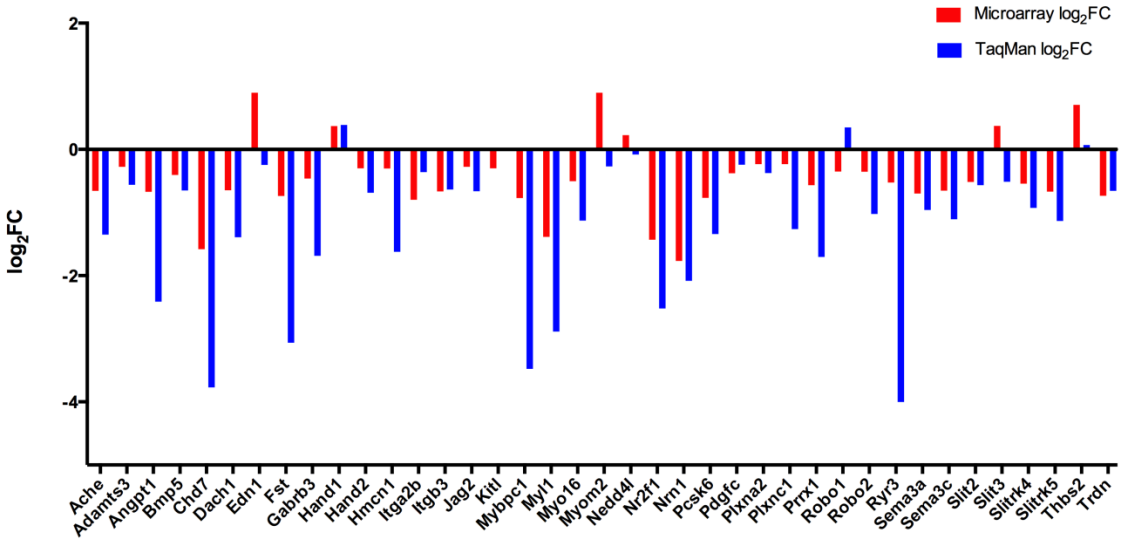

Figure 5-4: Comparison of gene expression changes identified at E13.5 through Microarray and TaqMan qRT-PCR analysis

Calculated log_2FC values from the microarray (red) and qRT-PCR (blue) experiments are shown for the panel of genes tested, which are listed along the x-axis of the graph. Error bars are not included for log_2FC values, as comparison focussed on the direction of gene expression change.

5.1.4 GO term analysis reflects processes associated with heart development

To further elucidate pathways that could be disrupted in *Chd7$^{fl/fl}$;Mesp1-Cre* hearts, the 100 significantly-altered genes with the highest fold changes from each up- or downregulated list from the microarrays was uploaded to the DAVID Bioinformatics resource for gene ontology (GO) analysis (Huang et al., 2009). The resulting GO term clusters are shown in Tables 5-6 to 5-9. This analysis highlighted a number of processes relevant for later cardiac development and the defects observed in the *Chd7$^{fl/fl}$;Mesp1-Cre* hearts. Interestingly, many of the GO clusters involved extracellular signalling pathways, rather than direct transcriptional regulators, such as cell surface receptor linked signal transduction, G-protein coupled receptor signalling pathways, Integrin-mediated signalling pathways, and negative regulation of signal transduction.

A number of clusters were directly relevant for the innervation and coronary vein defects seen in *Chd7$^{fl/fl}$;Mesp1-Cre* hearts, including neuron projection development, axonogenesis, regulation of neuron differentiation, regulation of neurotransmitter levels, and blood vessel development. These clusters contain many components of the Semaphorin and Slit-Robo signalling pathways, which beyond their guidance roles in neuronal and vascular development also have further key roles during heart development. In particular, Semaphorin 3C signalling is crucial for OFT development (Feiner et al., 2001), whilst deletion of various combinations of Slit and Robo genes leads to VSDs (Mathilda Mommersteeg, personal communication). Furthermore, *Sema3A*, *Slit2* and *Robo2* were significantly downregulated following multiple testing correction. These pathways were therefore selected for further investigation in *Chd7$^{fl/fl}$;Mesp1-Cre* embryos (see sections 5.2 and 5.3).

Regulation of muscle contraction also appeared in the GO analysis of the clusters from the heat map shown in Figure 5-2. Again, aberrant expression of *Trdn* and *Casq2*, which encode key components at the sarcoplasmic reticulum for excitation-contraction coupling of cardiomyocytes, was seen following multiple testing correction (Tables 5-3 and 5-4). A number of further genes involved in calcium handling were also disrupted, so this was also investigated further in *Chd7$^{fl/fl}$;Mesp1-Cre* cardiomyocytes (see section 5.4).

Whilst the microarray data and GO analysis suggested multiple relevant genes and pathways for a number of the defects seen in *Chd7$^{fl/fl}$;Mesp1-Cre* hearts, they did not reveal expression changes in genes with known roles in inflow tract development. This indicates that the transcriptional changes underlying the lack of vestibular spine and DILVs seen in these hearts occur earlier than E11.5. This will be addressed further in section 5.5.

Table 5-6: GO Term Clusters for Genes Downregulated at E11.5 in *Chd7$^{fl/fl}$;Mesp1-Cre* Hearts

GO Term:	Count:	P Value:	Genes:
Neuron projection development	5	0.022988	*ROBO2, SEMA3A, LMX1A, GRIN3A, SLIT2*
Leukocyte differentiation	4	0.033534	*CALCR, IKZF1, MITF, IL15*
Hemopoiesis	5	0.035969	*CALCR, IKZF1, MITF, IL15, MB*
Regulation of neurotransmitter levels	3	0.037981	*ACHE, SNAP25, LIN7A*
Eye development	4	0.043124	*ACHE, CHD7, IKZF1, MITF*
Axonogenesis	4	0.047306	*ROBO2, SEMA3A, LMX1A, SLIT2*
Forebrain development	4	0.050202	*DKK1, IKZF1, LMX1A, NR2F1*
Hemopoietic or lymphoid organ development	5	0.050824	*CALCR, IKZF1, MITF, IL15, MB*
Negative regulation of signal transduction	4	0.053183	*DKK1, RGS5, RGS18, FRZB*
Brain development	5	0.054712	*DKK1, IKZF1, ROBO2, LMX1A, NR2F1*
Neuron projection morphogenesis	4	0.057027	*ROBO2, SEMA3A, LMX1A, SLIT2*
Myeloid cell differentiation	3	0.082361	*CALCR, MITF, MB*
Cell morphogenesis involved in differentiation	4	0.088384	*ROBO2, SEMA3A, LMX1A, SLIT2*
Lymph node development	2	0.090398	*IKZF1, IL15*
Regulation of neuron differentiation	3	0.091322	*ROBO2, SEMA3A, LMX1A*

Table 5-7: GO Term Clusters for Genes Upregulated at E11.5 in *Chd7$^{fl/fl}$;Mesp1-Cre* Hearts

GO Term:	Count:	P Value:	Genes:
Tissue development	10	0.00112	*SHOX2, ALDH1A2, ADM, RXFP1, HOXA5, IRF6, EDN1, SPRR2B, MET, NR4A3*
G-protein coupled receptor signalling pathway	16	0.007626	*RXFP1, PTH2R, OLFR538, OLFR1413, EDN1, OLFR559, OLFR735, OLFR1309, SSTR4, OLFR1042, OLFR1156, RGS6, OLFR878, OLFR1126, OLFR429, OLFR366*
Cell surface receptor linked signal transduction	19	0.009247	*PTH2R, RXFP1, OLFR538, OLFR1413, MET, EDN1, OLFR559, OLFR735, OLFR1309, SSTR4, SFRP5, OLFR1042, OLFR1156, RGS6, OLFR1126, OLFR878, OLFR429, GFRA2, OLFR366*
Mesenchyme development	3	0.018267	*ALDH1A2, HOXA5, EDN1*
Epithelium development	5	0.025821	*ALDH1A2, ADM, HOXA5, IRF6, SPRR2B*
Sensory perception	12	0.026766	*OLFR1042, OLFR1156, TRPM8, OLFR538, OLFR1413, OLFR559, OLFR878, OLFR1126, OLFR429, OLFR1309, OLFR735, OLFR366*
Embryonic organ morphogenesis	4	0.029166	*SHOX2, HOXA5, EDN1, NR4A3*
Cartilage development	3	0.041613	*SHOX2, HOXA5, EDN1*
Gland development	4	0.048366	*RXFP1, HOXA5, IRF6, MET*
Myotube differentiation	2	0.048767	*MET, MYH9*
Mammary gland development	3	0.049603	*RXFP1, IRF6, MET*
Negative regulation of cell proliferation	4	0.065965	*IRF6, HMOX1, IGFBP3, ALOX8*
Tissue morphogenesis	4	0.076102	*ALDH1A2, ADM, HOXA5, NR4A3*
Lung development	3	0.077653	*ALDH1A2, RXFP1, HOXA5*
Blood vessel development	4	0.080648	*ALDH1A2, HMOX1, EDN1, MYH9*

Table 5-8: GO term Clusters for Genes Downregulated at E13.5 in *Chd7$^{fl/fl}$;Mesp1-Cre* Hearts

GO Term:	Count:	P Value:	Genes:
Blood coagulation	6	3.07E-05	*F2RL2, GP5, PLEK, P2RX1, TREML1, GP9*
Platelet activation	3	0.003065	*PLEK, P2RX1, TREML1*
Cell surface receptor linked signal transduction	23	0.006099	*CALCR, F2RL2, GABRG3, ADAMTS19, GABRA1, PLEK, GABRA4, FST, BEX1, MSTN, RGS18, ITGB3, GPRC6A, OLFR173, GPR22, FZD10, CHRM2, P2RY1, MTNR1B, CNTN1, ANGPT1, ITGA2B, CLEC1B*
Axonogenesis	5	0.010275	*SLITRK3, ETV1, SEMA3A, NRN1, SLITRK5*
Platelet degranulation	2	0.010403	*PLEK, P2RX1*
Cell morphogenesis in neuron differentiation	5	0.014903	*SLITRK3, ETV1, SEMA3A, NRN1, SLITRK5*
Regulation of receptor recycling	2	0.025809	*ACHE, GRIA2*
Regulation of hair follicle development	2	0.035948	*INHBA, FST*
Blood vessel development	5	0.038304	*CHD7, MEOX2, PRRX1, SEMA3C, ANGPT1*
Generation of neurons	7	0.044383	*SLITRK3, BEX1, ETV1, SEMA3A, NRN1, SLITRK5, NR2F1*
Integrin-mediated signalling pathway	3	0.059648	*ADAMTS19, ITGB3, ITGA2B*
Inorganic anion transport	3	0.069607	*GABRG3, GABRA1, GABRA4*
Blood vessel morphogenesis	4	0.084404	*MEOX2, PRRX1, SEMA3C, ANGPT1*
Branching in salivary gland morphogenesis	2	0.089884	*SEMA3C, SEMA3A*
Positive regulation of ion transport	2	0.099366	*P2RX1, P2RY1*
Blood coagulation	6	3.07E-05	*F2RL2, GP5, PLEK, P2RX1, TREML1, GP9*

Table 5-9: GO Term Clusters for Genes Upregulated at E13.5 in *Chd7$^{fl/fl}$;Mesp1-Cre* Hearts

GO Term:	Count:	P Value:	Genes:
Unsaturated fatty acid metabolic process	3	0.008325	*EPHX2, ALOX8, MGST2*

5.2 Semaphorin Signalling

5.2.1 Roles of Class 3 Semaphorins during heart development

The Semaphorin family of glycoproteins can be divided into eight classes based on structural similarities (Semaphorin Nomenclature Committee, 1999). All members share a highly conserved 500 amino acid Sema domain near the N-terminus, which determines their binding specificity and is essential for their signalling function (Gherardi et al., 2004). They were first identified as axon guidance factors, which induce the collapse of neuronal growth cones (Kolodkin et al., 1992; Luo et al., 1993). Many further roles for Semaphorin signalling have since been discovered, including in angiogenesis, axon attraction and repulsion, immune response, organogenesis, and tumour suppression and promotion (Roth et al., 2009; Staton, 2011; Takamatsu and Kumanogoh, 2012; Yazdani and Terman, 2006). The Class 3 Semaphorins are the only soluble secreted Semaphorin proteins, the other classes being either transmembranous or anchored to the membrane following glycophosphatidylinositol (GPI) post-translational modification. There are seven members of the Class 3 Semaphorins, of which both Semaphorin 3A and 3C are known to be important during cardiovascular development.

Semaphorin 3A is a potent neural chemorepellant for sensory and sympathetic neurons (Tanelian et al., 1997). Strong expression of *Sema3a* is seen in the cardiac ventricles at E12.0, which then decreases with an inverse relationship to the increase in sympathetic innervation as the heart develops (Ieda et al., 2007). Innervation patterning is disrupted in homozygous null *Sema3a*$^{-/-}$ mice leading to sinus bradycardia, so most *Sema3a*$^{-/-}$ mice die within the first postnatal week and only 20% survive until weaning (Taniguchi et al., 1997). Meanwhile, transgenic mice with cardiac-specific overexpression of *Sema3a,* driven by the α-myosin heavy chain promoter, also displayed reduced sympathetic innervation and susceptibility to ventricular tachycardia (Ieda et al., 2007). Therefore the correct levels of *Sema3a* expression during heart development are essential for cardiac innervation and control of heart rate.

Semaphorin 3C is required for OFT development and aortic arch patterning: homozygous ablation of *Sema3c* in mice results in a range of structural cardiac defects, including common arterial trunk (CAT), interrupted aortic arch (predominantly type B, but also type C), VSD and DORV (Feiner et al., 2001). *Sema3c* is expressed in the OFT and subpulmonary myocardium between E10.5 and E12.5, during the key period of OFT septation and remodelling, as well as in the condensed mesenchyme of the cardiac outflow tract, which is populated by NCCs (Brown et al., 2001). Overlapping expression of *Sema3C* and the Semaphorin receptor *PlexinA2*

is seen in cardiac NCCs, and in *Sema3C*$^{-/-}$ mutant embryos *PlexinA2* expressing cells are abnormally patterned: they do not reach as far distally within the OFT mesenchyme, and do not form the characteristic condensed clusters of mesenchyme (Brown et al., 2001). It is therefore proposed that Semaphorin 3C/PlexinA2 signalling affects the migration and positioning of NCCs in the OFT, contributing to the morphogenesis of the OFT and aortic arch (Brown et al., 2001; Feiner et al., 2001). Both *PlexinA2* expression in the cardiac neural crest and *Sema3C* expression in neural crest and OFT myocardium are directly regulated by the transcription factor GATA6, with mutations to GATA6 disrupting Semaphorin-Plexin signalling and leading to OFT malformations (Kodo et al., 2009; Lepore et al., 2006).

Two further Semaphorin receptors have key roles during cardiovascular development, PlexinD1 and Neuropilin-1. *PlexinD1* and *Npn-1* knock-out mutants show very similar OFT and aortic arch defects to *Sema3C* mutant mice (Gitler et al., 2004; Gu et al., 2003), and a combination of genetic and biochemical studies suggest that Semaphorin signalling to PlexinD1-Neuropilin complexes in endothelial cells, in concert with Vegf/KDR/Neuropilin-1 paracrine signalling, is required for OFT septation and great vessel remodelling (Figure 5-5).

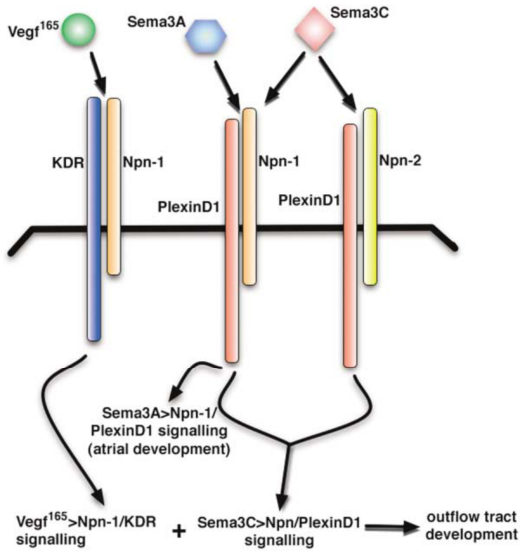

Figure 5-5: Model for integrated Semaphorin and VEGF signalling during cardiovascular development

Neuropilin receptors (Npn-1 and Npn-2) form heterodimers with either PlexinD1 or the VEGF receptor KDR in endothelial cells. OFT development requires signalling through these neuropilin-containing complexes, mediated by both Vegf165/KDR and Sema3C/PlexinD1. Sema3A signalling via a Npn-1-PlexinD1 receptor complex is also required for atrial development.

Figure from Gitler et al. (2004)

5.2.2 *Sema3A and Sema3C are downregulated in Chd7$^{fl/fl}$;Mesp1-Cre hearts*

Table 5-10 shows the microarray results for *Sema3A* and *Sema3C*, showing significant downregulation of both genes in *Chd7$^{fl/fl}$;Mesp1-Cre* hearts at E11.5 and E13.5. *Sema3E* was also slightly upregulated at E13.5. qRT-PCR analysis confirmed reduction of expression of *Sema3C* and *Sema3A* at both time points, and although calculation of p-values using the two-tailed Student's t-Test did not find significance for *Sema3A* at E11.5, the trend of downregulation is still seen (Figure 5-6). The slight increase in Sema3E expression at E13.5 was not seen in qRT-PCR dataset, and no change in expression was seen for the closely related *Sema3D* gene either. Therefore, CHD7 activity appears to be specifically affecting the Semaphorin 3A and 3C members of the Class 3 Semaphorin family, and is required for their correct expression during heart development, although whether this regulation is direct or indirect remains unclear.

Table 5-10: Microarray results for Semaphorin pathway genes

Symbol:	Gene name:	E11.5 log_2FC:	E11.5 P Value:	E13.5 log_2FC:	E13.5 P Value:
Sema3A	semaphorin 3A	-0.89409	9.87E-07	-0.70435	1.63E-05
Sema3C	semaphorin 3C	-0.63997	0.001107	-0.65304	0.000936
Sema3E	semaphorin 3E	NS	NS	0.554481	0.030159

NS indicates not significant

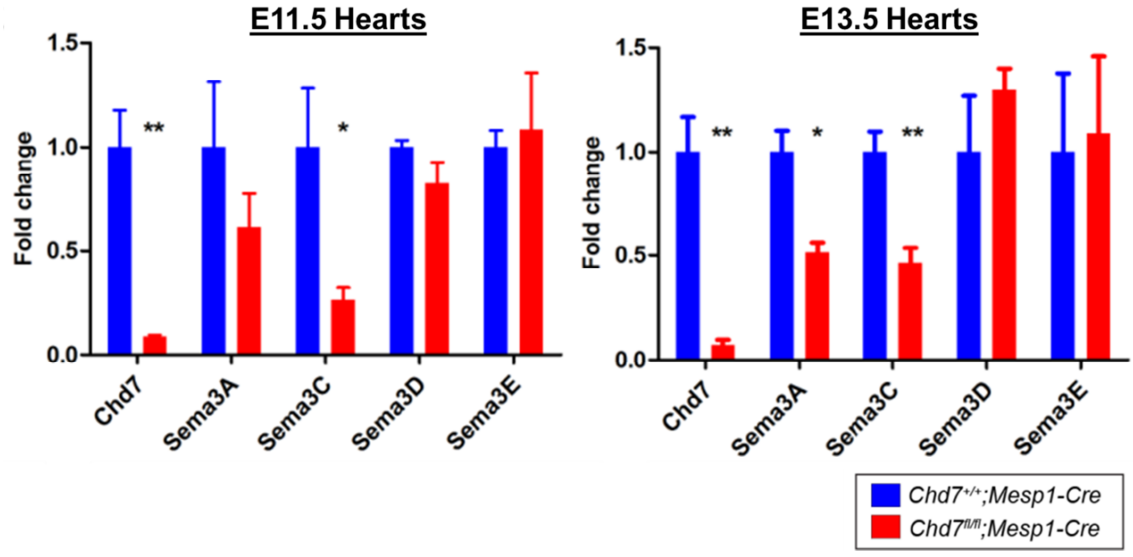

Figure 5-6: qRT-PCR analysis of Semaphorin gene expression in E11.5 and E13.5 hearts

Sema3A, *Sema3C*, *Sema3D* and *Sema3E* mRNA expression levels were compared in *Chd7$^{+/+}$;Mesp1-Cre* (blue) and *Chd7$^{fl/fl}$;Mesp1-Cre* (red) hearts. Data were normalised to *Gapdh* expression, and *Chd7* expression levels are shown to confirm its reduction in *Chd7$^{fl/fl}$;Mesp1-Cre* hearts. * $p < 0.05$, ** $p < 0.01$.

5.2.3 *Sema3A expression in the trabeculae is reduced after Chd7 ablation in the mesoderm*

The microarray and qRT-PCR experiments provide useful quantitative analysis for the levels of mRNA expression of genes that potentially lie downstream of CHD7 activity in the heart. However, they do not provide data on the specific location of the differentially-expressed genes within the heart. This can also be informative, for example in identifying the specific cell populations in which gene expression is affected. *In situ* hybridisation was therefore used to compare a number of genes of interest from the microarrays, to look at their specific expression in control *Chd7*$^{fl/fl}$ and mutant *Chd7*$^{fl/fl}$*;Mesp1-Cre* hearts.

Figure 5-7 shows that *Sema3A* is expressed specifically in the trabeculae of E13.5 hearts, which is consistent with previous reports (Ieda et al., 2007). Throughout the ventricles, this trabecular expression was lost in *Chd7*$^{fl/fl}$*;Mesp1-Cre* hearts, confirming the microarray and qRT-PCR data. Given the reported role of *Sema3A* in the sympathetic innervation of the heart (Ieda et al., 2007), it may be that this downstream loss of *Sema3A* expression is contributing to the innervation defects seen in *Chd7*$^{fl/fl}$*;Mesp1-Cre* hearts. Alternatively, given the location of its expression, it may be influencing the trabeculation and compaction of the ventricles, which are also affected in *Chd7*$^{fl/fl}$*;Mesp1-Cre* hearts.

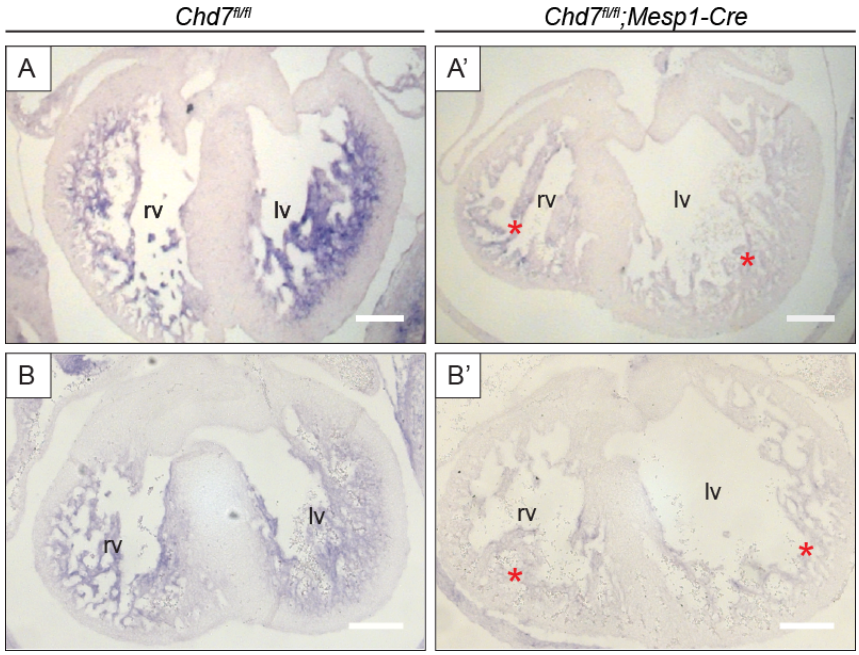

Figure 5-7: *Sema3A* expression in the trabeculae is lost in *Chd7*$^{fl/fl}$*;Mesp1-Cre* hearts

Sema3A ISH revealed strong expression in the trabeculae of E13.5 *Chd7*$^{fl/fl}$ control hearts (A and B), whilst this expression was clearly reduced in *Chd7*$^{fl/fl}$*;Mesp1-Cre* hearts (red stars, A' and B'). The two panels (A,A' and B,B') are from two separate repeats of the ISH experiment.

Scale bars represent 0.2mm. Rv indicates right ventricle; lv, left ventricle.

5.2.4 Expression of Sema3C is lost in the myocardial cuff of the distal OFT

ISH was also used to examine the expression of *Sema3C* in *Chd7*$^{fl/fl}$ and *Chd7*$^{fl/fl}$*;Mesp1-Cre* hearts (Figure 5-8). *Sema3C* was seen in the SHF-derived myocardial cuff of the OFT and in the NCC population in the distal endocardial cushions in E11.5 *Chd7*$^{fl/fl}$ hearts, again consistent with previously published data (Brown et al., 2001). Interestingly, at the proximal end of the OFT the expression of *Sema3C* appeared to be unchanged in *Chd7*$^{fl/fl}$*;Mesp1-Cre* hearts. However, at the distal end of the OFT a striking reduction in *Sema3C* expression can be seen in the myocardial cuff, indicating a spatial restriction on the region in which CHD7 activity affects *Sema3C* transcription.

As previously discussed, Semaphorin 3C-PlexinA2 signalling between the myocardium and migratory cardiac NCCs is crucial for OFT development, and when it is disrupted this results in a range of overlapping defects with the *Chd7*$^{fl/fl}$*;Mesp1-Cre* mice, including CAT, DORV, IAA-B and VSDs (Brown et al., 2001; Feiner et al., 2001). Furthermore, distal-proximal migration of NCCs in the OFT appears to be abrogated in *Chd7*$^{fl/fl}$*;Mesp1-Cre* hearts, as shown by *PlexinA2* ISH (see Figure 3-13), which is also noted in *Sema3C*$^{-/-}$ embryos (Brown et al., 2001). Downregulation of *Sema3C* expression in the distal OFT as a result of loss of CHD7 activity therefore is likely to be contributing to the disruption to NCC migration in *Chd7*$^{fl/fl}$*;Mesp1-Cre* OFTs, which leads to the overlapping structural defects.

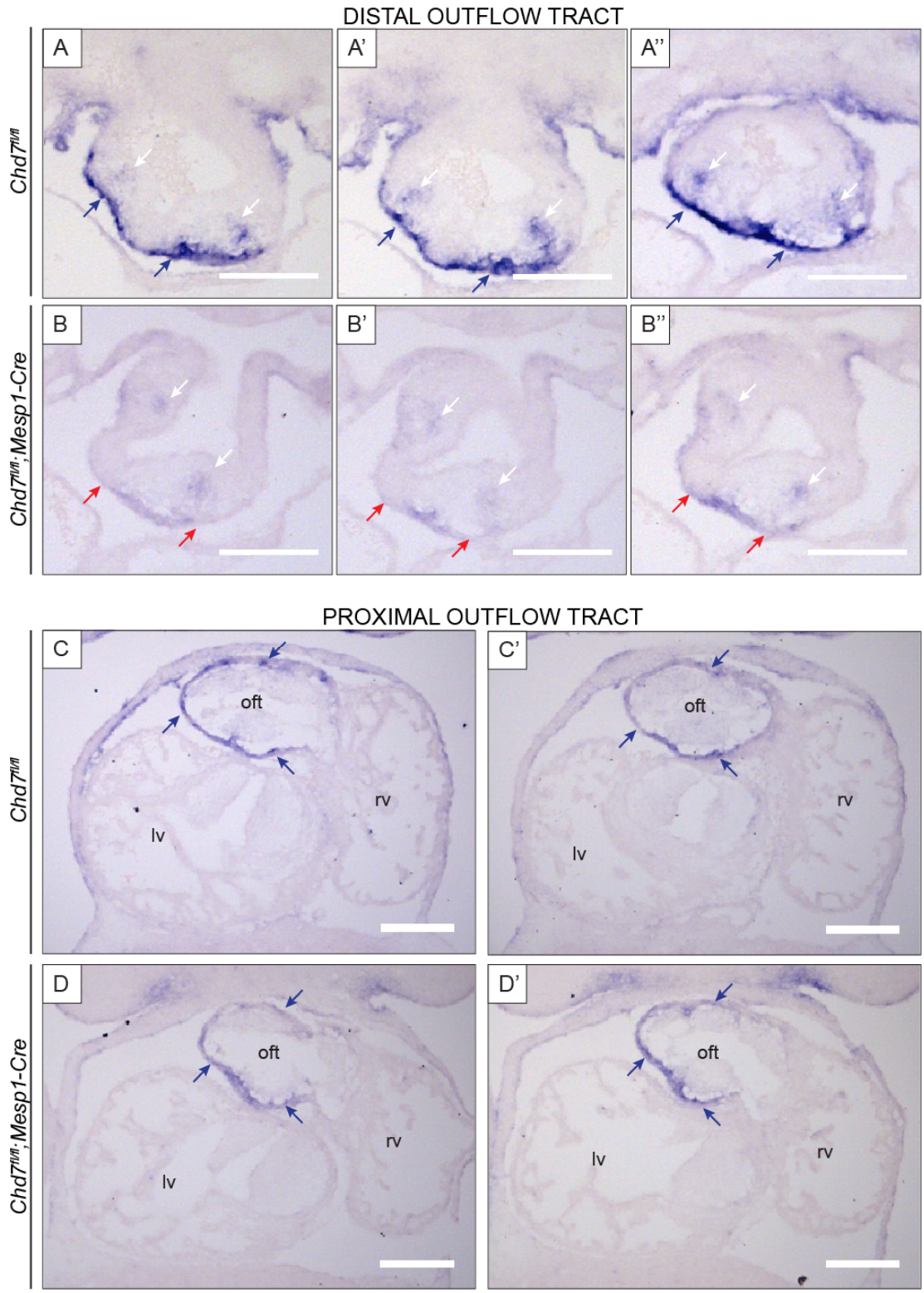

Figure 5-8: *Sema3C* expression is reduced specifically in the distal OFT

(A, B) *Sema3C* ISH on coronal sections through the distal OFT of an E11.5 *Chd7*$^{fl/fl}$ embryos shows strong expression in the myocardial cuff (blue arrows, A-A''), as well as in NCCs in the cushions (white arrows). In *Chd7*$^{fl/fl}$*;Mesp1-Cre* embryos, the myocardial cuff expression is almost entirely lost (red arrows, B-B''), whilst there is also some reduction in the NCC expression (white arrows).

(C, D) At the proximal end of the OFT, the myocardial expression of *Sema3C* appears the same in both *Chd7*$^{fl/fl}$ (blue arrows, C-C') and *Chd7*$^{fl/fl}$*;Mesp1-Cre* (blue arrows, D-D') hearts.

Scale bars represent 0.2mm. oft indicates outflow tract; rv, right ventricle; lv, left ventricle.

5.2.5 Epistasis between Chd7 and Sema3C could not be detected in the mesoderm

To investigate further the link between *Chd7* and *Sema3C* during OFT development, a conditional *Sema3C* allele was utilised to look for genetic interaction between these genes. Initially, heterozygous conditionally-ablated *Chd7$^{fl/+}$;Sema3C$^{fl/+}$;Mesp1-Cre* embryos were generated. Neither *Chd7$^{fl/+}$;Mesp1-Cre* or *Sema3C$^{fl/+}$;Mesp1-Cre* embryos present with a cardiac phenotype, so if any defects were seen in *Chd7$^{fl/+}$;Sema3C$^{fl/+}$;Mesp1-Cre* embryos this would indicate a synergistic relationship between these genes. However, examination of *Chd7$^{fl/+}$;Sema3C$^{fl/+}$;Mesp1-Cre* embryos at E13.5 (n=2) and at E15.5 (n=8) did not reveal any cardiac defects (data not shown).

To increase the level of *Chd7* ablation, the conditional *Chd7^{fl}* allele was replaced with the *Chd7^{Whi}* allele, so offspring would be constitutively heterozygous for *Chd7*. Whilst *Sema3C$^{fl/+}$;Chd7$^{Whi/+}$; Mesp1-Cre* embryos were difficult to generate due to the parent mice not breeding well, five embryos of the required genotype were collected at E15.5. Just one of these embryos showed a VSD, and no OFT or great vessel defects were seen (Figure 5-9). However, the VSD can be attributed to the presence of *Chd7^{Whi}* allele, as a previous study found 3 out of 5 *Chd7$^{Whi/+}$* embryos examined showed a VSD (Bosman et al., 2005), so additional cardiac defects would need to be seen to indicate that *Sema3C* and *Chd7* are in epistasis. Therefore, it seems that conditional ablation of *Sema3C* in the cardiogenic mesoderm, even on a constitutively heterozygous *Chd7* background, is not sufficient to show an epistatic relationship between these genes.

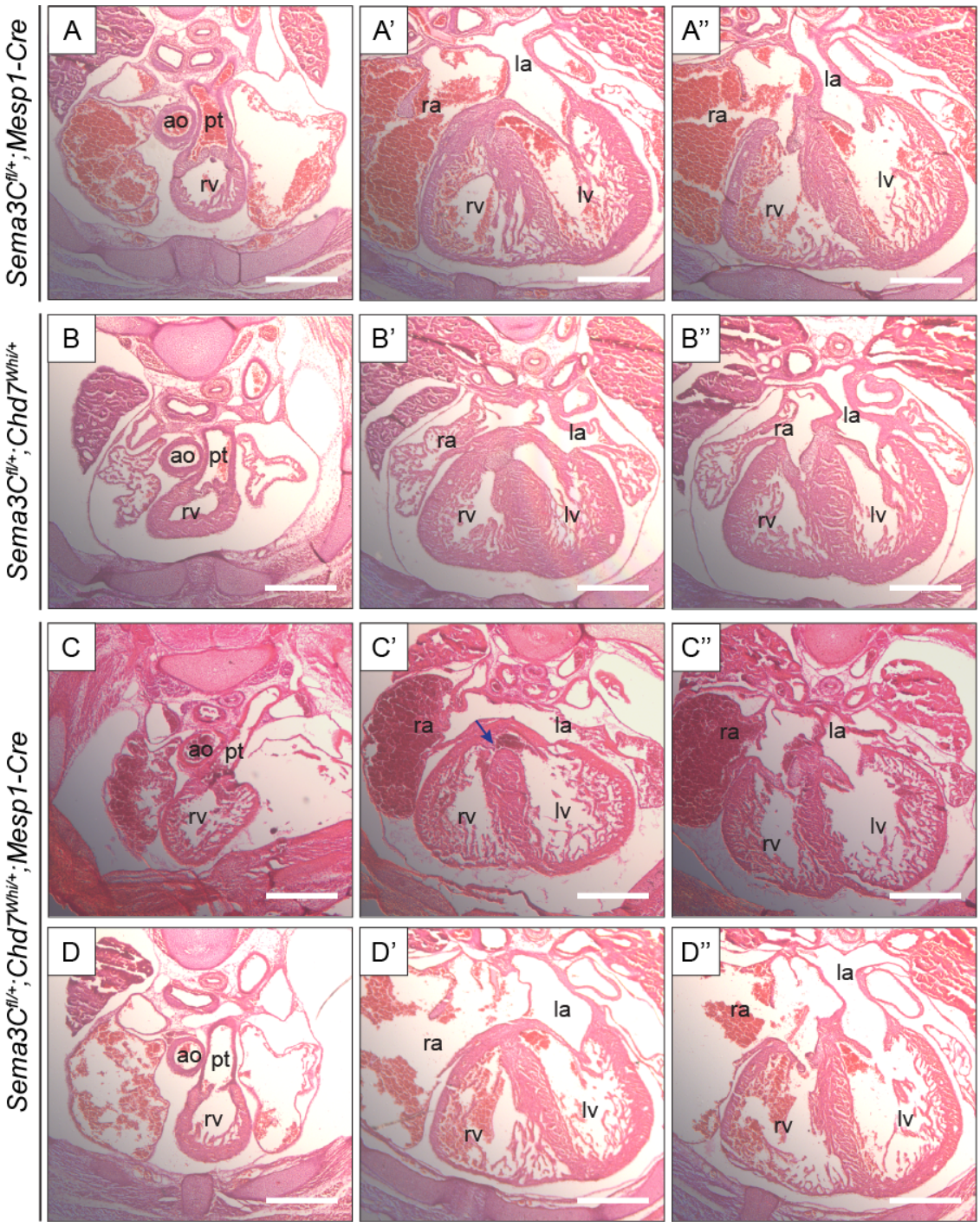

Figure 5-9: Lack of epistasis between *Sema3C* and *Chd7*

(A) H&E staining on transverse sections through E15.5 *Sema3C*$^{fl/+}$*;Mesp1-Cre* embryos (n=3) were examined for cardiac defects, for comparison to *Sema3C*$^{fl/+}$*;Chd7*^{Whi}*;Mesp1-Cre* hearts. No embryos of this genotype showed any abnormalities.

(B) Hearts of *Sema3C*$^{fl/+}$*;Chd7*$^{Whi/+}$ embryos (n=2) were also examined, which looked anatomically normal. Although none were seen here, previous reports have shown VSDs are observed in Chd7$^{Whi/+}$ embryos.

(C-D) One *Sema3C*$^{fl/+}$*;Chd7*^{Whi}*;Mesp1-Cre* heart out of five showed a small VSD (blue arrow, C'), but was otherwise normal.All other *Sema3C*$^{fl/+}$*;Chd7*^{Whi}*;Mesp1-Cre* hearts showed normal septation of the OFT and cardiac chambers (D-D').

5.3 Slit-Robo Signalling

5.3.1 Slit-Robo signalling during cardiac development

The Slit-Robo pathway was originally described as an extracellular signalling guidance system for axon pathfinding, promotion of axon branching and controlling neuronal migration (Brose et al., 1999). The Robo proteins are transmembrane receptors with large extracellular domains composed of immunoglobulin and fibronectin domains, whilst the Slit family act as ligands for these receptors (Fujiwara et al., 2006). It is now known that these two protein families can participate together in either repulsive or attractive signalling to a range of migrating cells, including neurons, leukocytes and muscle precursor cells (Kramer et al., 2001; Rothberg et al., 1988; Wu et al., 2001). Slit-Robo signalling is also now thought to be involved in signalling to migrating endothelial cells, implicating a role in angiogenesis: Robo4 is found expressed at sites of active angiogenesis (Huminiecki et al., 2002), with Slit2-Robo4 signalling thought to be an inhibitory cell migratory signal (Park et al., 2003), whilst Slit3 promotes angiogenesis during development (Zhang et al., 2009).

Several studies have highlighted roles for Slit-Robo signalling during early cardiac morphogenesis in *Drosophila*. Slit and Robo proteins are found at the dorsal midline at the time of linear tube formation by myocardial progenitors, and manipulation of localisation or overexpression of Slit results in defective heart tube alignment and assembly (Qian et al., 2005). Loss of Slit protein results in disruption to migration, cardiac cell alignment and cell-polarity marker localisation in the myocardium, whilst Robo2 mutants show a similar phenotype, with fewer migration defects (MacMullin and Jacobs, 2006). Furthermore, Slit-Robo signalling is important for development of the cardiac lumen during early heart tube formation: the lumen is created by the preferential attachment of the dorsal and ventral edges of the pairs of cardiogenic progenitors either side of the dorsal midline, and Slit-Robo signalling leads to the selected inhibition of E-cadherin adhesion in the central luminal domain (Medioni et al., 2008; Santiago-Martinez et al., 2008).

In the mouse, *Slit1*, *Slit2* and *Slit3* are expressed in the heart and pharyngeal region during development, along with *Robo1* and *Robo2* (Medioni et al., 2010). Slit2/3-Robo1/2 signalling has been shown to regulate cardiac cushion formation, through its effects on Notch signalling (Mathilda Mommersteeg, Weinstein conference 2014 abstract and personal communication). *Robo1* and *Robo2*, along with their ligands *Slit2* and *Slit3*, are expressed in or adjacent to the cardiac cushions. *Robo1* knockout mice displayed membranous VSDs, and whilst knockout of *Robo2* did not result in similar defects, *Robo1*;*Robo2* double mutants showed increased

incidence and severity in VSDs. *Slit3* mutants also showed VSDs, whilst *Slit2* mutants showed VSDs at E14.5 but these were all closed at E18.5. Furthermore, valve defects were observed in *Slit2*, *Slit3* and *Robo1;Robo2* mutants. Downregulation of Notch and downstream *Hey* and *Hes* genes was seen in *Robo1* mutants, which have well established roles in the development of the cardiac cushions and valves (Zhou and Liu, 2014). Slit-Robo signalling is also involved in development of the pericardium, the sinus horn myocardium and alignment of the caval veins. Loss of Slit3-Robo1 signalling causes impaired cardiac NCC survival, adhesion and migration, leading to pericardial defects (Mommersteeg et al., 2013).

5.3.2 Slit2, Robo2 and Slitrks are downregulated following mesodermal Chd7 ablation

Significant downregulation of *Robo2* and *Slit2* were identified in the microarray experiment in E11.5 *Chd7$^{fl/fl}$;Mesp1-Cre* hearts, and the downregulation of *Slit2* continued at E13.5 (Table 5-11). A number of *Slitrk* genes were also downregulated at E13.5. The Slitrk family of transmembrane proteins (Slitrk1-6) all contain an extracellular domain with two lycine-rich repeats (LRR) that are highly homologous to the LRR regions of Slit molecules (Aruga and Mikoshiba, 2003). The Slitrks are expressed predominantly in neural tissues, and are thought to function in the development of specific aspects of neuronal development (Beaubien and Cloutier, 2009). This data suggests they may have a role in cardiac innervation, or an additional different function in cardiovascular development.

qRT-PCR was again used to validate the aberrant gene expression of Slit-Robo pathway genes at E11.5 and E13.5 (Figure 5-10). Significant downregulation of *Robo2* was replicated at E11.5, and it appeared to be reduced at E13.5 as well, although this did not reach significance. Similarly, downregulation of *Slit2* at both time points can be seen on the graphs, although these did not quite reach significance (at E13.5, $p = 0.57$). *Slitrk* genes also showed reduced expression in *Chd7$^{fl/fl}$;Mesp1-Cre* hearts, further validating their expression downstream of CHD7 activity in the developing heart. It would have been interesting to examine the spatial expression of some of these *Slitrk* genes in the developing heart by ISH, and to see if their downregulation could be validated further. Unfortunately, however, attempts to generate specific ISH probes for several *Slitrk* genes were unsuccessful, so this was not pursued further.

Table 5-11: Microarray results for Slit-Robo pathway genes

Symbol:	Gene name:	E11.5 log_2FC	E11.5 P Value	E13.5 log_2FC	E13.5 P Value
Robo2	roundabout homolog 2 (Drosophila)	-0.90673	2.38E-05	NS	NS
Slit2	slit homolog 2 (Drosophila)	-0.98707	2.44E-08	-0.53024	4.66E-05
Slitrk3	SLIT and NTRK-like family, member 3	NS	NS	-0.65121	0.018027
Slitrk4	SLIT and NTRK-like family, member 4	NS	NS	-0.54174	0.01459
Slitrk5	SLIT and NTRK-like family, member 5	NS	NS	-0.67045	1.35E-05

NS indicates not significant

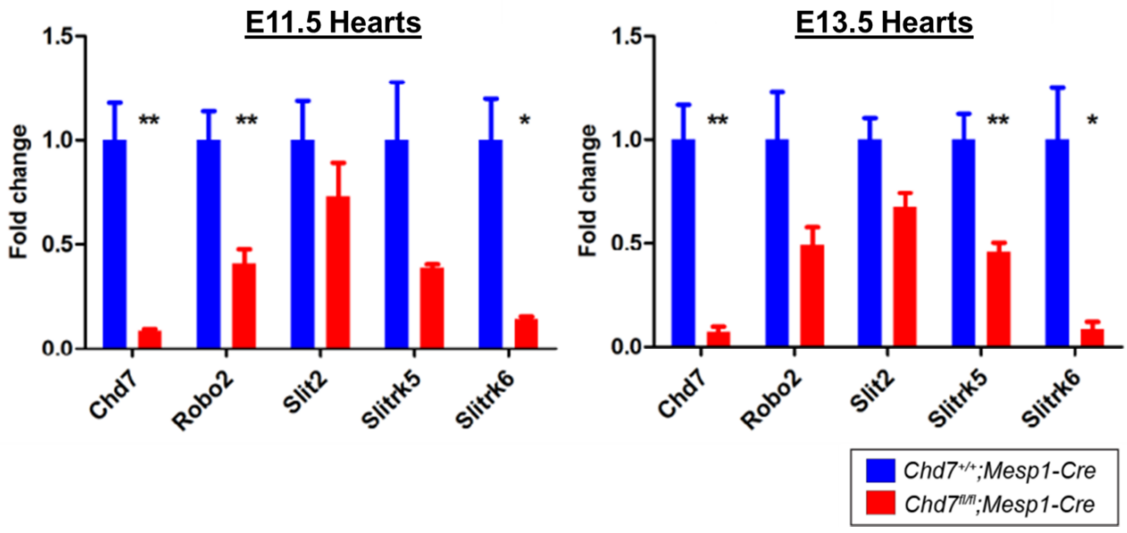

Figure 5-10: qRT-PCR analysis of Slit-Robo gene expression in E11.5 and E13.5 hearts

Robo2, Slit2, Slitrk5 and *Slitrk6* mRNA expression levels were compared in *Chd7*$^{+/+}$*;Mesp1-Cre* (blue) and *Chd7*$^{fl/fl}$*;Mesp1-Cre* (red) hearts. Data were normalised to *Gapdh* expression, and *Chd7* expression levels are shown to confirm its reduction in *Chd7*$^{fl/fl}$*;Mesp1-Cre* hearts. * $p < 0.05$, ** $p < 0.01$.

5.3.3 *Slit2 and Robo2 are downregulated by ISH*

At E8.5 and E9.5, *Slit2* is expressed in the pharyngeal surface ectoderm, whilst at E12.5 it is strongly expressed in the trabecular region of the ventricles (Medioni et al., 2010). *Slit2* expression was compared by ISH in *Chd7*$^{fl/fl}$ and *Chd7*$^{fl/fl}$*;Mesp-Cre* hearts at both E11.5 and E13.5. At the earlier time point, no difference was seen in the weak *Slit2* expression in the trabeculae of *Chd7*$^{fl/fl}$ and *Chd7*$^{fl/fl}$*;Mesp-Cre* hearts (Figure 5-11, panel A). However, at E13.5 much stronger expression was seen in *Chd7*$^{fl/fl}$ hearts, again in the trabeculae, which was strongly downregulated in *Chd7*$^{fl/fl}$*;Mesp-Cre* hearts (Figure 5-11, panel B). This indicates that expression of the Slit2 ligand is disrupted following ablation of *Chd7* in the cardiogenic mesoderm.

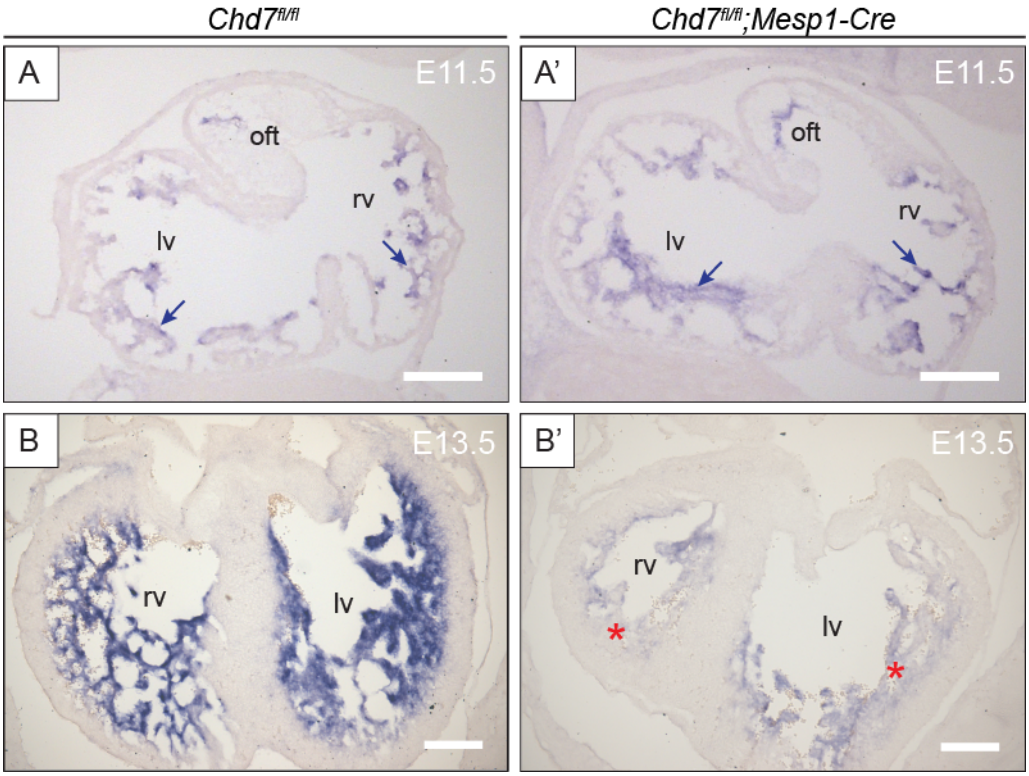

Figure 5-11: Reduction in *Slit2* expression is seen at E13.5

(A) *Slit2* ISH on coronal sections through the heart at E11.5 show some trabecular expression in the ventricular chambers (blue arrows), but there is no difference detected between the *Chd7*$^{fl/fl}$ (A) and *Chd7*$^{fl/fl}$*;Mesp1-Cre* hearts (A').

(B) At E13.5, strong *Slit2* expression is seen specifically in the trabeculae on transverse sections through the heart (B), with downregulation in both the dominant left ventricle and under-developed right ventricle of the *Chd7*$^{fl/fl}$*;Mesp1-Cre* heart (red stars, B').

Scale bars represent 0.2mm. Oft indicates outflow tract; rv, right ventricle; lv, left ventricle.

Previous studies have shown *Robo2* is expressed at the venous pole of the linear heart tube at E8.5, in both atria at E10.5, and in the aorta and pulmonary trunk at E12.5 (Medioni et al., 2010). Consistent with this, at E11.5 *Robo2* expression was clearly seen in the endocardial cushions throughout the OFT in *Chd7*$^{fl/fl}$ hearts, in a pattern that distally looks to be in the two characteristic 'prongs' of cardiac NCCs, and becomes more diffuse throughout the cushions at the proximal end of the OFT (Figure 5-12, A-F). However, whilst the more distal expression is maintained in *Chd7*$^{fl/fl}$*;Mesp1-Cre* hearts, the expression throughout the cushions in the proximal OFT is lost in mutant hearts (Figure 5-12, G-L). As with *Sema3C*, the region of *Robo2* expression affected by *Chd7* ablation is therefore restricted to a very distinct portion of the OFT.

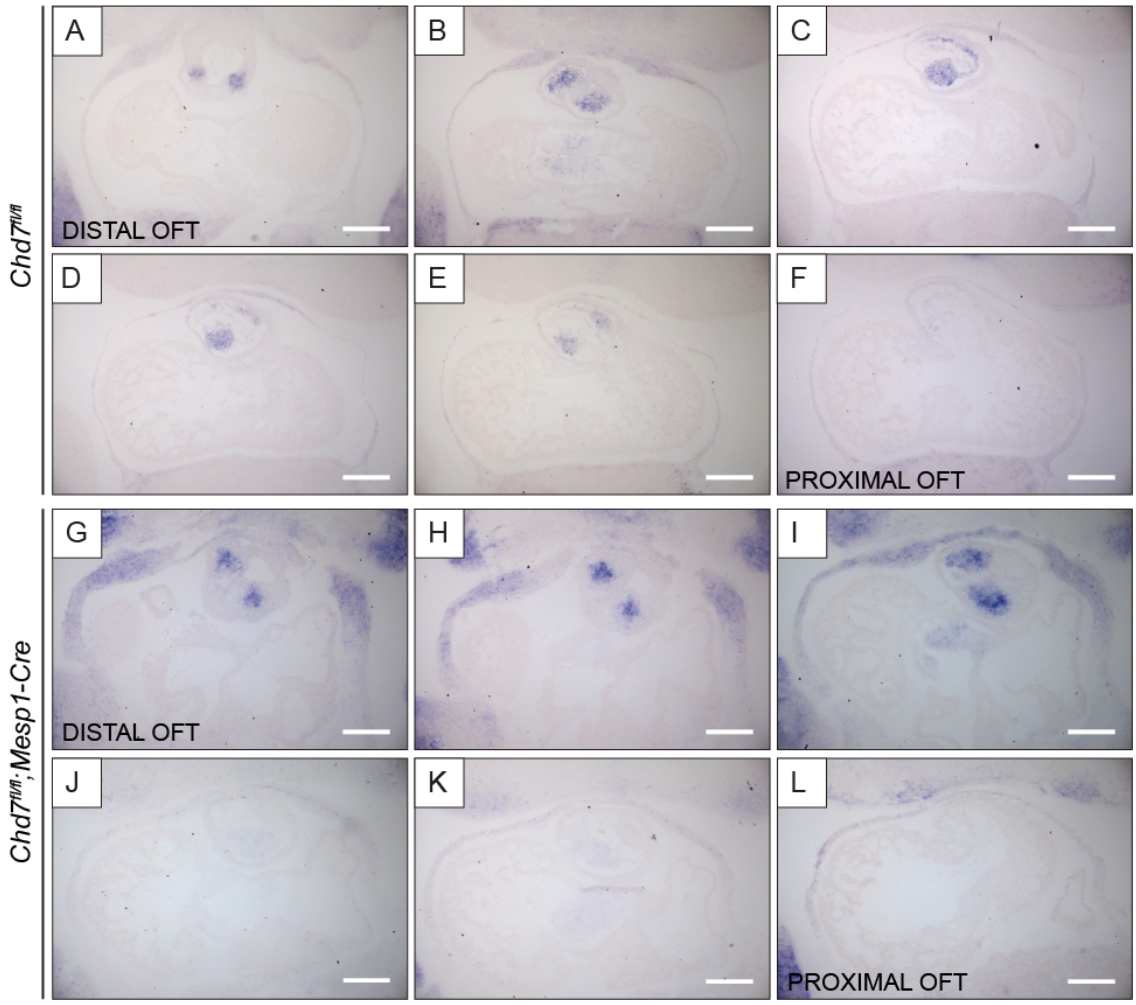

Figure 5-12: *Robo2* expression is lost in the proximal OFT at E11.5

Robo2 ISH was performed on coronal sections through the hearts of E11.5 *Chd7*$^{fl/fl}$ (A-F) and *Chd7*$^{fl/fl}$*;Mesp1-Cre* (G-L) hearts. In *Chd7*$^{fl/fl}$ hearts, expression is seen distally in two distinct 'prongs', likely overlapping with NCCs (A,B). More proximally, it becomes more diffuse, and is seen in the endocardial cushions as the OFT connects to the RV. In *Chd7*$^{fl/fl}$*;Mesp1-Cre* hearts, similar expression is seen in the distal OFT (G-I), however at the distal end of the OFT the more diffuse Robo2 expression is lost (J-L).

Scale bars represent 0.2mm.

In order to confirm the specificity of CHD7 activity on individual Slit-Robo pathway genes, *Robo1* ISH was also performed on *Chd7*$^{fl/fl}$ and *Chd7*$^{fl/fl}$*;Mesp1-Cre* E13.5 hearts, when it is seen at the base of the great arteries, at the tip of the inter-ventricular septum, and around the AV valves (Figure 5-13). This expression was not affected in the *Chd7*$^{fl/fl}$*;Mesp1-Cre* heart, which is consistent with no significant change being seen in the microarray and qRT-PCR analysis. Therefore, CHD7 activity lies upstream of the *Robo2* and *Slit2* expression in the developing heart, but not other Slit-Robo genes such as *Robo1.*

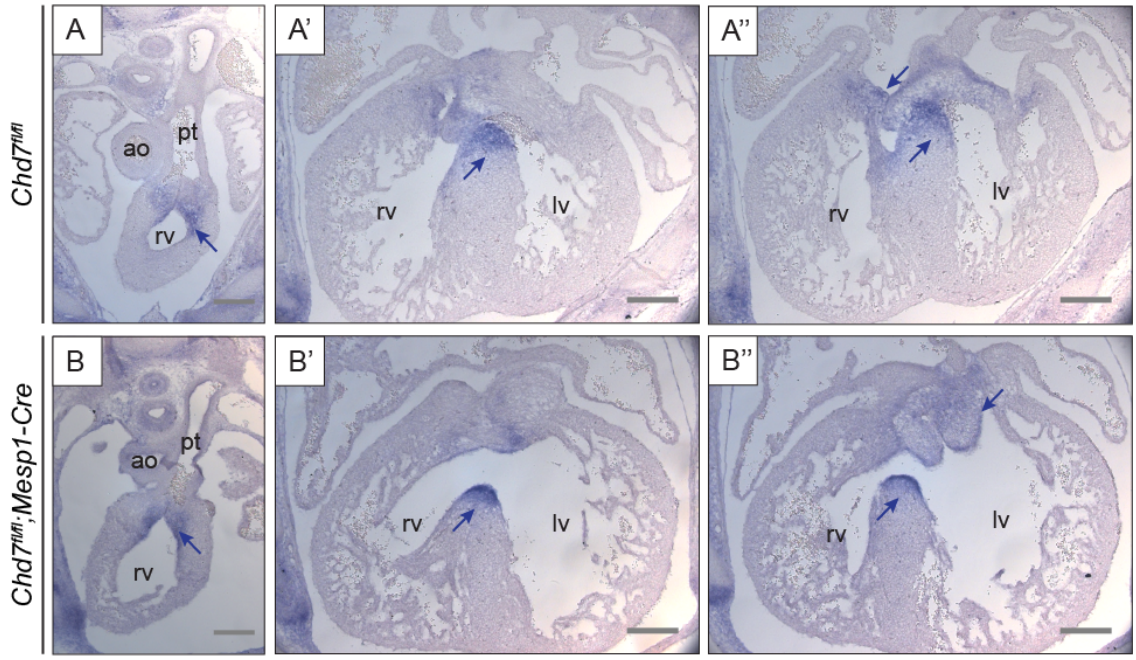

Figure 5-13: *Robo1* expression is unaffected in *Chd7*$^{fl/fl}$*;Mesp1-Cre* hearts

Transverse sections through E13.5 hearts showed *Robo1* expression (blue arrows) at the base of the great arteries, the tip of the interventricular septum and the AV valves in both *Chd7*$^{fl/fl}$ (A) and *Chd7*$^{fl/fl}$*;Mesp1-Cre* (B) hearts.

Scale bars represent 0.2mm. ao indicates aorta; pt, pulmonary trunk; rv, right ventricle; lv, left ventricle.

5.4 Calcium Handling

5.4.1 The importance of calcium in cardiomyocyte function

In addition to the complex morphological events underlying structural development of the heart, the ability of cardiomyocytes to undergo excitation-contraction coupling is essential for cardiovascular function. This process links the electrical stimulation of cardiomyocytes to the activation of myofilaments that cause contraction, so that cardiomyocyte contractions are coordinated and the heart can act as an efficient pump (reviewed in (Bers, 2002)).

The ubiquitous messenger Ca^{2+} is the key signalling molecule for this excitation-contraction coupling. Figure 5-14 summarises the process. Briefly, during the cardiac action potential, voltage-sensitive L-type Ca^{2+} channels (LTCCs) are activated by the depolarisation of the sarcolemmic membrane, producing a Ca^{2+} current into the cardiomyocyte cytoplasm. This Ca^{2+} influx triggers Ca^{2+} release from the sarcoplasmic reticulum (SR), and the combination of these two sources raises the intracellular Ca^{2+} concentration sufficiently to bind to the myofilament protein Troponin C. This binding activates the contractile machinery. For relaxation to occur, Ca^{2+} must dissociate from Troponin C, so the intracellular Ca^{2+} concentration needs to be rapidly reduced. This is achieved by the active transport of Ca^{2+} out of the cytoplasm by the SR Ca^{2+}-ATPase, which restores SR Ca^{2+} levels, sarcolemmal Na^{+}/Ca^{2+} exchange, sarcolemmal Ca^{2+} ATPase or mitochondrial Ca^{2+} uniport. These processes and transport systems are tightly inter-linked and highly dynamic.

The release of calcium from the SR in response to the Ca^{2+} influx – termed calcium-induced calcium release (CICR) – provides a crucial functional link between the depolarisation of the sarcolemmal membrane upon excitation and the contraction of the myofilaments. The SR Ca^{2+}-release channel Ryanodine Receptor (RyR) is centrally involved in this process. The main RyR isoform in cardiomyocytes is RyR2. RyRs form homotetrameric channels that sit within complex macromolecular structures on the SR membrane, which contain multiple regulatory components that affect RyR function (Bers, 2004). LTCCs and RyRs are organised into structures known as Ca^{2+}-release units (CRUs). As well as an LTCC and RyR channel, CRUs also contain the SR docking protein Junctophilin, the internal Ca^{2+}-binding protein Calsequestrin, and Triadin and Junctin, which mediate the Calsequestrin-RyR interaction (reviewed in (Wehrens et al., 2005)). When CICR or excitation-contraction coupling is disrupted, this leads to contractile dysfunction and arrhythmias in many pathological conditions (Pogwizd et al., 2001).

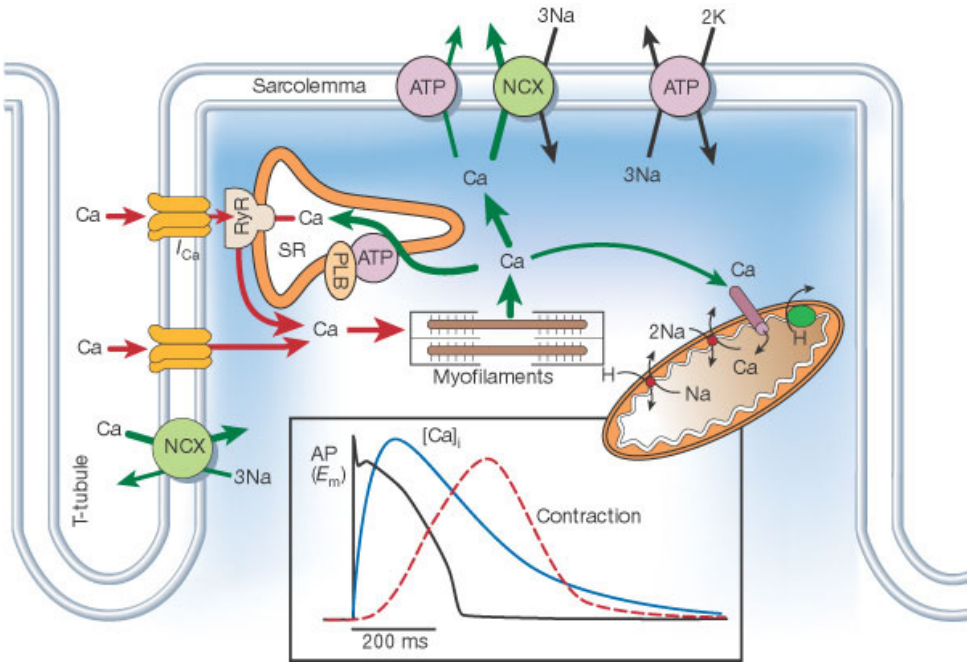

Figure 5-14: Calcium signalling during cardiac excitation-contraction coupling

The key processes in excitation-contraction coupling all involve Ca^{2+} movement and signalling, from the initial Ca^{2+} influx, calcium-induced calcium release at the SR, activation of myofilaments, and active transport of intracellular Ca^{2+} either back into the SR, out of the cell or into the mitochondria.

The inset shows the relationship between the time courses of an action potential (black line), intracellular free Ca^{2+} levels (blue line) and cardiomyocyte contraction (red dashed line) in a rabbit ventricular cardiomyocyte at 37°C.

Figure from Bers (2002). NCX indicates Na^{+}/Ca^{2+} exchange; ATP, ATP-ase; PLB, phospholamban; RyR, ryanodine receptor; SR sarcoplasmic reticulum.

5.4.2 Calcium handling genes are dysregulated

The lists of microarray genes that were significantly dysregulated following multiple testing correction (Table 5-3 and 5-4) contained both *Trdn* and *Casq2*, which encode the sarcoplasmic reticulum (SR) membrane-associated proteins Triadin and Calsequestrin. Transcripts of further genes, including the voltage-dependent calcium channels *Cacng7, Cacna2d3* and *Cacna1e*, were also affected (Table 5-12). These genes are all associated with Ca^{2+} handling during cardiomyocyte excitation-contraction coupling. At E13.5, a slight downregulation of *Ryr3* was also seen in the microarray data, which encodes the Ryanodine Receptor 3 (RyR3). Whilst RyR2 is the main isoform found in cardiac muscle, RyR3 is also weakly expressed in cardiac tissue (Bers, 2004; Nakashima et al., 1997). qRT-PCR confirmed that both *Ryr3* and *Trdn* were downregulated in *Chd7$^{fl/fl}$;Mesp1-Cre* hearts at E11.5 and E13.5 (Figure 5-15).

Table 5-12: Microarray results for genes associated with Ca^{2+} handling

Symbol:	Gene name:	E11.5 Log_2FC:	E11.5 P Value:	E13.5 log_2FC:	E13.5 P Value:
Cacna1e	calcium channel, voltage-dependent, R type, alpha 1E subunit	-0.504	0.000393	NS	NS
Cacna2d3	calcium channel, voltage-dependent, alpha2/delta subunit 3	-0.69777	0.004466	NS	NS
Cacng7	calcium channel, voltage-dependent, gamma subunit 7	-0.60886	0.0016	NS	NS
Casq2	calsequestrin 2	1.691003	1.98E-08	0.556697	0.003187
Trdn	triadin	-1.0781	6.84E-07	-0.8	2.28E-05
Ryr3	ryanodine receptor 3	NS	NS	-0.52855	0.000215

NS indicates not significant

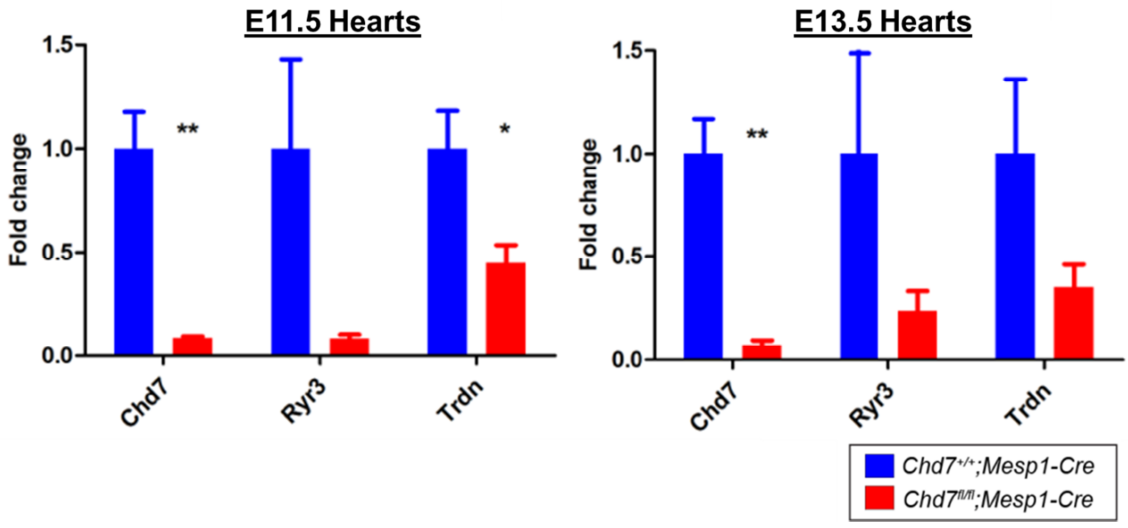

Figure 5-15: qRT-PCR analysis of calcium handling genes in E11.5 and E13.5 hearts

Ryr3 and *Trdn* mRNA expression levels were compared in *Chd7*$^{+/+}$*;Mesp1-Cre* (blue) and *Chd7*$^{fl/fl}$*;Mesp1-Cre* (red) hearts. Data were normalised to *Gapdh* expression, and *Chd7* expression levels are shown to confirm its reduction in *Chd7*$^{fl/fl}$*;Mesp1-Cre* hearts. * $p < 0.05$, ** $p < 0.01$.

5.4.3 *Culture of embryonic cardiomyocytes*

To determine whether the transcriptional changes to Ca^{2+} handling genes seen in *Chd7$^{fl/fl}$;Mesp1-Cre* hearts resulted in any functional effect, a protocol was developed for live imaging of Ca^{2+} transients in embryonic cardiomyocytes. Cardiomyocytes were isolated from E13.5 hearts, as more cardiomyocytes could be collected at this stage than at E11.5, but the hearts were not yet becoming necrotic as they may have been by E15.5. Several methods were tested for dissociating the cells of the dissected hearts, including incubation with Pancreatin, Collagenase or Trypsin-EDTA at 37°C. Treatment with 0.05% Trypsin-EDTA containing 10µg ml^{-1} DNase I was chosen, as this provided sufficient digestive activity for cells to be well dissociated but was not too damaging to the resulting cardiomyocyte cultures. An additional step was used whereby cells were plated for 1.5 hours to allow adherence of fibroblasts, which spread and adhere faster than cardiomyocytes, before re-plating of the supernatant to enrich the culture for cardiomyocytes. The full protocol can be found in the Experimental Procedures, section 2.6.1.

Following overnight culture at 37°C, 5% CO_2, cells could be seen beating in the culture dish. Whilst this was already convincing evidence that these were successfully-isolated cardiomyocytes, immunocytochemistry was also used to show expression of the cardiac transcription factor NKX2-5 and the cardiac-specific myosin heavy-chain 6 in cultured cardiomyocytes (Figure 5-16).

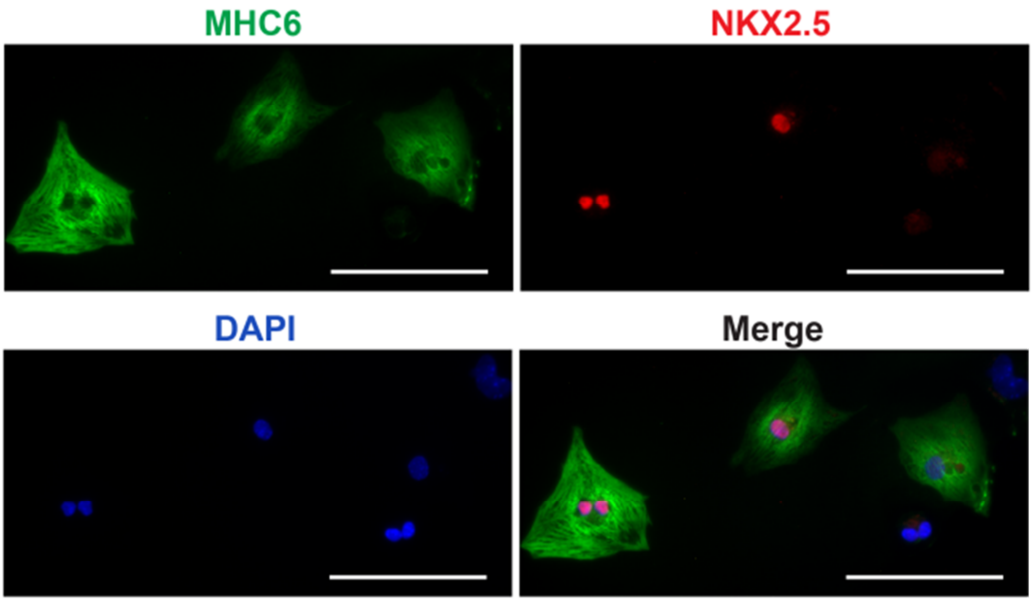

Figure 5-16: E13.5 embryonic cardiomyocytes

Immunocytochemistry showed cardiac-specific myosin heavy chain 6 (MHC6) and nuclear NKX2-5 levels in isolated E13.5 cardiomyocytes from CD1 embryos.

Scale bars represent 0.1mm.

5.4.4 *Excitation-contraction coupling is defective in Chd7$^{fl/fl}$;Mesp1-Cre cardiomyocytes*

In order to visualise Ca^{2+} transients in the cultured E13.5 cardiomyocytes, cells were loaded with the calcium-sensitive fluorogenic dye Cal-520^{TM}, which fluoresces green when bound to Ca^{2+} (K_d 320nM). Live imaging using confocal microscopy meant cells that were producing Ca^{2+} transients could be randomly selected for analysis, and these transients were recorded over time by rapid line scan analysis.

Initial trials of this technique showed that whilst Ca^{2+} transients could be recorded in both control *Chd7$^{fl/fl}$* and mutant *Chd7$^{fl/fl}$;Mesp1-Cre* cardiomyocytes, there was a very high level of variation in the frequency of the Ca^{2+} transients between all cells, regardless of genotype. For most cells the Ca^{2+} peaks were unevenly paced across the 40 seconds they were measured, such as the example in the top panel of Figure 5-17. This high variance would have made analysis and identification of any difference in *Chd7$^{fl/fl}$;Mesp1-Cre* cardiomyocytes compared to controls extremely difficult. Therefore, to overcome this issue, electrical pacing by field stimulation at 1Hz was introduced, in order to regulate the Ca^{2+} transients produced by cardiomyocytes (Figure 5-17).

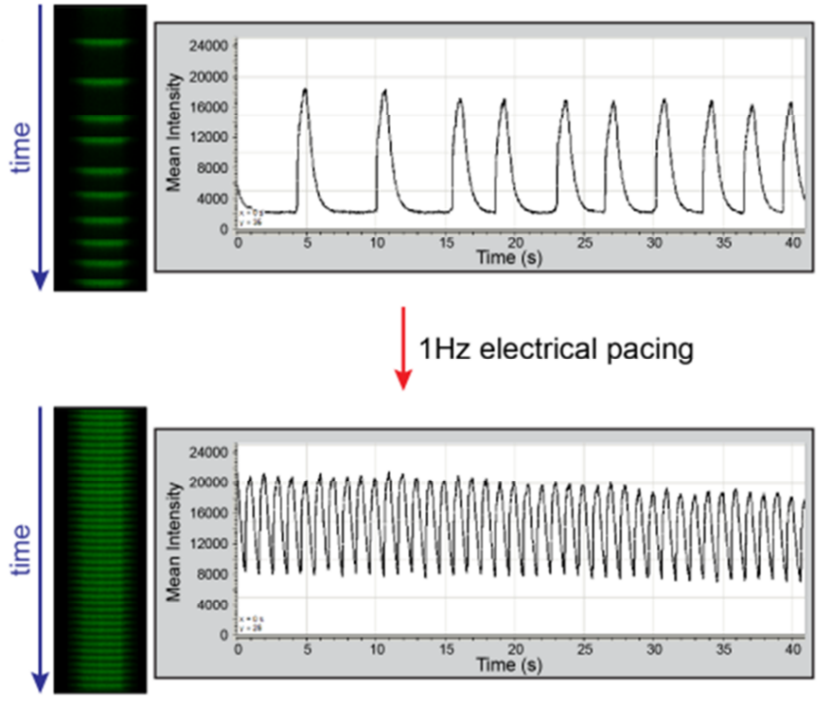

Figure 5-17: Cardiomyocytes could be paced by field stimulation

Rapid line scan analysis of Ca^{2+} transients over 40s in individual cells showed irregular cardiomyocyte contractions and high variation between all cells (top panel). Pacing of cells using electrical field stimulation at 1Hz by platinum electrodes meant that Ca^{2+} peaks could be regulated.

Comparison of the response to electrical pacing by control *Chd7*$^{fl/fl}$ or *Chd7*$^{fl/+}$ cells with *Chd7*$^{fl/fl}$*;Mesp1-Cre* cardiomyocytes revealed a striking difference. 95% (n=22) of control cardiomyocytes responded to electrical pacing with regular Ca^{2+} transients recorded at the expected 1s intervals, as seen in Figure 5-17. However, only 39% (n=23) of *Chd7*$^{fl/fl}$*;Mesp1-Cre* cells could be paced in this way ($p<0.0001$, Figure 5-18). This indicates the excitation-contraction coupling mechanism in cardiomyocytes is defective following ablation of *Chd7* in the cardiac mesoderm, which is likely due, at least in part, to the aberrant expression of Ca^{2+} handling genes.

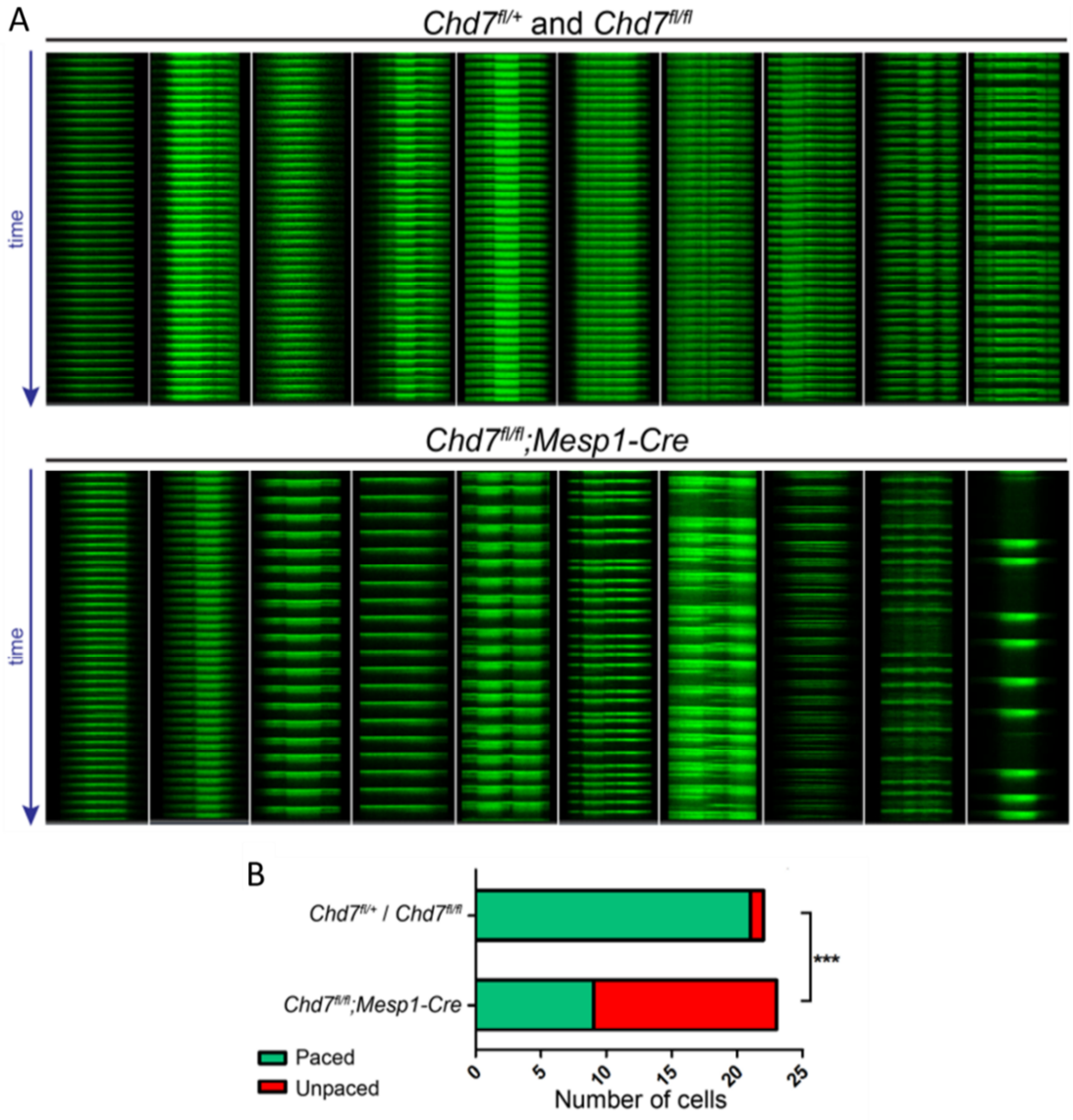

Figure 5-18: Excitation-contraction coupling is disrupted in *Chd7*$^{fl/fl}$*;Mesp1-Cre* cardiomyocytes

(A) Comparison of 10 representative control *Chd7*$^{fl/+}$ or *Chd7*$^{fl/fl}$ line scans (top panel) with *Chd7*$^{fl/fl}$*;Mesp1-Cre* (bottom panel) showed a range of pacing defects in *Chd7*$^{fl/fl}$*;Mesp1-Cre* cardiomyocytes. Only 1 control cell did not pace fully (far right, top panel).

(B) Significantly fewer *Chd7*$^{fl/fl}$*;Mesp1-Cre* cells responded to the electrical pacing compared to control cells. *** $p < 0.0001$.

5.5 Earlier transcriptional changes underlying the DILV phenotype

As previously mentioned, genes with known roles in early venous pole development were not identified in the E11.5 and E13.5 microarray datasets. Whilst the microarrays carried out provided much valuable information, with additional time and resources another microarray experiment at E9.5 may have identified disrupted genes and pathways that are important for AV canal septation and that may be contributing to the DILV phenotype see in *Chd7$^{fl/fl}$;Mesp1-Cre* embryos. It was recently reported that BMP activity is abrogated in the AV canals of *Chd7$^{-/-}$* mutant embryos around E10.0 (Liu et al., 2014). BMP signalling has a key role in development of the vestibular spine (Briggs et al., 2013), so it is likely that this disruption to BMP activity in the early heart tube following *Chd7* ablation is contributing to the DILV defect seen in all *Chd7$^{fl/fl}$;Mesp1-Cre* hearts.

To investigate further transcriptional changes that could also be affecting venous pole and vestibular spine development, two candidate genes were also tested by ISH at E9.5. *Tgfbr2* and *Wnt2* are both expressed in the early inflow tract, and their disruption during development can lead to DILVs and septation defects of the AV canal (Bartram et al., 2001; Jiao et al., 2006; Tian et al., 2010). However, preliminary ISH experiments indicated that there was no difference in their cardiac expression between *Chd7$^{fl/fl}$* and *Chd7$^{fl/fl}$;Mesp1-Cre* embryos, although quite a lot of background staining occured (Figure 5-19). This would indicate that CHD7 activity does not lie upstream of *Wnt2* or *Tgfbr2* expression during inflow tract development, although microarray or real-time data would be required to confirm this proposal. Therefore, loss of BMP signalling following *Chd7* ablation in the AV canal remains the most likely reason for the DILV phenotype, as observed in *Chd7$^{-/-}$* hearts (Liu et al., 2014).

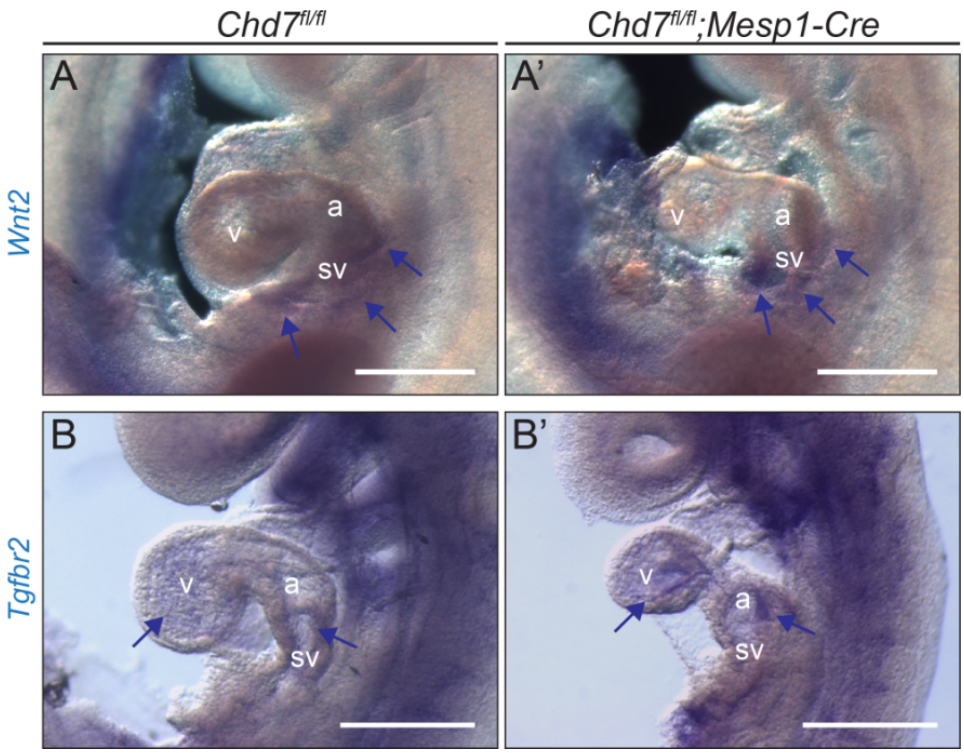

Figure 5-19: *Wnt2* and *Tgfbr2* expression are not altered in E9.5 *Chd7$^{fl/fl}$;Mesp1-Cre* hearts

(A) Wholemount ISH on E9.5 embryos showed similar expression of *Wnt2* in the sinus venosus and early atrial chamber in both *Chd7$^{fl/fl}$* (A) and *Chd7$^{fl/fl}$;Mesp1-Cre* (A') hearts, highlighted by blue arrows.

(B) *Tgfbr2* ISH showed expression throughout the heart in both *Chd7$^{fl/fl}$* (B) and *Chd7$^{fl/fl}$;Mesp1-Cre* (B') hearts, again highlighted by blue arrows.

Scale bars represent 1mm. v indicates ventricle; a, atrium; sv, sinus venosus.

5.6 Discussion

This chapter has addressed the transcriptional changes caused by loss of CHD7 activity in the cardiogenic mesoderm, and linked them to the phenotypes seen in *Chd7$^{fl/fl}$;Mesp1-Cre* hearts. Microarrays were performed at E11.5 and E13.5, when key septation events are taking place in the developing heart, and differentially-expressed gene lists were analysed for over-represented gene ontology (GO) terms. Many of these related to the structural, innervation and vascular defects seen in *Chd7$^{fl/fl}$;Mesp1-Cre* hearts, including Class 3 Semaphorin and Slit-Robo pathway genes. qRT-PCR and ISH were used to validate a selection of these genes, and provide detailed spatial information on the cardiac regions in which CHD7 activity affects expression of these genes. Furthermore, Ca^{2+} handling genes with aberrant expression in the microarrays were also validated, and this was demonstrated to affect the excitation-contraction coupling function of *Chd7$^{fl/fl}$;Mesp1-Cre* cardiomyocytes.

5.6.1 Loss of CHD7 affects extracellular signalling pathways

Conditional ablation of *Chd7* has allowed elucidation of some of the later genes affected by CHD7 activity during cardiogenesis. Notably, these include many signalling and calcium handling genes, as opposed to master-regulator transcription factors such as NKX2-5, which is regulated in the early heart tube (Liu et al., 2014). This indicates a switch in the types of genes CHD7 regulates as cardiogenesis progresses. Other signalling pathways have also been shown to be affected by CHD7 activity: *Chd7* haploinsufficiency results in reduced *Fgf8* expression in the isthmus organiser during early cerebellar development (Yu et al., 2013) and misexpression of *Bmp4* in the forebrain (Jiang et al., 2012). Furthermore, CHD7 directly regulates the retinoic acid receptors *Rarb* and *Rxrg* in neural stem and progenitor cells, with cooperation between CHD7 and retinoic acid signalling important for inner ear development (Micucci et al., 2014).

Multiple downregulated genes were identified in the E11.5 and E13.5 microarray datasets with known signalling roles in ventricular septation, alignment and septation of the OFT, and great vessel remodelling. Of these, further work focussed on components of the Semaphorin and Slit-Robo extracellular signalling pathways. Semaphorin 3C, which was downregulated at both time points, is a secreted glycoprotein that was proposed to act as a guidance molecule to migratory NCCs expressing semaphorin receptors such as PlexinA2 (Brown et al., 2001; Feiner et al., 2001). *Sema3C$^{-/-}$* mice have defects in the morphogenetic patterning of the aortic arch and OFT, such as IAA-B, CAT and DORV (Feiner et al., 2001). It is therefore likely that diminished Semaphorin 3C signalling contributes to the very similar defects seen in *Chd7$^{fl/fl}$;Mesp1-Cre* and *Chd7$^{Whi/fl}$;Mesp1-Cre* hearts. Unpublished work on conditional *Sema3C*

mutants in our lab has shown that *Sema3C* expression is required in both cardiac NCCs and in the SHF-derived myocardial cuff for OFT septation, which signals to endothelial cells via Nrp1 receptors to promote endothelial-mesenchymal transitions for the formation of the OFT endocardial cushions (Amelie Calmont and Catherine Roberts, personal communication). This is consistent with the loss of *Sema3C* expression seen in the myocardial cuff of the OFT of *Chd7$^{fl/fl}$;Mesp1-Cre* hearts contributing to the OFT defects seen in these hearts.

To test the hypothesis that the *Chd7* and *Sema3C* genes epistatically interact in the cardiogenic mesoderm, compound conditional heterozygotes were generated. It was disappointing that these offspring did not exhibit any notable cardiac defects when examined at E13.5 or E15.5. This could indicate that further genes important for OFT development are affected by the loss of CHD7 and also contribute to the OFT defects observed in *Chd7$^{fl/fl}$;Mesp1-Cre* hearts, so looking for epistasis with *Sema3C* alone was insufficient to reproduce defects. Alternatively, it could be that the levels of ablation of *Chd7* and *Sema3C* ablation in the models tested were not efficient enough to produce an epistatic effect, although the use of the *Chd7^{Whi}* allele should have reduced the possibility of this. Constitutively heterozygous *Chd7$^{+/-}$;Sema3C$^{+/-}$* mutants are now being generated to see if extending the knockdown of both genes to multiple tissues will produce an epistatic effect, either on OFT development or great vessel remodelling, as it is clear that *Sema3C* expression is affected by the loss of CHD7 activity.

Sema3A was also downregulated following mesodermal *Chd7* ablation, with ISH showing its trabecular expression was clearly reduced in *Chd7$^{fl/fl}$;Mesp1-Cre* hearts. *Sema3A* has a well-characterised role in the regulation of sympathetic innervation of the heart, which is crucial for the maintenance of a normal heart rhythm. The developing heart is extremely sensitive to *Sema3A* dosage: transgenic mice with cardiac-specific *Sema3A* overexpression demonstrate sudden death and susceptibility to ventricular tachycardia, whilst *Sema3A$^{-/-}$* mice show sinus bradycardia, right ventricular hypertrophy and a dilated right atrium, and usually die before P7 (Behar et al., 1996; Ieda et al., 2007; Taniguchi et al., 1997). Therefore, loss of *Sema3A* expression very likely underlies the sympathetic cardiac innervation defects seen in *Chd7$^{fl/fl}$;Mesp1-Cre* hearts.

Loss-of-function mutations of *SEMA3A* are associated with human Kallmann syndrome (Hanchate et al., 2012), a disorder characterised by defects overlapping with CHARGE. Non-synonymous *SEMA3A* variations have been found in 3 of 45 CHD7-negative CHARGE patients, and *Sema3A* expression is lost after morpholino-knockdown of *Chd7* in *Xenopus* (Schulz et al., 2014b). Hypomorphic mutation of *SEMA3A* has also been reported in a patient with short stature, thoracic abnormalities, and a small self-healing atrial septal defect (Hofmann et al.,

2013). This work therefore strengthens the link between *CHD7* and *SEMA3A* and indicates it is relevant in the context of heart development. Furthermore, it is in agreement with and extends a recent report that *Sema3A* and *Sema3C* have diminished expression in whole E9.5 *Chd7*$^{-/-}$ embryos (Schulz et al., 2014b).

The Slit-Robo pathway is important for endocardial cushion formation and ventricular septation, with membranous VSDs observed at E14.5 in *Slit2*, *Slit3*, *Robo1* and *Robo1;Robo2* mutant mice (Mathilda Mommersteeg, personal communication). Downregulation of *Slit2* and *Robo2* expression is therefore likely to be contributing to the septation defects observed in the conditional *Chd7* mutant embryos. Slit-Robo signalling to endothelial cells is also implicated in vascular development (Park et al., 2003; Zhang et al., 2009). Therefore, the observation of truncated coronary veins after mesodermal, but not endothelial, ablation of *Chd7* may at least in part also be attributed to downregulation of Slit-Robo signalling from cardiomyocytes to migratory endothelial cells. Furthermore, Class 3 Semaphorins and Slit-Robo signalling have been shown to act together for directional control of neuronal migration, in the context of both ventral forebrain and corneal innervation (Hernandez-Miranda et al., 2011; Kubilus and Linsenmayer, 2010). The compound effect of disruption to components of both pathways could therefore contribute to the innervation defects present in *Chd7*$^{fl/fl}$*;Mesp1-Cre* hearts.

Given the highly-penetrant haemorrhagic phenotype in *Chd7*$^{fl/fl}$*;Mesp1Cre* embryos and the disruption to coronary vessel development, it was interesting to see not only Slit-Robo genes dysregulated, but other factors associated with angiogenesis. Angiopoietin-1, which is downregulated in the E11.5 and E13.5 microarray datasets, is a secreted glycoprotein growth factor and a key regulator of blood vessel development, along with its receptor Tie2: *Angpt-1*$^{-/-}$ and *Tie2*$^{-/-}$ mice show early embryonic lethality due to severe vascular defects (Sato et al., 1995; Suri et al., 1996). Cardiomyocyte-specific deletion using *Nkx2.5Cre* also results in embryonic lethality and almost identical phenotype, with vascular remodelling defects seen from E10.5 occurring secondary to cardiac trabeculation defects observed from E9.5, indicating that the vascular abnormalities may be caused by abnormal flow and hemodynamics (Jeansson et al., 2011). Although the phenotypes seen in these knockout studies occur earlier in development than the vascular defects seen in *Chd7*$^{fl/fl}$*;Mesp1Cre* mice, this could be due to a dosage effect, with a smaller reduction in *Angpt-1* expression when CHD7 activity is lost compared to its complete ablation in knockout mice. Poor trabeculation and myocardial compaction is also seen in *Chd7*$^{fl/fl}$*;Mesp1Cre* hearts, so loss of Angiopoietin-1 signalling may be contributing to this. Similarly, the endogenous inhibitor of angiogenesis Thrombospondin-2 (Streit et al., 1999) is upregulated in the *Chd7*$^{fl/fl}$*;Mesp1Cre* hearts, so disruption to a

combination of vascular development genes may be affecting the development of the coronary vasculature.

Finally, consistent with the loss of innervation of *Chd7$^{fl/fl}$;Mesp1-Cre* hearts, a large number of genes associated with neuronal function were also downregulated in *Chd7$^{fl/fl}$;Mesp1-Cre* hearts. Multiple genes for subunits of the GABA A receptor, a chloride channel that mediates inhibitory synaptic transmission, were all downregulated in mutant hearts. This included *Gabrb2*, which was significantly downregulated following multiple testing correction at both E11.5 and E13.5. *Ache* also passed multiple testing correction at E11.5, which encodes acetylcholinesterase, a hydrolase for the synaptic junction neurotransmitter acetylcholine. Many ion channels associated with propagation of electrical signals in neuronal axons were also seen in the lists of downregulated genes. The cardiac sympathetic neurons are derived from the cardiac neural crest (Hasan, 2013), so will not have Cre-driven *Chd7* ablation in *Chd7$^{fl/fl}$;Mesp1-Cre* embryos. The reduction of mRNA transcripts for these genes seen in the microarrays is therefore most likely reflecting the absence of neuronal axons in *Chd7$^{fl/fl}$;Mesp1-Cre* hearts, which would usually be expressing these genes, rather than a role for CHD7 in the transcriptional regulation of these genes.

5.6.2 Direct regulation of Sema3C expression in vivo

The microarray datasets have provided interesting insights into the pathways disrupted in *Chd7$^{fl/fl}$;Mesp1-Cre* hearts, which can be linked with the defects observed. However, the direct targets of CHD7 in the cardiogenic mesoderm still cannot be determined: the differentially-expressed genes identified in the microarrays may be CHD7 targets, with CHD7 binding at their enhancer or promoter regions for direct transcriptional regulation through chromatin remodelling activity, or they may be downstream effects of other CHD7-DNA binding events.

Interrogation of CHD7 occupancy across the genome by chromatin immunoprecipitation (ChIP) followed by high-throughput DNA sequencing (ChIP-seq) would be extremely informative for addressing this issue. CHD7 binding sites in the heart at E11.5 and E13.5 could be compared to the genes with aberrant expression in *Chd7$^{fl/fl}$;Mesp1-Cre* hearts. Unfortunately, despite the use of several antibodies, attempts at genome-wide ChIP-seq by other lab members have not produced an adequate signal-to-noise ratio, either *in vitro* or *in vivo*. This is discussed further in section 6.2.1. However, using chromatin extracted from CD1 E11.5 hearts, it was possible to perform a ChIP experiment followed by qRT-PCR (ChIP-PCR) to show that CHD7 is located specifically at the promoter of *Sema3C.* Primer pairs were designed along the *Sema3C* locus to overlap with areas of DNase I hypersensitivity and histone modification marks associated with

suspected promoter and enhancer regions, based on ENCODE datasets (Figure 5-20, panel A). Enrichment for CHD7 was seen specifically at the promoter region of *Sema3C* (Figure 5-20, panel B).

Furthermore, DNase I hypersensitivity assays were designed to test the accessibility of this region of DNA, giving a readout of chromatin remodelling activity. Sensitivity to increasing concentrations of DNase I was significantly reduced in *Chd7$^{fl/fl}$;Mesp1-Cre* samples compared to control *Chd7$^{fl/fl}$* samples (Figure 5-20, panel C). The promoters of *Gapdh* and *Nanog* were largely unchanged, with the former demonstrating a greater overall level of hypersensitivity (as a reflection of "housekeeping" gene expression). This assay indicates that DNA proximal to the *Sema3C* promoter is in a more condensed conformation when CHD7 activity is abolished. This is consistent with the loss of *Sema3C* expression in the distal OFT of *Chd7$^{fl/fl}$;Mesp1-Cre* hearts. We therefore propose that CHD7 localises to the *Sema3C* promoter during OFT development, where it functions in remodelling the chromatin to ensure transcriptional machinery accessibility.

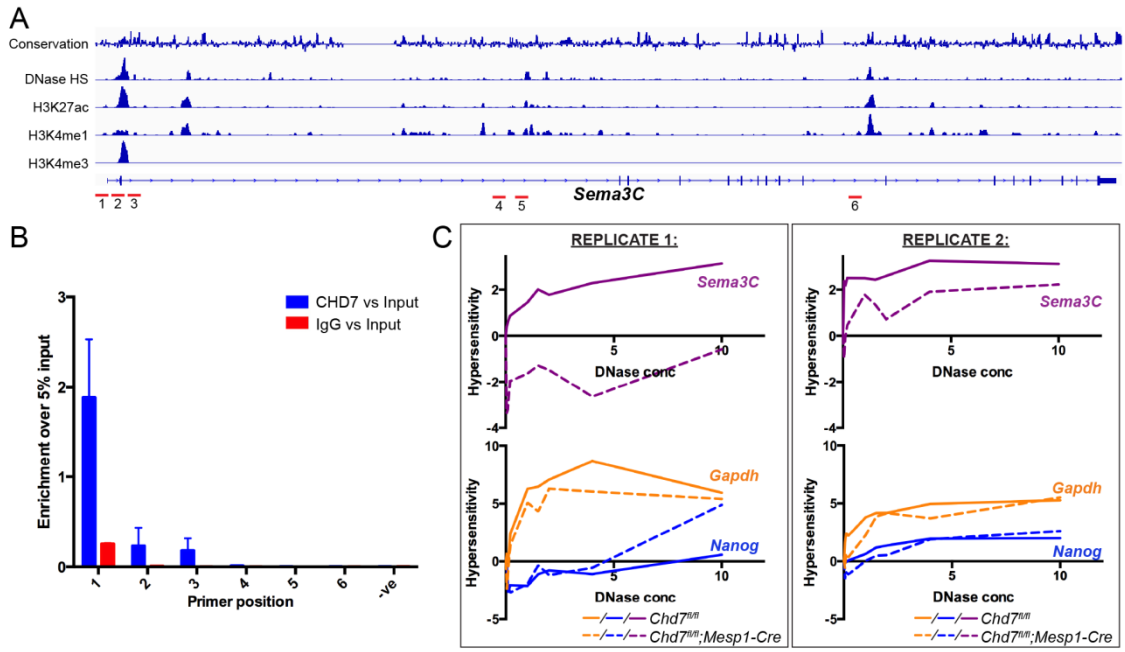

Figure 5-20: CHD7 localises to the Sema3C promoter *in vivo*

(A) ENCODE data around the *Sema3c* locus was used to design primer sets (denoted in red) around potential enhancer and known promoter sites.

(B) ChIP-PCR demonstrated CHD7 binding around the promoter using Primer 1.

(C) DNase hypersensitivity assay showed greater chromatin compaction in *Chd7$^{fl/fl}$;Mesp1-Cre* hearts (dotted line) than littermate controls (solid line) at the *Sema3c* promoter. Little change was seen at the *Gapdh* or *Nanog* promoters, although *Gapdh* displayed greater hypersensitivity, correlating with its constitutive expression. Individual replicates are shown, due to extreme biological variability.

Figure taken from manuscript by Payne et al. (submitted to Circulation Research), experiments carried out by Matthew Burney and included with his permission.

5.6.3 CHD7 activity impacts on excitation-contraction coupling

Following mesodermal ablation of *Chd7,* gene expression alterations were also detected that are associated with Ca^{2+} signalling, resulting in functional defects in the ability of embryonic cardiomyocytes to respond to electrical pacing *in vitro*. This indicated a failure of the key process of excitation-contraction coupling. The developing mouse heart beats from about E8.5, and it is uncertain whether membrane voltage-activated Ca^{2+} channels or spontaneous Ca^{2+} release from SR stores in cardiomyocytes drives this process (Rapila et al., 2008). Either way, genes encoding both Ca^{2+} channels and key components involved in Ca^{2+}-induced Ca^{2+} release (CICR) from the SR were dysregulated in *Chd7$^{fl/fl}$;Mesp1-Cre* hearts. The loss of coordinated excitation-contraction coupling is therefore likely a contributing cause of the cardiac failure leading to the severe oedema seen in *Chd7$^{fl/fl}$;Mesp1-Cre* embryos and embryonic lethality. This oedema was not seen in *Tie2-Cre* embryos and is therefore not likely to be secondary to a role for CHD7 in vascular endothelial cells. Furthermore, it is becoming evident that coordinated Ca^{2+} release is itself an important factor in regulating cardiac morphogenesis, for example through secretion of signalling molecules and force generation (Puceat and Jaconi, 2005). Therefore, the disruption to Ca^{2+} handling may have relevance for the structural malformations observed in *Chd7$^{fl/fl}$;Mesp1-Cre* mice.

The low expression of L-type voltage-dependent Ca^{2+} channels in *Chd7$^{fl/fl}$;Mesp1-Cre* cardiomyocytes likely results in the inability to generate a sufficient Ca^{2+} influx at the sarcolemmal membrane in response to electrical excitation. This would lead to the observed phenotype in which immature *Chd7$^{fl/fl}$;Mesp1-Cre* cardiomyocytes could not be fully paced by electrical field stimulation. Whilst some mutant cardiomyocytes did not appear to respond at all to the electrical pacing, continuing to show apparently random Ca^{2+} transient peaks, many appeared to respond to alternate electrical stimuli – i.e. peaks were seen every 2 seconds instead of every second- for at least some of the period of observation (see bottom panel, Figure 5-18). This would be consistent with a situation in which two membrane depolarisations are required for sufficient Ca^{2+} current into the cell to raise the intracellular Ca^{2+} to a level to trigger CICR from the SR stores. The variation between the severity of the phenotype between *Chd7$^{fl/fl}$;Mesp1-Cre* cardiomyocytes probably reflects varying levels of reduction of gene expression between cells, as well as the presence of cardiomyocytes of varying maturity within the population of isolated cells. It is possible that the overall population of *Chd7$^{fl/fl}$;Mesp1-Cre* cardiomyocytes was less developmentally mature than the *Chd7$^{fl/fl}$* controls, which could also explain the differences in excitation-contraction coupling, but if so then the disruption to the Ca^{2+} handling genes would still likely be involved in this maturity delay.

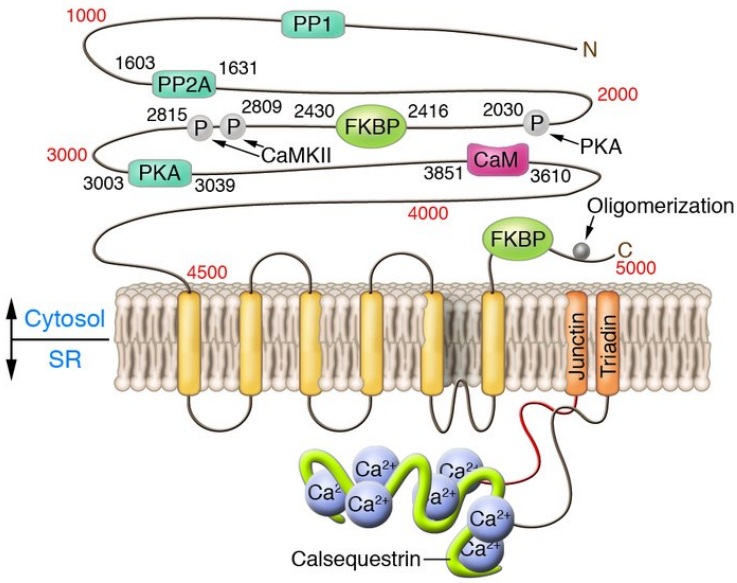

Figure 5-21: The cardiac Ryanodine Receptor structure at the SR membrane

The Ryanodine Receptor is shown at the SR membrane with six predicted transmembrane regions and a large cytoplasmic domain. It is associated at the SR membrane with both Triadin and Junctin, and the SR protein Calsequestrin. Phosphorylation sites and sites of interaction with ancillary proteins in the cytoplasmic domain are also shown.

Figure from Priori and Napolitano (2005). PP indicates protein phosphatase; P, phosphorylation site; CaM, Calmodulin; CaMKII, Calmodulin-dependent protein kinase II.

Transcripts for key SR proteins involved in CICR were also dysregulated, which would exacerbate the disruption to excitation-contraction coupling. At the SR membrane, Calsequestrin 2, Triadin and Junction form a complex that helps regulate SR Ca^{2+} release through interactions with the cardiac Ryanodine Receptor (RyR) 2 channel (see Figure 5-21) (Zhang et al., 1997). Calsequestrin 2 and Triadin transcripts were aberrantly expressed in *Chd7$^{fl/fl}$;Mesp1-Cre* hearts, along with RyR3. Mutations to *Casq2* and *Trdn* are both associated with inherited arrhythmogenic diseases, showing their importance for excitation-contraction coupling (Lahat et al., 2001; Roux-Buisson et al., 2012). Furthermore, Triadin has been shown to have an additional role in maintaining the structural integrity of the cardiac calcium release unit (CRU), with its ablation leading to impaired excitation-contraction coupling (Chopra et al., 2009). Downregulation of these genes in *Chd7$^{fl/fl}$;Mesp1-Cre* hearts is therefore also likely making a significant contribution to the observed Ca^{2+} handling defect.

This work has identified a novel role for CHD7 activity upstream of the expression of multiple components critical for the coordinated excitability of cardiomyocytes. To the author's knowledge, dysregulation of these components has not been remarked upon in any other transcriptomics analysis of hearts mutant for chromatin regulators. Interestingly, however,

embryos mutant for the splicing regulator SRp38 also show disruption to Triadin and Calsequestrin 2 expression, leading to cardiac defects and abnormal Ca^{2+} release from the SR (Feng et al., 2009). This was shown to be due to altered splicing of Triadin pre-mRNAs in the absence of SRp38. Ca^{2+} transients were examined in similar primary cultures of embryonic cardiomyocytes from E14.5 hearts, although this analysis focussed on the properties of the Ca^{2+} sparks, which are the elementary Ca^{2+} release events from the SR that underlie excitation-contraction coupling (Cheng et al., 1993). Spark frequency was significantly increased in *SRp38*$^{-/-}$ cardiomyocytes compared to wild-type controls, whilst the amplitude was reduced, demonstrating disruption to the Ca^{2+} handing at the SR. It would have been interesting to look at Ca^{2+} sparks in the *Chd7*$^{fl/fl}$*;Mesp1-Cre* cardiomyocytes as well, to see if a similar disruption could be detected: Ca^{2+} sparks were noted in both *Chd7*$^{fl/fl}$ and *Chd7*$^{fl/fl}$*;Mesp1-Cre* cells, but no quantitative analysis was carried out to compare their frequency between genotypes. Cardiac defects were also noted in *SRp38*$^{-/-}$ embryos, including severe oedema, thin and disorganised myocardial walls, and AVSDs, which are markedly similar to those seen in *Chd7*$^{fl/fl}$*;Mesp1-Cre* cells. This again supports the hypothesis that the disruption to Ca^{2+} handling and the coordination of cardiomyocyte contractions contributes to the structural malformations seen in *Chd7*$^{fl/fl}$*;Mesp1-Cre* mice.

5.6.4 Disruption to NKX2.5 activity and BMP signalling likely underlies the DILV phenotype

CHD7 has previously been shown to interact with BMP-activated SMAD1/5/8 during early cardiogenesis, to regulate directly the cardiac differentiation marker *Nkx2.5* (Liu et al., 2014). BMP activity was abrogated in the AV canals of *Chd7* mutant embryos around E10.0, leading to reduced myocardial proliferation and defective cushion formation. BMP signalling is vital for development of the vestibular spine and AV septation: conditional deletion of the BMP receptor Alk3 in the SHF leads to impaired formation of the vestibular spine and ostium primum defects, caused by a lack of expansion of the SHF-derived vestibular spine population at the venous pole (Briggs et al., 2013). Disruption to NKX2-5-mediated BMP signalling in the early heart tube following *Chd7* ablation therefore offers a likely molecular basis for the common AV valves and DILVs seen in *Chd7*$^{fl/fl}$*;Mesp1-Cre* hearts. However, aberrant expression of *Nkx2.5* was not identified in the E11.5 and E13.5 microarrays, although it is known to still be expressed in the atrial and ventricular chambers at E12.5 (Lints et al., 1993), so it seems that later in cardiac development CHD7 no longer regulates *Nkx2.5* expression.

Other pathways at E9.5 with known roles in venous pole development were also examined. TGFβ signalling is important for endocardial cushion development and myocardialisation of the developing heart (Azhar et al., 2003). Endocardial inactivation of the *Tgfbr2* receptor provides a model for DILV (Jiao et al., 2006), whilst homozygous mutation of *Tgfb2* can result in DILV and AVSDs (Bartram et al., 2001). *Wnt2* expression in the posterior second heart field is also crucial for correct development of the inflow tract, with *Wnt2*$^{-/-}$ mutants also displaying AVSDs (Tian et al., 2010). However, neither *Tgfbr2* or *Wnt2* expression was affected at E9.5, indicating that disruption to BMP signalling, as described by Liu and colleagues, is most likely the major contributor to the venous pole component of the *Chd7*$^{fl/fl}$*;Mesp1-Cre* cardiac phenotype.

It would be useful to perform genome-wide transcriptional analysis at E9.5, to confirm that BMP signalling is disrupted, as well as to identify any additional pathways or transcription factors that lie downstream of CHD7 activity in the early heart tube. It would be preferable to use RNA-sequencing (RNA-Seq) technology for transcriptome profiling of *Chd7*$^{fl/fl}$ and *Chd7*$^{fl/fl}$*;Mesp1-Cre* hearts. RNA-Seq uses deep-sequencing technology rather than the hybridisation methods used in the DNA microarray. A population of RNA molecules can be converted to a library of cDNA fragments that have adaptors added to one or both ends, and then each individual molecule is sequenced and compared to a reference genome. The result is a genome-scale transcriptional map with information on both transcriptional structure and the level of expression for each gene, which has less background signal and a much higher dynamic range compared with DNA microarray (Wang et al., 2009). Furthermore, the bias caused by probe specificity and binding strength during hybridisation in microarrays is not an issue with RNA-seq, and it is able to measure non-coding RNAs. At the time of performing the E11.5 and E13.5 microarrays presented here, protocols for the analysis of microarray datasets were better established than for RNA-Seq datasets. However, better tools and standardised protocols are now available for this analysis (Anders et al., 2013; Luo and Brouwer, 2013; Ramsköld, 2012).

Overall, this chapter has shown genome-wide analysis of differential transcription in *Chd7*$^{fl/fl}$*;Mesp1-Cre* hearts at two developmental time points. Of particular interest, Slit-Robo and Semaphorin extracellular signalling pathway genes with known roles in heart development were found to be aberrantly expressed, and were validated further. Functional analysis of Ca^{2+} transients in *Chd7*$^{fl/fl}$*;Mesp1-Cre* cardiomyocytes was also performed, showing that differential expression of Ca^{2+} handling genes affects the excitation-contraction coupling capability of mutant cardiomyocytes. Together, these gene expression changes correlate well with the cardiac malformations seen in *Chd7*$^{fl/fl}$*;Mesp1-Cre* hearts.

CHAPTER SIX

OVERALL DISCUSSION AND FUTURE WORK

6.1 Final discussion and conclusions

Chromatin remodelling allows the dynamic regulation of gene expression programmes, which is required for the complex morphological changes that occur with both temporal and spatial precision in the developing heart. The ATP-dependent chromatin remodeller CHD7 has been shown here to be present throughout the early heart until around E13.5, with its activity in the cardiogenic mesoderm crucial for formation of cardiac structures, heart function, and embryonic survival. CHD7 activity affects transcription of a large number of genes instrumental for cardiovascular development, including components of the Slit-Robo and Semaphorin signalling pathways and the excitation-contraction coupling machinery. Thus, it is clear that transcriptional regulation by CHD7 in the cardiogenic mesoderm and its derivatives is crucial during heart development.

Correct alignment and septation of the developing cardiac components ensures the complete separation of the pulmonary and systemic circulations, which is vital for effective cardiovascular function. Mesodermal *Mesp1-Cre*-driven deletion of *Chd7* produced a serious defect combining DILV and DORV with spiralling arterial trunks. This is analogous to the "Holmes heart" seen in humans, although in the heart initially described by Holmes the ventriculo-arterial trunks, whilst spiralling, were concordantly connected in the heart (Dobell and Van Praagh, 1996). Common AV junction, caused at least in part by failure of the formation of the vestibular spine and disorganisation of the AV endocardial cushions, and great vessel defects were also frequently observed. Many of these defects had not been previously described in *Chd7* mutant mice due to the p53-dependent severe growth delay observed in constitutive mutants (Van Nostrand et al., 2014). This bypass of early lethality through the use of conditional *Chd7* ablation has therefore allowed the exploration of more specific effects on heart development. Furthermore, the cardiovascular defects described in *Chd7*$^{fl/fl}$*;Mesp1-Cre* embryos correlate well with the malformations seen in CHARGE patients, in which AVSDs and OFT defects are common (Corsten-Janssen et al., 2013a), supporting the importance of CHD7 activity in the cardiogenic mesoderm.

Investigation into other conditional *Chd7* mutants, driven by *Nkx2.5-Cre*, *Mef2c-Cre* and *Tie2-Cre,* demonstrated a requirement for *Chd7* activity in multiple lineages within the cardiogenic

mesoderm. Each cross resulted in a milder subset of the cardiac defects observed after mesodermal ablation, with varying severity and penetrance. *Chd7$^{fl/fl}$;Nkx2.5-Cre* embryos showed the most similar cardiac defects to *Chd7$^{fl/fl}$;Mesp1-Cre* embryos, which was reflected in the perinatal lethality for this genotype. However, it appears ablation in both endocardial and myocardial precursors is required to produce the characteristic combination of DORV and DILV seen in *Chd7$^{fl/fl}$;Mesp1-Cre* embryos. Meanwhile, the interrupted aortic arch phenotype can be attributed to loss of CHD7 activity in the anterior SHF, as *Chd7$^{fl/fl}$;Mef2c-Cre* recapitulated the great vessel defects. This requirement for *Chd7* in multiple lineages derived from *Mesp1*-expressing progenitors is consistent both with the presence of CHD7 throughout the developing heart until E13.5, and with the range of cardiovascular defects observed in *Chd7$^{fl/fl}$;Mesp1-Cre* embryos affecting structures derived from various cardiac tissues.

Datasets generated by microarray experiments showed aberrant expression of a large number of genes in the heart following ablation of *Chd7* in the cardiogenic mesoderm. This is consistent with previous reports that CHD7 acts as a 'transcriptional rheostat' to modulate the expression of its target genes in either a positive or negative direction (Schnetz et al., 2010). Downregulation of *Sema3C* in the distal OFT of *Chd7$^{fl/fl}$;Mesp1-Cre* hearts is likely contributing to the alignment and septation defects observed at the arterial pole, whilst loss of *Sema3A* in the trabeculae may be contributing to the severe truncation of sympathetic neurons seen on the dorsal side of these hearts or to the thin myocardial walls. Disruption to the Slit-Robo pathway may also be exacerbating this innervation defect, as well as contributing to the endocardial cushion defects, which are linked to the septation defects observed. Extracellular signalling is vital during development for cells to communicate and direct key processes such as migration, differentiation, proliferation or apoptosis, so it is unsurprising that loss of key extracellular signals such as the Semaphorins can disrupt multiple components of cardiovascular development.

Disruption to the expression of genes associated with excitation-contraction coupling in cardiomyocytes was also seen in the microarray data, and this was shown to be having a functional affect through the analysis of Ca^{2+} transients in primary embryonic cardiomyocyte cultures. Loss of coordinated cardiomyocyte contractility due to aberrant Ca^{2+} handling would severely reduce cardiac function. This could have impacted on the structural cardiac malformations observed, in addition to contributing to the severe oedema seen from E13.5 in *Chd7$^{fl/fl}$;Mesp1-Cre* embryos.

Elucidating the roles of CHD7 in mesodermal derivatives alters our perspective on the etiology of the cardiovascular malformations associated with CHARGE syndrome. Whilst an additional

requirement for CHD7 in NCCs is not ruled out, the classification of CHARGE as a neurocristopathy appears to be an over-simplification, at least with regard to the heart defects. Furthermore, conditional deletion of *Chd7* has also allowed identification of some of the genes affected by CHD7 activity later during cardiogenesis than was possible with *Chd7*$^{-/-}$ embryos. Notably, these included extracellular signalling and calcium handling genes, as opposed to master-regulator transcription factors such as NKX2-5, suggesting a switch in the types of genes CHD7 regulates as cardiogenesis progresses. Overall, this work provides novel insights into the tissue-specific requirement and roles of CHD7 during cardiovascular development.

6.2 Future work

The work presented in this thesis has characterised the cardiovascular phenotype following various lineage-specific conditional ablations of *Chd7*, and addressed the transcriptional changes that occur in the developing heart when CHD7 activity is lost. This final section will briefly highlight a number of more general questions that remain in our understanding of the role of CHD7 during cardiovascular development.

6.2.1 Where does CHD7 bind on a genome-wide scale in the cardiogenic mesoderm?

As discussed in section 5.6.2, despite seeing major cardiovascular malformations when *Chd7* is ablated in the developing heart, we have little information about CHD7 genome occupancy in the cardiogenic mesoderm. The optimal way to address this issue would be by genome-wide chromatin immunoprecipitation (ChIP) followed by high-throughput DNA sequencing (ChIP-seq), which would allow global comparison of CHD7 binding sites with altered gene expression. This has been attempted by other lab members, both *in vitro* and *in vivo*. Attempts *in vitro* involved utilising an ESC line transformed with a BAC construct expressing CHD7 with a C-terminal TAP tag, which contains three FLAG tags and two calmodulin-binding proteins for tandem affinity purification, that would be differentiated to a cardiomyocyte lineage. This was based on several recent studies that tracked epigenetic and transcriptional changes as ESCs were differentiated through a series of defined states to a cardiomyocyte lineage (Paige et al., 2012; Wamstad et al., 2012). However, this *in vitro* work was hampered by the fact that pure populations of cardiomyocytes cannot be generated through differentiation of ESCs. Unfortunately, attempts at labelling cells with fluorescently-tagged cardiomyocyte-specific proteins, to allow them to be sorted by FACS, were unsuccessful, so efforts were instead focussed on *in vivo* experiments.

The *in vitro* work did allow optimisation of the CHD7 ChIP protocol sufficiently to perform the ChIP-PCR experiment shown in Figure 5-20, which demonstrated localisation of CHD7 specifically at the *Sema3C* promoter at E11.5 *in vivo.* A key modification was the use of disuccinimidyl glutarate (DSG) rather than formamide for the fixation step in the ChIP protocol, as this fixative has a range of ~8Å, which is four times greater than formamide. The requirement for DSG fixation reflects the fact that CHD7 is thought to interact with histone modifications via its chromodomains, so the majority of this large protein is not in direct contact with the DNA. However, attempts at genome-wide ChIP-seq *in vivo* using chromatin extracted from approximately 50 wild-type hearts were unsuccessful, as insufficient material was retrieved for sequencing, so the resulting signal-to-noise ratio was too low (Matthew

Burney, personal communication). In the future, it could be useful to repeat this experiment with a significant increase in the number of hearts from which chromatin collected, to attempt to overcome this issue. Notably, the only ChIP-seq datasets that have been published for CHD7 were produced by Schnetz and colleagues on ESCs and other *in vitro* cell lines, using an Abcam antibody that is no longer available, so this appears to be a common problem for researchers working on CHD7 (Schnetz et al., 2009; Schnetz et al., 2010).

As an alternative to ChIP-seq, it would be interesting to compare *Chd7*$^{fl/fl}$ and *Chd7*$^{fl/fl}$*;Mesp1-Cre* samples using genome-wide mapping of DNase I or MNase hypersensitivity sites. A DNase I hypersensitivity assay was already successfully carried out specifically at the *Sema3C* locus, as discussed in section 5.6.2, with a reduction in DNase I hypersensitiy seen in *Chd7*$^{fl/fl}$*;Mesp1-Cre* hearts indicating a more closed chromatin conformation in the absence of CHD7. To extend this, these endonuclease assays can be followed by massively-parallel sequencing to give an indication of the accessibility of regions of DNA on a genome-wide scale (Crawford et al., 2006). The loci of genes differentially regulated in *Chd7*$^{fl/fl}$*;Mesp1-Cre* hearts could therefore be interrogated for changes in their chromatin structure and accessibility when CHD7 activity is ablated, to identify potential regulatory elements. A more recently-developed, highly sensitive assay for transposase-accessible chromatin using sequencing (ATAC-seq) could also be informative: this protocol is based on direct *in vitro* transposition of sequencing adaptors into native chromatin to capture open chromatin sites, so it could be utilised to compare cultured embryonic cardiomyocytes (Buenrostro et al., 2013).

Whilst the identification of genomic loci with altered chromatin structure in *Chd7*$^{fl/fl}$*;Mesp1-Cre* heart would not confirm direct CHD7 binding, they could still be extremely useful for identifying further candidate genes that may be directly regulated by CHD7 in the cardiogenic mesoderm, as CHD7 activity involves the repositioning of nucleosomes. The identification of possible regulatory elements at which CHD7 is located would be extremely useful, as in the absence of ChIP-seq data, the next best option is ChIP-PCR at candidate genes. However, this technique requires prediction of the exact locus where CHD7 potentially binds, as primers need to be designed to test these sites by qRT-PCR following the CHD7 ChIP. This can be extremely challenging, and is an obvious limitation of this technique, so if data is available on loci with altered chromatin structure, primers could be designed around these sites to look for CHD7 enrichment using ChIP-PCR.

6.2.2 What are the interaction partners of CHD7 during cardiogenesis?

Genome-wide data on CHD7 binding sites would not only be informative for correlating the direct CHD7 cardiovascular targets versus downstream effects of CHD7 activity, but could also help to identify interaction partners for CHD7 during cardiogenesis. DNA-interacting proteins that overlap with CHD7 on the genome or are in close proximity may be in a common complex, or be involved in the recruitment of CHD7 to target loci on the genome. Therefore, the regions around CHD7 binding sites could be interrogated for known transcription factor binding sites or other regulatory sequences, using motif-finding software such as TFM-Scan, which utilises Position Weight Matrices to locate large sets of putative transcription factor binding sites on a DNA sequence (Liefooghe A., 2006). This analysis could focus particularly on the regions surrounding differentially-expressed genes identified in *Chd7$^{fl/fl}$;Mesp1-Cre* hearts.

ENCODE datasets from other ChIP-seq experiments focussing on cardiogenic factors could also be compared to CHD7 ChIP-seq data, to identify overlapping binding sites. For example, ChIP-seq data is available for the genome occupancy of the cardiac transcription factors GATA4, Nkx2-5, Tbx5, SRF and Mef2A in the HL1 cell line (He et al., 2011), as well as predicted cardiac enhancers based on p300 genome occupancy in E11.5 hearts (Blow et al., 2010). Candidate genes identified through this bioinformatics approach could then be tested by co-immunoprecipitation, *in vitro* using the tagged constructs previously mentioned, or *in vivo* using native protein extracted from dissected embryonic hearts.

In the absence of CHD7 ChIP-seq data, a yeast two-hybrid assay could be performed using a *Chd7* bait construct. This has been carried out for a number of other proteins important for cardiovascular development, such as TBX20 and SMAD1, with screening libraries generated from cDNA isolated from embryonic hearts (Debenedittis et al., 2011; Liu et al., 2014). Alternatively, immunoprecipitation of CHD7 followed by mass spectrometry would be a sensitive and accurate method for identification of protein complexes and interaction partners (ten Have et al., 2011). Obtaining information about proteins that interact with CHD7 during cardiogenesis would further our understanding about the mechanisms through which specificity for CHD7 localisation on the genome is achieved, and how CHD7 activity influences the transcriptional networks that regulates cardiovascular development. As previously mentioned, it appears that CHD7 regulates master transcription factors such as Nkx2-5 early in cardiogenesis, but later affects the transcription of intra- and extracellular signalling pathways. This switch could be through the recruitment of CHD7 to target genes by different protein complexes, which are cell-type and stage-specific during cardiovascular development. CHD7 binding on the genome has previously been shown to be cell-type specific (Schnetz et al.,

2009), and whilst this was associated with changes in H3K4me patterns, interactions between CHD7 and other nuclear proteins may also play a key role in this specificity.

6.2.3 Is CHD7 required in other tissues for cardiovascular development?

Tissue-specific ablation of *Chd7* in the cardiogenic mesoderm, cardiomyocytes, SHF and endothelial cells has been demonstrated here to be sufficient to produce a range of cardiovascular defects of varying severity and penetrance. This alters our perspective on the etiology of CHARGE syndrome, which has traditionally been considered a neurocristopathy, by showing that CHD7 activity plays a key role in the cardiogenic mesoderm. However, this work does not rule out an additional role for *Chd7* in cardiac NCCs, which could be contributing to the heart defects seen in CHARGE patients.

Conditional ablation of *Chd7* in NCCs, driven by *Wnt1-Cre*, has been described recently by Sperry and colleagues. Whilst major craniofacial defects were observed in *Chd7$^{fl/fl}$;Wnt1-Cre* embryos, consistent with the known contribution of NCCs to the cartilage and bones during craniofacial morphogenesis (Cordero et al., 2011), cardiac defects were not identified. Hearts were examined for pharyngeal arch artery defects at E10.5, and great vessel defects or septation defects at E16.5, but all hearts examined looked normal (Sperry et al., 2014). This would indicate that *Chd7* is not required in cardiac NCCs for heart or great vessel development. However, *Chd7$^{fl/fl}$;Wnt1-Cre* embryos were also examined in our lab, and although great vessel defects were also absent, a number of these embryos showed VSDs and one had a common arterial trunk (Karen McCue, personal communication). This indicates that CHD7 activity is required in NCCs as they contribute to the septation of the OFT and ventricles. Further work is therefore required to resolve this contradiction, and to identify genes potentially regulated by CHD7 activity in cardiac NCCs.

Given the importance of both *Chd7* and *Tbx1* dosage in the pharyngeal surface ectoderm for great vessel development (Randall et al., 2009), it would also be interesting to investigate the cardiovascular phenotype in mice with *Chd7* ablation driven by *AP2αIRES-Cre*. There is currently not a *Cre* line available that is active only in the pharyngeal surface ectoderm, but *AP2αIRES-Cre* drives recombination in both NCCs and the pharyngeal ectoderm. Any additional defects seen in *Chd7$^{fl/fl}$; AP2αIRES-Cre* embryos compared to *Chd7$^{fl/fl}$;Wnt1-Cre* embryos therefore could be attributed to the loss of *Chd7* in the ectoderm.

6.2.4 What happens if Chd7 is reactivated after myocardial injury?

In Chapter Three, the possibility that *Chd7* expression could be reactivated in pathological situations was discussed. This was hypothesised based on the similarity in embryonic, but not postnatal, cardiac expression between *Chd7* and *Brg1*, and their similar chromatin remodelling activity. Briefly, *Brg1* has been found to be re-expressed in hypertrophic hearts in response to cardiac stresses, which induces a pathological switch between adult and fetal myosin heavy chain isotopes (Hang et al., 2010). If Chd7 were also re-activated, this could identify it as a new therapeutic target. Another intriguing research question that arises from the work presented in this thesis is whether CHD7 reactivation following myocardial injury would have a therapeutic benefit. Novel roles have been identified for CHD7 upstream of cardiac innervation, coronary venous development and calcium handling in cardiogenic progenitors, which are all processes that could aid with the repair of damaged tissue following infarction.

Many recent studies have focussed on reprogramming of non-myocytes into cardiomyocytes by inducing expression of key transcription factors or miRNAs with known roles during heart development (reviewed in (Xin et al., 2013)). Similarly, the actin sequestering protein thymosin β4 (Tβ4) was found to regulate coronary vasculature development during embryogenesis and stimulate neovascularisation following myocardial infarction and ischaemia (Smart et al., 2007). Re-expression of a chromatin remodeller such as CHD7, itself affecting multiple gene expression programmes, could have a broad effect on gene expression programmes to help stimulate cardiac regeneration and repair.

6.3 Summary

Chromatin remodelling activity by CHD7 plays a crucial role in the cardiogenic mesoderm for the transcriptional regulation of multiple genes involved in cardiovascular development. Serious cardiac malformations result from conditional ablation of *Chd7* in the cardiogenic mesoderm, which are analogous to the rare human Holmes heart, leading to cardiac failure and embryonic lethality around E15.5. CHD7 activity lies upstream of Class 3 Semaphorin and Slit-Robo signalling in the developing heart, as well as components critical for the excitation-contraction coupling of cardiomyocytes. Together, these molecular changes contribute to the range of defects seen in conditional *Chd7* mutants. This work therefore furthers our understanding of both the tissue-specific requirements for *Chd7* during cardiovascular development and the downstream transcriptional changes caused by loss of CHD7 activity.

REFERENCES

Akcaboy, M.I., Cengiz, F.B., Inceoglu, B., Ucar, T., Atalay, S., Tutar, E., and Tekin, M. (2008). The effect of p.Arg25Cys alteration in NKX2-5 on conotruncal heart anomalies: mutation or polymorphism? Pediatr Cardiol *29*, 126-129.

Alavizadeh, A., Kiernan, A.E., Nolan, P., Lo, C., Steel, K.P., and Bucan, M. (2001). The Wheels mutation in the mouse causes vascular, hindbrain, and inner ear defects. Dev Biol *234*, 244-260.

Anders, S., McCarthy, D.J., Chen, Y., Okoniewski, M., Smyth, G.K., Huber, W., and Robinson, M.D. (2013). Count-based differential expression analysis of RNA sequencing data using R and Bioconductor. Nature protocols *8*, 1765-1786.

Anderson, R.H., Brown, N.A., and Webb, S. (2002). Development and structure of the atrial septum. Heart *88*, 104-110.

Anderson, R.H., Webb, S., Brown, N.A., Lamers, W., and Moorman, A. (2003a). Development of the heart: (2) Septation of the atriums and ventricles. Heart *89*, 949-958.

Anderson, R.H., Webb, S., Brown, N.A., Lamers, W., and Moorman, A. (2003b). Development of the heart: (3) formation of the ventricular outflow tracts, arterial valves, and intrapericardial arterial trunks. Heart *89*, 1110-1118.

Antonarakis, S.E., Krawczak, M., and Cooper, D.N. (2000). Disease-causing mutations in the human genome. Eur J Pediatr *159 Suppl 3*, S173-178.

Aramaki, M., Udaka, T., Kosaki, R., Makita, Y., Okamoto, N., Yoshihashi, H., Oki, H., Nanao, K., Moriyama, N., Oku, S*., et al.* (2006). Phenotypic spectrum of CHARGE syndrome with CHD7 mutations. J Pediatr *148*, 410-414.

Aruga, J., and Mikoshiba, K. (2003). Identification and characterization of Slitrk, a novel neuronal transmembrane protein family controlling neurite outgrowth. Molecular and cellular neurosciences *24*, 117-129.

Asahina, K., Tsai, S.Y., Li, P., Ishii, M., Maxson, R.E., Jr., Sucov, H.M., and Tsukamoto, H. (2009). Mesenchymal origin of hepatic stellate cells, submesothelial cells, and perivascular mesenchymal cells during mouse liver development. Hepatology *49*, 998-1011.

Atkinson, S., and Armstrong, L. (2008). Epigenetics in embryonic stem cells: regulation of pluripotency and differentiation. Cell and tissue research *331*, 23-29.

Azhar, M., Schultz Jel, J., Grupp, I., Dorn, G.W., 2nd, Meneton, P., Molin, D.G., Gittenberger-de Groot, A.C., and Doetschman, T. (2003). Transforming growth factor beta in cardiovascular development and function. Cytokine Growth Factor Rev *14*, 391-407.

Azpiazu, N., and Frasch, M. (1993). tinman and bagpipe: two homeo box genes that determine cell fates in the dorsal mesoderm of Drosophila. Genes Dev *7*, 1325-1340.

Bajpai, R., Chen, D.A., Rada-Iglesias, A., Zhang, J., Xiong, Y., Helms, J., Chang, C.P., Zhao, Y., Swigut, T., and Wysocka, J. (2010). CHD7 cooperates with PBAF to control multipotent neural crest formation. Nature *463*, 958-962.

Bartels, C.F., Scacheri, C., White, L., Scacheri, P.C., and Bale, S. (2010). Mutations in the CHD7 gene: the experience of a commercial laboratory. Genetic testing and molecular biomarkers *14*, 881-891.

Barth, J.L., Clark, C.D., Fresco, V.M., Knoll, E.P., Lee, B., Argraves, W.S., and Lee, K.H. (2010). Jarid2 is among a set of genes differentially regulated by Nkx2.5 during outflow tract morphogenesis. Developmental dynamics : an official publication of the American Association of Anatomists *239*, 2024-2033.

Bartram, U., Molin, D.G., Wisse, L.J., Mohamad, A., Sanford, L.P., Doetschman, T., Speer, C.P., Poelmann, R.E., and Gittenberger-de Groot, A.C. (2001). Double-outlet right ventricle and overriding tricuspid valve reflect disturbances of looping, myocardialization, endocardial cushion differentiation, and apoptosis in TGF-beta(2)-knockout mice. Circulation *103*, 2745-2752.

Basch, M.L., and Bronner-Fraser, M. (2006). Neural crest inducing signals. Adv Exp Med Biol *589*, 24-31.

Basson, C.T., Bachinsky, D.R., Lin, R.C., Levi, T., Elkins, J.A., Soults, J., Grayzel, D., Kroumpouzou, E., Traill, T.A., Leblanc-Straceski, J.*, et al.* (1997). Mutations in human TBX5 [corrected] cause limb and cardiac malformation in Holt-Oram syndrome. Nat Genet *15*, 30-35.

Batsukh, T., Pieper, L., Koszucka, A.M., von Velsen, N., Hoyer-Fender, S., Elbracht, M., Bergman, J.E., Hoefsloot, L.H., and Pauli, S. (2010). CHD8 interacts with CHD7, a protein which is mutated in CHARGE syndrome. Hum Mol Genet *19*, 2858-2866.

Batsukh, T., Schulz, Y., Wolf, S., Rabe, T.I., Oellerich, T., Urlaub, H., Schaefer, I.M., and Pauli, S. (2012). Identification and characterization of FAM124B as a novel component of a CHD7 and CHD8 containing complex. PLoS One *7*, e52640.

Beaubien, F., and Cloutier, J.F. (2009). Differential expression of Slitrk family members in the mouse nervous system. Dev Dyn *238*, 3285-3296.

Becker, P.B. (2002). Nucleosome sliding: facts and fiction. Embo J *21*, 4749-4753.

Becker, P.B., and Horz, W. (2002). ATP-dependent nucleosome remodeling. Annu Rev Biochem *71*, 247-273.

Behar, O., Golden, J.A., Mashimo, H., Schoen, F.J., and Fishman, M.C. (1996). Semaphorin III is needed for normal patterning and growth of nerves, bones and heart. Nature *383*, 525-528.

Benjamini, Y.a.H., Y (1995). Controlling the False Discovery Rate: a Practical and Powerful Approach to Multiple Testing. Journal of the Royal Statistical Society B *57*, 289 -300.

Bergemann, A.D., Cole, F., and Hirschhorn, K. (2005). The etiology of Wolf-Hirschhorn syndrome. Trends in genetics : TIG *21*, 188-195.

Bergman, J.E., de Ronde, W., Jongmans, M.C., Wolffenbuttel, B.H., Drop, S.L., Hermus, A., Bocca, G., Hoefsloot, L.H., and van Ravenswaaij-Arts, C.M. (2012). The results of CHD7 analysis in clinically well-characterized patients with Kallmann syndrome. J Clin Endocrinol Metab *97*, E858-862.

Bernstein, B.E., Mikkelsen, T.S., Xie, X., Kamal, M., Huebert, D.J., Cuff, J., Fry, B., Meissner, A., Wernig, M., Plath, K.*, et al.* (2006). A bivalent chromatin structure marks key developmental genes in embryonic stem cells. Cell *125*, 315-326.

Bers, D.M. (2002). Cardiac excitation-contraction coupling. Nature *415*, 198-205.

Bers, D.M. (2004). Macromolecular complexes regulating cardiac ryanodine receptor function. J Mol Cell Cardiol *37*, 417-429.

Blake, K.D., Davenport, S.L., Hall, B.D., Hefner, M.A., Pagon, R.A., Williams, M.S., Lin, A.E., and Graham, J.M., Jr. (1998). CHARGE association: an update and review for the primary pediatrician. Clinical pediatrics *37*, 159-173.

Blake, K.D., and Prasad, C. (2006). CHARGE syndrome. Orphanet journal of rare diseases *1*, 34.

Blow, M.J., McCulley, D.J., Li, Z., Zhang, T., Akiyama, J.A., Holt, A., Plajzer-Frick, I., Shoukry, M., Wright, C., Chen, F*., et al.* (2010). ChIP-Seq identification of weakly conserved heart enhancers. Nature genetics *42*, 806-810.

Bodmer, R. (1993). The gene tinman is required for specification of the heart and visceral muscles in Drosophila. Development *118*, 719-729.

Bondue, A., and Blanpain, C. (2010). Mesp1: a key regulator of cardiovascular lineage commitment. Circ Res *107*, 1414-1427.

Bosley, T.M., Alorainy, I.A., Salih, M.A., Aldhalaan, H.M., Abu-Amero, K.K., Oystreck, D.T., Tischfield, M.A., Engle, E.C., and Erickson, R.P. (2008). The clinical spectrum of homozygous HOXA1 mutations. Am J Med Genet A *146A*, 1235-1240.

Bosman, E.A., Penn, A.C., Ambrose, J.C., Kettleborough, R., Stemple, D.L., and Steel, K.P. (2005). Multiple mutations in mouse Chd7 provide models for CHARGE syndrome. Hum Mol Genet *14*, 3463-3476.

Bouazoune, K., and Kingston, R.E. (2012). Chromatin remodeling by the CHD7 protein is impaired by mutations that cause human developmental disorders. Proc Natl Acad Sci U S A *109*, 19238-19243.

Boyer, L.A., Latek, R.R., and Peterson, C.L. (2004). The SANT domain: a unique histone-tail-binding module? Nat Rev Mol Cell Biol *5*, 158-163.

Bradshaw, L., Chaudhry, B., Hildreth, V., Webb, S., and Henderson, D.J. (2009). Dual role for neural crest cells during outflow tract septation in the neural crest-deficient mutant Splotch(2H). J Anat *214*, 245-257.

Briggs, L.E., Phelps, A.L., Brown, E., Kakarla, J., Anderson, R.H., van den Hoff, M.J., and Wessels, A. (2013). Expression of the BMP receptor Alk3 in the second heart field is essential for development of the dorsal mesenchymal protrusion and atrioventricular septation. Circ Res *112*, 1420-1432.

Brose, K., Bland, K.S., Wang, K.H., Arnott, D., Henzel, W., Goodman, C.S., Tessier-Lavigne, M., and Kidd, T. (1999). Slit proteins bind Robo receptors and have an evolutionarily conserved role in repulsive axon guidance. Cell *96*, 795-806.

Brown, C.B., Feiner, L., Lu, M.M., Li, J., Ma, X., Webber, A.L., Jia, L., Raper, J.A., and Epstein, J.A. (2001). PlexinA2 and semaphorin signaling during cardiac neural crest development. Development *128*, 3071-3080.

Bruneau, B.G. (2010). Chromatin remodeling in heart development. Curr Opin Genet Dev *20*, 505-511.

Buckingham, M., Meilhac, S., and Zaffran, S. (2005). Building the mammalian heart from two sources of myocardial cells. Nat Rev Genet *6*, 826-835.

Buenrostro, J.D., Giresi, P.G., Zaba, L.C., Chang, H.Y., and Greenleaf, W.J. (2013). Transposition of native chromatin for fast and sensitive epigenomic profiling of open chromatin, DNA-binding proteins and nucleosome position. Nature methods *10*, 1213-1218.

Bultman, S., Gebuhr, T., Yee, D., La Mantia, C., Nicholson, J., Gilliam, A., Randazzo, F., Metzger, D., Chambon, P., Crabtree, G.*, et al.* (2000). A Brg1 null mutation in the mouse reveals functional differences among mammalian SWI/SNF complexes. Mol Cell *6*, 1287-1295.

Cai, C.L., Liang, X., Shi, Y., Chu, P.H., Pfaff, S.L., Chen, J., and Evans, S. (2003). Isl1 identifies a cardiac progenitor population that proliferates prior to differentiation and contributes a majority of cells to the heart. Dev Cell *5*, 877-889.

Carmeliet, P., and Tessier-Lavigne, M. (2005). Common mechanisms of nerve and blood vessel wiring. Nature *436*, 193-200.

Chang, C.P., and Bruneau, B.G. (2012). Epigenetics and cardiovascular development. Annu Rev Physiol *74*, 41-68.

Chang, S., McKinsey, T.A., Zhang, C.L., Richardson, J.A., Hill, J.A., and Olson, E.N. (2004). Histone deacetylases 5 and 9 govern responsiveness of the heart to a subset of stress signals and play redundant roles in heart development. Mol Cell Biol *24*, 8467-8476.

Chen, T., Chang, T.C., Kang, J.O., Choudhary, B., Makita, T., Tran, C.M., Burch, J.B., Eid, H., and Sucov, H.M. (2002). Epicardial induction of fetal cardiomyocyte proliferation via a retinoic acid-inducible trophic factor. Dev Biol *250*, 198-207.

Chen, W.V., Delrow, J., Corrin, P.D., Frazier, J.P., and Soriano, P. (2004). Identification and validation of PDGF transcriptional targets by microarray-coupled gene-trap mutagenesis. Nat Genet *36*, 304-312.

Cheng, H., Lederer, W.J., and Cannell, M.B. (1993). Calcium sparks: elementary events underlying excitation-contraction coupling in heart muscle. Science *262*, 740-744.

Chhin, B., Hatayama, M., Bozon, D., Ogawa, M., Schon, P., Tohmonda, T., Sassolas, F., Aruga, J., Valard, A.G., Chen, S.C.*, et al.* (2007). Elucidation of penetrance variability of a ZIC3 mutation in a family with complex heart defects and functional analysis of ZIC3 mutations in the first zinc finger domain. Human mutation *28*, 563-570.

Chiba, H., Muramatsu, M., Nomoto, A., and Kato, H. (1994). Two human homologues of Saccharomyces cerevisiae SWI2/SNF2 and Drosophila brahma are transcriptional coactivators cooperating with the estrogen receptor and the retinoic acid receptor. Nucleic Acids Res *22*, 1815-1820.

Chopra, N., Yang, T., Asghari, P., Moore, E.D., Huke, S., Akin, B., Cattolica, R.A., Perez, C.F., Hlaing, T., Knollmann-Ritschel, B.E.*, et al.* (2009). Ablation of triadin causes loss of cardiac Ca2+ release units, impaired excitation-contraction coupling, and cardiac arrhythmias. Proceedings of the National Academy of Sciences of the United States of America *106*, 7636-7641.

Christoffels, V.M., Mommersteeg, M.T., Trowe, M.O., Prall, O.W., de Gier-de Vries, C., Soufan, A.T., Bussen, M., Schuster-Gossler, K., Harvey, R.P., Moorman, A.F.*, et al.* (2006). Formation of the venous pole of the heart from an Nkx2-5-negative precursor population requires Tbx18. Circulation Research *98*, 1555-1563.

Colin, C., Tobaruella, F.S., Correa, R.G., Sogayar, M.C., and Demasi, M.A. (2010). Cloning and characterization of a novel alternatively spliced transcript of the human CHD7 putative helicase. BMC Res Notes *3*, 252.

Collins, E.C., Pannell, R., Simpson, E.M., Forster, A., and Rabbitts, T.H. (2000). Inter-chromosomal recombination of Mll and Af9 genes mediated by cre-loxP in mouse development. EMBO Rep *1*, 127-132.

Conway, S.J., Kruzynska-Frejtag, A., Kneer, P.L., Machnicki, M., and Koushik, S.V. (2003). What cardiovascular defect does my prenatal mouse mutant have, and why? Genesis *35*, 1-21.

Cordero, D.R., Brugmann, S., Chu, Y., Bajpai, R., Jame, M., and Helms, J.A. (2011). Cranial neural crest cells on the move: their roles in craniofacial development. Am J Med Genet A *155A*, 270-279.

Corsten-Janssen, N., du Marchie Sarvaas, G.J., Kerstjens-Frederikse, W.S., Hoefsloot, L.H., van Beynum, I.M., Kapusta, L., and van Ravenswaaij-Arts, C.M. (2014). CHD7 mutations are not a major cause of atrioventricular septal and conotruncal heart defects. Am J Med Genet A *164*, 3003-3009.

Corsten-Janssen, N., Kerstjens-Frederikse, W.S., du Marchie Sarvaas, G.J., Baardman, M.E., Bakker, M.K., Bergman, J.E., Hove, H.D., Heimdal, K.R., Rustad, C.F., Hennekam, R.C*., et al.* (2013a). The cardiac phenotype in patients with a CHD7 mutation. Circulation Cardiovascular genetics *6*, 248-254.

Corsten-Janssen, N., Saitta, S.C., Hoefsloot, L.H., McDonald-McGinn, D.M., Driscoll, D.A., Derks, R., Dickinson, K.A., Kerstjens-Frederikse, W.S., Emanuel, B.S., Zackai, E.H*., et al.* (2013b). More Clinical Overlap between 22q11.2 Deletion Syndrome and CHARGE Syndrome than Often Anticipated. Molecular syndromology *4*, 235-245.

Crawford, G.E., Holt, I.E., Whittle, J., Webb, B.D., Tai, D., Davis, S., Margulies, E.H., Chen, Y., Bernat, J.A., Ginsburg, D*., et al.* (2006). Genome-wide mapping of DNase hypersensitive sites using massively parallel signature sequencing (MPSS). Genome Res *16*, 123-131.

Christoffels, V.M., Burch, J.B., and Moorman, A.F. (2004). Architectural plan for the heart: early patterning and delineation of the chambers and the nodes. Trends Cardiovasc Med *14*, 301-307.

Daubresse, G., Deuring, R., Moore, L., Papoulas, O., Zakrajsek, I., Waldrip, W.R., Scott, M.P., Kennison, J.A., and Tamkun, J.W. (1999). The Drosophila kismet gene is related to chromatin-remodeling factors and is required for both segmentation and segment identity. Development *126*, 1175-1187.

de Lange, F.J., Moorman, A.F., Anderson, R.H., Manner, J., Soufan, A.T., de Gier-de Vries, C., Schneider, M.D., Webb, S., van den Hoff, M.J., and Christoffels, V.M. (2004). Lineage and morphogenetic analysis of the cardiac valves. Circ Res *95*, 645-654.

Debenedittis, P., Harmelink, C., Chen, Y., Wang, Q., and Jiao, K. (2011). Characterization of the novel interaction between muskelin and TBX20, a critical cardiogenic transcription factor. Biochem Biophys Res Commun *409*, 338-343.

Dettman, R.W., Denetclaw, W., Jr., Ordahl, C.P., and Bristow, J. (1998). Common epicardial origin of coronary vascular smooth muscle, perivascular fibroblasts, and intermyocardial fibroblasts in the avian heart. Dev Biol *193*, 169-181.

Dobell, A.R., and Van Praagh, R. (1996). The Holmes heart: historic associations and pathologic anatomy. Am Heart J *132*, 437-445.

Dode, C., Levilliers, J., Dupont, J.M., De Paepe, A., Le Du, N., Soussi-Yanicostas, N., Coimbra, R.S., Delmaghani, S., Compain-Nouaille, S., Baverel, F.*, et al.* (2003). Loss-of-function mutations in FGFR1 cause autosomal dominant Kallmann syndrome. Nat Genet *33*, 463-465.

Dode, C., Teixeira, L., Levilliers, J., Fouveaut, C., Bouchard, P., Kottler, M.L., Lespinasse, J., Lienhardt-Roussie, A., Mathieu, M., Moerman, A.*, et al.* (2006). Kallmann syndrome: mutations in the genes encoding prokineticin-2 and prokineticin receptor-2. PLoS Genet *2*, e175.

Dodou, E., Verzi, M.P., Anderson, J.P., Xu, S.M., and Black, B.L. (2004). Mef2c is a direct transcriptional target of ISL1 and GATA factors in the anterior heart field during mouse embryonic development. Development *131*, 3931-3942.

Doerks, T., Copley, R.R., Schultz, J., Ponting, C.P., and Bork, P. (2002). Systematic identification of novel protein domain families associated with nuclear functions. Genome Res *12*, 47-56.

Dyer, L.A., and Kirby, M.L. (2009). The role of secondary heart field in cardiac development. Dev Biol *336*, 137-144.

Edmondson, D.G., Lyons, G.E., Martin, J.F., and Olson, E.N. (1994). Mef2 gene expression marks the cardiac and skeletal muscle lineages during mouse embryogenesis. Development *120*, 1251-1263.

Edwards, J.E. (1948). Vascular rings related to anomalies of the aortic arches. Modern concepts of cardiovascular disease *17*, 1.

Elliott, D.A., Kirk, E.P., Yeoh, T., Chandar, S., McKenzie, F., Taylor, P., Grossfeld, P., Fatkin, D., Jones, O., Hayes, P.*, et al.* (2003). Cardiac homeobox gene NKX2-5 mutations and congenital heart disease: associations with atrial septal defect and hypoplastic left heart syndrome. J Am Coll Cardiol *41*, 2072-2076.

Engelen, E., Akinci, U., Bryne, J.C., Hou, J., Gontan, C., Moen, M., Szumska, D., Kockx, C., van Ijcken, W., Dekkers, D.H.*, et al.* (2011). Sox2 cooperates with Chd7 to regulate genes that are mutated in human syndromes. Nat Genet *43*, 607-611.

Ernst, P., and Vakoc, C.R. (2012). WRAD: enabler of the SET1-family of H3K4 methyltransferases. Briefings in functional genomics *11*, 217-226.

Etchevers, H.C., Amiel, J., and Lyonnet, S. (2006). Molecular Bases of Human Neurocristopathies. In Neural Crest Induction and Differentiation, J.P. Saint-Jeannet, ed. (Georgetown, Texas, U.S.A.: Landes Bioscience / Eurekah.com), pp. 213-234.

Fantes, J., Ragge, N.K., Lynch, S.A., McGill, N.I., Collin, J.R., Howard-Peebles, P.N., Hayward, C., Vivian, A.J., Williamson, K., van Heyningen, V.*, et al.* (2003). Mutations in SOX2 cause anophthalmia. Nature genetics *33*, 461-463.

Farley, F.W., Soriano, P., Steffen, L.S., and Dymecki, S.M. (2000). Widespread recombinase expression using FLPeR (flipper) mice. Genesis *28*, 106-110.

Feiner, L., Webber, A.L., Brown, C.B., Lu, M.M., Jia, L., Feinstein, P., Mombaerts, P., Epstein, J.A., and Raper, J.A. (2001). Targeted disruption of semaphorin 3C leads to persistent truncus arteriosus and aortic arch interruption. Development *128*, 3061-3070.

Feng, W., Khan, M.A., Bellvis, P., Zhu, Z., Bernhardt, O., Herold-Mende, C., and Liu, H.K. (2013). The chromatin remodeler CHD7 regulates adult neurogenesis via activation of SoxC transcription factors. Cell stem cell *13*, 62-72.

Feng, Y., Valley, M.T., Lazar, J., Yang, A.L., Bronson, R.T., Firestein, S., Coetzee, W.A., and Manley, J.L. (2009). SRp38 regulates alternative splicing and is required for Ca(2+) handling in the embryonic heart. Dev Cell *16*, 528-538.

Flanagan, J.F., Mi, L.Z., Chruszcz, M., Cymborowski, M., Clines, K.L., Kim, Y., Minor, W., Rastinejad, F., and Khorasanizadeh, S. (2005). Double chromodomains cooperate to recognize the methylated histone H3 tail. Nature *438*, 1181-1185.

Franco, D., Chinchilla, A., Daimi, H., Dominguez, J.N., and Aranega, A. (2011). Modulation of conductive elements by Pitx2 and their impact on atrial arrhythmogenesis. Cardiovasc Res *91*, 223-231.

Franklin, R.C., Spiegelhalter, D.J., Anderson, R.H., Macartney, F.J., Rossi Filho, R.I., Douglas, J.M., Rigby, M.L., and Deanfield, J.E. (1991). Double-inlet ventricle presenting in infancy. I. Survival without definitive repair. J Thorac Cardiovasc Surg *101*, 767-776.

Fujiwara, M., Ghazizadeh, M., and Kawanami, O. (2006). Potential role of the Slit/Robo signal pathway in angiogenesis. Vasc Med *11*, 115-121.

Gage, F.H. (2000). Mammalian neural stem cells. Science *287*, 1433-1438.

Gallant, P. (2007). Control of transcription by Pontin and Reptin. Trends in cell biology *17*, 187-192.

Gangaraju, V.K., and Bartholomew, B. (2007). Dependency of ISW1a chromatin remodeling on extranucleosomal DNA. Mol Cell Biol *27*, 3217-3225.

Garcia-Martinez, V., and Schoenwolf, G.C. (1993). Primitive-streak origin of the cardiovascular system in avian embryos. Dev Biol *159*, 706-719.

Garg, V., Kathiriya, I.S., Barnes, R., Schluterman, M.K., King, I.N., Butler, C.A., Rothrock, C.R., Eapen, R.S., Hirayama-Yamada, K., Joo, K.*, et al.* (2003). GATA4 mutations cause human congenital heart defects and reveal an interaction with TBX5. Nature *424*, 443-447.

Gautier, L., Cope, L., Bolstad, B.M., and Irizarry, R.A. (2004). affy--analysis of Affymetrix GeneChip data at the probe level. Bioinformatics *20*, 307-315.

Gentleman, R.C., Carey, V.J., Bates, D.M., Bolstad, B., Dettling, M., Dudoit, S., Ellis, B., Gautier, L., Ge, Y., Gentry, J.*, et al.* (2004). Bioconductor: open software development for computational biology and bioinformatics. Genome Biol *5*, R80.

Gherardi, E., Love, C.A., Esnouf, R.M., and Jones, E.Y. (2004). The sema domain. Current opinion in structural biology *14*, 669-678.

Gioli-Pereira, L., Pereira, A.C., Mesquita, S.M., Xavier-Neto, J., Lopes, A.A., and Krieger, J.E. (2010). NKX2.5 mutations in patients with non-syndromic congenital heart disease. International journal of cardiology *138*, 261-265.

Gitler, A.D., Lu, M.M., and Epstein, J.A. (2004). PlexinD1 and semaphorin signaling are required in endothelial cells for cardiovascular development. Dev Cell *7*, 107-116.

Glaros, S., Cirrincione, G.M., Palanca, A., Metzger, D., and Reisman, D. (2008). Targeted knockout of BRG1 potentiates lung cancer development. Cancer Res *68*, 3689-3696.

Goldmuntz, E., Geiger, E., and Benson, D.W. (2001). NKX2.5 mutations in patients with tetralogy of fallot. Circulation *104*, 2565-2568.

Gong, W., Gottlieb, S., Collins, J., Blescia, A., Dietz, H., Goldmuntz, E., McDonald-McGinn, D.M., Zackai, E.H., Emanuel, B.S., Driscoll, D.A*., et al.* (2001). Mutation analysis of TBX1 in non-deleted patients with features of DGS/VCFS or isolated cardiovascular defects. J Med Genet *38*, E45.

Graham, A. (2003). Development of the pharyngeal arches. American journal of medical genetics Part A *119A*, 251-256.

Griffin, C.T., Brennan, J., and Magnuson, T. (2008). The chromatin-remodeling enzyme BRG1 plays an essential role in primitive erythropoiesis and vascular development. Development *135*, 493-500.

Gu, C., Rodriguez, E.R., Reimert, D.V., Shu, T., Fritzsch, B., Richards, L.J., Kolodkin, A.L., and Ginty, D.D. (2003). Neuropilin-1 conveys semaphorin and VEGF signaling during neural and cardiovascular development. Dev Cell *5*, 45-57.

Gudbjartsson, D.F., Arnar, D.O., Helgadottir, A., Gretarsdottir, S., Holm, H., Sigurdsson, A., Jonasdottir, A., Baker, A., Thorleifsson, G., Kristjansson, K*., et al.* (2007). Variants conferring risk of atrial fibrillation on chromosome 4q25. Nature *448*, 353-357.

Hall, B.D. (1979). Choanal atresia and associated multiple anomalies. J Pediatr *95*, 395-398.

Hanchate, N.K., Giacobini, P., Lhuillier, P., Parkash, J., Espy, C., Fouveaut, C., Leroy, C., Baron, S., Campagne, C., Vanacker, C*., et al.* (2012). SEMA3A, a gene involved in axonal pathfinding, is mutated in patients with Kallmann syndrome. PLoS Genet *8*, e1002896.

Hang, C.T., Yang, J., Han, P., Cheng, H.L., Shang, C., Ashley, E., Zhou, B., and Chang, C.P. (2010). Chromatin regulation by Brg1 underlies heart muscle development and disease. Nature *466*, 62-67.

Hargreaves, D.C., and Crabtree, G.R. (2011). ATP-dependent chromatin remodeling: genetics, genomics and mechanisms. Cell Res *21*, 396-420.

Harvey, R.P., Lai, D., Elliott, D., Biben, C., Solloway, M., Prall, O., Stennard, F., Schindeler, A., Groves, N., Lavulo, L*., et al.* (2002). Homeodomain factor Nkx2-5 in heart development and disease. Cold Spring Harb Symp Quant Biol *67*, 107-114.

Hasan, W. (2013). Autonomic cardiac innervation: development and adult plasticity. Organogenesis *9*, 176-193.

Hatemi, A.C., Gulec, C., Cine, N., Vural, B., Hatirnaz, O., Sayitoglu, M., Oztunc, F., Saltik, L., Kansiz, E., and Erginel Unaltuna, N. (2011). Sequence variations of NKX2-5 and HAND1 genes in patients with atrial isomerism. Anadolu kardiyoloji dergisi : AKD = the Anatolian journal of cardiology *11*, 319-328.

He, A., Kong, S.W., Ma, Q., and Pu, W.T. (2011). Co-occupancy by multiple cardiac transcription factors identifies transcriptional enhancers active in heart. Proc Natl Acad Sci U S A *108*, 5632-5637.

Heathcote, K., Braybrook, C., Abushaban, L., Guy, M., Khetyar, M.E., Patton, M.A., Carter, N.D., Scambler, P.J., and Syrris, P. (2005). Common arterial trunk associated with a homeodomain mutation of NKX2.6. Hum Mol Genet *14*, 585-593.

Hernandez-Miranda, L.R., Cariboni, A., Faux, C., Ruhrberg, C., Cho, J.H., Cloutier, J.F., Eickholt, B.J., Parnavelas, J.G., and Andrews, W.D. (2011). Robo1 regulates semaphorin signaling to guide the migration of cortical interneurons through the ventral forebrain. J Neurosci *31*, 6174-6187.

Hernanz-Schulman, M. (2005). Vascular rings: a practical approach to imaging diagnosis. Pediatric radiology *35*, 961-979.

Herrmann, F., Gross, A., Zhou, D., Kestler, H.A., and Kuhl, M. (2012). A boolean model of the cardiac gene regulatory network determining first and second heart field identity. PLoS One *7*, e46798.

Hirayama-Yamada, K., Kamisago, M., Akimoto, K., Aotsuka, H., Nakamura, Y., Tomita, H., Furutani, M., Imamura, S., Takao, A., Nakazawa, M.*, et al.* (2005). Phenotypes with GATA4 or NKX2.5 mutations in familial atrial septal defect. Am J Med Genet A *135*, 47-52.

Hiruma, T., Nakajima, Y., and Nakamura, H. (2002). Development of pharyngeal arch arteries in early mouse embryo. J Anat *201*, 15-29.

Hitotsumachi, S., Carpenter, D.A., and Russell, W.L. (1985). Dose-repetition increases the mutagenic effectiveness of N-ethyl-N-nitrosourea in mouse spermatogonia. Proc Natl Acad Sci U S A *82*, 6619-6621.

Ho, L., and Crabtree, G.R. (2010). Chromatin remodelling during development. Nature *463*, 474-484.

Ho, L., Ronan, J.L., Wu, J., Staahl, B.T., Chen, L., Kuo, A., Lessard, J., Nesvizhskii, A.I., Ranish, J., and Crabtree, G.R. (2009). An embryonic stem cell chromatin remodeling complex, esBAF, is essential for embryonic stem cell self-renewal and pluripotency. Proceedings of the National Academy of Sciences of the United States of America *106*, 5181-5186.

Hofmann, K., Zweier, M., Sticht, H., Zweier, C., Wittmann, W., Hoyer, J., Uebe, S., van Haeringen, A., Thiel, C.T., Ekici, A.B.*, et al.* (2013). Biallelic SEMA3A defects cause a novel type of syndromic short stature. Am J Med Genet A *161A*, 2880-2889.

Hosoda, T., Komuro, I., Shiojima, I., Hiroi, Y., Harada, M., Murakawa, Y., Hirata, Y., and Yazaki, Y. (1999). Familial atrial septal defect and atrioventricular conduction disturbance associated with a point mutation in the cardiac homeobox gene CSX/NKX2-5 in a Japanese patient. Japanese circulation journal *63*, 425-426.

Hu, Y., Lai, Y., and Zhu, D. (2014). Transcription regulation by CHD proteins to control plant development. Frontiers in plant science *5*, 223.

Huang da, W., Sherman, B.T., and Lempicki, R.A. (2009). Systematic and integrative analysis of large gene lists using DAVID bioinformatics resources. Nat Protoc *4*, 44-57.

Huang, D.W., Sherman, B.T., and Lempicki, R.A. (2009). Bioinformatics enrichment tools: paths toward the comprehensive functional analysis of large gene lists. Nucleic Acids Res *37*, 1-13.

Huang, X., Gao, X., Diaz-Trelles, R., Ruiz-Lozano, P., and Wang, Z. (2008). Coronary development is regulated by ATP-dependent SWI/SNF chromatin remodeling component BAF180. Dev Biol *319*, 258-266.

Huminiecki, L., Gorn, M., Suchting, S., Poulsom, R., and Bicknell, R. (2002). Magic roundabout is a new member of the roundabout receptor family that is endothelial specific and expressed at sites of active angiogenesis. Genomics *79*, 547-552.

Hurd, E.A., Capers, P.L., Blauwkamp, M.N., Adams, M.E., Raphael, Y., Poucher, H.K., and Martin, D.M. (2007). Loss of Chd7 function in gene-trapped reporter mice is embryonic lethal and associated with severe defects in multiple developing tissues. Mamm Genome *18*, 94-104.

Hurd, E.A., Poucher, H.K., Cheng, K., Raphael, Y., and Martin, D.M. (2010). The ATP-dependent chromatin remodeling enzyme CHD7 regulates pro-neural gene expression and neurogenesis in the inner ear. Development *137*, 3139-3150.

Hutson, M.R., and Kirby, M.L. (2007). Model systems for the study of heart development and disease. Cardiac neural crest and conotruncal malformations. Semin Cell Dev Biol *18*, 101-110.

Ieda, M., Kanazawa, H., Kimura, K., Hattori, F., Ieda, Y., Taniguchi, M., Lee, J.K., Matsumura, K., Tomita, Y., Miyoshi, S.*, et al.* (2007). Sema3a maintains normal heart rhythm through sympathetic innervation patterning. Nat Med *13*, 604-612.

Ikeda, Y., Hiroi, Y., Hosoda, T., Utsunomiya, T., Matsuo, S., Ito, T., Inoue, J., Sumiyoshi, T., Takano, H., Nagai, R.*, et al.* (2002). Novel point mutation in the cardiac transcription factor CSX/NKX2.5 associated with congenital heart disease. Circ J *66*, 561-563.

Indra, A.K., Dupe, V., Bornert, J.M., Messaddeq, N., Yaniv, M., Mark, M., Chambon, P., and Metzger, D. (2005). Temporally controlled targeted somatic mutagenesis in embryonic surface ectoderm and fetal epidermal keratinocytes unveils two distinct developmental functions of BRG1 in limb morphogenesis and skin barrier formation. Development *132*, 4533-4544.

Ishii, Y., Langberg, J.D., Hurtado, R., Lee, S., and Mikawa, T. (2007). Induction of proepicardial marker gene expression by the liver bud. Development *134*, 3627-3637.

Jacobs-McDaniels, N.L., and Albertson, R.C. (2011). Chd7 plays a critical role in controlling left-right symmetry during zebrafish somitogenesis. Dev Dyn *240*, 2272-2280.

Janssen, N., Bergman, J.E., Swertz, M.A., Tranebjaerg, L., Lodahl, M., Schoots, J., Hofstra, R.M., van Ravenswaaij-Arts, C.M., and Hoefsloot, L.H. (2012). Mutation update on the CHD7 gene involved in CHARGE syndrome. Human mutation *33*, 1149-1160.

Jay, P.Y., Harris, B.S., Maguire, C.T., Buerger, A., Wakimoto, H., Tanaka, M., Kupershmidt, S., Roden, D.M., Schultheiss, T.M., O'Brien, T.X.*, et al.* (2004). Nkx2-5 mutation causes anatomic hypoplasia of the cardiac conduction system. J Clin Invest *113*, 1130-1137.

Jay, P.Y., Rozhitskaya, O., Tarnavski, O., Sherwood, M.C., Dorfman, A.L., Lu, Y., Ueyama, T., and Izumo, S. (2005). Haploinsufficiency of the cardiac transcription factor Nkx2-5 variably affects the expression of putative target genes. Faseb J *19*, 1495-1497.

Jeansson, M., Gawlik, A., Anderson, G., Li, C., Kerjaschki, D., Henkelman, M., and Quaggin, S.E. (2011). Angiopoietin-1 is essential in mouse vasculature during development and in response to injury. The Journal of clinical investigation *121*, 2278-2289.

Jiang, X., Rowitch, D.H., Soriano, P., McMahon, A.P., and Sucov, H.M. (2000). Fate of the mammalian cardiac neural crest. Development *127*, 1607-1616.

Jiang, X., Zhou, Y., Xian, L., Chen, W., Wu, H., and Gao, X. (2012). The mutation in Chd7 causes misexpression of Bmp4 and developmental defects in telencephalic midline. Am J Pathol *181*, 626-641.

Jiao, K., Langworthy, M., Batts, L., Brown, C.B., Moses, H.L., and Baldwin, H.S. (2006). Tgfbeta signaling is required for atrioventricular cushion mesenchyme remodeling during in vivo cardiac development. Development *133*, 4585-4593.

Jongmans, M.C., Admiraal, R.J., van der Donk, K.P., Vissers, L.E., Baas, A.F., Kapusta, L., van Hagen, J.M., Donnai, D., de Ravel, T.J., Veltman, J.A.*, et al.* (2006). CHARGE syndrome: the phenotypic spectrum of mutations in the CHD7 gene. J Med Genet *43*, 306-314.

Jongmans, M.C., van Ravenswaaij-Arts, C.M., Pitteloud, N., Ogata, T., Sato, N., Claahsen-van der Grinten, H.L., van der Donk, K., Seminara, S., Bergman, J.E., Brunner, H.G.*, et al.* (2009). CHD7 mutations in patients initially diagnosed with Kallmann syndrome--the clinical overlap with CHARGE syndrome. Clin Genet *75*, 65-71.

Kallmann FJ, S.W., Barrera SE (1944). The genetic aspects of primary eunuchoidism Am J Ment Defic. Am J Ment Defic *48*, 203–236.

Kameda, Y. (2009). Hoxa3 and signaling molecules involved in aortic arch patterning and remodeling. Cell Tissue Res *336*, 165-178.

Kang, S., Graham, J.M., Jr., Olney, A.H., and Biesecker, L.G. (1997). GLI3 frameshift mutations cause autosomal dominant Pallister-Hall syndrome. Nature genetics *15*, 266-268.

Kelberman, D., Rizzoti, K., Avilion, A., Bitner-Glindzicz, M., Cianfarani, S., Collins, J., Chong, W.K., Kirk, J.M., Achermann, J.C., Ross, R.*, et al.* (2006). Mutations within Sox2/SOX2 are associated with abnormalities in the hypothalamo-pituitary-gonadal axis in mice and humans. J Clin Invest *116*, 2442-2455.

Kelly, R.G., Brown, N.A., and Buckingham, M.E. (2001). The arterial pole of the mouse heart forms from Fgf10-expressing cells in pharyngeal mesoderm. Developmental cell *1*, 435-440.

Kim, H.G., Kurth, I., Lan, F., Meliciani, I., Wenzel, W., Eom, S.H., Kang, G.B., Rosenberger, G., Tekin, M., Ozata, M.*, et al.* (2008a). Mutations in CHD7, encoding a chromatin-remodeling protein, cause idiopathic hypogonadotropic hypogonadism and Kallmann syndrome. Am J Hum Genet *83*, 511-519.

Kim, S.H., Hu, Y., Cadman, S., and Bouloux, P. (2008b). Diversity in fibroblast growth factor receptor 1 regulation: learning from the investigation of Kallmann syndrome. Journal of neuroendocrinology *20*, 141-163.

Kirby, M.L., Gale, T.F., and Stewart, D.E. (1983). Neural crest cells contribute to normal aorticopulmonary septation. Science *220*, 1059-1061.

Kirby, M.L., and Waldo, K.L. (1990). Role of neural crest in congenital heart disease. Circulation *82*, 332-340.

Kirk, E.P., Sunde, M., Costa, M.W., Rankin, S.A., Wolstein, O., Castro, M.L., Butler, T.L., Hyun, C., Guo, G., Otway, R.*, et al.* (2007). Mutations in cardiac T-box factor gene TBX20 are associated

with diverse cardiac pathologies, including defects of septation and valvulogenesis and cardiomyopathy. Am J Hum Genet *81*, 280-291.

Kisanuki, Y.Y., Hammer, R.E., Miyazaki, J., Williams, S.C., Richardson, J.A., and Yanagisawa, M. (2001). Tie2-Cre transgenic mice: a new model for endothelial cell-lineage analysis in vivo. Developmental Biology *230*, 230-242.

Kita, Y., Nishiyama, M., and Nakayama, K.I. (2012). Identification of CHD7S as a novel splicing variant of CHD7 with functions similar and antagonistic to those of the full-length CHD7L. Genes Cells *17*, 536-547.

Kodo, K., Nishizawa, T., Furutani, M., Arai, S., Ishihara, K., Oda, M., Makino, S., Fukuda, K., Takahashi, T., Matsuoka, R.*, et al.* (2012). Genetic analysis of essential cardiac transcription factors in 256 patients with non-syndromic congenital heart defects. Circ J *76*, 1703-1711.

Kodo, K., Nishizawa, T., Furutani, M., Arai, S., Yamamura, E., Joo, K., Takahashi, T., Matsuoka, R., and Yamagishi, H. (2009). GATA6 mutations cause human cardiac outflow tract defects by disrupting semaphorin-plexin signaling. Proc Natl Acad Sci U S A *106*, 13933-13938.

Kodo, K., and Yamagishi, H. (2011). A decade of advances in the molecular embryology and genetics underlying congenital heart defects. Circ J *75*, 2296-2304.

Koike, H., Horie, K., Fukuyama, H., Kondoh, G., Nagata, S., and Takeda, J. (2002). Efficient biallelic mutagenesis with Cre/loxP-mediated inter-chromosomal recombination. EMBO Rep *3*, 433-437.

Kolodkin, A.L., Matthes, D.J., O'Connor, T.P., Patel, N.H., Admon, A., Bentley, D., and Goodman, C.S. (1992). Fasciclin IV: sequence, expression, and function during growth cone guidance in the grasshopper embryo. Neuron *9*, 831-845.

Kornberg, R.D. (1974). Chromatin structure: a repeating unit of histones and DNA. Science *184*, 868-871.

Kramer, S.G., Kidd, T., Simpson, J.H., and Goodman, C.S. (2001). Switching repulsion to attraction: changing responses to slit during transition in mesoderm migration. Science *292*, 737-740.

Kubilus, J.K., and Linsenmayer, T.F. (2010). Developmental guidance of embryonic corneal innervation: roles of Semaphorin3A and Slit2. Dev Biol *344*, 172-184.

Kuhlbrodt, K., Herbarth, B., Sock, E., Hermans-Borgmeyer, I., and Wegner, M. (1998). Sox10, a novel transcriptional modulator in glial cells. J Neurosci *18*, 237-250.

Laforest, B., and Nemer, M. (2011). GATA5 interacts with GATA4 and GATA6 in outflow tract development. Dev Biol *358*, 368-378.

Lahat, H., Pras, E., Olender, T., Avidan, N., Ben-Asher, E., Man, O., Levy-Nissenbaum, E., Khoury, A., Lorber, A., Goldman, B.*, et al.* (2001). A missense mutation in a highly conserved region of CASQ2 is associated with autosomal recessive catecholamine-induced polymorphic ventricular tachycardia in Bedouin families from Israel. Am J Hum Genet *69*, 1378-1384.

Lalani, S.R., Safiullah, A.M., Fernbach, S.D., Harutyunyan, K.G., Thaller, C., Peterson, L.E., McPherson, J.D., Gibbs, R.A., White, L.D., Hefner, M.*, et al.* (2006). Spectrum of CHD7 mutations in 110 individuals with CHARGE syndrome and genotype-phenotype correlation. Am J Hum Genet *78*, 303-314.

Lalani, S.R., Safiullah, A.M., Molinari, L.M., Fernbach, S.D., Martin, D.M., and Belmont, J.W. (2004). SEMA3E mutation in a patient with CHARGE syndrome. J Med Genet *41*, e94.

Lange, M., Kaynak, B., Forster, U.B., Tonjes, M., Fischer, J.J., Grimm, C., Schlesinger, J., Just, S., Dunkel, I., Krueger, T*., et al.* (2008). Regulation of muscle development by DPF3, a novel histone acetylation and methylation reader of the BAF chromatin remodeling complex. Genes Dev *22*, 2370-2384.

Lavine, K.J., and Ornitz, D.M. (2009). Shared circuitry: developmental signaling cascades regulate both embryonic and adult coronary vasculature. Circ Res *104*, 159-169.

Lavine, K.J., Yu, K., White, A.C., Zhang, X., Smith, C., Partanen, J., and Ornitz, D.M. (2005). Endocardial and epicardial derived FGF signals regulate myocardial proliferation and differentiation in vivo. Dev Cell *8*, 85-95.

Layman, W.S., Hurd, E.A., and Martin, D.M. (2010). Chromodomain proteins in development: lessons from CHARGE syndrome. Clin Genet *78*, 11-20.

Layman, W.S., Hurd, E.A., and Martin, D.M. (2011). Reproductive dysfunction and decreased GnRH neurogenesis in a mouse model of CHARGE syndrome. Hum Mol Genet *20*, 3138-3150.

Layman, W.S., McEwen, D.P., Beyer, L.A., Lalani, S.R., Fernbach, S.D., Oh, E., Swaroop, A., Hegg, C.C., Raphael, Y., Martens, J.R*., et al.* (2009). Defects in neural stem cell proliferation and olfaction in Chd7 deficient mice indicate a mechanism for hyposmia in human CHARGE syndrome. Hum Mol Genet *18*, 1909-1923.

Lee, Y., Song, A.J., Baker, R., Micales, B., Conway, S.J., and Lyons, G.E. (2000). Jumonji, a nuclear protein that is necessary for normal heart development. Circ Res *86*, 932-938.

Legouis, R., Hardelin, J.P., Levilliers, J., Claverie, J.M., Compain, S., Wunderle, V., Millasseau, P., Le Paslier, D., Cohen, D., Caterina, D*., et al.* (1991). The candidate gene for the X-linked Kallmann syndrome encodes a protein related to adhesion molecules. Cell *67*, 423-435.

Lenz, D.R.D., A.A.; Wekselman, G.; Fuchs, H.; Angelis, M.H.E.; Avraham, K.B. (2010). The inner ear phenotype of Volchok (Vlk): An ENU-induced mouse model for CHARGE syndrome. Audiological Medicine *8*, 110–119.

Lepore, J.J., Mericko, P.A., Cheng, L., Lu, M.M., Morrisey, E.E., and Parmacek, M.S. (2006). GATA-6 regulates semaphorin 3C and is required in cardiac neural crest for cardiovascular morphogenesis. J Clin Invest *116*, 929-939.

Lescroart, F., Chabab, S., Lin, X., Rulands, S., Paulissen, C., Rodolosse, A., Auer, H., Achouri, Y., Dubois, C., Bondue, A*., et al.* (2014). Early lineage restriction in temporally distinct populations of Mesp1 progenitors during mammalian heart development. Nat Cell Biol *16*, 829-840.

Lessard, J., Wu, J.I., Ranish, J.A., Wan, M., Winslow, M.M., Staahl, B.T., Wu, H., Aebersold, R., Graef, I.A., and Crabtree, G.R. (2007). An essential switch in subunit composition of a chromatin remodeling complex during neural development. Neuron *55*, 201-215.

Li, E., Bestor, T.H., and Jaenisch, R. (1992). Targeted mutation of the DNA methyltransferase gene results in embryonic lethality. Cell *69*, 915-926.

Li, W., Xiong, Y., Shang, C., Twu, K.Y., Hang, C.T., Yang, J., Han, P., Lin, C.Y., Lin, C.J., Tsai, F.C*., et al.* (2013). Brg1 governs distinct pathways to direct multiple aspects of mammalian neural crest cell development. Proc Natl Acad Sci U S A *110*, 1738-1743.

Li, Y., Bogershausen, N., Alanay, Y., Simsek Kiper, P.O., Plume, N., Keupp, K., Pohl, E., Pawlik, B., Rachwalski, M., Milz, E.*, et al.* (2011). A mutation screen in patients with Kabuki syndrome. Hum Genet *130*, 715-724.

Liberatore, C.M., Searcy-Schrick, R.D., Vincent, E.B., and Yutzey, K.E. (2002). Nkx-2.5 gene induction in mice is mediated by a Smad consensus regulatory region. Dev Biol *244*, 243-256.

Lickert, H., Takeuchi, J.K., Von Both, I., Walls, J.R., McAuliffe, F., Adamson, S.L., Henkelman, R.M., Wrana, J.L., Rossant, J., and Bruneau, B.G. (2004). Baf60c is essential for function of BAF chromatin remodelling complexes in heart development. Nature *432*, 107-112.

Liefooghe A., T.H.a.V.J.-S. (2006). Large scale matching for Position Weight Matrices In Combinatorial Pattern Matching (Springer), pp. 401-412.

Lien, C.L., Wu, C., Mercer, B., Webb, R., Richardson, J.A., and Olson, E.N. (1999). Control of early cardiac-specific transcription of Nkx2-5 by a GATA-dependent enhancer. Development *126*, 75-84.

Lin, A.E., Chin, A.J., Devine, W., Park, S.C., and Zackai, E. (1987). The pattern of cardiovascular malformation in the CHARGE association. Am J Dis Child *141*, 1010-1013.

Lin, C.J., Lin, C.Y., Chen, C.H., Zhou, B., and Chang, C.P. (2012). Partitioning the heart: mechanisms of cardiac septation and valve development. Development *139*, 3277-3299.

Lin, X., Huo, Z., Liu, X., Zhang, Y., Li, L., Zhao, H., Yan, B., Liu, Y., Yang, Y., and Chen, Y.H. (2010). A novel GATA6 mutation in patients with tetralogy of Fallot or atrial septal defect. Journal of human genetics *55*, 662-667.

Lincoln, J., Alfieri, C.M., and Yutzey, K.E. (2004). Development of heart valve leaflets and supporting apparatus in chicken and mouse embryos. Dev Dyn *230*, 239-250.

Lindsay, E.A., and Baldini, A. (2001). Recovery from arterial growth delay reduces penetrance of cardiovascular defects in mice deleted for the DiGeorge syndrome region. Human molecular genetics *10*, 997-1002.

Lindsay, E.A., Botta, A., Jurecic, V., Carattini-Rivera, S., Cheah, Y.C., Rosenblatt, H.M., Bradley, A., and Baldini, A. (1999). Congenital heart disease in mice deficient for the DiGeorge syndrome region. Nature *401*, 379-383.

Lints, T.J., Parsons, L.M., Hartley, L., Lyons, I., and Harvey, R.P. (1993). Nkx-2.5: a novel murine homeobox gene expressed in early heart progenitor cells and their myogenic descendants. Development *119*, 969.

Liu, A., and Eggenschwiler, J. (2014). Identifying essential genes in mouse development via an ENU-based forward genetic approach. Methods Mol Biol *1092*, 95-118.

Liu, C., Liu, W., Palie, J., Lu, M.F., Brown, N.A., and Martin, J.F. (2002). Pitx2c patterns anterior myocardium and aortic arch vessels and is required for local cell movement into atrioventricular cushions. Development *129*, 5081-5091.

Liu, C., Shen, A., Li, X., Jiao, W., Zhang, X., and Li, Z. (2008). T-box transcription factor TBX20 mutations in Chinese patients with congenital heart disease. Eur J Med Genet *51*, 580-587.

Liu, C.X., Shen, A.D., Li, X.F., Jiao, W.W., Bai, S., Yuan, F., Guan, X.L., Zhang, X.G., Zhang, G.R., and Li, Z.Z. (2009). Association of TBX5 gene polymorphism with ventricular septal defect in the Chinese Han population. Chinese medical journal *122*, 30-34.

Liu, J., and Stainier, D.Y. (2010). Tbx5 and Bmp signaling are essential for proepicardium specification in zebrafish. Circ Res *106*, 1818-1828.

Liu, J., Willet, S.G., Bankaitis, E.D., Xu, Y., Wright, C.V., and Gu, G. (2013). Non-parallel recombination limits Cre-LoxP-based reporters as precise indicators of conditional genetic manipulation. Genesis *51*, 436-442.

Liu, Y., Harmelink, C., Peng, Y., Chen, Y., Wang, Q., and Jiao, K. (2014). CHD7 interacts with BMP R-SMADs to epigenetically regulate cardiogenesis in mice. Hum Mol Genet *23*, 2145-2156.

Livak, K.J., and Schmittgen, T.D. (2001). Analysis of relative gene expression data using real-time quantitative PCR and the 2(-Delta Delta C(T)) Method. Methods *25*, 402-408.

Long, M.A., and Rossi, F.M. (2009). Silencing inhibits Cre-mediated recombination of the Z/AP and Z/EG reporters in adult cells. PLoS One *4*, e5435.

Luger, K., Dechassa, M.L., and Tremethick, D.J. (2012). New insights into nucleosome and chromatin structure: an ordered state or a disordered affair? Nat Rev Mol Cell Biol *13*, 436-447.

Luger, K., Mader, A.W., Richmond, R.K., Sargent, D.F., and Richmond, T.J. (1997). Crystal structure of the nucleosome core particle at 2.8 A resolution. Nature *389*, 251-260.

Luo, W., and Brouwer, C. (2013). Pathview: an R/Bioconductor package for pathway-based data integration and visualization. Bioinformatics *29*, 1830-1831.

Luo, Y., Raible, D., and Raper, J.A. (1993). Collapsin: a protein in brain that induces the collapse and paralysis of neuronal growth cones. Cell *75*, 217-227.

Lusser, A., and Kadonaga, J.T. (2003). Chromatin remodeling by ATP-dependent molecular machines. Bioessays *25*, 1192-1200.

Lyons, I., Parsons, L.M., Hartley, L., Li, R., Andrews, J.E., Robb, L., and Harvey, R.P. (1995). Myogenic and morphogenetic defects in the heart tubes of murine embryos lacking the homeo box gene Nkx2-5. Genes Dev *9*, 1654-1666.

MacMullin, A., and Jacobs, J.R. (2006). Slit coordinates cardiac morphogenesis in Drosophila. Dev Biol *293*, 154-164.

Maitra, M., Koenig, S.N., Srivastava, D., and Garg, V. (2010). Identification of GATA6 sequence variants in patients with congenital heart defects. Pediatr Res *68*, 281-285.

Manner, J., Perez-Pomares, J.M., Macias, D., and Munoz-Chapuli, R. (2001). The origin, formation and developmental significance of the epicardium: a review. Cells Tissues Organs *169*, 89-103.

Marcos, S., Sarfati, J., Leroy, C., Fouveaut, C., Parent, P., Metz, C., Wolczynski, S., Gerard, M., Bieth, E., Kurtz, F.*, et al.* (2014). The prevalence of CHD7 missense versus truncating mutations is higher in patients with Kallmann syndrome than in typical CHARGE patients. J Clin Endocrinol Metab, jc20142110.

Maria V. de la Cruz, C.S.G., and Raul Cayre (1991). The developmental components of the ventricles: their significance in congenital malformations. Cardiol Young *1*, 123-128.

Marmorstein, R., and Roth, S.Y. (2001). Histone acetyltransferases: function, structure, and catalysis. Curr Opin Genet Dev *11*, 155-161.

Martin, D.M., Probst, F.J., Fox, S.E., Schimmenti, L.A., Semina, E.V., Hefner, M.A., Belmont, J.W., and Camper, S.A. (2002). Exclusion of PITX2 mutations as a major cause of CHARGE association. Am J Med Genet *111*, 27-30.

Martinez-Estrada, O.M., Lettice, L.A., Essafi, A., Guadix, J.A., Slight, J., Velecela, V., Hall, E., Reichmann, J., Devenney, P.S., Hohenstein, P.*, et al.* (2010). Wt1 is required for cardiovascular progenitor cell formation through transcriptional control of Snail and E-cadherin. Nat Genet *42*, 89-93.

May, D., Blow, M.J., Kaplan, T., McCulley, D.J., Jensen, B.C., Akiyama, J.A., Holt, A., Plajzer-Frick, I., Shoukry, M., Wright, C.*, et al.* (2012). Large-scale discovery of enhancers from human heart tissue. Nat Genet *44*, 89-93.

McBratney-Owen, B., Iseki, S., Bamforth, S.D., Olsen, B.R., and Morriss-Kay, G.M. (2008). Development and tissue origins of the mammalian cranial base. Dev Biol *322*, 121-132.

McCulley, D.J., and Black, B.L. (2012). Transcription factor pathways and congenital heart disease. Curr Top Dev Biol *100*, 253-277.

McKnight, J.N., Jenkins, K.R., Nodelman, I.M., Escobar, T., and Bowman, G.D. (2011). Extranucleosomal DNA binding directs nucleosome sliding by Chd1. Mol Cell Biol *31*, 4746-4759.

Medioni, C., Astier, M., Zmojdzian, M., Jagla, K., and Semeriva, M. (2008). Genetic control of cell morphogenesis during Drosophila melanogaster cardiac tube formation. J Cell Biol *182*, 249-261.

Medioni, C., Bertrand, N., Mesbah, K., Hudry, B., Dupays, L., Wolstein, O., Washkowitz, A.J., Papaioannou, V.E., Mohun, T.J., Harvey, R.P.*, et al.* (2010). Expression of Slit and Robo genes in the developing mouse heart. Developmental dynamics : an official publication of the American Association of Anatomists *239*, 3303-3311.

Megarbane, A., Salem, N., Stephan, E., Ashoush, R., Lenoir, D., Delague, V., Kassab, R., Loiselet, J., and Bouvagnet, P. (2000). X-linked transposition of the great arteries and incomplete penetrance among males with a nonsense mutation in ZIC3. Eur J Hum Genet *8*, 704-708.

Meilhac, S.M., Esner, M., Kelly, R.G., Nicolas, J.F., and Buckingham, M.E. (2004). The clonal origin of myocardial cells in different regions of the embryonic mouse heart. Developmental cell *6*, 685-698.

Melicharek, D.J., Ramirez, L.C., Singh, S., Thompson, R., and Marenda, D.R. (2010). Kismet/CHD7 regulates axon morphology, memory and locomotion in a Drosophila model of CHARGE syndrome. Human molecular genetics *19*, 4253-4264.

Merki, E., Zamora, M., Raya, A., Kawakami, Y., Wang, J., Zhang, X., Burch, J., Kubalak, S.W., Kaliman, P., Izpisua Belmonte, J.C.*, et al.* (2005). Epicardial retinoid X receptor alpha is required for myocardial growth and coronary artery formation. Proceedings of the National Academy of Sciences of the United States of America *102*, 18455-18460.

Mertsalov, I.B., Ninkina, N.N., Wanless, J.S., Buchman, V.L., Korochkin, L.I., and Kulikova, D.A. (2008). Generation of mutant mice with targeted disruption of two members of the d4 gene family: neuro-d4 and cer-d4. Doklady Biochemistry and biophysics *419*, 65-68.

Micucci, J.A., Layman, W.S., Hurd, E.A., Sperry, E.D., Frank, S.F., Durham, M.A., Swiderski, D.L., Skidmore, J.M., Scacheri, P.C., Raphael, Y.*, et al.* (2014). CHD7 and retinoic acid signaling cooperate to regulate neural stem cell and inner ear development in mouse models of CHARGE syndrome. Human molecular genetics *23*, 434-448.

Mikkelsen, T.S., Ku, M., Jaffe, D.B., Issac, B., Lieberman, E., Giannoukos, G., Alvarez, P., Brockman, W., Kim, T.K., Koche, R.P.*, et al.* (2007). Genome-wide maps of chromatin state in pluripotent and lineage-committed cells. Nature *448*, 553-560.

Mjaatvedt, C.H., Nakaoka, T., Moreno-Rodriguez, R., Norris, R.A., Kern, M.J., Eisenberg, C.A., Turner, D., and Markwald, R.R. (2001). The outflow tract of the heart is recruited from a novel heart-forming field. Dev Biol *238*, 97-109.

Molkentin, J.D. (2000). The zinc finger-containing transcription factors GATA-4, -5, and -6. Ubiquitously expressed regulators of tissue-specific gene expression. J Biol Chem *275*, 38949-38952.

Momma, K. (2010). Cardiovascular anomalies associated with chromosome 22q11.2 deletion syndrome. Am J Cardiol *105*, 1617-1624.

Mommersteeg, M.T., Andrews, W.D., Ypsilanti, A.R., Zelina, P., Yeh, M.L., Norden, J., Kispert, A., Chedotal, A., Christoffels, V.M., and Parnavelas, J.G. (2013). Slit-roundabout signaling regulates the development of the cardiac systemic venous return and pericardium. Circ Res *112*, 465-475.

Montgomery, R.L., Davis, C.A., Potthoff, M.J., Haberland, M., Fielitz, J., Qi, X., Hill, J.A., Richardson, J.A., and Olson, E.N. (2007). Histone deacetylases 1 and 2 redundantly regulate cardiac morphogenesis, growth, and contractility. Genes Dev *21*, 1790-1802.

Moorman, A., Webb, S., Brown, N.A., Lamers, W., and Anderson, R.H. (2003). Development of the heart: (1) formation of the cardiac chambers and arterial trunks. Heart *89*, 806-814.

Moorman, A.F., and Christoffels, V.M. (2003). Cardiac chamber formation: development, genes, and evolution. Physiol Rev *83*, 1223-1267.

Morin, S., Charron, F., Robitaille, L., and Nemer, M. (2000). GATA-dependent recruitment of MEF2 proteins to target promoters. Embo J *19*, 2046-2055.

Morrison, A.J., and Shen, X. (2009). Chromatin remodelling beyond transcription: the INO80 and SWR1 complexes. Nature reviews Molecular cell biology *10*, 373-384.

Moses, K.A., DeMayo, F., Braun, R.M., Reecy, J.L., and Schwartz, R.J. (2001). Embryonic expression of an Nkx2-5/Cre gene using ROSA26 reporter mice. Genesis *31*, 176-180.

Munshi, N.V., McAnally, J., Bezprozvannaya, S., Berry, J.M., Richardson, J.A., Hill, J.A., and Olson, E.N. (2009). Cx30.2 enhancer analysis identifies Gata4 as a novel regulator of atrioventricular delay. Development *136*, 2665-2674.

Nakashima, Y., Nishimura, S., Maeda, A., Barsoumian, E.L., Hakamata, Y., Nakai, J., Allen, P.D., Imoto, K., and Kita, T. (1997). Molecular cloning and characterization of a human brain ryanodine receptor. FEBS Lett *417*, 157-162.

Nam, J., Onitsuka, I., Hatch, J., Uchida, Y., Ray, S., Huang, S., Li, W., Zang, H., Ruiz-Lozano, P., and Mukouyama, Y.S. (2013). Coronary veins determine the pattern of sympathetic innervation in the developing heart. Development *140*, 1475-1485.

Nemer, G., Fadlalah, F., Usta, J., Nemer, M., Dbaibo, G., Obeid, M., and Bitar, F. (2006). A novel mutation in the GATA4 gene in patients with Tetralogy of Fallot. Human mutation *27*, 293-294.

Nemer, G., and Nemer, M. (2003). Transcriptional activation of BMP-4 and regulation of mammalian organogenesis by GATA-4 and -6. Dev Biol *254*, 131-148.

Ng, S.B., Bigham, A.W., Buckingham, K.J., Hannibal, M.C., McMillin, M.J., Gildersleeve, H.I., Beck, A.E., Tabor, H.K., Cooper, G.M., Mefford, H.C.*, et al.* (2010). Exome sequencing identifies MLL2 mutations as a cause of Kabuki syndrome. Nat Genet *42*, 790-793.

Nimura, K., Ura, K., Shiratori, H., Ikawa, M., Okabe, M., Schwartz, R.J., and Kaneda, Y. (2009). A histone H3 lysine 36 trimethyltransferase links Nkx2-5 to Wolf-Hirschhorn syndrome. Nature *460*, 287-291.

Ogier, J.M., Carpinelli, M.R., Arhatari, B.D., Symons, R.C., Kile, B.T., and Burt, R.A. (2014). CHD7 deficiency in "Looper", a new mouse model of CHARGE syndrome, results in ossicle malformation, otosclerosis and hearing impairment. PLoS One *9*, e97559.

Okano, M., Bell, D.W., Haber, D.A., and Li, E. (1999). DNA methyltransferases Dnmt3a and Dnmt3b are essential for de novo methylation and mammalian development. Cell *99*, 247-257.

Okubo, A., Miyoshi, O., Baba, K., Takagi, M., Tsukamoto, K., Kinoshita, A., Yoshiura, K., Kishino, T., Ohta, T., Niikawa, N.*, et al.* (2004). A novel GATA4 mutation completely segregated with atrial septal defect in a large Japanese family. J Med Genet *41*, e97.

Okuno, T., Takahashi, H., Shibahara, Y., Hashida, Y., and Sando, I. (1990). Temporal bone histopathologic findings in Alagille's syndrome. Arch Otolaryngol Head Neck Surg *116*, 217-220.

Oley, C.A., Baraitser, M., and Grant, D.B. (1988). A reappraisal of the CHARGE association. J Med Genet *25*, 147-156.

Oliveira, L.M., Seminara, S.B., Beranova, M., Hayes, F.J., Valkenburgh, S.B., Schipani, E., Costa, E.M., Latronico, A.C., Crowley, W.F., Jr., and Vallejo, M. (2001). The importance of autosomal genes in Kallmann syndrome: genotype-phenotype correlations and neuroendocrine characteristics. J Clin Endocrinol Metab *86*, 1532-1538.

Pabst, S., Wollnik, B., Rohmann, E., Hintz, Y., Glanzer, K., Vetter, H., Nickenig, G., and Grohe, C. (2008). A novel stop mutation truncating critical regions of the cardiac transcription factor NKX2-5 in a large family with autosomal-dominant inherited congenital heart disease. Clinical research in cardiology : official journal of the German Cardiac Society *97*, 39-42.

Paffett-Lugassy, N., Singh, R., Nevis, K.R., Guner-Ataman, B., O'Loughlin, E., Jahangiri, L., Harvey, R.P., Burns, C.G., and Burns, C.E. (2013). Heart field origin of great vessel precursors relies on nkx2.5-mediated vasculogenesis. Nat Cell Biol *15*, 1362-1369.

Pagon, R.A., Graham, J.M., Jr., Zonana, J., and Yong, S.L. (1981). Coloboma, congenital heart disease, and choanal atresia with multiple anomalies: CHARGE association. J Pediatr *99*, 223-227.

Paige, S.L., Thomas, S., Stoick-Cooper, C.L., Wang, H., Maves, L., Sandstrom, R., Pabon, L., Reinecke, H., Pratt, G., Keller, G.*, et al.* (2012). A temporal chromatin signature in human embryonic stem cells identifies regulators of cardiac development. Cell *151*, 221-232.

Park, K.W., Morrison, C.M., Sorensen, L.K., Jones, C.A., Rao, Y., Chien, C.B., Wu, J.Y., Urness, L.D., and Li, D.Y. (2003). Robo4 is a vascular-specific receptor that inhibits endothelial migration. Dev Biol *261*, 251-267.

Park, M.K. (2008). Vascular Ring. In Pediatric Cardiology for Practitioners, 5th Edition, M.K. Park, ed. (St. Louis: Mosby), pp. 303-307.

Patient, R.K., and McGhee, J.D. (2002). The GATA family (vertebrates and invertebrates). Curr Opin Genet Dev *12*, 416-422.

Paylor, R., Glaser, B., Mupo, A., Ataliotis, P., Spencer, C., Sobotka, A., Sparks, C., Choi, C.H., Oghalai, J., Curran, S.*, et al.* (2006). Tbx1 haploinsufficiency is linked to behavioral disorders in mice and humans: implications for 22q11 deletion syndrome. Proc Natl Acad Sci U S A *103*, 7729-7734.

Persson, J., and Ekwall, K. (2010). Chd1 remodelers maintain open chromatin and regulate the epigenetics of differentiation. Exp Cell Res *316*, 1316-1323.

Pinto, G., Abadie, V., Mesnage, R., Blustajn, J., Cabrol, S., Amiel, J., Hertz-Pannier, L., Bertrand, A.M., Lyonnet, S., Rappaport, R.*, et al.* (2005). CHARGE syndrome includes hypogonadotropic hypogonadism and abnormal olfactory bulb development. J Clin Endocrinol Metab *90*, 5621-5626.

Plageman, T.F., Jr., and Yutzey, K.E. (2005). T-box genes and heart development: putting the "T" in heart. Developmental dynamics : an official publication of the American Association of Anatomists *232*, 11-20.

Pogwizd, S.M., Schlotthauer, K., Li, L., Yuan, W., and Bers, D.M. (2001). Arrhythmogenesis and contractile dysfunction in heart failure: Roles of sodium-calcium exchange, inward rectifier potassium current, and residual beta-adrenergic responsiveness. Circ Res *88*, 1159-1167.

Posch, M.G., Gramlich, M., Sunde, M., Schmitt, K.R., Lee, S.H., Richter, S., Kersten, A., Perrot, A., Panek, A.N., Al Khatib, I.H.*, et al.* (2010). A gain-of-function TBX20 mutation causes congenital atrial septal defects, patent foramen ovale and cardiac valve defects. J Med Genet *47*, 230-235.

Prall, O.W., Menon, M.K., Solloway, M.J., Watanabe, Y., Zaffran, S., Bajolle, F., Biben, C., McBride, J.J., Robertson, B.R., Chaulet, H.*, et al.* (2007). An Nkx2-5/Bmp2/Smad1 negative feedback loop controls heart progenitor specification and proliferation. Cell *128*, 947-959.

Priori, S.G., and Napolitano, C. (2005). Cardiac and skeletal muscle disorders caused by mutations in the intracellular Ca2+ release channels. J Clin Invest *115*, 2033-2038.

Pu, W.T., Ishiwata, T., Juraszek, A.L., Ma, Q., and Izumo, S. (2004). GATA4 is a dosage-sensitive regulator of cardiac morphogenesis. Dev Biol *275*, 235-244.

Puceat, M., and Jaconi, M. (2005). Ca2+ signalling in cardiogenesis. Cell calcium *38*, 383-389.

Qian, L., Liu, J., and Bodmer, R. (2005). Slit and Robo control cardiac cell polarity and morphogenesis. Curr Biol *15*, 2271-2278.

Ragge, N.K., Lorenz, B., Schneider, A., Bushby, K., de Sanctis, L., de Sanctis, U., Salt, A., Collin, J.R., Vivian, A.J., Free, S.L.*, et al.* (2005). SOX2 anophthalmia syndrome. American journal of medical genetics Part A *135*, 1-7; discussion 8.

Rajagopal, S.K., Ma, Q., Obler, D., Shen, J., Manichaikul, A., Tomita-Mitchell, A., Boardman, K., Briggs, C., Garg, V., Srivastava, D.*, et al.* (2007). Spectrum of heart disease associated with murine and human GATA4 mutation. J Mol Cell Cardiol *43*, 677-685.

Ramsköld, D.K., E.; Sandberg, R. (2012). How to Analyze Gene Expression Using RNA-Sequencing Data. In Next Generation Microarray Bioinformatics, J.C.T. Wang, A,; Tian, T., ed. (Humana Press), pp. 259-274.

Randall, V., McCue, K., Roberts, C., Kyriakopoulou, V., Beddow, S., Barrett, A.N., Vitelli, F., Prescott, K., Shaw-Smith, C., Devriendt, K.*, et al.* (2009). Great vessel development requires biallelic expression of Chd7 and Tbx1 in pharyngeal ectoderm in mice. J Clin Invest *119*, 3301-3310.

Rapila, R., Korhonen, T., and Tavi, P. (2008). Excitation-contraction coupling of the mouse embryonic cardiomyocyte. The Journal of general physiology *132*, 397-405.

Rauch, A., Devriendt, K., Koch, A., Rauch, R., Gewillig, M., Kraus, C., Weyand, M., Singer, H., Reis, A., and Hofbeck, M. (2004). Assessment of association between variants and haplotypes of the remaining TBX1 gene and manifestations of congenital heart defects in 22q11.2 deletion patients. J Med Genet *41*, e40.

Reamon-Buettner, S.M., and Borlak, J. (2004). TBX5 mutations in non-Holt-Oram syndrome (HOS) malformed hearts. Human mutation *24*, 104.

Red-Horse, K., Ueno, H., Weissman, I.L., and Krasnow, M.A. (2010). Coronary arteries form by developmental reprogramming of venous cells. Nature *464*, 549-553.

Reyes, J.C., Barra, J., Muchardt, C., Camus, A., Babinet, C., and Yaniv, M. (1998). Altered control of cellular proliferation in the absence of mammalian brahma (SNF2alpha). Embo J *17*, 6979-6991.

Ringrose, L., and Paro, R. (2004). Epigenetic regulation of cellular memory by the Polycomb and Trithorax group proteins. Annu Rev Genet *38*, 413-443.

Roessler, E., Ouspenskaia, M.V., Karkera, J.D., Velez, J.I., Kantipong, A., Lacbawan, F., Bowers, P., Belmont, J.W., Towbin, J.A., Goldmuntz, E.*, et al.* (2008). Reduced NODAL signaling strength via mutation of several pathway members including FOXH1 is linked to human heart defects and holoprosencephaly. Am J Hum Genet *83*, 18-29.

Roth, L., Koncina, E., Satkauskas, S., Cremel, G., Aunis, D., and Bagnard, D. (2009). The many faces of semaphorins: from development to pathology. Cell Mol Life Sci *66*, 649-666.

Rothberg, J.M., Hartley, D.A., Walther, Z., and Artavanis-Tsakonas, S. (1988). slit: an EGF-homologous locus of D. melanogaster involved in the development of the embryonic central nervous system. Cell *55*, 1047-1059.

Rottbauer, W., Saurin, A.J., Lickert, H., Shen, X., Burns, C.G., Wo, Z.G., Kemler, R., Kingston, R., Wu, C., and Fishman, M. (2002). Reptin and pontin antagonistically regulate heart growth in zebrafish embryos. Cell *111*, 661-672.

Roux-Buisson, N., Cacheux, M., Fourest-Lieuvin, A., Fauconnier, J., Brocard, J., Denjoy, I., Durand, P., Guicheney, P., Kyndt, F., Leenhardt, A.*, et al.* (2012). Absence of triadin, a protein of the calcium release complex, is responsible for cardiac arrhythmia with sudden death in human. Hum Mol Genet *21*, 2759-2767.

Saga, Y., Hata, N., Kobayashi, S., Magnuson, T., Seldin, M.F., and Taketo, M.M. (1996). MesP1: a novel basic helix-loop-helix protein expressed in the nascent mesodermal cells during mouse gastrulation. Development *122*, 2769-2778.

Saga, Y., Miyagawa-Tomita, S., Takagi, A., Kitajima, S., Miyazaki, J., and Inoue, T. (1999). MesP1 is expressed in the heart precursor cells and required for the formation of a single heart tube. Development *126*, 3437-3447.

Sanlaville, D., Etchevers, H.C., Gonzales, M., Martinovic, J., Clement-Ziza, M., Delezoide, A.L., Aubry, M.C., Pelet, A., Chemouny, S., Cruaud, C.*, et al.* (2006). Phenotypic spectrum of CHARGE syndrome in fetuses with CHD7 truncating mutations correlates with expression during human development. J Med Genet *43*, 211-217.

Santiago-Martinez, E., Soplop, N.H., Patel, R., and Kramer, S.G. (2008). Repulsion by Slit and Roundabout prevents Shotgun/E-cadherin-mediated cell adhesion during Drosophila heart tube lumen formation. J Cell Biol *182*, 241-248.

Sarkozy, A., Conti, E., Neri, C., D'Agostino, R., Digilio, M.C., Esposito, G., Toscano, A., Marino, B., Pizzuti, A., and Dallapiccola, B. (2005). Spectrum of atrial septal defects associated with mutations of NKX2.5 and GATA4 transcription factors. J Med Genet *42*, e16.

Sato, T.N., Qin, Y., Kozak, C.A., and Audus, K.L. (1993). Tie-1 and tie-2 define another class of putative receptor tyrosine kinase genes expressed in early embryonic vascular system. Proc Natl Acad Sci U S A *90*, 9355-9358.

Sato, T.N., Tozawa, Y., Deutsch, U., Wolburg-Buchholz, K., Fujiwara, Y., Gendron-Maguire, M., Gridley, T., Wolburg, H., Risau, W., and Qin, Y. (1995). Distinct roles of the receptor tyrosine kinases Tie-1 and Tie-2 in blood vessel formation. Nature *376*, 70-74.

Schlaeger, T.M., Bartunkova, S., Lawitts, J.A., Teichmann, G., Risau, W., Deutsch, U., and Sato, T.N. (1997). Uniform vascular-endothelial-cell-specific gene expression in both embryonic and adult transgenic mice. Proc Natl Acad Sci U S A *94*, 3058-3063.

Schluterman, M.K., Krysiak, A.E., Kathiriya, I.S., Abate, N., Chandalia, M., Srivastava, D., and Garg, V. (2007). Screening and biochemical analysis of GATA4 sequence variations identified in patients with congenital heart disease. Am J Med Genet A *143A*, 817-823.

Schnetz, M.P., Bartels, C.F., Shastri, K., Balasubramanian, D., Zentner, G.E., Balaji, R., Zhang, X., Song, L., Wang, Z., Laframboise, T.*, et al.* (2009). Genomic distribution of CHD7 on chromatin tracks H3K4 methylation patterns. Genome Res *19*, 590-601.

Schnetz, M.P., Handoko, L., Akhtar-Zaidi, B., Bartels, C.F., Pereira, C.F., Fisher, A.G., Adams, D.J., Flicek, P., Crawford, G.E., Laframboise, T.*, et al.* (2010). CHD7 targets active gene enhancer elements to modulate ES cell-specific gene expression. PLoS Genet *6*, e1001023.

Schott, J.J., Benson, D.W., Basson, C.T., Pease, W., Silberbach, G.M., Moak, J.P., Maron, B.J., Seidman, C.E., and Seidman, J.G. (1998). Congenital heart disease caused by mutations in the transcription factor NKX2-5. Science *281*, 108-111.

Schroeder, A., Mueller, O., Stocker, S., Salowsky, R., Leiber, M., Gassmann, M., Lightfoot, S., Menzel, W., Granzow, M., and Ragg, T. (2006). The RIN: an RNA integrity number for assigning integrity values to RNA measurements. BMC molecular biology *7*, 3.

Schuettengruber, B., Chourrout, D., Vervoort, M., Leblanc, B., and Cavalli, G. (2007). Genome regulation by polycomb and trithorax proteins. Cell *128*, 735-745.

Schulz, Y., Freese, L., Manz, J., Zoll, B., Volter, C., Brockmann, K., Bogershausen, N., Becker, J., Wollnik, B., and Pauli, S. (2014a). CHARGE and Kabuki syndromes: a phenotypic and molecular link. Hum Mol Genet *23*, 4396-4405.

Schulz, Y., Wehner, P., Opitz, L., Salinas-Riester, G., Bongers, E.M., van Ravenswaaij-Arts, C.M., Wincent, J., Schoumans, J., Kohlhase, J., Borchers, A.*, et al.* (2014b). CHD7, the gene mutated in CHARGE syndrome, regulates genes involved in neural crest cell guidance. Hum Genet *133*, 997-1009.

Schwartz, Y.B., and Pirrotta, V. (2007). Polycomb silencing mechanisms and the management of genomic programmes. Nat Rev Genet *8*, 9-22.

Searcy, R.D., Vincent, E.B., Liberatore, C.M., and Yutzey, K.E. (1998). A GATA-dependent nkx-2.5 regulatory element activates early cardiac gene expression in transgenic mice. Development *125*, 4461-4470.

Semaphorin Nomenclature Committee (1999). Unified nomenclature for the semaphorins/collapsins. Semaphorin Nomenclature Committee. Cell *97*, 551-552.

Sepulveda, J.L., Vlahopoulos, S., Iyer, D., Belaguli, N., and Schwartz, R.J. (2002). Combinatorial expression of GATA4, Nkx2-5, and serum response factor directs early cardiac gene activity. J Biol Chem *277*, 25775-25782.

Shen, L., Li, X.F., Shen, A.D., Wang, Q., Liu, C.X., Guo, Y.J., Song, Z.J., and Li, Z.Z. (2010). Transcription factor HAND2 mutations in sporadic Chinese patients with congenital heart disease. Chinese medical journal *123*, 1623-1627.

Shi-Joon Yoo, T.J.B. (2009). Vascular Rings, Pulmonary Arterial Sling, and Related Conditions. In Paediatric Cardiology, E.J.B. Robert H. Anderson, Daniel J. Penny, Andrew N. Redington, Michael L. Rigby, and Gil Wernovsky, ed. (Elsevier), pp. 967-989.

Shikama, N., Lutz, W., Kretzschmar, R., Sauter, N., Roth, J.F., Marino, S., Wittwer, J., Scheidweiler, A., and Eckner, R. (2003). Essential function of p300 acetyltransferase activity in heart, lung and small intestine formation. Embo J *22*, 5175-5185.

Shirai, M., Osugi, T., Koga, H., Kaji, Y., Takimoto, E., Komuro, I., Hara, J., Miwa, T., Yamauchi-Takihara, K., and Takihara, Y. (2002). The Polycomb-group gene Rae28 sustains Nkx2.5/Csx expression and is essential for cardiac morphogenesis. The Journal of clinical investigation *110*, 177-184.

Shiratori, H., and Hamada, H. (2006). The left-right axis in the mouse: from origin to morphology. Development *133*, 2095-2104.

Siebert, J.R., Graham, J.M., Jr., and MacDonald, C. (1985). Pathologic features of the CHARGE association: support for involvement of the neural crest. Teratology *31*, 331-336.

Smart, N., Risebro, C.A., Melville, A.A., Moses, K., Schwartz, R.J., Chien, K.R., and Riley, P.R. (2007). Thymosin beta4 induces adult epicardial progenitor mobilization and neovascularization. Nature *445*, 177-182.

Smith, C.L., and Peterson, C.L. (2005). ATP-dependent chromatin remodeling. Curr Top Dev Biol *65*, 115-148.

Smith, Z.D., and Meissner, A. (2013). DNA methylation: roles in mammalian development. Nat Rev Genet *14*, 204-220.

Smyth, G.K. (2004). Linear models and empirical bayes methods for assessing differential expression in microarray experiments. Statistical applications in genetics and molecular biology *3*, Article3.

Sperling, S., Grimm, C.H., Dunkel, I., Mebus, S., Sperling, H.P., Ebner, A., Galli, R., Lehrach, H., Fusch, C., Berger, F*., et al.* (2005). Identification and functional analysis of CITED2 mutations in patients with congenital heart defects. Human mutation *26*, 575-582.

Sperry, E.D., Hurd, E.A., Durham, M.A., Reamer, E.N., Stein, A.B., and Martin, D.M. (2014). The chromatin remodeling protein CHD7, mutated in CHARGE syndrome, is necessary for proper craniofacial and tracheal development. Dev Dyn *243*, 1055-1066.

Srinivas, S., Watanabe, T., Lin, C.S., William, C.M., Tanabe, Y., Jessell, T.M., and Costantini, F. (2001). Cre reporter strains produced by targeted insertion of EYFP and ECFP into the ROSA26 locus. BMC Dev Biol *1*, 4.

Srinivasan, S., Armstrong, J.A., Deuring, R., Dahlsveen, I.K., McNeill, H., and Tamkun, J.W. (2005). The Drosophila trithorax group protein Kismet facilitates an early step in transcriptional elongation by RNA Polymerase II. Development *132*, 1623-1635.

Srinivasan, S., Dorighi, K.M., and Tamkun, J.W. (2008). Drosophila Kismet regulates histone H3 lysine 27 methylation and early elongation by RNA polymerase II. PLoS genetics *4*, e1000217.

Srivastava, D. (2006). Making or breaking the heart: from lineage determination to morphogenesis. Cell *126*, 1037-1048.

Stanford, W.L., Cohn, J.B., and Cordes, S.P. (2001). Gene-trap mutagenesis: past, present and beyond. Nat Rev Genet *2*, 756-768.

Stankunas, K., Hang, C.T., Tsun, Z.Y., Chen, H., Lee, N.V., Wu, J.I., Shang, C., Bayle, J.H., Shou, W., Iruela-Arispe, M.L*., et al.* (2008). Endocardial Brg1 represses ADAMTS1 to maintain the microenvironment for myocardial morphogenesis. Developmental cell *14*, 298-311.

Staton, C.A. (2011). Class 3 semaphorins and their receptors in physiological and pathological angiogenesis. Biochem Soc Trans *39*, 1565-1570.

Streit, M., Riccardi, L., Velasco, P., Brown, L.F., Hawighorst, T., Bornstein, P., and Detmar, M. (1999). Thrombospondin-2: a potent endogenous inhibitor of tumor growth and angiogenesis. Proceedings of the National Academy of Sciences of the United States of America *96*, 14888-14893.

Sun, X.J., Wei, J., Wu, X.Y., Hu, M., Wang, L., Wang, H.H., Zhang, Q.H., Chen, S.J., Huang, Q.H., and Chen, Z. (2005). Identification and characterization of a novel human histone H3 lysine 36-specific methyltransferase. J Biol Chem *280*, 35261-35271.

Suri, C., Jones, P.F., Patan, S., Bartunkova, S., Maisonpierre, P.C., Davis, S., Sato, T.N., and Yancopoulos, G.D. (1996). Requisite role of angiopoietin-1, a ligand for the TIE2 receptor, during embryonic angiogenesis. Cell *87*, 1171-1180.

Suzuki, M.M., and Bird, A. (2008). DNA methylation landscapes: provocative insights from epigenomics. Nat Rev Genet *9*, 465-476.

Takada, I., Mihara, M., Suzawa, M., Ohtake, F., Kobayashi, S., Igarashi, M., Youn, M.Y., Takeyama, K., Nakamura, T., Mezaki, Y.*, et al.* (2007). A histone lysine methyltransferase activated by non-canonical Wnt signalling suppresses PPAR-gamma transactivation. Nat Cell Biol *9*, 1273-1285.

Takamatsu, H., and Kumanogoh, A. (2012). Diverse roles for semaphorin-plexin signaling in the immune system. Trends in immunology *33*, 127-135.

Takeuchi, J.K., and Bruneau, B.G. (2009). Directed transdifferentiation of mouse mesoderm to heart tissue by defined factors. Nature *459*, 708-711.

Takeuchi, J.K., Lou, X., Alexander, J.M., Sugizaki, H., Delgado-Olguin, P., Holloway, A.K., Mori, A.D., Wylie, J.N., Munson, C., Zhu, Y.*, et al.* (2011). Chromatin remodelling complex dosage modulates transcription factor function in heart development. Nat Commun *2*, 187.

Takeuchi, J.K., Mileikovskaia, M., Koshiba-Takeuchi, K., Heidt, A.B., Mori, A.D., Arruda, E.P., Gertsenstein, M., Georges, R., Davidson, L., Mo, R.*, et al.* (2005). Tbx20 dose-dependently regulates transcription factor networks required for mouse heart and motoneuron development. Development *132*, 2463-2474.

Tanaka, M., Chen, Z., Bartunkova, S., Yamasaki, N., and Izumo, S. (1999). The cardiac homeobox gene Csx/Nkx2.5 lies genetically upstream of multiple genes essential for heart development. Development *126*, 1269-1280.

Tanelian, D.L., Barry, M.A., Johnston, S.A., Le, T., and Smith, G.M. (1997). Semaphorin III can repulse and inhibit adult sensory afferents in vivo. Nat Med *3*, 1398-1401.

Taniguchi, M., Yuasa, S., Fujisawa, H., Naruse, I., Saga, S., Mishina, M., and Yagi, T. (1997). Disruption of semaphorin III/D gene causes severe abnormality in peripheral nerve projection. Neuron *19*, 519-530.

Tellier, A.L., Amiel, J., Delezoide, A.L., Audollent, S., Auge, J., Esnault, D., Encha-Razavi, F., Munnich, A., Lyonnet, S., Vekemans, M.*, et al.* (2000). Expression of the PAX2 gene in human embryos and exclusion in the CHARGE syndrome. Am J Med Genet *93*, 85-88.

Tellier, A.L., Cormier-Daire, V., Abadie, V., Amiel, J., Sigaudy, S., Bonnet, D., de Lonlay-Debeney, P., Morrisseau-Durand, M.P., Hubert, P., Michel, J.L.*, et al.* (1998). CHARGE syndrome: report of 47 cases and review. Am J Med Genet *76*, 402-409.

ten Have, S., Boulon, S., Ahmad, Y., and Lamond, A.I. (2011). Mass spectrometry-based immuno-precipitation proteomics - the user's guide. Proteomics *11*, 1153-1159.

Tian, C., Yu, H., Yang, B., Han, F., Zheng, Y., Bartels, C.F., Schelling, D., Arnold, J.E., Scacheri, P.C., and Zheng, Q.Y. (2012). Otitis media in a new mouse model for CHARGE syndrome with a deletion in the Chd7 gene. PLoS One *7*, e34944.

Tian, Y., Yuan, L., Goss, A.M., Wang, T., Yang, J., Lepore, J.J., Zhou, D., Schwartz, R.J., Patel, V., Cohen, E.D.*, et al.* (2010). Characterization and in vivo pharmacological rescue of a Wnt2-Gata6 pathway required for cardiac inflow tract development. Developmental cell *18*, 275-287.

Tomita-Mitchell, A., Maslen, C.L., Morris, C.D., Garg, V., and Goldmuntz, E. (2007). GATA4 sequence variants in patients with congenital heart disease. J Med Genet *44*, 779-783.

Toyoda, M., Shirato, H., Nakajima, K., Kojima, M., Takahashi, M., Kubota, M., Suzuki-Migishima, R., Motegi, Y., Yokoyama, M., and Takeuchi, T. (2003). jumonji downregulates cardiac cell proliferation by repressing cyclin D1 expression. Dev Cell *5*, 85-97.

Turgeon, B., and Meloche, S. (2009). Interpreting neonatal lethal phenotypes in mouse mutants: insights into gene function and human diseases. Physiol Rev *89*, 1-26.

Turkoz, A., Can, M.G., and Vuran, C. (2012). Paravertebral block for vascular ring operation in a patient with CHARGE syndrome. Paediatric anaesthesia *22*, 306-307.

van Bokhoven, H., Celli, J., van Reeuwijk, J., Rinne, T., Glaudemans, B., van Beusekom, E., Rieu, P., Newbury-Ecob, R.A., Chiang, C., and Brunner, H.G. (2005). MYCN haploinsufficiency is associated with reduced brain size and intestinal atresias in Feingold syndrome. Nature genetics *37*, 465-467.

van den Hoff, M.J., Moorman, A.F., Ruijter, J.M., Lamers, W.H., Bennington, R.W., Markwald, R.R., and Wessels, A. (1999). Myocardialization of the cardiac outflow tract. Dev Biol *212*, 477-490.

van der Flier, A., Badu-Nkansah, K., Whittaker, C.A., Crowley, D., Bronson, R.T., Lacy-Hulbert, A., and Hynes, R.O. (2010). Endothelial alpha5 and alphav integrins cooperate in remodeling of the vasculature during development. Development *137*, 2439-2449.

Van Holde, K.E., Sahasrabuddhe, C.G., and Shaw, B.R. (1974). A model for particulate structure in chromatin. Nucleic Acids Res *1*, 1579-1586.

Van Nostrand, J.L., Brady, C.A., Jung, H., Fuentes, D.R., Kozak, M.M., Johnson, T.M., Lin, C.Y., Lin, C.J., Swiderski, D.L., Vogel, H.*, et al.* (2014). Inappropriate p53 activation during development induces features of CHARGE syndrome. Nature.

Vanpraagh, R., Ongley, P.A., and Swan, H.J. (1964). Anatomic Types of Single or Common Ventricle in Man. Morphologic and Geometric Aspects of 60 Necropsied Cases. Am J Cardiol *13*, 367-386.

Verloes, A. (2005). Updated diagnostic criteria for CHARGE syndrome: a proposal. Am J Med Genet A *133A*, 306-308.

Verzi, M.P., McCulley, D.J., De Val, S., Dodou, E., and Black, B.L. (2005). The right ventricle, outflow tract, and ventricular septum comprise a restricted expression domain within the secondary/anterior heart field. Developmental Biology *287*, 134-145.

Vignali, M., Hassan, A.H., Neely, K.E., and Workman, J.L. (2000). ATP-dependent chromatin-remodeling complexes. Mol Cell Biol *20*, 1899-1910.

Vincent, S.D.B., M. (2010). How to Make a Heart: The Origin and Regulation of Cardiac Progenitors. In Current Topics in Developmental Biology - Organogenesis in Development, P. Koopman, ed. (Elsevier), pp. 1-41.

Vincentz, J.W., Barnes, R.M., Firulli, B.A., Conway, S.J., and Firulli, A.B. (2008). Cooperative interaction of Nkx2.5 and Mef2c transcription factors during heart development. Dev Dyn *237*, 3809-3819.

Vissers, L.E., van Ravenswaaij, C.M., Admiraal, R., Hurst, J.A., de Vries, B.B., Janssen, I.M., van der Vliet, W.A., Huys, E.H., de Jong, P.J., Hamel, B.C*., et al.* (2004). Mutations in a new member of the chromodomain gene family cause CHARGE syndrome. Nat Genet *36*, 955-957.

Vitelli, F., Morishima, M., Taddei, I., Lindsay, E.A., and Baldini, A. (2002). Tbx1 mutation causes multiple cardiovascular defects and disrupts neural crest and cranial nerve migratory pathways. Human molecular genetics *11*, 915-922.

von Both, I., Silvestri, C., Erdemir, T., Lickert, H., Walls, J.R., Henkelman, R.M., Rossant, J., Harvey, R.P., Attisano, L., and Wrana, J.L. (2004). Foxh1 is essential for development of the anterior heart field. Dev Cell *7*, 331-345.

Vooijs, M., Jonkers, J., and Berns, A. (2001). A highly efficient ligand-regulated Cre recombinase mouse line shows that LoxP recombination is position dependent. EMBO Rep *2*, 292-297.

Waldo, K.L., Hutson, M.R., Stadt, H.A., Zdanowicz, M., Zdanowicz, J., and Kirby, M.L. (2005). Cardiac neural crest is necessary for normal addition of the myocardium to the arterial pole from the secondary heart field. Dev Biol *281*, 66-77.

Waldo, K.L., Kumiski, D.H., Wallis, K.T., Stadt, H.A., Hutson, M.R., Platt, D.H., and Kirby, M.L. (2001). Conotruncal myocardium arises from a secondary heart field. Development *128*, 3179-3188.

Wamstad, J.A., Alexander, J.M., Truty, R.M., Shrikumar, A., Li, F., Eilertson, K.E., Ding, H., Wylie, J.N., Pico, A.R., Capra, J.A*., et al.* (2012). Dynamic and coordinated epigenetic regulation of developmental transitions in the cardiac lineage. Cell *151*, 206-220.

Wang, J., Lu, Y., Chen, H., Yin, M., Yu, T., and Fu, Q. (2011). Investigation of somatic NKX2-5, GATA4 and HAND1 mutations in patients with tetralogy of Fallot. Pathology *43*, 322-326.

Wang, J., Nagy, A., Larsson, J., Dudas, M., Sucov, H.M., and Kaartinen, V. (2006). Defective ALK5 signaling in the neural crest leads to increased postmigratory neural crest cell apoptosis and severe outflow tract defects. BMC developmental biology *6*, 51.

Wang, W., Xue, Y., Zhou, S., Kuo, A., Cairns, B.R., and Crabtree, G.R. (1996). Diversity and specialization of mammalian SWI/SNF complexes. Genes Dev *10*, 2117-2130.

Wang, Y., Wysocka, J., Perlin, J.R., Leonelli, L., Allis, C.D., and Coonrod, S.A. (2004a). Linking covalent histone modifications to epigenetics: the rigidity and plasticity of the marks. Cold Spring Harb Symp Quant Biol *69*, 161-169.

Wang, Z., Gerstein, M., and Snyder, M. (2009). RNA-Seq: a revolutionary tool for transcriptomics. Nat Rev Genet *10*, 57-63.

Wang, Z., Zhai, W., Richardson, J.A., Olson, E.N., Meneses, J.J., Firpo, M.T., Kang, C., Skarnes, W.C., and Tjian, R. (2004b). Polybromo protein BAF180 functions in mammalian cardiac chamber maturation. Genes Dev *18*, 3106-3116.

Ware, S.M., Peng, J., Zhu, L., Fernbach, S., Colicos, S., Casey, B., Towbin, J., and Belmont, J.W. (2004). Identification and functional analysis of ZIC3 mutations in heterotaxy and related congenital heart defects. Am J Hum Genet *74*, 93-105.

Watanabe, Y., Benson, D.W., Yano, S., Akagi, T., Yoshino, M., and Murray, J.C. (2002). Two novel frameshift mutations in NKX2.5 result in novel features including visceral inversus and sinus venosus type ASD. J Med Genet *39*, 807-811.

Webb, S., Brown, N.A., and Anderson, R.H. (1998). Formation of the atrioventricular septal structures in the normal mouse. Circ Res *82*, 645-656.

Webb, S., Kanani, M., Anderson, R.H., Richardson, M.K., and Brown, N.A. (2001). Development of the human pulmonary vein and its incorporation in the morphologically left atrium. Cardiol Young *11*, 632-642.

Webb, S., Qayyum, S.R., Anderson, R.H., Lamers, W.H., and Richardson, M.K. (2003). Septation and separation within the outflow tract of the developing heart. J Anat *202*, 327-342.

Wehrens, X.H., Lehnart, S.E., and Marks, A.R. (2005). Intracellular calcium release and cardiac disease. Annu Rev Physiol *67*, 69-98.

Wigle, J.T., and Oliver, G. (1999). Prox1 function is required for the development of the murine lymphatic system. Cell *98*, 769-778.

Williamson, K.A., Hever, A.M., Rainger, J., Rogers, R.C., Magee, A., Fiedler, Z., Keng, W.T., Sharkey, F.H., McGill, N., Hill, C.J.*, et al.* (2006a). Mutations in SOX2 cause anophthalmia-esophageal-genital (AEG) syndrome. Human molecular genetics *15*, 1413-1422.

Williamson, K.A., Hever, A.M., Rainger, J., Rogers, R.C., Magee, A., Fiedler, Z., Keng, W.T., Sharkey, F.H., McGill, N., Hill, C.J.*, et al.* (2006b). Mutations in SOX2 cause anophthalmia-esophageal-genital (AEG) syndrome. Hum Mol Genet *15*, 1413-1422.

Woodage, T., Basrai, M.A., Baxevanis, A.D., Hieter, P., and Collins, F.S. (1997). Characterization of the CHD family of proteins. Proc Natl Acad Sci U S A *94*, 11472-11477.

Wu, J.I., Lessard, J., Olave, I.A., Qiu, Z., Ghosh, A., Graef, I.A., and Crabtree, G.R. (2007). Regulation of dendritic development by neuron-specific chromatin remodeling complexes. Neuron *56*, 94-108.

Wu, J.Y., Feng, L., Park, H.T., Havlioglu, N., Wen, L., Tang, H., Bacon, K.B., Jiang, Z., Zhang, X., and Rao, Y. (2001). The neuronal repellent Slit inhibits leukocyte chemotaxis induced by chemotactic factors. Nature *410*, 948-952.

Wyse, R.K., al-Mahdawi, S., Burn, J., and Blake, K. (1993). Congenital heart disease in CHARGE association. Pediatr Cardiol *14*, 75-81.

Xin, M., Davis, C.A., Molkentin, J.D., Lien, C.L., Duncan, S.A., Richardson, J.A., and Olson, E.N. (2006). A threshold of GATA4 and GATA6 expression is required for cardiovascular development. Proc Natl Acad Sci U S A *103*, 11189-11194.

Xin, M., Olson, E.N., and Bassel-Duby, R. (2013). Mending broken hearts: cardiac development as a basis for adult heart regeneration and repair. Nat Rev Mol Cell Biol *14*, 529-541.

Yagi, H., Furutani, Y., Hamada, H., Sasaki, T., Asakawa, S., Minoshima, S., Ichida, F., Joo, K., Kimura, M., Imamura, S.*, et al.* (2003). Role of TBX1 in human del22q11.2 syndrome. Lancet *362*, 1366-1373.

Yamagishi, H., Yamagishi, C., Nakagawa, O., Harvey, R.P., Olson, E.N., and Srivastava, D. (2001). The combinatorial activities of Nkx2.5 and dHAND are essential for cardiac ventricle formation. Dev Biol *239*, 190-203.

Yao, T.P., Oh, S.P., Fuchs, M., Zhou, N.D., Ch'ng, L.E., Newsome, D., Bronson, R.T., Li, E., Livingston, D.M., and Eckner, R. (1998). Gene dosage-dependent embryonic development and proliferation defects in mice lacking the transcriptional integrator p300. Cell *93*, 361-372.

Yazdani, U., and Terman, J.R. (2006). The semaphorins. Genome biology *7*, 211.

Yoshida, T., Vivatbutsiri, P., Morriss-Kay, G., Saga, Y., and Iseki, S. (2008). Cell lineage in mammalian craniofacial mesenchyme. Mech Dev *125*, 797-808.

Yu, T., Meiners, L.C., Danielsen, K., Wong, M.T., Bowler, T., Reinberg, D., Scambler, P.J., van Ravenswaaij-Arts, C.M., and Basson, M.A. (2013). Deregulated FGF and homeotic gene expression underlies cerebellar vermis hypoplasia in CHARGE syndrome. eLife *2*, e01305.

Zaffran, S., Kelly, R.G., Meilhac, S.M., Buckingham, M.E., and Brown, N.A. (2004). Right ventricular myocardium derives from the anterior heart field. Circ Res *95*, 261-268.

Zaidi, S., Choi, M., Wakimoto, H., Ma, L., Jiang, J., Overton, J.D., Romano-Adesman, A., Bjornson, R.D., Breitbart, R.E., Brown, K.K.*, et al.* (2013). De novo mutations in histone-modifying genes in congenital heart disease. Nature *498*, 220-223.

Zentner, G.E., Hurd, E.A., Schnetz, M.P., Handoko, L., Wang, C., Wang, Z., Wei, C., Tesar, P.J., Hatzoglou, M., Martin, D.M.*, et al.* (2010a). CHD7 functions in the nucleolus as a positive regulator of ribosomal RNA biogenesis. Hum Mol Genet *19*, 3491-3501.

Zentner, G.E., Layman, W.S., Martin, D.M., and Scacheri, P.C. (2010b). Molecular and phenotypic aspects of CHD7 mutation in CHARGE syndrome. Am J Med Genet A *152A*, 674-686.

Zhang, B., Dietrich, U.M., Geng, J.G., Bicknell, R., Esko, J.D., and Wang, L. (2009). Repulsive axon guidance molecule Slit3 is a novel angiogenic factor. Blood *114*, 4300-4309.

Zhang, L., Kelley, J., Schmeisser, G., Kobayashi, Y.M., and Jones, L.R. (1997). Complex formation between junctin, triadin, calsequestrin, and the ryanodine receptor. Proteins of the cardiac junctional sarcoplasmic reticulum membrane. J Biol Chem *272*, 23389-23397.

Zhang, M., Chen, M., Kim, J.R., Zhou, J., Jones, R.E., Tune, J.D., Kassab, G.S., Metzger, D., Ahlfeld, S., Conway, S.J.*, et al.* (2011). SWI/SNF complexes containing Brahma or Brahma-related gene 1 play distinct roles in smooth muscle development. Molecular and cellular biology *31*, 2618-2631.

Zhang, P., Lee, H., Brunzelle, J.S., and Couture, J.F. (2012). The plasticity of WDR5 peptide-binding cleft enables the binding of the SET1 family of histone methyltransferases. Nucleic Acids Res *40*, 4237-4246.

Zhao, R., Watt, A.J., Battle, M.A., Li, J., Bondow, B.J., and Duncan, S.A. (2008). Loss of both GATA4 and GATA6 blocks cardiac myocyte differentiation and results in acardia in mice. Dev Biol *317*, 614-619.

Zhou, X.L., and Liu, J.C. (2014). Role of Notch signaling in the mammalian heart. Brazilian journal of medical and biological research = Revista brasileira de pesquisas medicas e biologicas / Sociedade Brasileira de Biofisica [et al] *47*, 1-10.

APPENDIX A – FIGURE LEGENDS FOR MOVIES

Movie 1 – Normal OFT septation in an E13.5 *Chd7$^{Whi/+}$* heart

OPT movie through a *Chd7$^{Whi/+}$* heart (transverse plane) shows septation of the OFT into the separate aorta and pulmonary trunk. The AV cushions have not quite fused to close the embryonic interventricular communication, although the alignment of the chambers is normal, with separate right and left AV junctions. The venous valves are normally formed. See Figure 3-10 for labelling of the aorta and pulmonary trunk.

Movie 2 – Common arterial trunk and double inlet left ventricle in an E13.5 *Chd7$^{Whi/fl}$;Mesp1-Cre* heart

OPT movie through a *Chd7$^{Whi/fl}$;Mesp1-Cre* heart shows a common arterial trunk (CAT) arising from an incomplete right ventricle. The CAT shows pulmonary dominance, whilst the aortic component is hypoplastic and interrupted, supplying only the common carotid arteries. The atrial chambers connect through a common AV valve to the dominant left ventricle, and it can clearly be seen there is no connection between the incomplete right ventricle and the atria. The venous valves are grossly hypoplastic, and the vestibular spine has failed to form.

Movie 3 – Vestibular spine formation and normal endocardial cushion alignment in an E11.5 *Chd7$^{fl/fl}$* heart

OPT movie through a control E11.5 heart (transverse plane) shows formation of the primary atrial septum and vestibular spine, which fuses with the inferior AV endocardial cushion. As the movie plays the superior endocardial cushion is seen first, followed by the inferior cushion. See Figure 3-14 for labelling of key structures.

Movie 4 – Absence of the vestibular spine and abnormal positioning of the endocardial cushions in an E11.5 *Chd7$^{fl/fl}$;Mesp-Cre* heart

OPT movie through a *Chd7$^{fl/fl}$;Mesp-Cre* heart, in which the primary atrial septum can be seen, but the vestibular spine is completely absent. This means the atrial septum and endocardial cushions are not brought together for septation of the AV canal. Furthermore, both the superior and inferior AV endocardial cushions are seen adjacent in the same transverse plane, highlighting their abnormal position when compared to the control heart.

APPENDIX B – E11.5 AND E13.5 MICROARRAY GENE LISTS

Tables B1-B4 contain lists of genes downregulated or upregulated in *Chd7$^{fl/fl}$;Mesp1-Cre* hearts compared to *Chd7$^{+/+}$;Mesp1-Cre* hearts, based on microarray analysis at two time points using GeneChip® Mouse Gene 1.0 ST Arrays. Only genes with $Log_2FC > 0.7$, and p value < 0.05, are included.

For each table, Chrom indicates the chromosome on which the gene is found, and FC indicates fold change.

Table B1: Genes downregulated in the heart at E11.5 following mesodermal ablation of *Chd7*

Ensembl ID:	Symbol:	Chrom:	Description:	Log_2FC:	P.Value:
ENSMUSG00000026678	Rgs5	1	regulator of G-protein signaling 5	-2.0388	6.76E-05
ENSMUSG00000041235	Chd7	4	chromodomain helicase DNA binding protein 7	-1.6829	6.11E-09
ENSMUSG00000028332	Hemgn	4	hemogen	-1.6068	0.004013
ENSMUSG00000019906	Lin7a	10	lin-7 homolog A (C. elegans)	-1.5660	1.80E-05
ENSMUSG00000027463	Slc52a3	2	solute carrier protein family 52, member 3	-1.3710	4.54E-05
ENSMUSG00000035551	Igfbpl1	4	insulin-like growth factor binding protein-like 1	-1.3022	1.08E-07
ENSMUSG00000012405	Rpl15	14	ribosomal protein L15	-1.2700	0.001382
ENSMUSG00000038997	Asb17	3	ankyrin repeat and SOCS box-containing 17	-1.2556	0.000156
ENSMUSG00000020061	Mybpc1	10	myosin binding protein C, slow-type	-1.2496	5.32E-05
ENSMUSG00000069171	Nr2f1	13	nuclear receptor subfamily 2, group F, member 1	-1.2412	4.09E-05
ENSMUSG00000045573	Penk	4	preproenkephalin	-1.2337	0.002035
ENSMUSG00000024868	Dkk1	19	dickkopf homolog 1 (Xenopus laevis)	-1.2324	1.13E-05
ENSMUSG00000018893	Mb	15	Myoglobin	-1.1955	3.24E-06
ENSMUSG00000028132	Tmem56	3	transmembrane protein 56	-1.1809	0.005723
ENSMUSG00000025488	Cox8b	7	cytochrome c oxidase, subunit VIIIb	-1.1717	6.16E-05
ENSMUSG00000068686	Cd59b	2	CD59b antigen	-1.1620	0.006512
ENSMUSG00000039200	Atf7ip2	16	activating transcription factor 7 interacting protein 2	-1.1565	0.000397
ENSMUSG00000035158	Mitf	6	microphthalmia-associated transcription factor	-1.1052	0.00042
ENSMUSG00000042219	Olfr631	7	olfactory receptor 631	-1.1040	0.006613
ENSMUSG00000031125	3830403N 18Rik	X	RIKEN cDNA 3830403N18 gene	-1.0910	0.025038
ENSMUSG00000035472	Slc25a21	12	solute carrier family 25 (mitochondrial oxodicarboxylate carrier), member 21	-1.0866	0.014794
ENSMUSG00000019787	Trdn	10	triadin	-1.0781	6.84E-07
ENSMUSG00000033737	Fndc3c1	X	fibronectin type III domain containing 3C1	-1.0672	8.05E-05
ENSMUSG00000023964	Calcr	6	calcitonin receptor	-1.0667	0.000169
ENSMUSG00000030762	Aqp8	7	aquaporin 8	-1.0530	0.013353

Ensembl ID:	Symbol:	Chrom:	Description:	Log_2FC:	P.Value:
ENSMUSG00000026357	Rgs18	1	regulator of G-protein signaling 18	-1.0468	0.017992
ENSMUSG00000041324	Inhba	13	inhibin beta-A	-1.0163	0.000459
ENSMUSG00000020460	Rps27a	11	ribosomal protein S27A	-1.0159	0.00233
ENSMUSG00000059742	Kcnh7	2	potassium voltage-gated channel, subfamily H (eag-related), member 7	-0.9919	8.03E-05
ENSMUSG00000031558	Slit2	5	slit homolog 2 (Drosophila)	-0.9871	2.44E-08
ENSMUSG00000074491	Clec4g	8	C-type lectin domain family 4, member g	-0.9857	2.52E-05
ENSMUSG00000042333	Tnfrsf14	4	tumor necrosis factor receptor superfamily, member 14 (herpesvirus entry mediator)	-0.9821	0.010138
ENSMUSG00000036687	Tmem184a	5	transmembrane protein 184a	-0.9805	0.001076
ENSMUSG00000036446	Lum	10	lumican	-0.9794	0.048496
ENSMUSG00000039579	Grin3a	4	glutamate receptor ionotropic, NMDA3A	-0.9720	6.21E-07
ENSMUSG00000075145	Olfr1155	2	olfactory receptor 1155	-0.9680	0.010133
ENSMUSG00000095528	Gm10375	14	predicted gene 10375	-0.9444	0.022939
ENSMUSG00000018659	Pnpo	11	pyridoxine 5'-phosphate oxidase	-0.9249	0.004907
ENSMUSG00000026100	Mstn	1	myostatin	-0.9244	0.013116
ENSMUSG00000053119	Chmp3	6	charged multivesicular body protein 3	-0.9186	0.006818
ENSMUSG00000032028	Nxpe2	9	family with sequence similarity 55, member B	-0.9170	0.022996
ENSMUSG00000061816	Myl1	1	myosin, light polypeptide 1	-0.9105	0.012749
ENSMUSG00000018983	E2f2	4	E2F transcription factor 2	-0.9097	0.000247
ENSMUSG00000052516	Robo2	16	roundabout homolog 2 (Drosophila)	-0.9067	2.38E-05
ENSMUSG00000001542	Ell2	13	elongation factor RNA polymerase II 2	-0.9039	0.001301
ENSMUSG00000000244	Tspan32	7	tetraspanin 32	-0.8990	0.016638
ENSMUSG00000090326	Gm17384	5	predicted gene, 17384	-0.8973	0.000603
ENSMUSG00000028883	Sema3a	5	sema domain, immunoglobulin domain (Ig), short basic domain, secreted, (semaphorin) 3A	-0.8941	9.87E-07
ENSMUSG00000031712	Il15	8	interleukin 15	-0.8940	0.00145
ENSMUSG00000029650	Slc46a3	5	solute carrier family 46, member 3	-0.8917	0.012711
ENSMUSG00000075307	Klhl41	2	kelch repeat and BTB (POZ) domain containing 10	-0.8915	0.000816
ENSMUSG00000073938	Olfr632	7	olfactory receptor 632	-0.8909	0.004545
ENSMUSG00000030048	Gkn3	6	gastrokine 3	-0.8885	0.001937
ENSMUSG00000070890	Gm12794	4	predicted gene 12794	-0.8845	0.002194
ENSMUSG00000027620	Rbm39	2	RNA binding motif protein 39	-0.8815	0.000696
ENSMUSG00000026532	Spta1	1	spectrin alpha 1	-0.8765	0.031537
ENSMUSG00000060499	Rpl10l	12	ribosomal protein L10-like	-0.8741	0.003779
ENSMUSG00000018654	Ikzf1	11	IKAROS family zinc finger 1	-0.8710	0.006988
ENSMUSG00000026686	Lmx1a	1	LIM homeobox transcription factor 1 alpha	-0.8684	0.008522
ENSMUSG00000053441	Adamts19	18	a disintegrin-like and metallopeptidase (reprolysin type) with thrombospondin type 1 motif, 19	-0.8653	0.000156

Ensembl ID:	Symbol:	Chrom:	Description:	Log_2FC:	P.Value:
ENSMUSG00000036295	Lrrn3	12	leucine rich repeat protein 3, neuronal	-0.8634	0.000156
ENSMUSG00000019890	Nts	10	neurotensin	-0.8571	0.012237
ENSMUSG00000027559	Car3	3	carbonic anhydrase 3	-0.8550	0.029583
ENSMUSG00000026815	Gfi1b	2	growth factor independent 1B	-0.8550	0.033986
ENSMUSG00000015354	Pcolce2	9	procollagen C-endopeptidase enhancer 2	-0.854	0.000306
ENSMUSG00000058331	Zfp85-rs1	13	zinc finger protein 85, related sequence 1	-0.8529	0.011325
ENSMUSG00000060636	Rpl35a	16	ribosomal protein L35A	-0.8524	0.024588
ENSMUSG00000034810	Scn7a	2	sodium channel, voltage-gated, type VII, alpha	-0.8463	0.016847
ENSMUSG00000047686	Zcchc5	X	zinc finger, CCHC domain containing 5	-0.8452	0.008625
ENSMUSG00000037872	Darc	1	Duffy blood group, chemokine receptor	-0.8442	0.003441
ENSMUSG00000044067	Gpr22	12	G protein-coupled receptor 22	-0.8386	2.11E-05
ENSMUSG00000073764	Gm12888	4	predicted gene 12888	-0.8374	4.38E-05
ENSMUSG00000022309	Angpt1	15	angiopoietin 1	-0.8342	0.000677
ENSMUSG00000044921	Rassf9	10	Ras association (RalGDS/AF-6) domain family (N-terminal) member 9	-0.8295	0.003028
ENSMUSG00000007653	Gabrb2	11	gamma-aminobutyric acid (GABA) A receptor, subunit beta 2	-0.8214	5.02E-05
ENSMUSG00000001348	Acp5	9	acid phosphatase 5, tartrate resistant	-0.8145	0.034052
ENSMUSG00000024448	H2-M10.1	17	histocompatibility 2, M region locus 10.1	-0.8144	0.007766
ENSMUSG00000014980	Tsen15	1	tRNA splicing endonuclease 15 homolog (S. cerevisiae)	-0.8107	0.003469
ENSMUSG00000027500	Stmn2	3	stathmin-like 2	-0.8079	0.008879
ENSMUSG00000059371	Olfr427	1	olfactory receptor 427	-0.8042	0.000692
ENSMUSG00000027820	Mme	3	membrane metallo endopeptidase	-0.8010	0.001894
ENSMUSG00000023903	Mmp25	17	matrix metallopeptidase 25	-0.8000	0.000335
ENSMUSG00000023328	Ache	5	acetylcholinesterase	-0.7994	0.000137
ENSMUSG00000079363	Gbp4	5	guanylate binding protein 4	-0.7937	0.010563
ENSMUSG00000059674	Cdh24	14	cadherin-like 24	-0.7912	0.001852
ENSMUSG00000061923	Odf1	15	outer dense fiber of sperm tails 1	-0.7904	0.001316
ENSMUSG00000057778	Cyb5d2	11	cytochrome b5 domain containing 2	-0.7896	0.036574
ENSMUSG00000034566	Atp5h	11	ATP synthase, H+ transporting, mitochondrial F0 complex, subunit d	-0.7862	0.010195
ENSMUSG00000035031	C8a	4	complement component 8, alpha polypeptide	-0.7774	0.005477
ENSMUSG00000056853	Olfr765	10	olfactory receptor 765	-0.773	0.013631
ENSMUSG00000063297	Luzp2	7	leucine zipper protein 2	-0.7728	0.017801
ENSMUSG00000068617	Efcab1	16	EF hand calcium binding domain 1	-0.7721	0.003809
ENSMUSG00000027004	Frzb	2	frizzled-related protein	-0.7716	0.001185
ENSMUSG00000053897	Slc39a8	3	solute carrier family 39 (metal ion transporter), member 8	-0.7691	0.007979
ENSMUSG00000004552	Ctse	1	cathepsin E	-0.7681	0.022571
ENSMUSG00000027273	Snap25	2	synaptosomal-associated protein 25	-0.7678	0.000898

Ensembl ID:	Symbol:	Chrom:	Description:	Log_2FC:	P.Value:
ENSMUSG00000022658	Tagln3	16	transgelin 3	-0.7668	0.000616
ENSMUSG00000034555	Tex16	X	testis expressed gene 16	-0.7646	0.000735
ENSMUSG00000019659	Ccdc12	9	coiled-coil domain containing 12	-0.7630	0.009235
ENSMUSG00000020638	Cmpk2	12	cytidine monophosphate (UMP-CMP) kinase 2, mitochondrial	-0.7625	0.021755
ENSMUSG00000059898	Dsc3	18	desmocollin 3	-0.7577	0.000348
ENSMUSG00000054626	Xlr	X	X-linked lymphocyte-regulated complex	-0.7567	0.04652
ENSMUSG00000071493	Vmn1r208	13	vomeronasal 1 receptor 208	-0.7565	0.013412
ENSMUSG00000096747	Olfr823	10	olfactory receptor 823	-0.7547	0.022869
ENSMUSG00000025573	6030468B 19Rik	11	RIKEN cDNA 6030468B19 gene	-0.7510	0.023917
ENSMUSG00000023093	Gm7257	9	predicted gene 7257	-0.7503	0.00032
ENSMUSG00000051361	6030498E 09Rik	X	RIKEN cDNA 6030498E09 gene	-0.7437	0.00289
ENSMUSG00000078942	Naip6	13	NLR family, apoptosis inhibitory protein 6	-0.7312	0.001002
ENSMUSG00000035875	AI182371	2	expressed sequence AI182371	-0.7292	0.001658
ENSMUSG00000057170	Prl3d1	13	prolactin family 3, subfamily d, member 1	-0.7242	0.008561
ENSMUSG00000055026	Gabrg3	7	gamma-aminobutyric acid (GABA) A receptor, subunit gamma 3	-0.7237	0.000183
ENSMUSG00000006235	Epor	9	erythropoietin receptor	-0.7210	0.025758
ENSMUSG00000039057	Myo16	8	myosin XVI	-0.7174	0.000113
ENSMUSG00000048697	Vmn1r26	6	vomeronasal 1 receptor 26	-0.7169	0.003378
ENSMUSG00000030222	Rerg	6	RAS-like, estrogen-regulated, growth-inhibitor	-0.7159	0.021202
ENSMUSG00000060044	Tmem26	10	transmembrane protein 26	-0.7135	0.002711
ENSMUSG00000016998	Svs4	2	seminal vesicle secretory protein 4	-0.7134	0.010077
ENSMUSG00000073680	Tmem88b	4	transmembrane protein 88B	-0.7093	0.004922
ENSMUSG00000027555	Car13	3	carbonic anhydrase 13	-0.7091	0.000803
ENSMUSG00000072774	Zfp951	5	zinc finger protein 951	-0.7029	0.005338
ENSMUSG00000020020	Usp44	10	ubiquitin specific peptidase 44	-0.7012	0.000345
ENSMUSG00000041216	Clvs1	4	clavesin 1	-0.7007	0.000285

Table B2: Genes upregulated in the heart at E11.5 following mesodermal ablation of *Chd7*

Ensembl ID:	Symbol:	Chrom:	Description:	Log_2FC:	P.Value:
ENSMUSG00000020891	Alox8	11	arachidonate 8-lipoxygenase	0.7030	0.013438
ENSMUSG00000075144	Olfr1156	2	olfactory receptor 1156	0.7055	0.016192
ENSMUSG00000049350	Zg16	7	zymogen granule protein 16	0.7056	0.001515
ENSMUSG00000095180	Rhox5	X	reproductive homeobox 5	0.7060	0.000503
ENSMUSG00000079015	Serpina1c	12	serine (or cysteine) peptidase inhibitor, clade A, member 1C	0.7075	0.009398
ENSMUSG00000009376	Met	6	met proto-oncogene	0.7145	0.000382
ENSMUSG00000003541	Ier3	17	immediate early response 3	0.7193	0.040657
ENSMUSG00000068947	Olfr366	2	olfactory receptor 366	0.7215	0.007234
ENSMUSG00000029309	Sparcl1	5	SPARC-like 1	0.7226	0.000106
ENSMUSG00000043421	Hilpda	6	hypoxia inducible lipid droplet associated	0.7263	0.011431
ENSMUSG00000028128	F3	3	coagulation factor III	0.7282	0.019032
ENSMUSG00000095241	Gm5478	15		0.7317	5.85E-05
ENSMUSG00000018822	Sfrp5	19	secreted frizzled-related sequence protein 5	0.7334	0.002257
ENSMUSG00000056158	Car10	11	carbonic anhydrase 10	0.7354	0.000179
ENSMUSG00000038092	Hsd3b5	3	hydroxy-delta-5-steroid dehydrogenase, 3 beta- and steroid delta-isomerase 5	0.7414	0.02908
ENSMUSG00000097451	Rian	NA	NA	0.7457	8.35E-05
ENSMUSG00000065353	Snora73b	4	small nucleolar RNA, H/ACA box 73b	0.7490	0.022449
ENSMUSG00000053420	Gm4792	10	predicted gene 4792	0.7503	0.000753
ENSMUSG00000021638	Ocln	13	occludin	0.7548	0.001376
ENSMUSG00000005413	Hmox1	8	heme oxygenase (decycling) 1	0.7569	0.009623
ENSMUSG00000093007	Mir15a	14	microRNA 15a	0.7577	0.011795
ENSMUSG00000024479	Mal2	15	mal, T cell differentiation protein 2	0.7583	0.029476
ENSMUSG00000074158	9830147E 19Rik	7	RIKEN cDNA 9830147E19 gene	0.7669	0.003389
ENSMUSG00000023043	Krt18	15	keratin 18	0.7683	0.008522
ENSMUSG00000013584	Aldh1a2	9	aldehyde dehydrogenase family 1, subfamily A2	0.7697	0.003966
ENSMUSG00000051940	5031410I0 6Rik	5	RIKEN cDNA 5031410I06 gene	0.7762	0.001219
ENSMUSG00000039215	Svs1	6	seminal vesicle secretory protein 1	0.7815	0.014586
ENSMUSG00000058904	Olfr1413	1	olfactory receptor 1413	0.7827	0.003613
ENSMUSG00000074968	Ano3	2	anoctamin 3	0.7834	0.000396
ENSMUSG00000066363	Serpina3f	12	serine (or cysteine) peptidase inhibitor, clade A, member 3F	0.7851	0.010171
ENSMUSG00000030787	Lyve1	7	lymphatic vessel endothelial hyaluronan receptor 1	0.7874	0.001096
ENSMUSG00000046210	Olfr735	14	olfactory receptor 735	0.7882	0.000877
ENSMUSG00000066677	Pydc3	1	pyrin domain containing 3	0.7965	0.002785
ENSMUSG00000070529	Wfdc10	2	WAP four-disulfide core domain 10	0.8057	0.011004
ENSMUSG00000055780	Usp26	X	ubiquitin specific peptidase 26	0.8135	0.000713
ENSMUSG00000040405	Havcr1	11	hepatitis A virus cellular receptor 1	0.8153	0.038827
ENSMUSG00000049528	Olfr429	1	olfactory receptor 429	0.8199	0.004907

Ensembl ID:	Symbol:	Chrom:	Description:	Log_2FC:	P.Value:
ENSMUSG00000096819	Srsy	Y	Serine-rich secreted Y-linked protein	0.8223	0.002995
ENSMUSG00000061126	Cyp4f39	17	cytochrome P450, family 4, subfamily f, polypeptide 39	0.8271	0.000437
ENSMUSG00000009654	Oit3	10	oncoprotein induced transcript 3	0.8320	0.005785
ENSMUSG00000021367	Edn1	13	endothelin 1	0.8365	0.005362
ENSMUSG00000056973	Ces1d	8	carboxylesterase 1D	0.8474	0.000698
ENSMUSG00000020427	Igfbp3	11	insulin-like growth factor binding protein 3	0.8543	0.00012
ENSMUSG00000070867	Trabd2b	4	predicted gene 12824	0.8600	2.19E-06
ENSMUSG00000028341	Nr4a3	4	nuclear receptor subfamily 4, group A, member 3	0.8613	0.011819
ENSMUSG00000070933	Speer4d	5	spermatogenesis associated glutamate (E)-rich protein 4d	0.8779	0.00011
ENSMUSG00000024395	Lims2	18	LIM and senescent cell antigen like domains 2	0.8783	0.018917
ENSMUSG00000005125	Ndrg1	15	N-myc downstream regulated gene 1	0.8825	0.047623
ENSMUSG00000054966	Ifltd1	6	intermediate filament tail domain containing 1	0.8839	0.000238
ENSMUSG00000054258	Gm5082	13	predicted gene 5082	0.8924	0.022338
ENSMUSG00000024273	2700062C 07Rik	18	RIKEN cDNA 2700062C07 gene	0.8932	0.001515
ENSMUSG00000050092	Sprr2b	3	small proline-rich protein 2B	0.8939	0.000757
ENSMUSG00000021219	Rgs6	12	regulator of G-protein signaling 6	0.8952	4.07E-06
ENSMUSG00000061306	Slc38a10	11	solute carrier family 38, member 10	0.8953	0.001151
ENSMUSG00000022949	Clic6	16	chloride intracellular channel 6	0.9168	0.000488
ENSMUSG00000021943	Gdf10	14	growth differentiation factor 10	0.9221	0.000475
ENSMUSG00000096109	Olfr1537	9	olfactory receptor 1537, pseudogene 1	0.9242	0.003063
ENSMUSG00000053519	Kcnip1	11	Kv channel-interacting protein 1	0.9434	4.62E-05
ENSMUSG00000035165	Kcne3	7	potassium voltage-gated channel, Isk-related subfamily, gene 3	0.9551	0.028108
ENSMUSG00000020159	Gabrp	11	gamma-aminobutyric acid (GABA) A receptor, pi	0.9618	0.014963
ENSMUSG00000070686	C87414	5	expressed sequence C87414	0.9826	0.001085
ENSMUSG00000075202	Olfr1042	2	olfactory receptor 1042	0.9863	0.003242
ENSMUSG00000065944	Rnu2-10	11	U2 spliceosomal RNA	0.9884	0.030422
ENSMUSG00000039145	Camk1d	2	calcium/calmodulin-dependent protein kinase ID	0.9985	0.000176
ENSMUSG00000024087	Cyp1b1	17	cytochrome P450, family 1, subfamily b, polypeptide 1	1.0252	0.000516
ENSMUSG00000051663	Pcdhb1	18	protocadherin beta 1	1.0293	0.000159
ENSMUSG00000027833	Shox2	3	short stature homeobox 2	1.0311	0.004779
ENSMUSG00000038253	Hoxa5	6	homeobox A5	1.0373	0.001617
ENSMUSG00000031461	Myom2	8	myomesin 2	1.0488	0.000249
ENSMUSG00000066747	Olfr878	9	olfactory receptor 878	1.0570	0.001186
ENSMUSG00000058952	Cfi	3	complement component factor i	1.1009	0.000113
ENSMUSG00000066272	Olfr559	7	olfactory receptor 559	1.1289	0.006041
ENSMUSG00000040621	Gemin8	X	gem (nuclear organelle) associated protein 8	1.1387	0.01319
ENSMUSG00000023885	Thbs2	17	thrombospondin 2	1.1814	0.002338
ENSMUSG00000094637	Vmn1r204	13	vomeronasal 1 receptor 204	1.1849	0.000483

Ensembl ID:	Symbol:	Chrom:	Description:	Log_2FC:	P.Value:
ENSMUSG00000022103	Gfra2	14	glial cell line derived neurotrophic factor family receptor alpha 2	1.1899	8.69E-06
ENSMUSG00000030790	Adm	7	adrenomedullin	1.2141	0.001756
ENSMUSG00000095901	Olfr538	7	olfactory receptor 538	1.2193	0.009645
ENSMUSG00000026471	Mr1	1	major histocompatibility complex, class I-related	1.2335	1.12E-06
ENSMUSG00000024164	C3	17	complement component 3	1.2641	0.02604
ENSMUSG00000074852	Hpse2	19	heparanase 2	1.4621	0.000145
ENSMUSG00000025196	Cpn1	19	carboxypeptidase N, polypeptide 1	1.4687	6.39E-06
ENSMUSG00000053930	Shisa6	11	shisa homolog 6 (Xenopus laevis)	1.4714	0.000489
ENSMUSG00000027861	Casq2	3	calsequestrin 2	1.6910	1.98E-08
ENSMUSG00000027942	4933434E 20Rik	3	RIKEN cDNA 4933434E20 gene	1.7283	9.34E-05
ENSMUSG00000029322	Plac8	5	placenta-specific 8	1.8213	5.56E-06

Table B3: Genes downregulated in the heart at E13.5 following mesodermal ablation of *Chd7*

Ensembl ID:	Symbol:	Chrom:	Description:	Log_2FC	P.Value
ENSMUSG00000039114	Nrn1	13	neuritin 1	-1.7590	0.000601
ENSMUSG00000041235	Chd7	4	chromodomain helicase DNA binding protein 7	-1.5832	1.41E-08
ENSMUSG00000069171	Nr2f1	13	nuclear receptor subfamily 2, group F, member	-1.4321	8.43E-06
ENSMUSG00000023964	Calcr	6	calcitonin receptor	-1.3886	1.04E-05
ENSMUSG00000061816	Myl1	1	myosin, light polypeptide 1	-1.3862	0.000619
ENSMUSG00000026357	Rgs18	1	regulator of G-protein signaling 18	-1.1937	0.008457
ENSMUSG00000029372	Ppbp	5	pro-platelet basic protein	-1.1640	0.007009
ENSMUSG00000000320	Alox12	11	arachidonate 12-lipoxygenase	-1.1156	0.005136
ENSMUSG00000073007	Fam46d	X	family with sequence similarity 46, member D	-1.1136	1.24E-05
ENSMUSG00000019906	Lin7a	10	lin-7 homolog A (C. elegans)	-1.0430	0.000947
ENSMUSG00000073414	AU023871	17	expressed sequence AU023871	-1.0338	0.000555
ENSMUSG00000039070	Cpa4	6	carboxypeptidase A4	-1.0257	0.002821
ENSMUSG00000030054	Gp9	6	glycoprotein 9 (platelet)	-1.0243	0.004286
ENSMUSG00000036295	Lrrn3	12	leucine rich repeat protein 3, neuronal	-1.0178	2.86E-05
ENSMUSG00000046080	Clec9a	6	C-type lectin domain family 9, member a	-0.9958	0.001965
ENSMUSG00000023993	Treml1	17	triggering receptor expressed on myeloid cells-like 1	-0.9882	0.001068
ENSMUSG00000031712	Il15	8	interleukin 15	-0.9556	0.000839
ENSMUSG00000034028	Cd226	18	CD226 antigen	-0.9521	0.001591
ENSMUSG00000018893	Mb	15	myoglobin	-0.9403	4.81E-05
ENSMUSG00000027559	Car3	3	carbonic anhydrase 3	-0.9383	0.018601
ENSMUSG00000016255	Tubb1	2	tubulin, beta 1 class VI	-0.9360	0.010849
ENSMUSG00000049630	C1ql3	2	C1q-like 3	-0.9282	0.000148
ENSMUSG00000059742	Kcnh7	2	potassium voltage-gated channel, subfamily H (eag-related), member 7	-0.9195	0.000171
ENSMUSG00000090326	Gm17384	5	predicted gene, 17384	-0.8545	0.000917
ENSMUSG00000007682	Dio2	12	deiodinase, iodothyronine, type II	-0.8515	0.000568
ENSMUSG00000026824	Kcnj3	2	potassium inwardly-rectifying channel, subfamily J, member 3	-0.8471	0.000328
ENSMUSG00000021675	F2rl2	13	coagulation factor II (thrombin) receptor-like 2	-0.8339	0.045735
ENSMUSG00000007653	Gabrb2	11	gamma-aminobutyric acid (GABA) A receptor, subunit beta 2	-0.8292	4.54E-05
ENSMUSG00000026100	Mstn	1	myostatin	-0.8267	0.023805
ENSMUSG00000033737	Fndc3c1	X	fibronectin type III domain containing 3C1	-0.8239	0.000895
ENSMUSG00000020120	Plek	11	pleckstrin	-0.8206	0.006375
ENSMUSG00000069515	Lyz1	10	lysozyme 1	-0.8151	0.01912
ENSMUSG00000030159	Clec1b	6	C-type lectin domain family 1, member b	-0.8114	0.017341
ENSMUSG00000019787	Trdn	10	triadin	-0.8000	2.28E-05
ENSMUSG00000034664	Itga2b	11	integrin alpha 2b	-0.7963	0.010892
ENSMUSG00000028132	Tmem56	3	transmembrane protein 56	-0.7850	0.049338
ENSMUSG00000020061	Mybpc1	10	myosin binding protein C, slow-type	-0.7775	0.003493

Ensembl ID:	Symbol:	Chrom:	Description:	Log_2FC	P.Value
ENSMUSG00000027022	Xirp2	2	xin actin-binding repeat containing 2	-0.7727	0.001448
ENSMUSG00000030513	Pcsk6	7	proprotein convertase subtilisin/kexin type 6	-0.7685	0.000395
ENSMUSG00000006389	Mpl	4	myeloproliferative leukemia virus oncogene	-0.7675	0.001706
ENSMUSG00000051361	6030498E09Rik	X	RIKEN cDNA 6030498E09 gene	-0.7666	0.002309
ENSMUSG00000001865	Cpa3	3	carboxypeptidase A3, mast cell	-0.7648	0.043466
ENSMUSG00000081420	Olfr29-ps1	4	olfactory receptor 29, pseudogene 1	-0.7625	0.007148
ENSMUSG00000044573	Acp1	12	acid phosphatase 1, soluble	-0.7608	0.007456
ENSMUSG00000055026	Gabrg3	7	gamma-aminobutyric acid (GABA) A receptor, subunit gamma 3	-0.7523	0.000125
ENSMUSG00000076009	Mir688	15	microRNA 688	-0.7502	0.013937
ENSMUSG00000021613	Hapln1	13	hyaluronan and proteoglycan link protein 1	-0.7425	0.002363
ENSMUSG00000036144	Meox2	12	mesenchyme homeobox 2	-0.7408	0.045293
ENSMUSG00000021765	Fst	13	follistatin	-0.7367	0.002261
ENSMUSG00000045613	Chrm2	6	cholinergic receptor, muscarinic 2, cardiac	-0.7344	0.001451
ENSMUSG00000022129	Dct	14	dopachrome tautomerase	-0.7333	0.018173
ENSMUSG00000027971	Ndst4	3	N-deacetylase/N-sulfotransferase (heparin glucosaminyl) 4	-0.7284	0.008727
ENSMUSG00000044067	Gpr22	12	G protein-coupled receptor 22	-0.7236	9.98E-05
ENSMUSG00000010803	Gabra1	11	gamma-aminobutyric acid (GABA) A receptor, subunit alpha 1	-0.7212	0.00565
ENSMUSG00000094808	1810009J06Rik	6	RIKEN cDNA 1810009J06 gene	-0.7082	0.004729
ENSMUSG00000028883	Sema3a	5	sema domain, immunoglobulin domain (Ig), short basic domain, secreted, (semaphorin) 3A	-0.7044	1.63E-05

Table B4: Genes upregulated in the heart at E13.5 following mesodermal ablation of *Chd7*

Ensembl ID:	Symbol:	Chrom:	Description:	Log_2FC:	P.Value:
ENSMUSG00000024935	Slc1a1	19	solute carrier family 1 (neuronal/epithelial high affinity glutamate transporter, system Xag), member 1	0.7050	0.00653
ENSMUSG00000090084	Srpx	X	sushi-repeat-containing protein	0.71538	0.011908
ENSMUSG00000094637	Vmn1r204	13	vomeronasal 1 receptor 204	0.71874	0.016967
ENSMUSG00000023885	Thbs2	17	thrombospondin 2	0.7229	0.04108
ENSMUSG00000054272	Zscan4c	7	zinc finger and SCAN domain containing 4C	0.7360	0.037541
ENSMUSG00000022180	Slc7a8	14	solute carrier family 7 (cationic amino acid transporter, y+ system), member 8	0.7479	0.000112
ENSMUSG00000024395	Lims2	18	LIM and senescent cell antigen like domains 2	0.7641	0.037096
ENSMUSG00000000983	Wfdc18	11	extracellular proteinase inhibitor	0.7653	0.024953
ENSMUSG00000074604	Mgst2	3	microsomal glutathione S-transferase 2	0.7662	0.003838
ENSMUSG00000053930	Shisa6	11	shisa homolog 6 (Xenopus laevis)	0.7694	0.035461
ENSMUSG00000039304	Tnfsf10	3	tumor necrosis factor (ligand) superfamily, member 10	0.7708	0.016122
ENSMUSG00000073530	Pappa2	1	pappalysin 2	0.7767	0.011317
ENSMUSG00000058147	Xlr3c	X	X-linked lymphocyte-regulated 3C	0.7880	0.039376
ENSMUSG00000090166	Ear10	14	eosinophil-associated, ribonuclease A family, member 10	0.7931	0.010262
ENSMUSG00000040564	Apoc1	7	apolipoprotein C-I	0.7975	0.010643
ENSMUSG00000022949	Clic6	16	chloride intracellular channel 6	0.7985	0.001558
ENSMUSG00000028415	Spink4	4	serine peptidase inhibitor, Kazal type 4	0.8016	0.000465
ENSMUSG00000039145	Camk1d	2	calcium/calmodulin-dependent protein kinase ID	0.8113	0.001127
ENSMUSG00000022661	Cd200	16	CD200 antigen	0.8163	0.001337
ENSMUSG00000073811	Ifna12	4	interferon alpha 12	0.8216	0.027747
ENSMUSG00000052217	Hbb-bh1	7	hemoglobin Z, beta-like embryonic chain	0.8421	0.015833
ENSMUSG00000032496	Ltf	9	lactotransferrin	0.8481	0.018048
ENSMUSG00000021638	Ocln	13	occludin	0.8496	0.000507
ENSMUSG00000026471	Mr1	1	major histocompatibility complex, class I-related	0.8561	7.08E-05
ENSMUSG00000029088	Kcnip4	5	Kv channel interacting protein 4	0.8600	0.004185
ENSMUSG00000074852	Hpse2	19	heparanase 2	0.8635	0.009457
ENSMUSG00000020891	Alox8	11	arachidonate 8-lipoxygenase	0.8728	0.003362
ENSMUSG00000022902	Stfa2	16	stefin A2	0.8830	0.012863
ENSMUSG00000031461	Myom2	8	myomesin 2	0.8968	0.000998
ENSMUSG00000021367	Edn1	13	endothelin 1	0.9035	0.003137
ENSMUSG00000055312	0610012H 03Rik	2	RIKEN cDNA 0610012H03 gene	0.9106	3.92E-06
ENSMUSG00000058952	Cfi	3	complement component factor i	0.9620	0.000408
ENSMUSG00000023078	Cxcl13	5	chemokine (C-X-C motif) ligand 13	1.0092	0.031794
ENSMUSG00000056054	S100a8	3	S100 calcium binding protein A8 (calgranulin A)	1.0283	0.007609

Ensembl ID:	Symbol:	Chrom:	Description:	Log_2FC:	P.Value:
ENSMUSG00000069041	Slc25a31	3	solute carrier family 25 (mitochondrial carrier; adenine nucleotide translocator), member 31	1.0969	0.03699
ENSMUSG00000073125	Xlr3b	X	X-linked lymphocyte-regulated 3B	1.1154	0.013755
ENSMUSG00000017737	Mmp9	2	matrix metallopeptidase 9	1.1458	0.000173
ENSMUSG00000072601	Ear1	14	eosinophil-associated, ribonuclease A family, member 1	1.1506	0.001791
ENSMUSG00000031362	Xlr4c	X	X-linked lymphocyte-regulated 4C	1.1589	0.005512
ENSMUSG00000059657	Stfa2l1	16	stefin A2 like 1	1.1889	0.004943
ENSMUSG00000071561	BC100530	16	cDNA sequence BC100530	1.2444	0.01268
ENSMUSG00000054258	Gm5082	13	predicted gene	1.2495	0.002798
ENSMUSG00000032484	Ngp	9	neutrophilic granule protein	1.3976	0.012473
ENSMUSG00000022487	Gtsf1	15	gametocyte specific factor 1	1.4706	3.09E-05
ENSMUSG00000029322	Plac8	5	placenta-specific 8	1.5681	2.99E-05
ENSMUSG00000069792	Wfdc17	11	predicted gene 11428	1.6059	7.76E-06
ENSMUSG00000025196	Cpn1	19	carboxypeptidase N, polypeptide 1	1.9251	2.32E-07